Tribological and surface analytical measurements on the reaction mechanism of forming additives

zur Erlangung des akademischen Grades eines DOKTORS DER NATURWISSENSCHAFTEN (Dr. rer. nat.) der Fakultät für Naturwissenschaften der Universität Paderborn

genehmigte DISSERTATION

von

Dipl.-Chemiker Christoph Müller

geboren am 10.03.1982 in Moers

im Januar 2018

Erstgutachter:	Prof. Dr.-Ing. Guido Grundmeier
Zweitgutachter:	Prof. Dr.-Ing. Werner Homberg
Tag der Einreichung:	09.01.2018
Tag der mündlichen Prüfung:	20.03.2018

Danksagung/Acknowledgement

Diese Arbeit entstand in der Dortmunder OberflächenCentrum GmbH (DOC GmbH) (später thyssenkrupp Steel Europe AG (TKSE AG)), und in der Arbeitsgruppe von Herrn Prof. Dr.-Ing. Guido Grundmeier im Department für Technische und Makromolekulare Chemie an der Universität Paderborn.

Ich danke der DOC GmbH und der TKSE AG für die finanzielle Unterstützung während der Arbeit, für die umfangreiche Bereitstellung von Materialien und für die Möglichkeit des Zugriffs auf den vielseitigen Gerätepark. Ich danke dem Laborteam von Frau Dr. Brinkbäumer für die Unterstützung bei der Verarbeitung endloser Stahlbleche, den DOCtorandInnen für die gegenseitigen Aufmunterungen und Unterhaltungen, sowie den Mitarbeitern der Umformtechnik und der Oberflächenanalytik, insbesondere Frau Wierhake für die Durchführung von WLI und XPS Messungen, Herrn Huchler für zahlreiche Streifenzüge und Herrn Weiß für die ToF-SIMS-Messungen.

Bedanken möchte ich mich auch bei Herrn Prof. Manfred Neumann (Universität Osnabrück) für die Möglichkeit XPS-Messungen in seinem Arbeitskreis durchzuführen.

Besonders bedanken möchte ich mich bei Herrn Dr. Müller für die andauernde Unterstützung und zahlreichen nützlichen Anregungen, ebenso wie bei Frau Dr. Brinkbäumer für die Unterstützung meiner Arbeit und die inspirierende Teamführung. Vielen Dank auch an meinem Betreuer Herrn Dr. Flechtner für viele hilfreiche Diskussionen.

Ganz besonders möchte ich Herrn Prof. Dr.-Ing. Guido Grundmeier für die Aufnahme in seinen Arbeitskreis, die Betreuung dieser Arbeit auch über diesen langen Zeitraum und die hilfreichen Diskussionen danken.

Herrn Prof. Dr.-Ing. Werner Homberg danke ich für die Übernahme des Koreferates, Frau Prof. Dr. Sabine Fechner für den Vorsitz der Prüfungskommission sowie Herrn PD Dr. rer. nat. Hans Egold für die Tätigkeit als 3. Prüfer.

Bei allen Mitarbeitern des AK Grundmeier möchte ich mich für die gegenseitige Unterstützung und die herausragende Atmosphäre bedanken. Insbesondere danke ich Frau Dr. Katharina Pohl für die Hilfestellungen bei Raman- und Kelvinsonden-Messungen, Frau Dr. Agatha Pomorska für die Zusammenarbeit an der QCM, Herrn Dr. Berkem Özkaya für die Messungen am AFM, Herrn Dr. Christian Kunze und Herrn Markus Voigt für die Aufnahme von XPS-Spektren und Frau Sandra Szillies für die angenehme Atmosphäre im Büro und zahlreiche nützliche Diskussionen.

Darüber hinaus möchte ich Herrn Dr. Stephan Cludius-Brandt für die zahlreichen und nützlichen Anregungen und Diskussionen bedanken, ohne die diese Arbeit wohl kein Ende gefunden hätte.

Nicht zuletzt gilt mein ganz besonderer Dank meiner Frau Dr. Stefanie Müller für ihre immerwährende Unterstützung, für hilfreiche Anregungen und Diskussionen. Ohne Sie wäre diese Arbeit nicht möglich gewesen.

Content

1 Introduction

This chapter provides a basic overview on the broad field of tribology. First, a short historical background is given to show the origins of interest and the actual working fields.

Afterwards it contributes a fundamental background of tribology to establish the basic knowledge of this work. Terms like friction, wear and lubrication are introduced and mechanisms of touching surfaces are explained.

In more detail, it describes the basics of steel sheet processing from a practical point of view. The basics and application methods of thin and ultrathin lubrication layers are also explained which leads to the explanation of oil-based lubrication on galvanized steel sheets as the main topic of this thesis.

The following parts describe the state of the art of additive investigation in lubrication. In addition, the ancillary corrosive resistance characteristics of lubrication films are described.

1.1 History of tribology

"The word *tribology* is based upon the Greek word *tribos*, meaning rubbing" [1].

According to this definition, the topic tribology describes all kinds of contacted surfaces in relative motion and "includes the study of lubricants, lubrication, friction, wear and bearings" [1]. This knowledge is important for almost every machine or transportation system. The importance was already recognized in ancient Egypt and used for example to reduce the friction and therefore the required workforce while moving heavy statues and stone blocks. This was achieved via the pouring of water as a lubricant in front of sledges.[1, 2]

Leonardo da Vinci (1452-1519) achieved the first scientific approach in the field of tribology during the Renaissance. He simply experimented with dragging objects along plain and smooth surfaces with varying weights. However, his conclusions inspired the first two laws of friction, namely:

1. The force of friction is directly proportional to the applied load.

Formula 1. First law of friction [1, 3]

2. The force of friction is independent of the apparent area of contact.

Formula 2. Second law of friction [1, 3]

These laws are not named after Leonardo da Vinci but rather after Guillaume Amontons (1663-1705), who regained this knowledge during the beginning industrial revolution in 1699 [1, 2]. So far, the nature of the lubricant was little described and developed. However, with the industrial revolution knowledge in this topic made a large progress. This progress was achieved partly because of findings in the field of fluid dynamics and also due to the increasing availability of mineral oils [2]. Sir Isaac Newton (1642-1737) defined the quotient of shear stress and shear rate as internal friction of a streaming fluid (1687) [2].

Scientists like von Segner (1758) and Coulomb (1785) provided more detailed analysis and interpretation of tribology in the late eighteenth century [1, 2].

From the nineteenth century up to today, the requirements of tribological systems became significantly more complex. Additives were frequently utilized to increase special characteristics of lubricants and synthetic lubricants were commonly used.

Due to the work of Osborne Reynolds (1842-1912) and importantly Richard Stribeck (1861-1950) who reported the connection of friction with speed and contact pressure (Figure 1), the hydrodynamic lubrication was further and more deeply understood.[2]

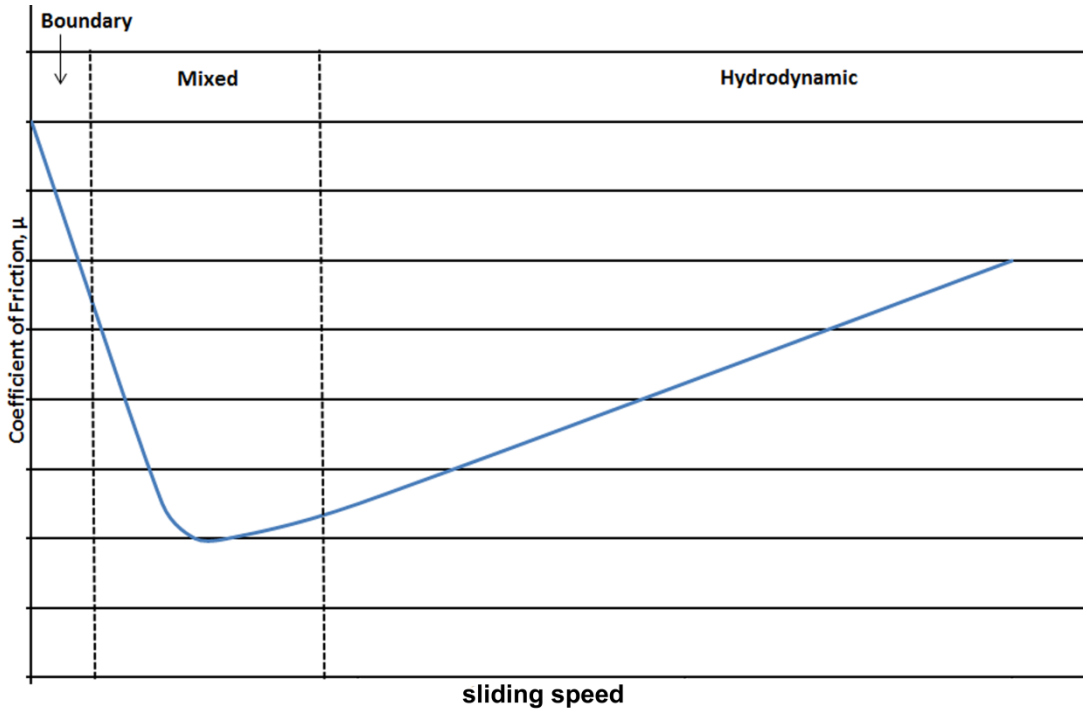

Figure 1. The Stribeck curve [4]

The Stribeck curve reveals that with beginning of relative motion, the coefficient of friction (COF) decreases. This region of "boundary lubrication" is dominated by the overcoming of contact interaction. With increasing sliding speed, a growing lubricant film develops and the coefficient of friction is rapidly decreased. A minimum of friction is reached in a region called "mixed lubrication". Afterwards, the hydrodynamic friction increases nearly linear with higher sliding speed.[4, 5]

1.2 Fundamentals of tribology

The main importance of tribology in engineering science is the minimization of friction and wear related energy and material losses. Working in this multidisciplinary field is based on the general understanding of major terms and definitions which will be introduced in this chapter. More detailed information can be found for instance in "Lubricants and Lubrication" [6], "Tribologie Handbuch" [7], "Kontaktmechanik und Reibung" [3], "Fundamentals of tribology" [8] or "Handbook of Tribology" [5].

Each tribological system (tribosystem) consists of a material pair (main body and counter body), an intermediate (lubricant) and the environment. This system is influenced by various variables such as type, speed and duration of movement, the involved forces and temperature. Resulting tribological parameters like friction, wear and contact temperature

can be measured. These characteristics are highly affected through numerous parameters of surface and contact geometry and lubrication.[6, 7]

As one of these parameters, the surface roughness is of great importance, it is described by specific surface roughness values. The arithmetic roughness index $\mathbf{R_a}$ (Formula 3 and Figure 2) is equal to the area included between the profile and the midline.[7]

$$R_a = \frac{1}{l}\int_{o}^{l} z\,(x)|\,dx$$

Formula 3. Mean roughness index R_a with reference length l

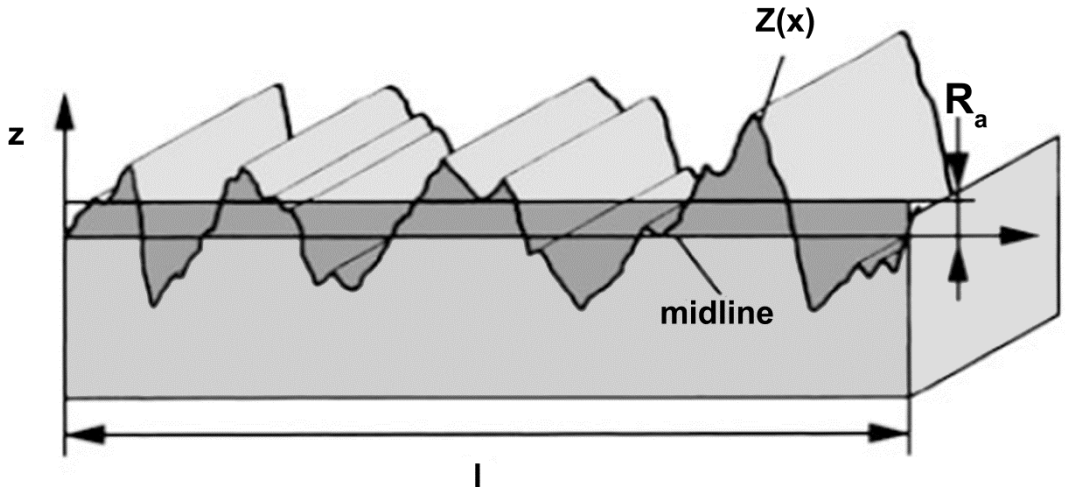

Figure 2. Schematic roughness profile with mean roughness index R_a and reference length l [9]

The averaged depth of roughness $\mathbf{R_z}$ (Formula 5 and Figure 4) is the arithmetic mean of single depths of roughness of a connected range $\mathbf{l_g}$. It is common to use $\mathbf{R_z}$ together with the maximal depth of roughness $\mathbf{R_{max}}$ (Figure 4 and Figure 5). The square mean value of profile deviation from the midline is the square mean roughness index $\mathbf{R_q}$ (Formula 4 and Figure 3).[7]

$$R_q = \sqrt{\frac{1}{l}\int_{0}^{l} z\,(x)^2|\,dx}$$

Formula 4. Square mean roughness index R_q

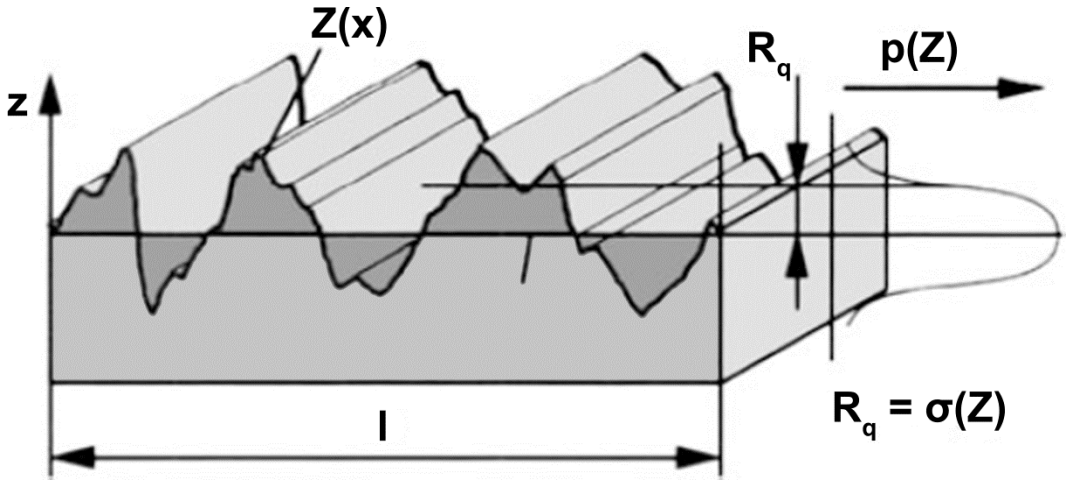

Figure 3. Schematic roughness profile with square mean roughness index R_q [9]

$$R_z = \frac{1}{5}\sum_{i=1}^{5} Z_i$$

Formula 5. Averaged depth of roughness R_z

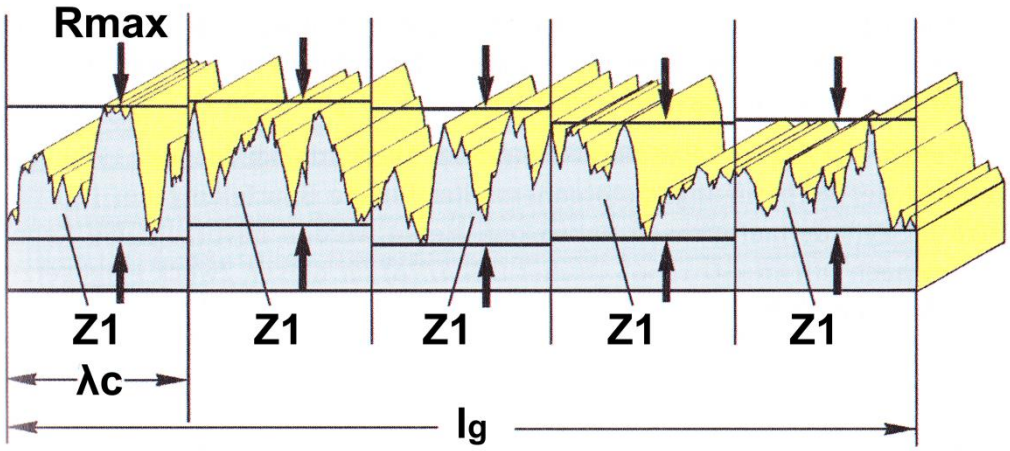

Figure 4. Schematic roughness profile with averaged depth of roughness R_z and maximal depth of roughness R_{max} [10]

The depth of roughness $\mathbf{R_t}$ (Figure 5) is defined as the vertical difference between the lowest and highest point.

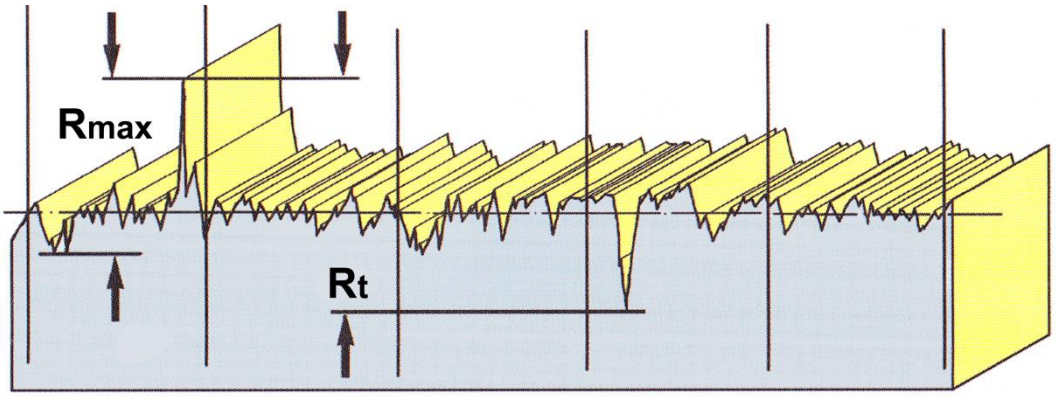

Figure 5. Schematic roughness profile with depth of roughness R_t and maximal depth of roughness R_{max} [10]

The averaged smoothing depth $\mathbf{R_p}$ (Formula 6 and Figure 6) is comparable to the averaged depth of roughness. It averages the distance between the midline and the highest peak $\mathbf{p_i}$ over five segments.

$$R_p = \frac{1}{5}\sum_{i=1}^{5} p_i$$

Formula 6. Averaged smoothing depth R_p

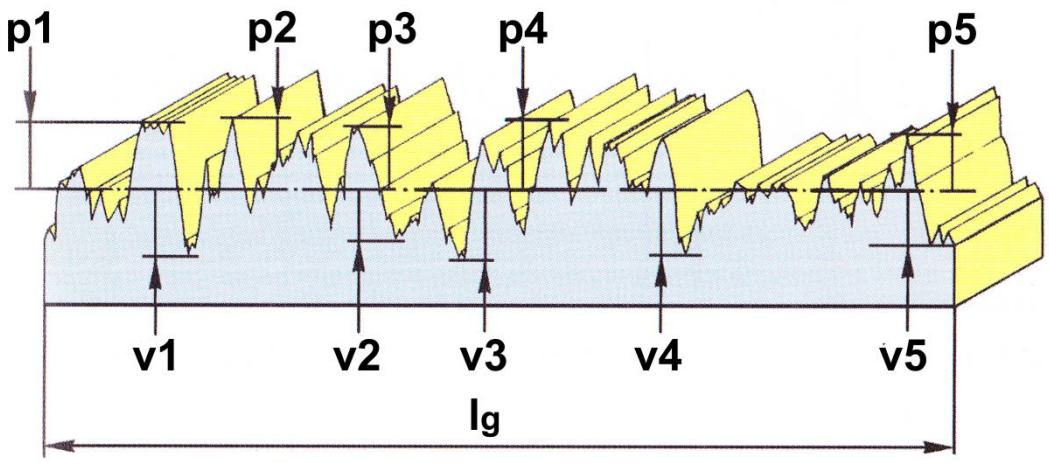

Figure 6. Schematic roughness profile with averaged smoothing depth R_p and averaged scoring depth R_v [10]

The calculation for $\mathbf{R_v}$ (Formula 7and Figure 6) is done in a similar manner as the calculation for $\mathbf{R_p}$.

$$R_v = \frac{1}{5}\sum_{i=1}^{5} v_i$$

Formula 7. Averaged scoring depth R_v

At this point, it is necessary to clarify the meanings of friction and wear. As mentioned in chapter 1.1, the laws of friction describe the resistance of a material pair to relative motion.

A parameter to describe the degree of friction is the friction coefficient **μ**, which pictures the ratio of the friction force $\mathbf{F_R}$ to the normal force $\mathbf{F_N}$.

$$\mu = \frac{F_R}{F_N}$$

Formula 8. Coefficient of friction described as ratio of friction force F_R to normal force F_N

The laws of friction (Formula 1 and Formula 2) are obeyed with some exceptions over a wide array of conditions.[5]

Considering the type of relative motion there are three categories of friction. Sliding friction, rolling friction and spinning friction, which can also overlap in technical applications. Examples for sliding friction are various kinds of bearings, rolling friction can be found for instance on wheels on rails or rack-wheels.

A phenomenon often observed in sliding friction is the so-called "stick-slip effect". This effect describes the oscillation of the friction coefficient in a sliding contact influenced by the relation of static friction and dynamic friction. Static friction correlates with the force necessary to overcome the initial resistance between two bodies. The dynamic friction describes the conditions of relative motion between two bodies.

Surface active additives can equalize the static and dynamic friction and by this way reduce the stick-slip effect.[6, 7]

The previously shown stribeck diagram (Figure 1) introduced further terms of tribological systems. Dry friction, boundary friction, fluid friction and mixed friction describe the contact state of friction partners. In dry friction, base body and counter body are in direct contact. Boundary friction describes systems with an ultrathin surface active lubrication layer between base body and counter body. A hydrostatic lubricant layer separates the friction partners in the contact state of fluid friction. Mixed friction describes a combination of dry and lubricated friction.[7]

After having introduced the fundamental terms of friction, the following part will define the basic terms of wear.

Wear is defined as the proceeding material loss of a body as a result of contacting solid, liquid or gas particles. These particles cause mechanical stress in consequence of relative motion.[7]

The nature of the interacting bodies determines the wear mode. In solid body – solid body pairs the following wear modes are possible: sliding wear, rolling wear impact wear or

oscillating wear. Solid body – particle pairs can demonstrate crenation or blasting wear. Also various solid – liquid and solid – gas wear modes are possible.[7]

The origin of material and geometrical changes of pairing bodies is based upon physical and chemical processes within the contact area. These wear mechanism can be classified into fatigue wear, abrasive wear, adhesive wear, corrosive wear, fretting wear and erosive wear.[3-6]

Fatigue wear occurs in succession of damage accumulation in areas with periodically interacting micro contacts. The resulting damage corresponds to surface disruption in terms of cracks.

Abrasive wear occurs if one of the contacting bodies is harder and rougher than the counter body. The resulting damage appears as micro blades or micro grooves.

Adhesive wear describes the effects of material transport processes as a result of cold shuts of higher hardness than the originating micro contacts.

A corrosive wear mechanism is a two-step process. The surface reacts in a tribochemical reaction with the environment and produces reaction layers. The second step describes the attrition of this layer as a result of previous described wear mechanisms.[3-5, 7]

By separation of the contacting bodies through lubrication or the modification of material parameters, wear can be reduced and as a result, the durability of tools can be increased.

1.3 Tribology in steel sheet processing

Of all steel processing techniques (e.g. master forming, forming, cutting, joining, material property changing and coating), this chapter will specialize on the topic of forming due to the portfolio requirements of thyssenkrupp Steel Europe AG (TKSE).

Precisely it will focus on the forming condition of push-pull forming and therein on the technique of deep drawing.

In a classical deep drawing process, a press is used to draw the steel sheet into a forming die. The main parts of this press are the punch, a forming die and a blank holder, which reduces wrinkling in the flange region. In such a shape transformation process with material retention, the sheet thickness remains unchanged. During this process the work piece is exposed to a radial drawing-force $\mathbf{F_R}$ and tangential compressive force $\mathbf{F_T}$.[11]

In the described system, illustrated in Figure 7, the friction conditions are very complex because one area needs a lower coefficient of friction while another area requires a higher one.

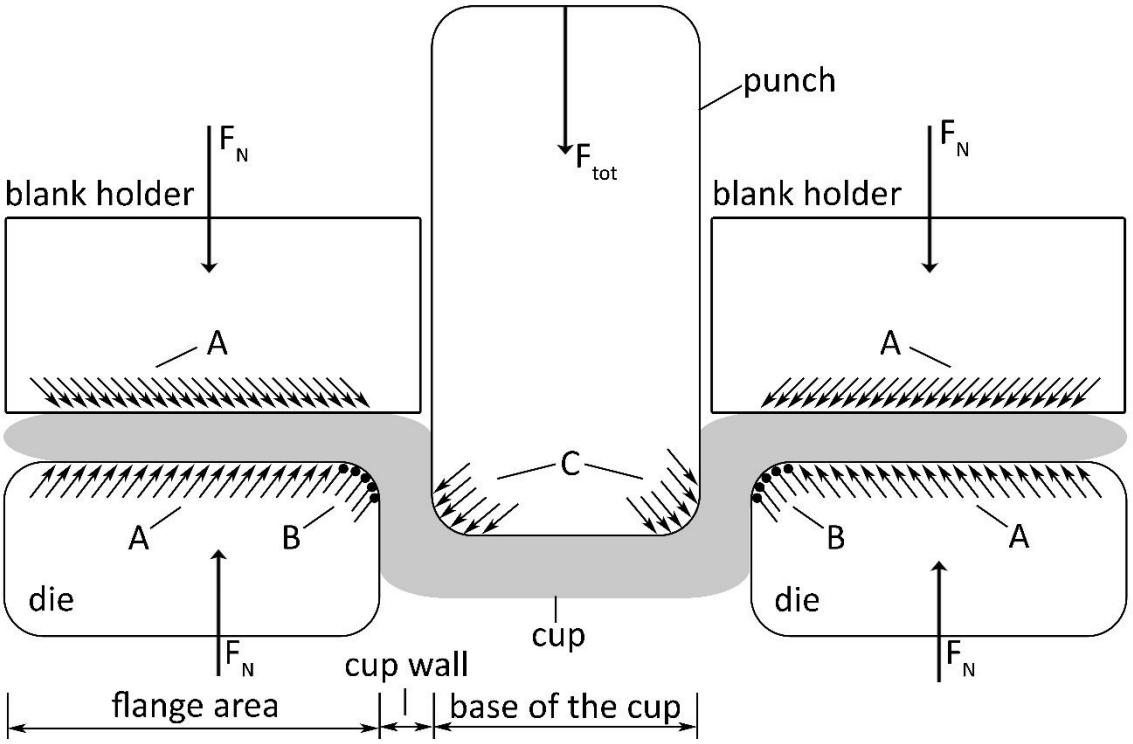

Figure 7. Friction areas when deep drawing a cup. A, friction area between sheet metal blank and holder and sheet metal blank die; B, friction area between sheet metal blank and the die radius; C, friction area between sheet metal blank and punch edges; F_{tot}, total drawing force; F_N, blank holder force [6]

A high coefficient of friction is needed in **area C** to transmit the drawing force from the base of the cup through the cup wall into the flange area, which can be achieved through a general thin lubricant film. To avoid any punch wear, this area can be protected for example with extreme pressure (EP)-additives.[6]

Compared to the described force transfer area the tribological processes in the deformation areas (**areas A and B**) are far more complicated. In these areas, the processes in the blank holder and the die radius are described. Deep drawing without lubricants or with solid lubricants increases the risk of wrinkle formation due to the loss of contact by the blank holder. Increasing the blank holder force or using of a hydrostatic supporting lubricant decreases the risk of wrinkling in this area. The goal of achieving minimum friction in the blank holder area counteracts with the need of maximum friction in the punch area which can be handled by partly lubrication or a higher surface roughness through dressing in the punch area.[6]

To determine the total friction in the region of the holder, the method of choice is the strip-drawing test (chapter 3.4.2; p. 31).

Parameters, which should be considered in tribological tests, are contact pressure, sliding speed, art of materials, surface roughness, lubrication, temperature and deformation.[12]

1.4 Tribological thin and ultrathin films

Already traces of particles between clean metallic surfaces yield to lowered friction and wear [13]. For equability reasons in technical solutions it is important to achieve regular thin or ultrathin films on surfaces. These layers can reach from micrometer scale to nanometer scale (monolayers) and have important influence on surface characteristics.

Methods used for thin film assembling need strict layer deposition control. Various physical or chemical techniques are known which offer this kind of control.

The physical techniques are dominated by various kinds of physical vapor deposition (PVD) methods. Chemical vapor deposition (CVD) is one important chemical deposition method alongside plating, various dip coating techniques, and spin coating.[14]

Thin and ultrathin films can also be described by their buildup mechanisms.

The liquid film formation is mostly affected by wettability characteristics of the surface. This again is influenced by surface roughness parameters and the surface tension of the liquid. Contact angle measurements can be applied to identify the wettability characteristics of a given surface.[3, 13]

The main buildup mechanism for thin and ultrathin layers is adsorption.

Adsorption is the adhesion of particles to a surface and the accumulation of these particles at the interface of two phases. The nature of the adhesion force is of physical nature (physisorption) and is caused by van der Waals forces. These weak forces originate in the interaction between induced or permanent electric dipoles and leave the adsorbing molecule and the surface unchanged. Physisorption processes already occur in ambient air and lead in general to monomolecular or polymolecular layers.[4, 13, 15]

Adsorption with stronger bonds between the adsorbent and the surface is called chemisorption. This kind of adsorption originates in chemical reactions between atoms or molecules and the surface. It means that new chemical bonds are created and that the nature of the surface is changed.[7, 16]

In contrast to physically adsorbed films the thickness of chemisorbed layers is limited to monolayers.[13]

Due to the kind of bonding of adsorbed molecules to the surface, their electronic states are changed. These differences in the electronic states can be used in x-ray photoelectron emission spectroscopy to identify physisorbed or chemisorbed molecule layers.[17]

An additional category in characterizing thin films is the technique of formation. It distinguishes between spontaneously formed layers or preformed layers. Layers formed spontaneously through the interaction between the surface and the environment allow the regeneration of these layers during the tribological process.[13]

Preformed reaction layers or conversion layers are "formed by reaction between a metallic surface and a gaseous, fluid or in solution reactant" [13]. Two important methods for obtaining friction and wear reducing layers are nitriding and phosphating. The main effect of nitriding for the tribological behavior is the resulting high hardness of the surface. Phosphating on the other hand forms strong adhesive amorphous or crystalline phosphate layers on the surface. These layers are important for the running-in phase because they enable high scuffing loads.[13]

The understanding of spontaneously formed layers on metallic surfaces is of high importance for tribological processes and is the main focus of this thesis.

Layer buildup and reformation have a strong impact in boundary lubrication and are influenced through surface roughness, the presence of unavoidable oxide layers, load and speed of the tribological process, temperature, the nature of the materials, the base oil, and the nature of the additives.[4, 13]

The base oil is important for solvation characteristics. In contrast to paraffinic base stocks naphthenic base stocks are good solvents for polar species. The solvation has an influence on the adsorption of additives on the surface.[4]

Pure base oils, whether mineral or synthetic, are inadequate for modern technical processes and require various supplementary additives. These synthetic chemical substances can enhance requested lubrication parameters, prevent undesired effects, for example foaming or oxidation, and raise completely new properties in the base fluids.[6, 18]

Additives can also interact with surfaces and modify their properties, e.g. friction coefficient, corrosion inhibition, wear resistance or extreme pressure behavior. On the other hand additives can influence the characteristics of the base fluids, e.g. oxidation stability, viscosity, demulsibility, neutralization of acidic products, cooling or foaming.[6, 7, 18]

Concentrations needed for this effects range from a few ppm up to double digit weight percentages. Some additives can fulfill multiple functions while others have synergistic or antagonistic effects among each other.[6]

Oxidation and corrosion inhibitors, which prevent the deterioration of the lubricants and protect against rust are further described in chapter 1.6 “Corrosion resistance of lubricant films” (p. 16).

The additive category of metal-containing extreme pressure and anti-wear additives is dominated by zinc dithiophosphates (ZnDTPs) which prevent contact between metallic parts under high contact pressures through solid lubricant-like layers in combustion engines and gears. This long known group of additives is influenced by their alkyl group chain lengths and has along their anti-wear performance in the mixed friction area characteristics as antioxidants. Thermal, oxidative or hydrolytic processes trigger the degradation of ZDPs. The corresponding reaction mechanism is still topic of ongoing research.[6, 18]

In general, the reaction of anti-wear and extreme pressure additives starts under mixed friction conditions when a hydrodynamic lubrication film is not yet build up or already consumed. Under these conditions with increasing temperature, the additive reaction layers, which prevent the contact between the tribopartners, are formed. Anti-wear additives are intended for medium process conditions whereas extreme pressure additives are designed to prevent catastrophic failure under very high stress levels.[6]

A second group of this kind of additives is the group of metal-free or ash-less anti-wear and extreme pressure additives. The reactive groups of these additives are similar to ZDPs dominated by phosphorus and sulphur compounds.[6, 18]

The additives used in the experiments in this thesis are mainly selected out of this group.

Organic phosphorus compounds are highly reactive under medium stress levels and “most of these additives are neutral or acidic phosphoric acid ester derivates, their metal or amine alts or amids” [6].[18]

Irgalube 349 (Figure 13, b; p. 25) is selected as a representative for the group of amine neutralized mixtures of mono- and dialkyl phosphoric acid partial esters.[6]

As a compound similar to ZDPs, containing sulfur and phosphorus, triphenylphosphorthionate (Figure 13, a; p. 25) belonging to the group of neutral thiophosphoric acid triester is used.[6, 18]

Important groups of extreme pressure and anti-wear additives not used in this thesis are chlorine compounds and the sulfur and nitrogen containing compounds, e. g. thiadiazoles and dithiocarbamates.[6]

The group of sulfur compounds of the general formula R-S_x-R on the other hand is represented in this thesis by two additives. A relative inactive and stable disulphide bridged sulfur carrier (x=2) is the additive diphenyldisulphide (Figure 12, a; p. 25). Whereas the second sulphur additive di-*tert*-nonyl polysulphide (Figure 12, b; p. 25) belongs to the more reactive pentasulphides.[6, 18]

Inactive sulphur additives need higher temperatures to liberate the sulphur than the reaction temperature of 600 °C of extreme pressure conditions. At this temperature occurs the physisorption followed by chemisorption and final breakup of sulphur-bridges in active sulphur additives.[6, 18, 19]

Efficient boosters in combination with sulphur additives are overbased sulphonates, in this thesis sodium salts, which belong to the group of passive extreme pressure (PEP) additives.[6]

Layers formed only by physisorbed additives, e. g. fatty acids, fatty oils, polyamides or polyimides, can only perform in low or mild stress levels where the previously mentioned additives are not yet reactive. This group of additives is called friction modifiers and is used to prevent stick-slip effects.[6]

A review on additives for antiwear and extreme-pressure lubrication is also given by *Papay* [20].

1.5 Understanding oil based films on galvanized steel

The influence of the surface is of high importance for adsorption processes, tribochemical reactions and subsequent tribological performance. In this thesis, galvanized steel sheets are the primary used basic material.

1.5.1 Zinc coated steel (HDG)

Galvanization is a metal protection process to prevent the rusting of steel or iron. The corrosion protection is caused through the barrier- and galvanic-protection of zinc layers coated onto the ferrous surface. The zinc layer acts as an additional protection layer between the corrosive environment and the steel. Also the zinc coating is less noble than

iron and sacrificially corrodes first in most environments at ambient temperatures. This galvanic protection is even active if the steel surface is exposed to the corrosive environment when the zinc coating is damaged. The galvanization is typically achieved by two processing techniques whereof both allow low-cost and long lasting protective layers. In eletrogalvanization (EG) processes the here cold rolled steel sheets are electroplated with zinc in an electrolyte solution with a zinc anode and the steel sheet working as cathode. The sample material used in this thesis belongs primarily to the second galvanization method. In hot-dip galvanization (HDG), the second galvanization method, the protective zinc layer is deposited onto the steel sheet through immersion in a liquid bath of zinc or zinc alloys. In continuous hot-dip processing the cleaned and preheated coiled steel is moved at speeds of 200 m/min through the ~450° C hot zinc (<0.5 % Al) bath to build up the zinc layer. After removing excess zinc through air streams the coiled steel is cooled and can undergo optional costumer requested finishing steps, e.g. roller leveling, temper rolling (skin pass rolling), phosphating and/or oiling and cutting. The added aluminum is necessary to prevent the formation of brittle ZnFe phases. An additional effect of aluminum adding is the reduction of zinc bath oxidation and the higher reflectivity of the formed zinc coating. The thickness of the formed zinc coating (Figure 8) varies according to the used parameters between 5 and 50 µm and includes an aluminum enriched Fe_2Al_5 phase at the iron zinc interphase and a continuous Al_2O_3 protective layer on the surface.[21, 22]

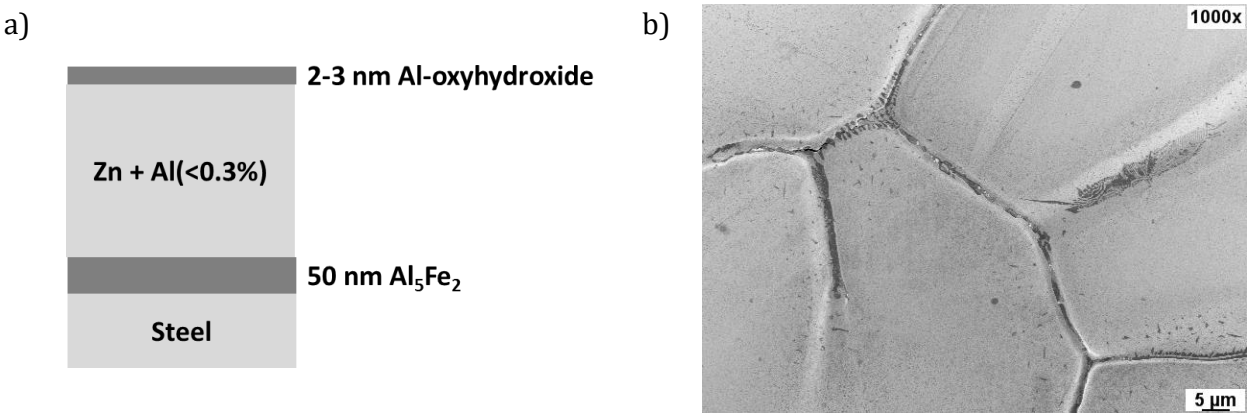

Figure 8. Schematic of the cross-section of HDG (a) [23] and FE-SEM image of a non-skin passed HDG surface (b)

The aluminum content in the zinc bath influences the formation of zinc spangles and therefore the surface texture. A homogenous surface morphology is formed through skin pass rolling as a finishing step.[21, 24, 25]

1.5.2 Zinc-Magnesium coated (ZMG)

While hot-dip galvanized zinc coatings work as good rust protection layers, enhanced corrosion resistance can be achieved through adding magnesium (Figure 9) to the zinc bath.[26]

Magnesium with its highly negative electrode potential in the galvanic series adds additional corrosion protection and enables the possible abstinence of organic protection layers. It also reduces the melting point and enables the hot dip galvanization of steel in low-melting Zn-Al-Mg baths.[27]

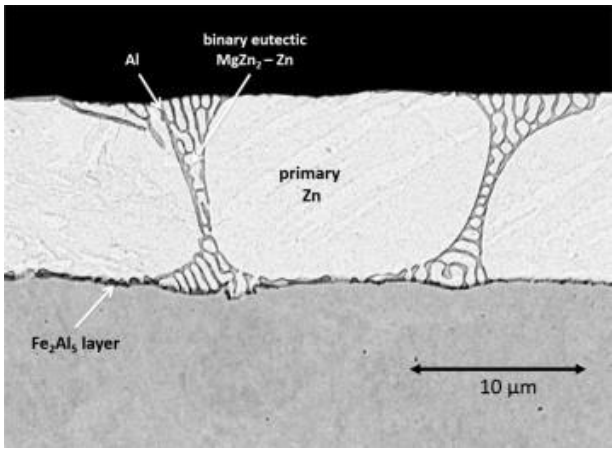

Figure 9. SEM micrograph of the cross-section of a steel substrate coated with a ZM layer [28]

A potential future production method described by *Schuhmacher et al.* [29] is the combination of conventional galvanization with physical vapor deposition (PVD) techniques.

1.5.3 Lubrication on galvanized steel

Although ZnO thin films [30] themselves offer improved tribological properties [31] and can also be used as bath additive in the galvanization process of steel to reduce wear characteristics [32], galvanized steel generally needs additional surface modifications, e.g. liquid lubricants, suspensions, pastes, greases, solid lubricants or coatings for modern tribological environments.[4]

Commonly galvanized steel is used for buildings or automotive parts [33]. These parts are primarily produced by sheet metal forming processes, e.g. deep drawing (1.3 Tribology in steel sheet processing; p. 8), in which oil based films are generally used as lubricants[6].

The galvanized steel sheets typically used for automotive parts are initially coated with an oil based corrosion protection film (1.6 Corrosion resistance of lubricant films; p. 16) in the steel mill. These films are usually applied by rolling, immersion or spraying in the finishing

lines of the steel mills immediately before the steel is rolled up to coils. The standard corrosion protective oil Anticorit RP 4107 S is used to reference all mill-applied oils and prelubes. Standard oils are used to protect the coils during transportation and storage against corrosion and offer basic tribological performance in mild forming processes. In order to increase the friction and wear reducing properties prelubes are used to combine modern tribological performance with corrosion protection properties. For challenging forming conditions, basic corrosion protection oils and prelubes don`t provide the demanded performance and additional lubrication is required. The full removability of all processing steps by cleaning processes is required to enable new lubrication, pretreatment steps, e.g. phosphating [34] or chromating [35], or finishing steps like painting [36]. The additional lubrication is often applied at critical points by spot lubrication before pressing.[5, 6]

Permanent thin organic coatings on resin basis could also be used in order to prevent wear on hot dip galvanized steel [37]. These acrylic polymers with film thicknesses lower than 2 µm work as dry lubricants and effectively reduce the coefficient of friction and have a high wear resistance.[38, 39]

Polymer coated steel sheets offer generally good tribological performances [40] but also cause removing problems previous to further treatments.

1.6 Corrosion resistance of lubricant films

Lubricant films are able to have an oxidation or corrosion inhibition effect additional to the designated friction and wear reducing abilities. Furthermore, it is possible to add specific antioxidants and antirust agents to the oil.

As described in chapter 1.5, steel coils are generally coated with oil based films in the steel mill to provide corrosion protection during transport and storage.[6]

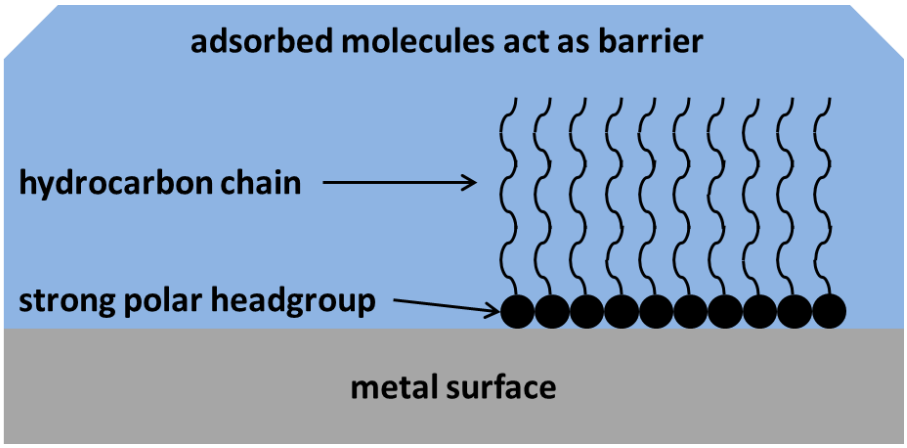

Figure 10. Schematic of adsorbed molecules as corrosion inhibitors

The corrosion inhibitors (Figure 10) added to these films consist preferentially of strong polar groups with long acyclic alkyl chains and are divided into their reaction with ferrous and non-ferrous metals. Antirust additives like sulfonates (p. 25) and derivates of carboxylic acids are used for the protection of ferrous metals. Metal passivators like thiazole and triazole derivates are used for non-ferrous metals. Both types of additives adsorb physically or chemically and compete with tribological active additives for the metal surface. These adsorbed layers present dense hydrophobic films which prevent oxygen and water contact of the metal surface.[6, 18]

1.7 Analysis of additives in lubrication

1.7.1 Characterization of additives in oil based systems

A lot of standardized analytical test methods are available to characterize the physical, chemical and tribological properties of lubricants (e.g. viscosity, corrosion, aging, etc.), an overview of international standards is given by *Mang et al*.[6]

This thesis however focuses on the characterization of additives and their interaction with metal surfaces. Therefore, this chapter describes analytical methods to study additives and lubricant films.

The identification of additives in oil based systems is possible through various analytical methods. Fourier transform infrared spectroscopy (FTIR), X-ray fluorescence spectroscopy (XRF), nuclear magnetic resonance spectroscopy (NMR), gas chromatography–mass spectrometry (GC-MS), atomic absorption spectroscopy (AAS), inductively coupled plasma optical emission spectrometry (ICP-OES) and Raman-spectroscopy enable the

screening of additives, the verification of additive purity and the degradation characteristics of additives.[18, 41]

It is also possible to measure the viscosity of oils by the use of a quartz crystal microbalance (QCM) and its high sensitive response on the resonant frequency by small-volume droplets of oil onto the oscillating quartz [42].

1.7.2 Characterization of lubricant films

The characterization of additives and lubricant films on metal surfaces is also possible through a wide range of surface analytical techniques. Multiple research groups used several combinations of microscopic and spectroscopic methods depending on their availability.[43]

The chemical, electronic and structural information of these systems is ideally observed *in situ*. Although ultra-high vacuum (UHV) tribotester for auger electron spectroscopy (AES) and X-ray photoelectron spectroscopy (XPS) are described by *Martin et al.* [44] most analytical methods require samples prepared for UHV compatibility.

This preparation for vacuum stability requires the removal of excess lubricants with the resulting uncertainty about the influence of this step on the tribofilm and surface characteristics. Despite of this, *Smith* [45] used UHV surface analytical methods such as XPS, AES and time-of-flight secondary-ion mass spectrometry (ToF-SIMS) for the study of ZnDTP based tribolfilms on ferrous substrates.

Through a special arrangement of tribotester and spectroscope, *Martin et al.* [46] were able to perform *in situ* X-ray absorption spectroscopy (XAS) and Raman-spectroscopy to study the chemical bonding and oxidation states of additives and metal surfaces.

In situ Raman spectroscopy is also used by *Bongaerts et al.* [47] for *in lubro* studies of rotating ball derived tribological regimes. A long working distance confocal Raman microscope allows the observation of glycerol based lubricant films between soft poly (dimethylsiloxane) spheres and quartz flats.

Raman spectroscopy is also used by *Yablon et al.* [48] in combination with atomic force microscopy (AFM) for the investigation of ZnDTP based antiwear films generated by high-frequency reciprocating rig (HFRR) tribometry.

Another *in situ* approach is attenuated total reflection (ATR) infrared spectroscopy (IR) tribometry of ZnDTP based tribofilms on steel surfaces. Supplemented through XPS and

ToF-SIMS, *Rossi et al.* [49] observed the existence of a decomposition reaction of zinc dithiophosphates under mild mechanical stress and high temperatures.

In addition, X-ray absorption near edge structure spectroscopy (XANES) [50, 51] and AFM are established for the chemical and mechanical characterization of ZnDTP lubricant films [52, 53]. Both methods were also used by *Najman et al.* [54] to study thermal- and tribochemical films of sulphurized ester, sulphurized isobutylene and dibutyldithiocarbamate on AISI 52100 steel using a Plint high-frequency wear tester. They reported oxidized forms of sulphur for the thermal films and iron sulphide films under EP conditions. *Rosset et al.* [55] also analyzed the thermal reaction of di-benzyl disulphide (DBDS) with iron by means of AES and XPS using single-pulse heating as preparation method.

De Barros et al. [56] also used the *ex situ* approach of XANES and XPS for the surface analysis of tribofilms generated by flat-on-disc tribometry. They used these methods for the study of synergistic effects between the antiwear additive ZnDTP and the friction-modifier molybdenum dithiocarbamate (MoDTC) on steel substrates. *Mathieu et al.* [57] used the same analytical method for the analysis of reaction layers formed during different wear tests and based on phosphorous/sulphur compounds. AES of tribolayers formed under Reichert wear test conditions applied by *Schumacher et al.* [58] supplemented their results.

XPS surface analysis in general has been used extensively for the analysis of reaction films based on surface active additives and formed by tribometry processes.[59]

Hipler et al. [60] also used XPS and XANES to study the adsorption of thiadiazoles on gold by means of PVD under UHV-conditions. XPS, in combination with scanning electron microscopy (SEM) and thermogravimetric analysis (TGA), was also the method of choice for *Liang et al.* [61] to characterize a system of benzothiazole additives in diester on AISI 52100 steel using a SRV (german: Schwingung-Reibung-Verschleiß; oscillation-friction-wear) machine. They reported excellent anti-wear and friction reduction properties due to the additives and the formation of primarily iron sulphide containing protective layers.

Grün et al. [62] used the combination of light microscopy, energy-dispersive X-ray spectroscopy (EDX), SEM, AFM and XPS for the study of various oil based additive systems and their ring-on-disc generated tribofilms on steel substrates.

Kar et al. [63] also applied the combination of SEM, transmission electron microscopy (TEM), EDX, AFM and XPS surface analysis for the characterization of polar additive based tribofilms generated by ball-on-disc tribometry.

The use of ToF-SIMS for the analysis of tribological boundary layers offers surface characteristics with lateral and depth distribution information [64]. The high surface sensitivity of this method offers the chance for the detection of monolayer thin tribofilms [65].

TEM combined with EDX and XPS analysis on focus ion beam (FIB) prepared cross-sections, creates also high depth distributions of reaction layer characteristics [66-68].

Also, ultrathin film interferometry has been used by *Ratoi et al.* [69] for the analysis of boundary film formation of oil based carboxylic acid additives.

A very broad combination of surface analytical methods, 3D-topography, SEM/EDX, AFM, XPS and ToF-SIMS was used by *Stadler et al.* [70] for the study of tribological boundary layers based on fully formed oils and generated through disc-on-disc tribometry on steel substrates. The results of this complex tribological system indicated the buildup of tribo-layers generated through additives and additive fragments.

1.7.3 Nanotribology

In recent years various research groups started an approach for the understanding of friction, wear and lubrication at the atomic level, called nanotribology.[71]

Nanotribology is based on atomic force microscopy (AFM) [72], friction force microscopy (FFM) [73], surface force apparatus (SFA) [74], ultrathin film interferometry (UTFI) and quartz crystal microbalance (QCM) [75] methods for the understanding of small scale interfacial phenomena [76-79].

AFM as an *in situ* method provides insight into "various tribological phenomena which include surface roughness, adhesion, friction, scratching, wear, detection of material transfer and boundary lubrication" [80]. It is also possible to generate nanoscale friction and wear maps with friction force values on a nano-Newton (nN) scale which can help in the identification of fundamental friction mechanism [81].

Gitis et al. [82] used an integrated scanning probe microscope with nanoindentation for the analysis of nanotribological characteristics of diamond-like carbon (DLC) coatings.

The QCM enables the comparison of macroscopic and microscopic characteristics of ultrathin lubricant films by measuring adsorption kinetics and viscoelastic properties [83-85]. This method is also used to analyze the velocity dependence of sliding friction of molecularly thin adsorbed layers on metallic surfaces [86-90]. A combination of a

QCM with scanning tunneling microscopy (STM) enables the measurement of the vibrational amplitude of transverse shear modes by directly imaging the surface oscillatory motion [91, 92].

A review on QCM tribology studies of thin adsorbed films is given by *Krim* [93] and a general review on QCM measurements is given by *Johannsmann* [94].

2 Objectives and scientific approach

Friction and wear are responsible for a high amount of energy and material losses in modern industry and transportation systems. To reduce the friction in moving parts and to increase the durability of tools it is important to have a broad understanding of the surface processes of tribological systems.

The aim of this thesis is to gain a broader knowledge of the tribochemical characteristics of forming additives on hot-dip-galvanized steel (HDG) in the holder region while deep drawing a cup. The method of choice to study the effects in this region is the strip-drawing test.

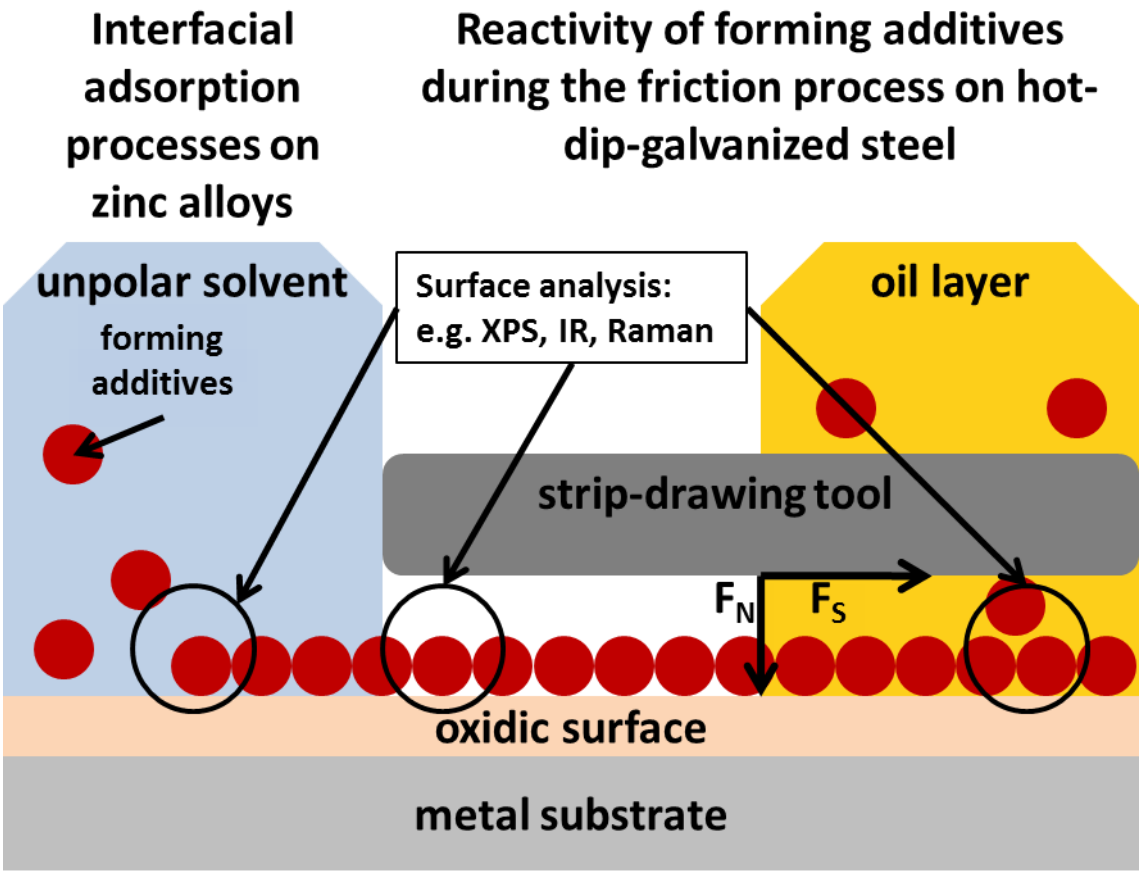

Figure 11. Schematic overview of the scientific approach followed in this thesis

The first step in the approach to understand the reaction mechanism of selected forming additives on HDG under tribological conditions in a strip-drawing test (Figure 11) is the "study of interfacial adsorption processes on zinc alloys" (chapter 4). Therefore, reference measurements of all used additives and substrates are collected. The adsorption process of selected additives on technically grade HDG is studied by means of spectroscopic techniques (e.g. IR, Raman, XPS) and compared to adsorption layers on laboratory grade zinc and zinc alloy (ZnAlMg).

The second step is the characterization of adsorbed additive layers under oil-free tribological conditions by means of spectroscopic and microscopic techniques (e.g. white light interferometry (WLI), laser-induced breakdown spectroscopy (LIBS), Raman) to study the “reactivity of forming additives during the friction process on hot-dip-galvanized steel” (chapter 5). The comparison of these results with the tribological performance of absorbed additive layers as pre-treatment in an oil-based strip-drawing test is the next step in the approach.

The main step is the contact-pressure resolved surface analysis of selected oil-based additive systems on HDG after the strip-drawing test by means of WLI, XPS, Raman-microscopy and ToF-SIMS to study tribochemical reaction products on HDG. This step is followed by a tribological treatment under stronger conditions by means of a multi-frottement strip-drawing test with surface characterization by means of spectroscopic techniques (e.g. ToF-SIMS).

The combination of these steps with comparison between adsorbed layers and tribochemical layers, adsorption on laboratory grade zinc surfaces and technically HDG, oil-free and oil-based systems and the use of various spectroscopic and microscopic techniques is outlined to identify and to understand the reaction processes of forming additives on hot-dip-galvanized steel.

3 Experimental

This chapter lists all used chemicals and materials and gives additional information about origin and structure.

It also gives a description of the applied cleaning methods and general sample preparation techniques. In addition, the fundamentals and parameters of the tribological and analytical techniques are presented.

3.1 Chemicals and Materials

3.1.1 Chemicals

3.1.1.1 Solvents

All used solvents (n-Hexan, light oil, ethanol, methanol, tetrahydrofuran (THF), and 2-propanol) were commercially purchased and used without further purification.

3.1.1.2 Base oils

All base oils were purchased from *Castrol*® and were used without further purification. In this thesis, only paraffinic and naphthenic base oils were used.

Table 1. Oil properties [95]

	Naphthenic	**Paraffinic**
Sulphur	<0,01 %	Typical 0,8 %
Aromate	Max. 10 % (IR)	~7 %
Naphthene	Typical 48 %	30 %
Paraffine	Typical 42 %	63 % (IR)
Flash point	184 °C	224 °C

3.1.1.3 Reference oils

The VDA approved commercially available reference products like the prelube *Anticorit PL 3802-39S* and the corrosion protection oil *Anticorit RP 4107 S* which is also suitable for drawing were purchased from *Fuchs Schmierstoffe GmbH* and used without further purification. These oils were used as references for the tribological measurements.

3.1.1.4 Additives

Sulphur-Additives

Diphenyldisulphide (DPDS) (Figure 12; a) and di-*tert*-nonyl polysulphide (DTNPS) (Figure 12; b) were commercially purchased from Aldrich® and used without further purification.

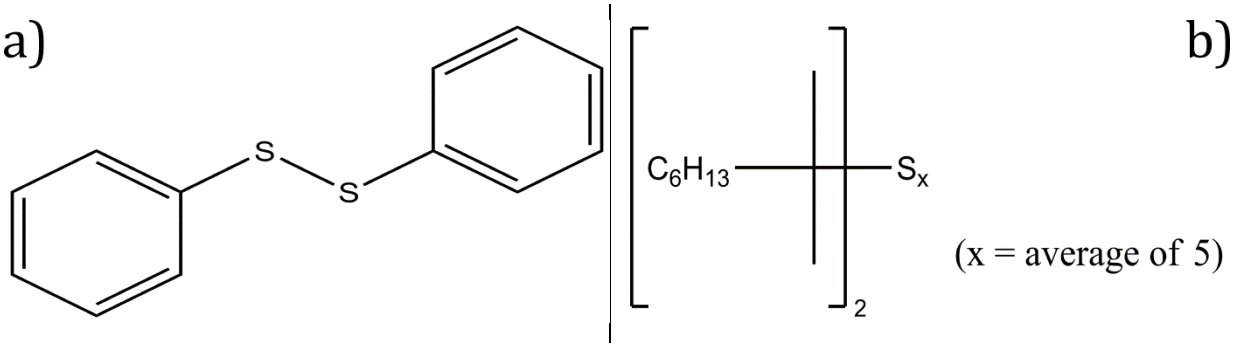

Figure 12. Chemical structures of DPDS (a) and DTNPS (b)

Phosphor-Additives

Triphenylphosphorthionate (Irgalube TPPT) (Figure 13; a) and Irgalube 349 (Figure 13; b) were purchased from *Ciba Specialty Chemical Ltd.* (Basel, Switzerland) and used without further purification.

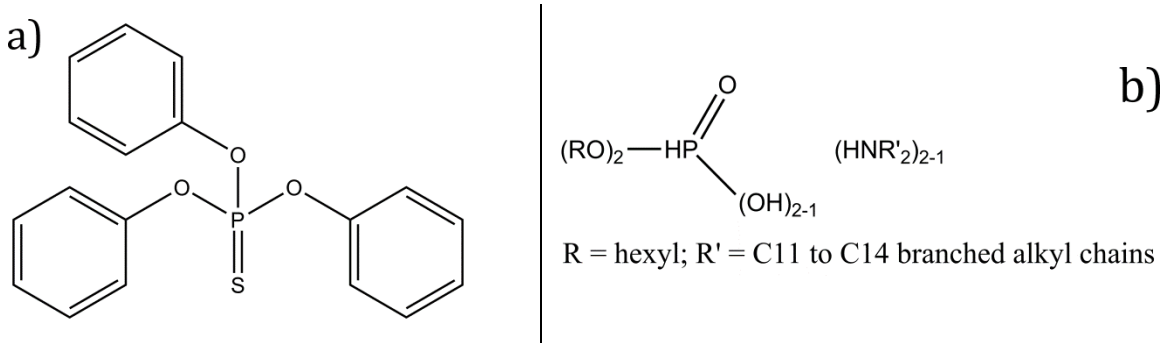

Figure 13. Chemical structures of Triphenylphosphorthionate (a) and Irgalube 349 (b)

Overbased sodium sulphonate (OBSS)

Overbased sodium sulphonate (OBSS) is an oil-soluble colloidal additive. These additives consist of a metal carbonate particle core which is stabilized by a monolayer of a surfactant, in this case a sulphonate.[96]

OBSS (Figure 14) was provided by *Castrol*® as in-oil solution. It was used without further purification as dilution with naphthenic base oil for all applications.

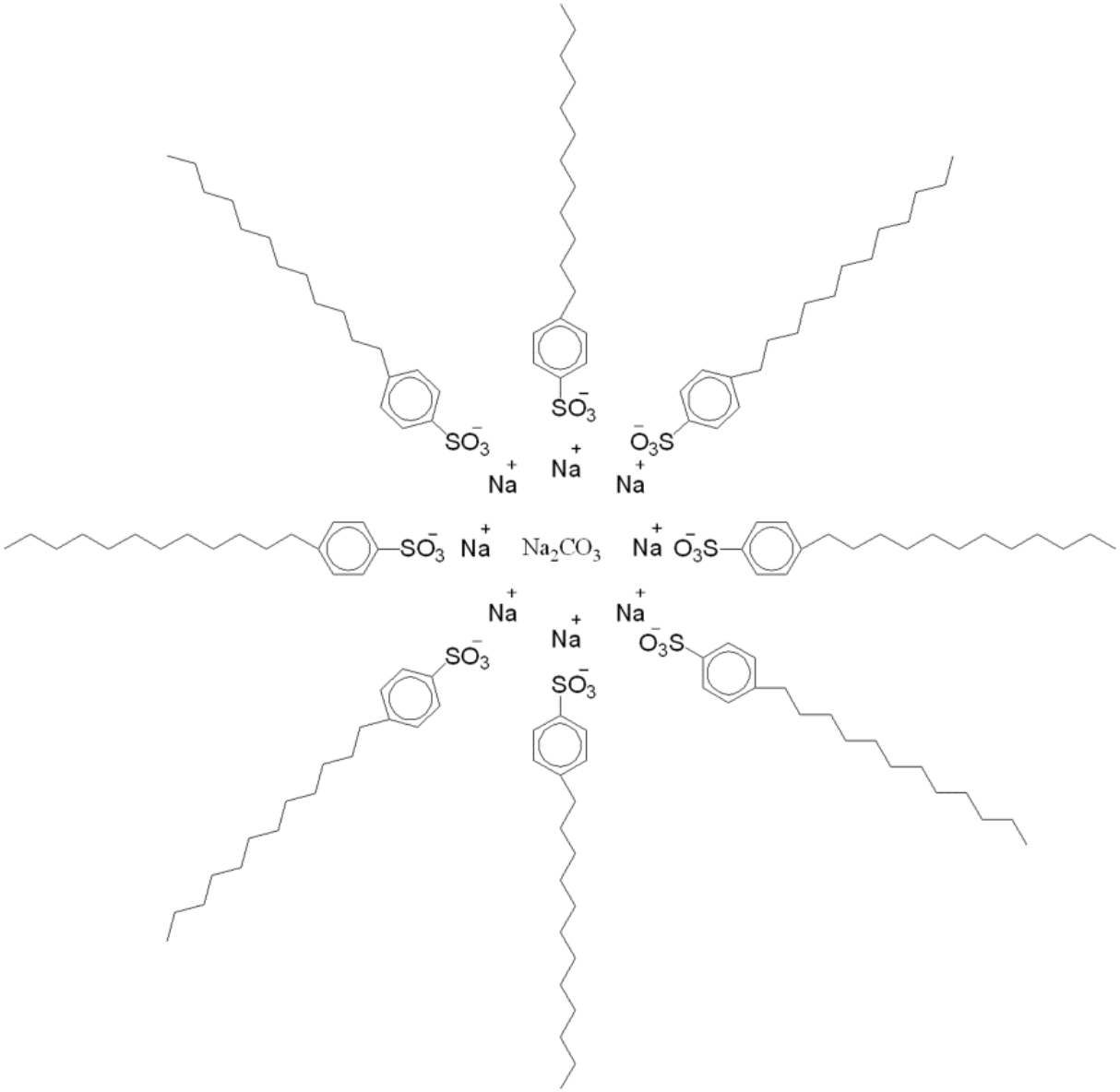

Figure 14. Schematic chemical structure of OBSS

3.1.2 Materials

Substrates

ZnAl(0.5) (Hot-dip galvanized steel; HDG)

Hot-dip galvanized (HDG) steel sheets were purchased from TKSE. Due to availability limitations from the hot-dip coating line, the steel sheets were delivered with two different surface modifications (skin-passed (HDG) and non-skin passed (NSP-HDG)). Both substrates differentiate slightly in their morphology. Therefore, high sensitive surface analytical methods like XPS and ToF-SIMS might reveal minor different results. The variations in surface roughness might lead to varying tribological performances.

Zinc (Zn)

Pure zinc samples were supplied by TKSE and analyzed with AES (Table 2) to characterize the composition.

Table 2. Zinc sample composition in atomic percentage

Al	**Cd**	**Cu**	**Fe**	**Mg**	**Ni**	**Pb**	**Sn**
w.-%	w.-%	w.-%	w.-%	w.-%	w.-%	w.-%	w.-%
0.006	<0.001	<0.001	0.006	<0.001	<0.001	0.002	<0.001

Zinc alloys (ZnAlMg)

Zinc alloy samples with zinc, magnesia and aluminum were supplied by TKSE and analyzed with AES (Table 3) to characterize the composition.

Table 3. Zinc alloy sample composition in atomic percentage

Al	**Cd**	**Cu**	**Fe**	**Mg**	**Ni**	**Pb**	**Sn**
w.-%	w.-%	w.-%	w.-%	w.-%	w.-%	w.-%	w.-%
1.19	<0.001	0.001	0.003	1.76	<0.001	0.002	<0.001

3.2 Cleaning

3.2.1 Standard cleaning

All glass materials were cleaned by using RCA 1 [97] cleaning solution with 1:1:1 ratio (water, ammonium solution, hydroperoxo solution) and boiling for one hour. The materials were rinsed afterwards with deionized water and dried in a nitrogen stream.

3.2.2 Solvent cleaning

All substrates with the exception of HDG steel sheets for tribological measurements were cleaned by using a three step solvent cleaning procedure. They were sonicated in each case for ten minutes in THF, 2-Porpanol and ethanol. After every step, the samples were rinsed with pure solvent and dried in a nitrogen stream.

3.2.3 Alkaline cleaning

The HDG steel sheets were cleaned using an automated cleaning system (WESERO GmbH, Sprockhövel, Germany). This cleaning procedure contained the use of Ridoline®-type alkaline cleaners (Henkel KGaA, Düsseldorf, Germany), rinsing with deionized water and drying in warm stream of air.

3.3 Sample preparation

This section describes the general sample preparation methods. Alternative techniques are mentioned in the respective experiment description.

3.3.1 Preparation of substrates for adsorption measurements

Technical non-skin passed hot-dip galvanized (NSP-HDG) was cut in 30 mm x 30 mm samples.

The zinc and zinc-magnesium blanks were cut in 12 mm x 12 mm x 3 mm samples, grinded and polished with 1 µm polishing solution.

All samples were cleaned afterwards with the cleaning procedure described in chapter 3.2.2.

The adsorption of all additives was realized by dipping the samples in 5 w.-% solution of the specific additive in n-Hexane. After 16 hours, the samples were removed, rinsed with fresh n-Hexane and dried in a stream of pure nitrogen.

3.3.2 Preparation of substrates for tribological measurements

3.3.2.1 Preparation of HDG steel sheets for oil-free strip drawing tests

HDG and NSP-HDG steel sheets were cut in 29 mm x 700 mm (± 3 mm) strips and cleaned with the cleaning procedure described in chapter 3.2.3.

The adsorption of all additives was realized by dipping the samples in 5 w.-% solution of the specific additive in light-oil. After 20 hours, the samples were removed and dried under atmospheric conditions.

After the strip drawing tests, a 29 mm x 100 mm (± 3 mm) sample was cut out of each stripe beginning around 40 mm from the starting position. These samples were used for further surface analysis.

3.3.2.2 Preparation of HDG steel sheets for strip drawing tests with adsorbed additives as pre-treatment

HDG steel sheets were cut in 50 mm x 700 mm (± 3 mm) strips and cleaned with the cleaning procedure described in chapter 3.2.3.

The adsorption of all additives was realized by dipping the samples in 5 w.-% solution of the specific additive in light-oil. After 20 hours, the samples were removed and dried under atmospheric conditions.

Afterwards, all sheets were coil-coated with 1.5 g/m^2 (± 0.2 g/m^2) naphthenic base oil. Additionally, two sets of steel sheets without additive adsorption were coated by the same procedure with naphthenic base oil respectively *Anticorit PL 3802-39S*.

3.3.2.3 Preparation of HDG steel sheets for oil-based strip drawing tests

HDG steel sheets were cut in 50 mm x 700 mm (± 3 mm) strips and cleaned with the cleaning procedure described in chapter 3.2.3.

The specific additives were diluted in naphthenic base oil to achieve oil solutions with 5 w.-% (± 0.1 w.-%) additive concentration. The multi-frottement strip-drawing tests were performed with additive concentrations of 2 w.-% (± 0.1 w.-%).

Afterwards, all sheets were coil-coated with 1.5 g/m^2 (± 0.2 g/m^2) of the respective oil solution. The base oil selection was performed with lower oil coverage of 1.0 g/m^2 (± 0.2 g/m^2).

The tribological tests were performed by means of strip-drawing tests with increasing contact pressure and with multi frottement strip-drawing tests (chapter 3.4.2.2; p. 32).

The steel strips were pre-cleaned by means of rinsing with light oil after the tribological treatment.

For surface analysis, the strips were then cut to 50 mm x 50 mm (± 3 mm) samples and again cleaned with light-oil. Each sample corresponds to a specific contact pressure or number of repetitions (multi frottement test).

3.4 Applied techniques

This section describes the fundamentals and the experimental parameters of the analytical instruments. Alternative specifications are mentioned at the particular point.

3.4.1 Gas chromatography-mass spectrometry (GC-MS)

Gas chromatography-mass spectrometry combines the advantages of gas-liquid chromatography and mass spectrometry to provide an analytical method for the high sensitive identification and quantification of substances within an unknown test sample. Modern gas chromatographs utilize long (up to 100 m) specific filled capillaries as separation columns, called the stationary phase. Through this columns streams a chemical inert carrier gas, called the mobile phase, such as nitrogen or helium. The unknown sample is injected into this stream and transported through the column. The motion of this transport is influenced by the specific interaction of each molecule with the filled column.[98]

Through this individual motion differences, the unknown sample is separated into their consisting molecules, which reach the exit of the column at different times (retention time)

The exiting molecules enter the mass spectrometer where they are ionized by various methods such as electron impact ionization. The mass spectra of the fragmented molecules are then usually detected by quadrupole analyzers or in advanced systems by Time-of-Flight (ToF; chapter 3.4.6; p. 35).[98]

Please refer to the "Handbook of GC/MS: Fundamentals and applications" [98] for further details.

This method was used to characterize the used additives and to check their purity.

Experimental

The gas chromatography-mass spectrometry measurements were performed by the analytical department of TKSE on a HP 5890 Series II gas chromatography system and a HP 5971 mass spectrometry system. The used column was a Zebron ZB-5ms-column with a length of 15 m, an inner diameter of 0.25 mm and a film thickness of 0.25 µm. The stationary phase consists of polysiloxan with 5 % phenyl- and 95 % methyl-side chains.

The samples were solved in CH_3Cl and injected split less with a volume of 1 µl. The temperature program was started with 50 °C constant for 2 minutes with a following temperature gradient of 20 °C/min up to 300 °C which was hold constant for 10 minutes. The transfer line to the mass spectrometer was also heated at 300 °C.

After transfer to the mass spectrometer a full scan with a range from 30 to 500 amu was performed.

3.4.2 Strip drawing test (SDT)

As mentioned in chapter 1.3, the experimental method of choice when emulating the conditions in the holder region when deep drawing a cup (Figure 7; p. 9) is the strip-drawing test (or flat die test). The coefficient of friction (Formula 9) is determined by drawing a sheet metal strip with a drawing force $\mathbf{F_S}$ between two flat dies to which a normal force $\mathbf{F_N}$ is applied pneumatically. Figure 15 shows a schematic of a steel sheet in a strip-drawing tester.[6]

$$\mu_s = \frac{F_S}{2F_N} = \frac{F_S}{2pA}$$

Formula 9. Coefficient of friction in a strip-drawing test. F_N = normal force; F_S = strip-drawing force; A = stressed surface; p = surface pressure [6]

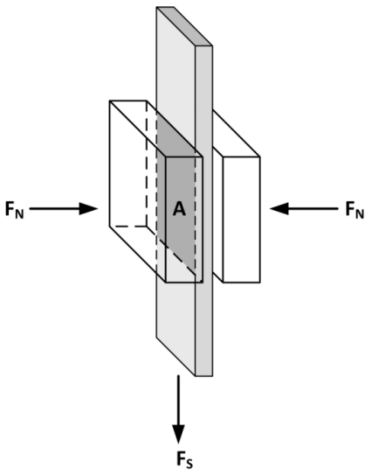

Figure 15. Schematic strip-drawing test. F_N = normal force; F_S = strip drawing force; A = stressed surface.[6]

A variation of the flat die test to produce heavier tribological conditions or even galling, is the multi frottement test. For this method a single steel strip is oiled once and drawn several times between two flat dies.[99]

Strip-drawing tests were used to characterize the performance of selected lubricants and simultaneously produce tribochemical reaction layers for surface analytical characterizations.

Experimental

3.4.2.1 Oil-free strip-drawing test

The oil-free strip-drawing tests were performed at the department of metal forming of TKSE.

An Erichsen strip-drawing machine was used with friction force measurement on both sides of the steel strip. The tool was cleaned with light oil prior to each test. The stripes were positioned between the tool (surface: 3780 mm^2; material number: 1.2379; roughness:

longitudinally fine honed, R_a~0.8) in the strip-drawing apparatus and a constant contact pressure was applied. Afterwards, the stripes were drawn at room temperature for 225 mm with a constant speed of ~6 m/min. The normal force and the drawing force were detected. In addition, the friction forces of both sides of the stripe were measured (showcase in Figure 77). After repeating this procedure multiple times, the measurements were continued with increased contact pressure.

The determination of the coefficient of friction was than performed by means of linear analysis of these forces over a drawing distance of 100 mm.

3.4.2.2 Oil-based strip-drawing test

Strip-drawing test with increasing contact pressure

The oil-based strip-drawing tests with increasing contact pressure were performed in the metal forming department of TKSE. An Erichsen strip-drawing machine (tool surface: 1200 mm^2 (max. contact pressure: 24 MPa), 600 mm^2 (max. contact pressure: 80 MPa); material: 1.2379 steel, roughness: longitudinally fine honed, R_a~0.8) was used for these measurements. The coefficient of friction was measured with increasing contact pressure from 1 MPa to 80 MPa and a drawing speed of 4000 mm/min over a distance of 500 mm.

Multi frottement strip-drawing test

The oil-based strip-drawing tests with constant contact pressure and multiple passes with the tool were performed in the metal forming department of TKSE. An Erichsen strip-drawing machine with a tool surface of 600 mm^2 (material: 1.2379 steel, roughness: longitudinally fine honed, R_a~0.8) was used for these measurements. The coefficient of friction was measured with constant contact pressures of 5 MPa and 10 MPa and a drawing speed of 1000 mm/min over a distance of ~60 mm. This measurement was performed for each set with one, three and five draws. The tool was pushed back with a contact pressure of one MPa to the starting point after each draw.

3.4.3 White light interferometry (WLI)

White light interferometry (WLI) (alternative coherence scanning interferometry (CSI)) is a non-contact optical surface measurement method. The method is used to measure characteristics like height or the topography of surfaces in nanometer or centimeter scales. WLI utilizes the interference of broadband light (white light) while scanning the surface

vertically with height regulation. A charge-coupled device (CCD) sensor automatically analyses the changes in the interferences. The correlation of maximum interference and height position of the instrument enables the assignment of height values for each sensor pixel.[100]

White light interferometry (WLI) was performed in the laboratory for surface analysis of the research and development department of TKSE. The department supplied the 2D- and 3D- morphological maps and the roughness parameters.

3.4.4 Raman Spectroscopy

Raman spectroscopy is a spectroscopic technique, which relies on inelastic scattering, or Raman scattering, of monochromatic light to observe vibrational, rotational, and other low-frequency modes. The monochromatic light, usually emitted by a laser in the visible, near infrared, or near ultraviolet range, interacts among others with molecular vibrations in the analyzed system resulting in energy shifts of the originally emitted laser photons.[101]

The frequency of the inelastic scattered light is lower than the laser light if energy is transferred from the laser photon onto the scattering molecule (Stokes shift). Contrariwise, the frequency of the inelastic scattered light is shifted higher if the final vibrational or rotational state of the scattering molecule is lower than the original state and energy is transferred from the molecule onto the photon (Anti-Stokes-shift).[101]

These energy shifts reveal information about the vibrational modes in the analyzed system. A requirement for vibrational modes to be Raman-active is that this vibration changes the polarizability of the molecules` electron shell. "A dipole moment is induced which is proportional to the electric field strength and to the molecular polarizability **α**.[101]

$$\left(\frac{\partial\,\alpha}{\partial\,q}\right)_0 \neq 0$$

Formula 10. Selection rule for Raman active vibrations [101]

For technical applications, the collected electromagnetic radiation from the illuminated system is send through a monochromator and the high intense elastic scattered laser light due (Rayleight scattering) is filtered out by notch filters, while the rest is forwarded onto the CCD-detector. Because of technological progress in the last decades, significantly increased Raman scattering cross sections, e.g. to $2 \times 10{-}14$ cm^2 per molecule, are achieved which enables the observation of Raman spectra even of a single molecule.[102]

The gathered information of vibrational modes is specific to chemical bonds and provides a fingerprint by which the analyzed molecule can be identified. The obtained spectrum also

provides information about the crystallinity, composition, crystal orientation and temperature.[101]

This high chemical sensitivity combined with modern techniques such as confocal-microscopy, chemical imaging or Surface-enhanced Raman spectroscopy (SERS) allow broad applications in solid-state physics, material sciences and biological and medical applications.[101]

Please refer to "Handbook of Raman Spectroscopy" [103], "Infrared and Raman spectroscopy: Methods and applications" [101] and "Infrared and Raman spectroscopic imaging" [104] for further details.

Raman spectroscopy is used in this thesis for the characterization of all used additives and substrates. The most important use, is the mapping of additive and reaction layers on zinc substrates.

Experimental

The Raman spectra were measured on a Renishaw In Via Raman Spectroscope (Renishaw plc, UK) connected with a Leica DM 2500 M microscope adjustable with five magnifications (5x, 10x, 20x, 50x, 100x). The obtained spectra were processed by means of cosmic ray removal and baseline correction.

3.4.5 Infrared Spectroscopy

Infrared spectroscopy (IR) is based on the interaction of electromagnetic radiation with molecules. Molecules with an alterable or inducible dipole moment $\boldsymbol{\mu_e}$ (see Formula 11 with **q** defined as coordinate of the vibration) can adsorb infrared radiation, which results in rotation or vibration of atomic structures. These adsorptions with specific frequencies reveal characteristic vibrations of bonds or structures of the analyzed molecule. Sub-classes of vibrations, vibrational modes, which can be distinguished, are symmetrical and asymmetrical stretching, rocking, scissoring, torsing, and wagging. A linear molecule with N atoms has 3N-5 degrees of vibrational modes while on the other hand nonlinear molecules have 3N-6 degrees of vibrational freedom.[105]

$$\left(\frac{\partial\, \mu_e}{\partial\, q}\right)_0 \neq 0$$

Formula 11. Selection rule for infrared active vibrations [101]

The identification of unknown molecules is based on characteristic vibrational modes of atomic groups, which are often found in the "fingerprint" area of 1500-800 cm^{-1} in the spectrum.

Diffuse reflectance infrared Fourier transform spectroscopy (DRIFTS)

The technique of choice to measure the reference spectra of the used additives was a special reflection method of the infrared spectroscopy called diffuse reflectance infrared Fourier transform spectroscopy (DRIFTS). With this method, it is possible to measure powders, liquids and very rough surfaces or in general samples with high scattering or absorbing samples. The high signal intensity results from two different effects. The radiation is partly reflected on the surface while other parts are scattered after penetrating the surface. After passing the surface again, this radiation is collected via large angles and concentrated on a detector.[105]

Infrared spectroscopy was used for reference measurements with the pure additives, oils and substrates. This was done to identify the characteristic spectroscopic bands of the substances.

Experimental

A diffuse reflectance unit within a Bruker Vertex 70 spectrometer was used for this method. The unit consists of multiple gold-coated mirrors to collect sufficient amounts of diffuse reflected radiation from the sample. Depending on the absorbance, the samples were mixed with a non-absorbing matrix (KBr) and pressed to pellets. A spectrum was collected by averaging 1024 single scans with a resolution of 4 cm^{-1}.

3.4.6 Time-of-Flight Secondary Ion Mass Spectroscopy (ToF-SIMS)

Time-of-flight Secondary Ion Mass Spectrometry (ToF-SIMS) utilizes fast ions to transfer unknown surface components into the gas phase. The high-energy (keV) vertical bombardment of metal surfaces with Ar^+-ions leads to average depth of penetration in the scale of a few dozen nm. Usually used primary ion sources are atomic or molecular ions like O_2^+, Cs^+, Ga^+, Ar^+, Bi^+ with energies in the range of 0.2–25 keV. The energy transfer of primary ion kinetic energy to solid body atoms results in several surface near processes like ion implantation, fragmentation or emission. In addition to electron and photon emission processes, the top surface layers can emit atomic or molecular surface components as neutral, positive or negative secondary ions. These particles obtain predominantly the information of the chemical composition of the analyzed surface.[106]

The analysis of these ions is conducted by the use of time-of-flight mass spectrometry. This method utilizes an electric field of known strength to accelerate the ions and measure the velocity distribution depending on the mass-to-charge-ratio of the ions.

This combined method enables the chemical analysis of monolayers on surfaces with a lateral resolution <0.1 µm and large mass arrays. Also, thermal sensitive and non-vaporizable macromolecular components are accessible through this method.[106]

Techniques like depth profiling and surface mapping complement ToF-SIMS as the most surface sensitive analysis method and lead to variable applications in material and surface sciences.

ToF-SIMS analysis was used in this thesis as high sensitive surface analytical method for the identification of adsorbed layers and tribochemical reaction products.

Experimental

The ToF-SIMS analysis was carried out in the laboratory for surface analysis of the research and development department of TKSE on a gridless reflectron based ToF-SIMS V (ION-TOF GmbH, Muenster, Germany) equipped with a bismuth-cluster ion source. All spectra and images were obtained using Bi^{3+} primary ions at 25 KeV energy in the high current bunched mode with a mass resolution of $m/\Delta m = 6000$. The beam diameter was about 3 – 5 µm and all measurements were made under static conditions (primary ion dose < FPI = 5 × 1012 ions cm^{-2}) on an area of 400 × 400 μm^2 with 2562 pixels.

3.4.7 Laser-Induced Breakdown Spectroscopy (LIBS)

Laser-Induced Breakdown Spectroscopy (LIBS), sometimes called Laser-Induced Plasma Spectroscopy (LIPS) or Laser Spark Spectroscopy (LSS), is a method to characterize the chemical composition of a sample. Next to conventional electrode sparks and inductively coupled plasmas (ICP), LIBS is the third common method for atomic optical emission spectroscopy (OES). It uses highly focused, low-energy laser pulses to vaporize a small amount of a sample and to generate a plasma. Light emitted by excited atoms, ions, and simple molecules in the plasma is analyzed in a detector and displayed as emission spectrum. A focus lens enables the generation of space-resolved chemical-composition images of sample surfaces. Reasonable surface sensitivity is possible above ~100 ppm.[107]

On metallic surfaces, a high spatial resolution of the order of 10-20 µm is possible.[108]

LIBS was used in this thesis for the identification of element distribution on HDG before and after tribological measurements.

Experimental

Laser-Induced Breakdown Spectroscopy (LIBS) was performed in the laboratory for surface analysis of the research and development department of TKSE. Therefore, a vacuum Paschen–Runge spectrometer ARL LaserSpark (Applied Research Laboratories, Ecublens, Switzerland) equipped with a 1080 mm^{-1} grating was used. 41 element channels were mounted as photomultiplier tubes on a 1000 mm Rowland-circle with a detection range from 130 nm to 777 nm. The laser system consisted of a diode-pumped Nd:YAG laser with a wavelength of 1064 nm and a pulse energy of 2 mJ, a pulse duration (FWHM) of approx. 8 ns. The measurements were performed under argon 5.0 ambient atmosphere.

3.4.8 X-ray Photoelectron Spectroscopy (XPS)

X-ray photoelectron spectroscopy (XPS), also known as ESCA (Electron Spectroscopy for Chemical Analysis), is a destructive surface analysis technique, which utilizes mono-energetic X-rays to irritate a sample and analyze the energy of the detected electrons. Usually monochromatic Al Kα (1486.6 eV) x-rays are used in high or ultra-high vacuum to interact with atoms in the top layer of a surface (a few micrometers). This interaction causes the photoemission of electrons with specific kinetic energy (KE; Formula 12).[109]

$$KE = h\nu - BE - \phi_s$$

Formula 12. Kinetic energy of XPS photoelectrons [109]

This formula (Formula 12) connects the kinetic energy **KE** of the emitted photoelectron with the energy of the initiating x-ray photons **hν**, the work function of the instrument $\boldsymbol{\phi_s}$ and the binding energy **BE** of the atomic orbital from which the electron originates. The energy levels of the p, d and f orbital are split up to $p_{1/2}$, $p_{3/2}$, $d_{3/2}$, $d_{5/2}$, $f_{5/2}$ and $f_{7/2}$ levels with a spin-orbit splitting ratio of 1:2 for p-levels, 2:3 for d-levels and 3:4 for f-levels. These energy levels are unique for each element and allow the quantitative identification of surface compositions.[109]

In addition, depth profiles of surface layers are detectable due to sputtering with high energetic ions and XPS measurements after each step.

XPS is used as an important surface analytical tool to characterize the chemical nature of adsorbed additive layers and tribological induced reaction products.

X-ray photoelectron spectroscopy was performed on three different setups.

Experimental

3.4.8.1 XPS 1

XPS 1 measurements were performed in the laboratory for surface analysis of the research and development department of TKSE on a Quantum 2000 ESCA Microprobe (Physical Electronics Inc., Eden Prairie, USA). For photoelectron excitation, a monochromatic Al-Kα X-ray source with a spot size of 100 µm x 100 µm was used. The spectra were recorded at a pass energies of 47 eV and a resolution of ±0.1 eV at an recording angle of 45°. The recording of depth profiles was possible trough sputtering with Ar^+-ions at 45° and an acceleration voltage of 2 kV. The depth calibration was realized with SiO_2 standards of kwon depth (10 nm/min).

3.4.8.2 XPS 2

XPS 2 measurements were performed in the working group of Prof. Neumann in the department of physics at the University of Osnabrück by means of a SPECS XR 50 type X-ray gun with a PHOIBOS HAS 150 (SPECS Surface Nano Analysis, Berlin, Germany) hemispherical energy analyzer. For photoelectron excitation a Al-Kα (1486.6 eV) X-ray source was used.

3.4.8.3 XPS 3

XPS 3 measurements were performed by means of an Omicron ESCA+ System (Omicron NanoTechnology GmbH, Germany) with a base pressure of $<3 \times 10^{-11}$ mPa. The system is equipped with a hemispherical energy analyzer, and the element spectra were recorded at pass energies of 25 eV. For photoelectron excitation a monochromatic Al-Kα (1486.3 eV) X-ray source with a spot diameter of 600 µm was used.

3.4.8.4 Data evaluation

The calibration of the spectra was performed using the binding energy of adventitious hydrocarbon (BE = 285.0 eV) as internal reference for charge correction.

The data were processed using CasaXPS software (version 2.3.15, Casa Software Ltd, Wilmslow, Cheshire, UK). After non-linear Shirley background subtraction, the peaks were fitted using the product of Gaussian and Lorentzian functions with a Gaussian to Lorentzian ratio of 30 (GL30). All quantification of the data was performed by integration of the peaks with regards to the relative sensitivity factors of the elements.

4 Interfacial adsorption processes on zinc alloys

To understand the interaction of additives and zinc surfaces under tribological conditions (chapter 5), it is necessary to characterize the components individually. First, the characteristics of additives and surfaces are analyzed by various methods such as gas chromatography-mass spectrometry, infrared spectroscopy, Raman spectroscopy, X-ray photoelectron spectroscopy, time-of-flight secondary ion mass spectrometry and white light interferometry.

Based on this, adsorbed films of the additives on model and technical zinc substrates are investigated.

4.1 Reference measurements

The characterizations of interfacial adsorption processes on zinc alloys require a broad knowledge of the analyzed components. Therefore, the recording of reference measurements of the used additives and zinc substrates is essential.

4.1.1 Additives

This part focuses on reference measurements with GC-MS, FT-IR, Raman spectroscopy and XPS of selected additives whose interactions with zinc-based surfaces are later analyzed in higher depth. The selected additives, with DTNPS as sulfur-based additive, triphenylphosphorthionate as sulfur- and phosphorus-based additive and OBSS as sulfur-based micelle-kind additive, represent different types of sulfur-based additives. Further reference measurements of phosphorus-based additives are given in the Appendix (chapter 12.1.1; p. 182).

4.1.1.1 Di-tert-nonyl polysulphide

The first examined additive is the sulphur-bridged di-*tert*-nonyl polysulphide (DTNPS). This additive is dominated by the long sulphur bridge, which combines two *tert*-nonyl groups. Characterization of this additive was performed by means of GC-MS, DRIFTS and Raman spectroscopy. XPS was not used for reference measurements because it requires permanent freezing which was not available in the used equipment.

GC-MS

The GC-MS (Figure 16) of DTNPS reveals none of the expected sulphur-chain molecule-fragments like a disulphide (m/z = 318), trisulphide (m/z = 350), or tetrasulphide (m/z = 382) (retention time: 6.24 minutes; Figure 17). However, typical fragments of the molecule like m/z = 159 ($C_9H_{19}S$), m/z = 127 (C_9H_{18}) and alkyl-chain fragments like m/z = 85, m/z = 71, m/z = 57 and m/z = 43 can be identified (retention time: 11.1 minutes; Figure 19). The highest GC peak with a retention time of 10.63 minutes is most likely elemental sulfur (S_8) (Figure 18).

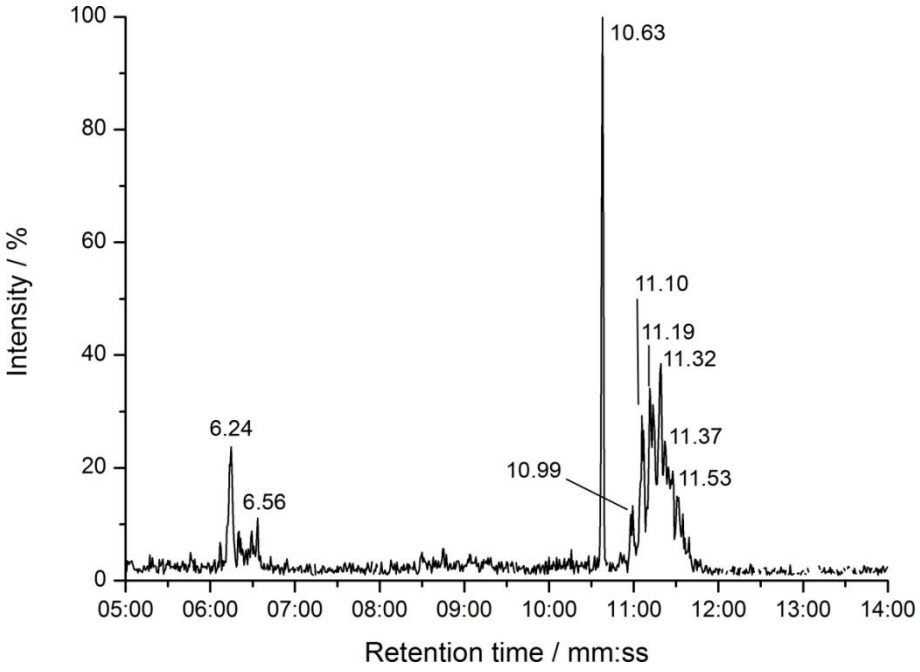

Figure 16. Gas chromatography spectrum of di-*tert*-nonyl polysulphide in $CDCl_3$

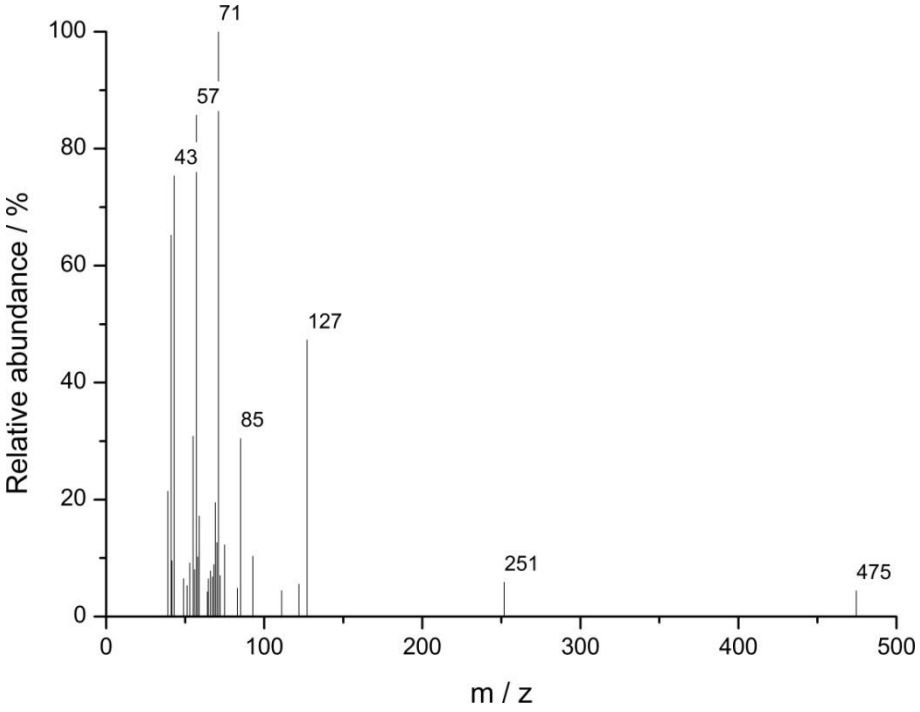

Figure 17. Mass spectrum of DTNPS at retention time 6.24 minutes

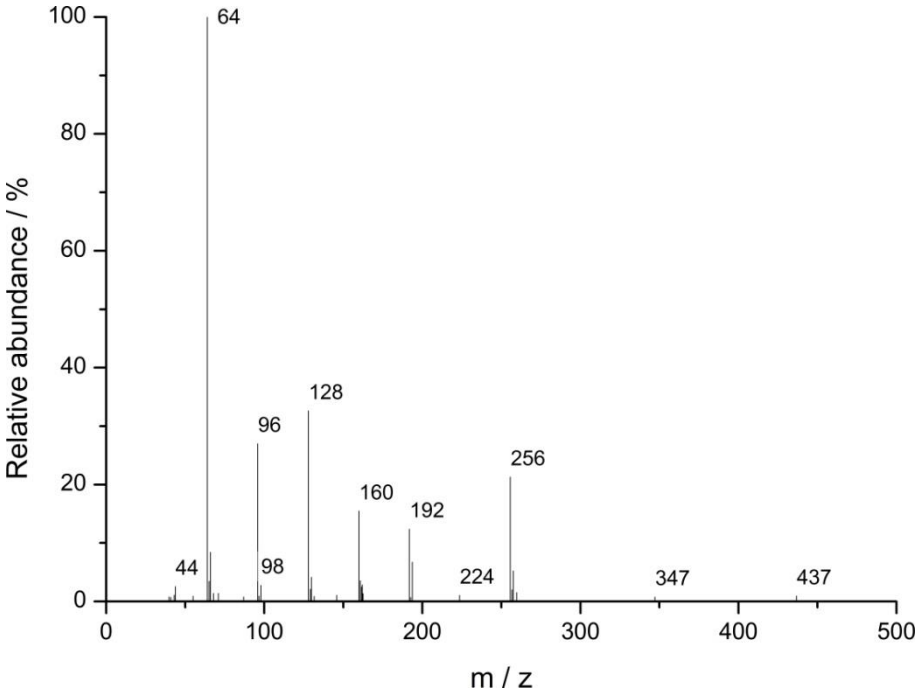

Figure 18. Mass spectrum of DTNPS at retention time 10.63 minutes

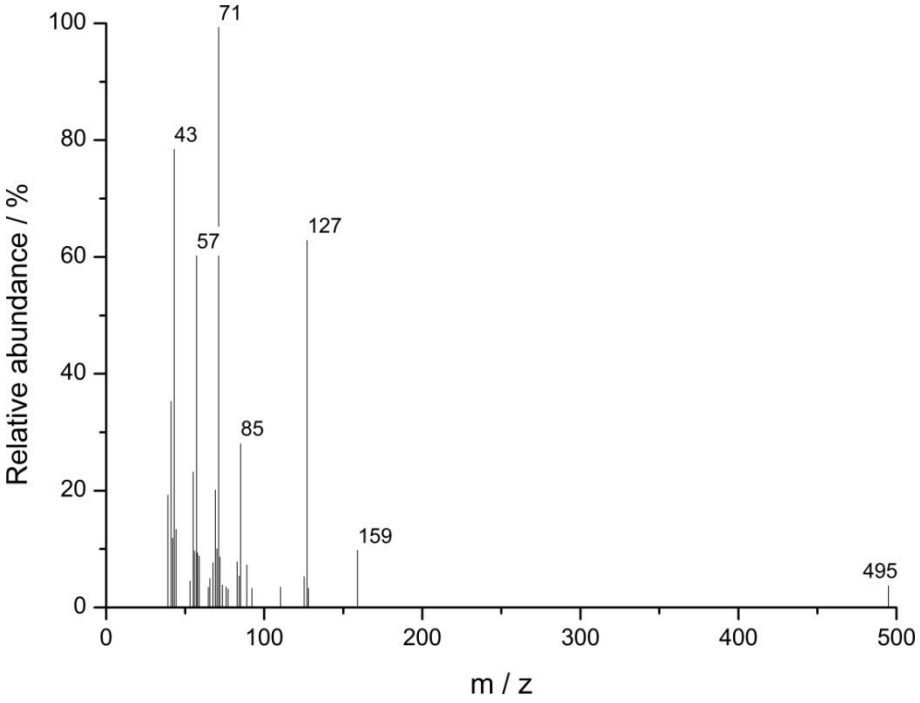

Figure 19. Mass spectrum of DTNPS at retention time 11.1 minutes

Diffuse reflectance infrared Fourier transformation spectroscopy (DRIFTS)

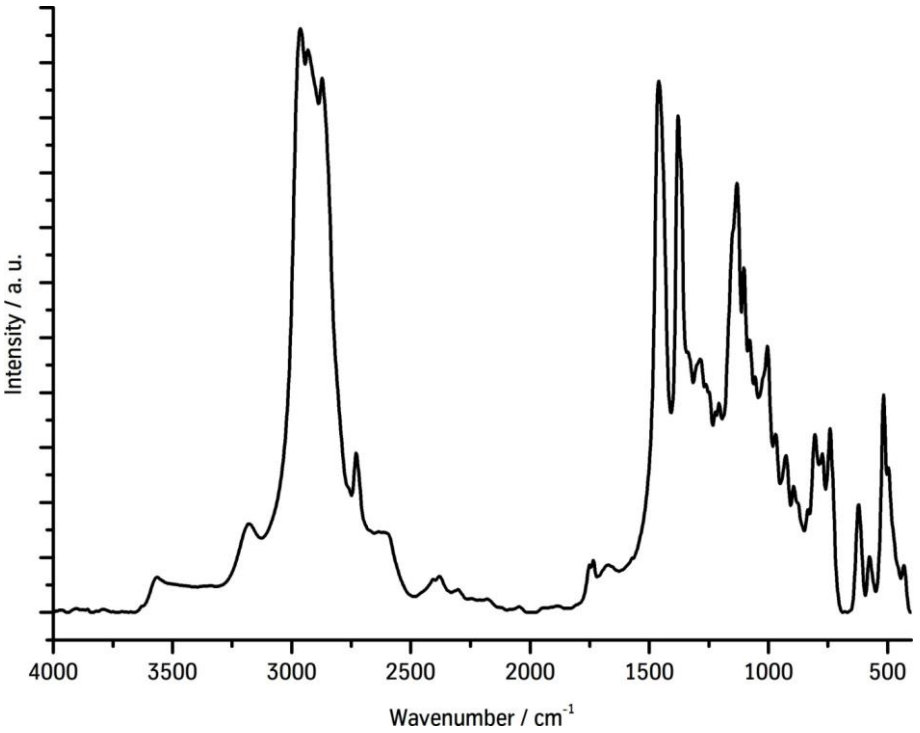

Figure 20. DRIFT spectrum of pure DTNPS with KBr

The infrared spectrum of DTNPS (Figure 20) shows the characteristic vibrations of a sulphur-bridged alkyl molecule. The S-S stretching mode is expected between 510-469 cm^{-1} and the spectrum shows two peaks at 517 cm^{-1} and 496 cm^{-1}. A peak at 622 cm^{-1} can be

assigned to the C-S stretching mode that is expected between 715-620 cm^{-1}. Also strong peaks in the region around ~2900 cm^{-1}, which are characteristic for a *tert*-nonyl alkyl chain, can be identified. Asymmetric stretching modes of CH_3 and CH_2 can be found at 2963 cm^{-1} and 2932 cm^{-1} while the symmetric stretching mode of CH_3 is located at 2872 cm^{-1}. The asymmetric bending mode of CH_3 correlates with a peak at 1461 cm^{-1} and the peak at 1379 cm^{-1} can be assigned to the symmetric bending mode. The peaks at 1286 cm^{-1} and 741 cm^{-1} can be assigned to the in phase twist and the in phase rocking mode of $-(CH_2)_n-$. In addition, the skeleton stretching modes of C-C and $-CR_3$ C-C are found at 1207 cm^{-1} and 1132 cm^{-1}.[110]

Raman spectroscopy

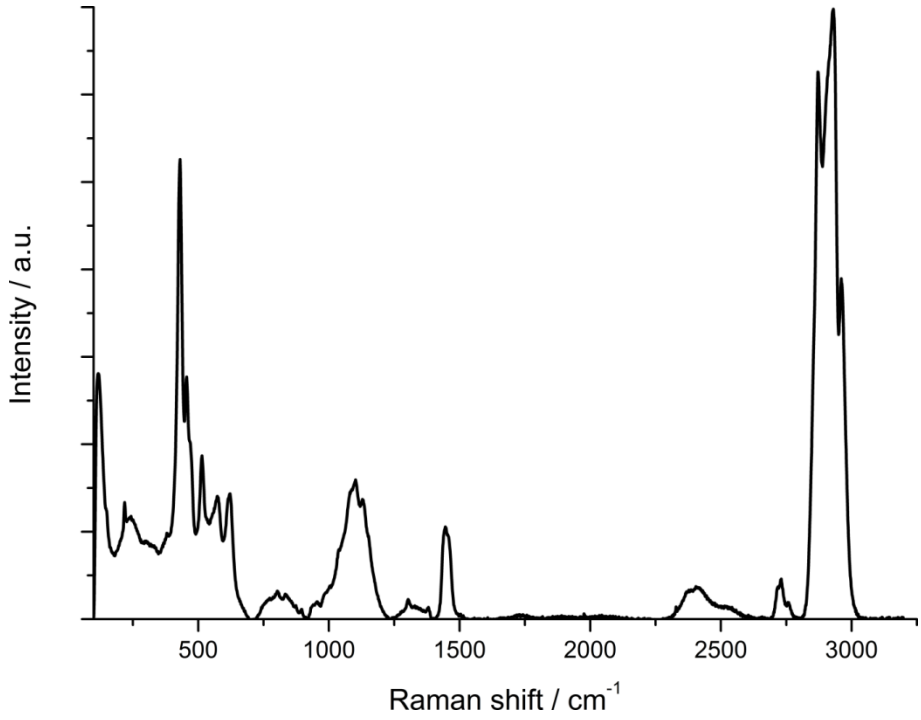

Figure 21. Raman spectrum of DTNPS

The strongest peak in the Raman spectrum of DTNPS next to the alkyl-group peaks around 2900 cm^{-1} is the peak at 430 cm^{-1}. This peak and the neighboring peak at 456 cm^{-1} are likely S-S bond vibrations of elemental sulphur, which supports the GC-MS results (Figure 18). The corresponding bending modes are likely around ~200 cm^{-1}. The peak at 456 cm^{-1} can also be assigned to S-S stretching modes of an S-S bond in di-alkyl polysulphides as well as the higher peaks up to 573 cm^{-1}. Peaks corresponding to C-S stretching modes of di-alkyl polysulphides can be found around 621 cm^{-1}. The peaks at 1104 cm^{-1} and 1131 cm^{-1} can be assigned to C-C skeleton stretching modes of the $-(CH_2)_n-$ alkyl chain while the peak at 1304 cm^{-1} can be assigned to in-phase twisting modes of this chain. The symmetric respectively asymmetric bending modes of CH_3 and CH_2 can be found at 1381 cm^{-1} and

1450 cm^{-1}. At peak 2850 cm^{-1} can be assigned to the symmetric stretching mode of CH_2 while the corresponding asymmetric stretching mode of CH_2 is found at 2930 cm^{-1}. The symmetric respectively asymmetric stretching modes of CH_3 can be found at 2872 cm^{-1} and 2960 cm^{-1}.[110-114]

The combination of GC-MS, infrared and Raman spectroscopy allows the identification of characteristic peaks and confirms the necessary purity of the additive. Therefore, this system can be used for the adsorption and tribological test.

4.1.1.2 Triphenylphosphorthionate (Irgalube TPPT)

The second additive that is analyzed in depth is triphenylphosphorthionate. The P=S double bond and the oxygen bridged phenyl groups are characteristic for this additive. The analysis was performed accordingly to the methods mentioned above (chapter 4.1.1.1).

GC-MS

The gas chromatography measurement of triphenylphosphorthionate reveals only one peak at a retention time of 12.5 minutes (Figure 22). This indicates a high purity of the additive and is further confirmed with the mass spectrometry measurement (Figure 23).

In this spectrum, characteristic signals belonging to the additive molecule can be identified. At m/z = 342 the molecule peak [M+] can be identified with high intensity. Furthermore molecule fragments like [Ph+] with m/z = 77, [M+-Ph] with m/z = 265 and [M+-Ph-O] with m/z = 249 can be found in the spectrum.

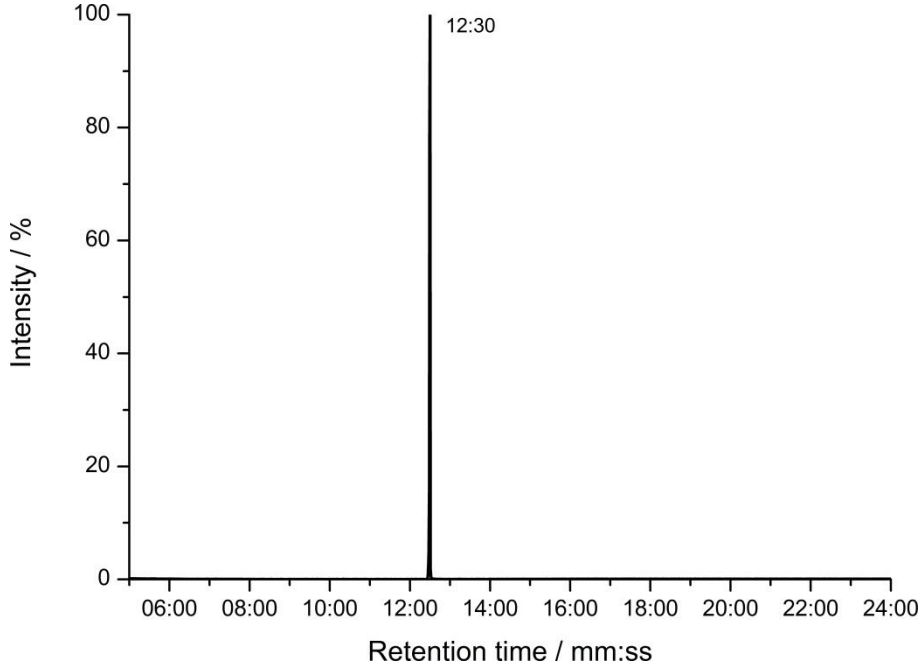

Figure 22. Gas chromatography spectrum of Irgalube TPPT in $CDCl_3$

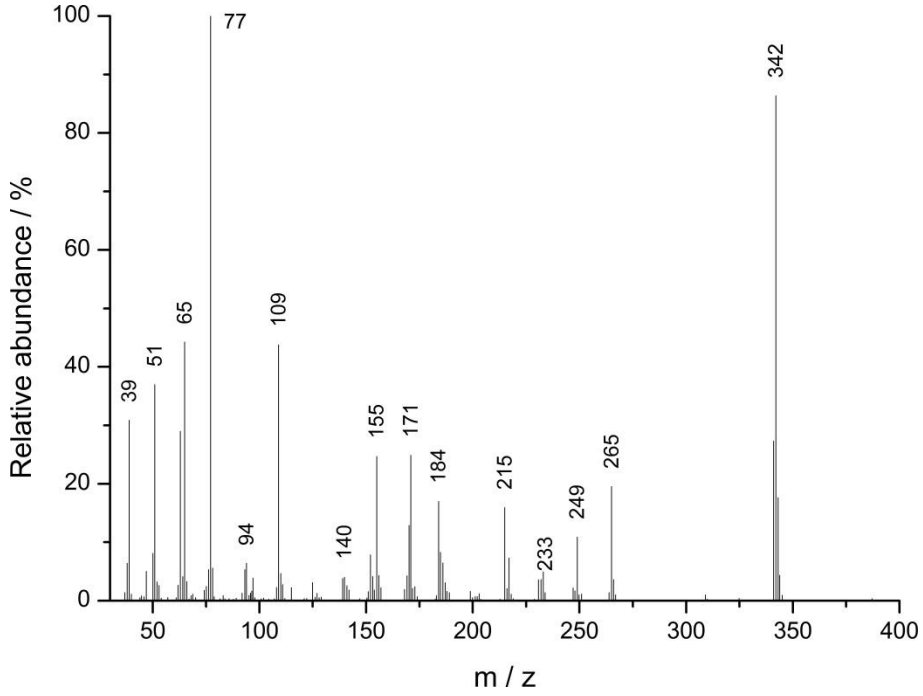

Figure 23. Mass spectrum of Irgalube TPPT at retention time of 12:30 (mm:ss)

Diffuse reflectance infrared fourier transform spectroscopy (DRIFTS)

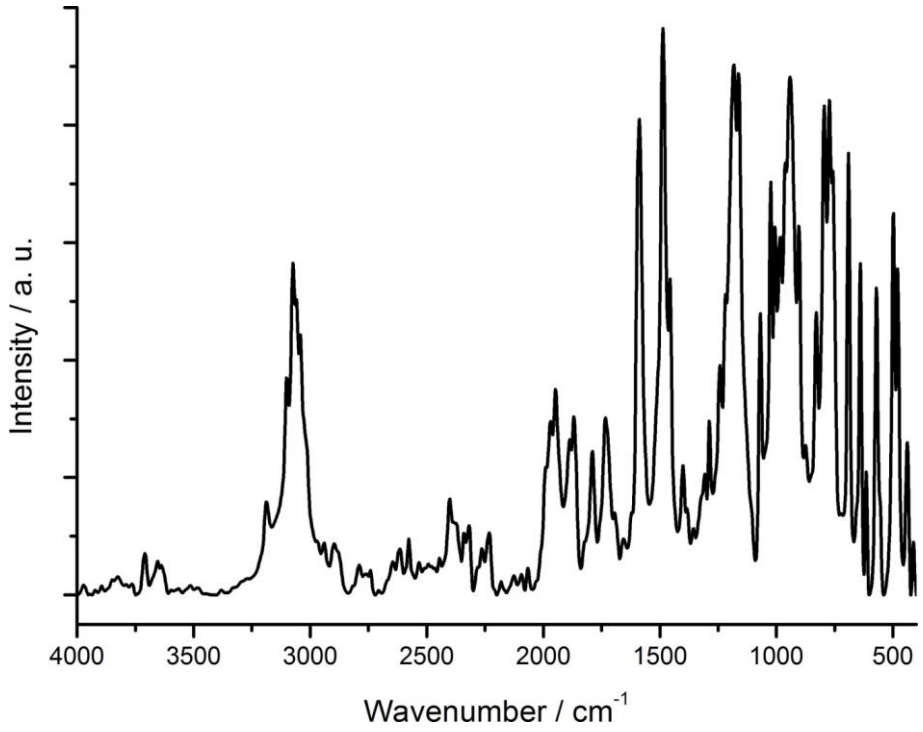

Figure 24. DRIFT spectrum of pure Irgalube TPPT with KBr

The infrared spectrum in Figure 24 reveals the characteristic vibrations of a phosphorthionate with phenyl groups. In the alkyl-region between 3101 cm^{-1} and 3042 cm^{-1}, various peaks can be assigned to the C-H stretching mode of the phenyl ring. The peaks at 1588 cm^{-1}, 1487 cm^{-1} and 1006 cm^{-1} are also characteristic phenyl stretching modes.

Multiple peaks in the broad region between 2066 cm^{-1} and 1694 cm^{-1} and signals at 984 cm^{-1}, 962 cm^{-1}, 903 cm^{-1} 830 cm^{-1}, 691 cm^{-1} and 498 cm^{-1} belong to overtones and combination of in-plane C-H deformation modes. Out-of-plane deformation modes of C-H can be found at 1288 cm^{-1}, 1242 cm^{-1}, 1218 cm^{-1} 1069 cm^{-1}, 1024 cm^{-1} and 615 cm^{-1}. The wagging mode of the P-O-Ar bridge is found at 1456 cm^{-1} while the corresponding deformation mode is found at 571 cm^{-1}. The stretching modes of this bridge compose of the C-O-(P) peaks at 1183 cm^{-1} and 1162 cm^{-1} and the P-O-(C) signals at 942 cm^{-1}, 772 cm^{-1} and 758 cm^{-1}. Finally, strong signals corresponding to P=S vibrations are found at 795 cm^{-1} and 640 cm^{-1}.[115]

Raman spectroscopy

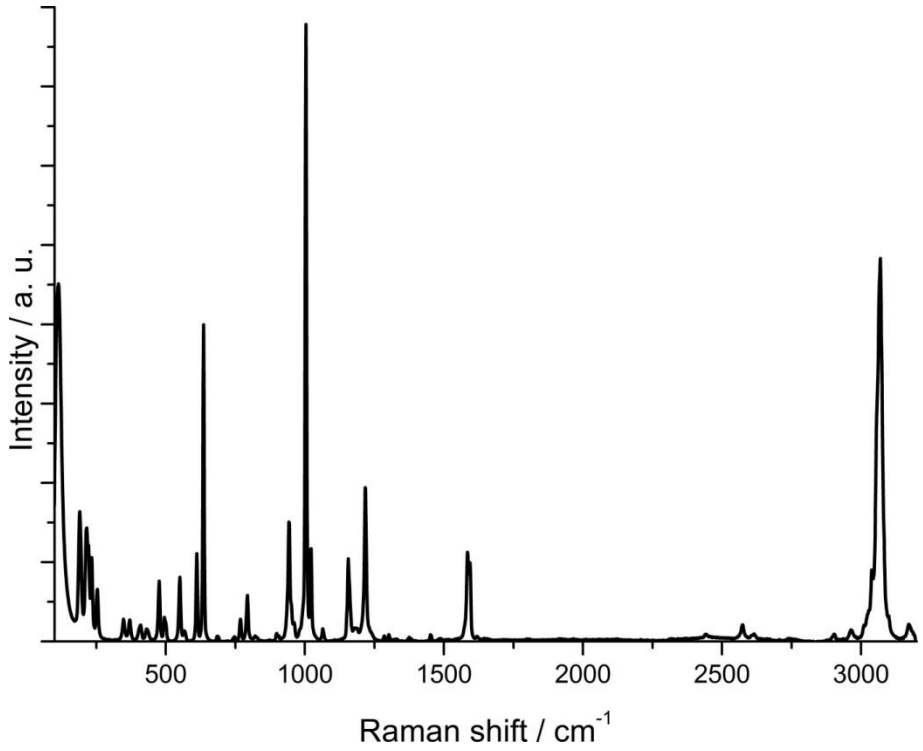

Figure 25. Raman spectra of solid Irgalube TPPT

The Raman spectrum (Figure 25) of solid triphenylphosphorthionate (Irgalube TPPT) shows the characteristic group peaks of thiophosphate and phenyl.

The strongest peak at 1004 cm^{-1} is assigned to the symmetric stretching mode of P-O while the corresponding asymmetric stretching mode is identified at 943 cm^{-1} with lower intensity. The peaks at 476 cm^{-1} and 611 cm^{-1} are assigned to the symmetric and asymmetric bending modes of PO_3. Vibrations of the P=S bond, which were strong in the infrared spectrum (Figure 24, p. 45), are found as weak peak at 431 cm^{-1} and are assigned as P-S stretching modes. Also weak is the peak at 348 cm^{-1} which is assigned to OPS bending modes.[116]

The characteristic signals of phenyl groups can be found as strong peak for C-H stretching modes at 3068 cm^{-1} and various peaks of medium to weak intensity between 1600-1000 cm^{-1} for in-plane C-H bending modes respectively between 1000-700 cm^{-1} for out-of-plane C-H bending modes.[110, 114]

The combination of GC-MS, infrared and Raman spectroscopy allows the identification of characteristic peaks and confirms the necessary purity of the additive. Therefore, this system can be used for the adsorption and tribological test.

4.1.1.3 Overbased sodium sulphonate (OBSS)

A reference measurement of OBSS by GC-MS was not available because it was provided as oil-based solution and thereby it was not possible to analyze it with the available equipment. An analysis with x-ray photoelectron spectroscopy was therefore also not possible as mentioned above (4.1.1.1). To obtain a reference Raman spectrum was also unsuccessful because of the strong resonance of the liquid sample. Despite the use of minimum laser power and short exposure time, no useful spectra could be obtained.

The reference analysis of OBSS is thereby limited to DRIFT spectroscopy because a Raman spectrum of the "in-oil solution" of OBSS couldn`t be obtained.

Diffuse reflectance infrared Fourier transform spectroscopy (DRIFTS)

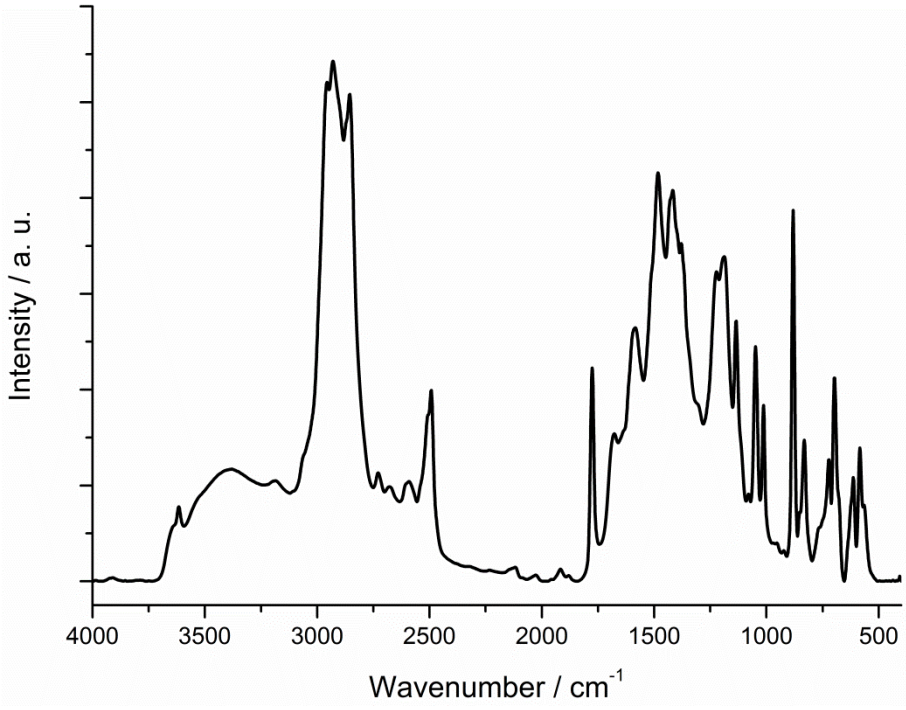

Figure 26. DRIFT spectrum of OBSS as in-oil solution with KBr

The infrared spectrum of OBSS with KBr reveals peaks of aliphatic groups as expected because of the base oil and the additive`s surfactant chain in the region between 3000-2800 cm^{-1} and 1600-1300 cm^{-1}. Also the presence of water is detectable due to the peak at 3379 cm^{-1}, which can be assigned to the hydroxyl-stretching mode, and the peak at 1677 cm^{-1}, which can be assigned to the corresponding bending mode. The symmetric stretching mode of the SO_3^- group is found at 1049 cm^{-1} while the corresponding asymmetric stretching mode is detected as spilt mode at 1223 cm^{-1} and 1188 cm^{-1}. The carbonate group is identified as asymmetric stretching mode of CO_3^{2-} at 1500 cm^{-1} (shoulder) and a symmetric out-of-plane bending mode of CO_3^{2-} at 851 cm^{-1}. A peak at 1776 cm^{-1} can be assigned to a hydrocarbon ion (HCO_3^-). The sharp peak at 881 cm^{-1} as well as the peaks at 1584 cm^{-1} and 1417 cm^{-1} can be assigned to the asymmetric bending respectively splitted symmetric bending modes of a crystalline carbonate (CO_3^{2-}).[117-120]

Infrared spectroscopy allows the identification of characteristic peaks and confirms the necessary purity of the additive. Therefore, this system can be used for the tribological test.

4.1.2 Substrates

The main substrate used in this thesis was skin-passed hot-dip galvanized steel (HDG), which was used in chapter 5 to study surface changes during tribological treatment.

Also, a non-skin-passed hot-dip galvanized (NSP-HDG) steel substrate was used to study the additive adsorption. This substrate enables the characterization of the unchanged hot-dip galvanized steel surface.

All HDG sheets were cleaned by means of the alkaline cleaning procedure as described in chapter 3.2.3 (p. 28).

The influence of this substrate on the tribological performance was studied as part of the oil-free strip-drawing measurements (chapter 5.1.1.2; p. 95).

In addition, two model substrates, pure zinc and a zinc alloy with alumina and magnesia, were used to understand the additive interaction with zinc based surfaces.

4.1.2.1 Skin-passed hot-dip galvanized steel (HDG)

X-ray photoelectron spectroscopy (XPS)

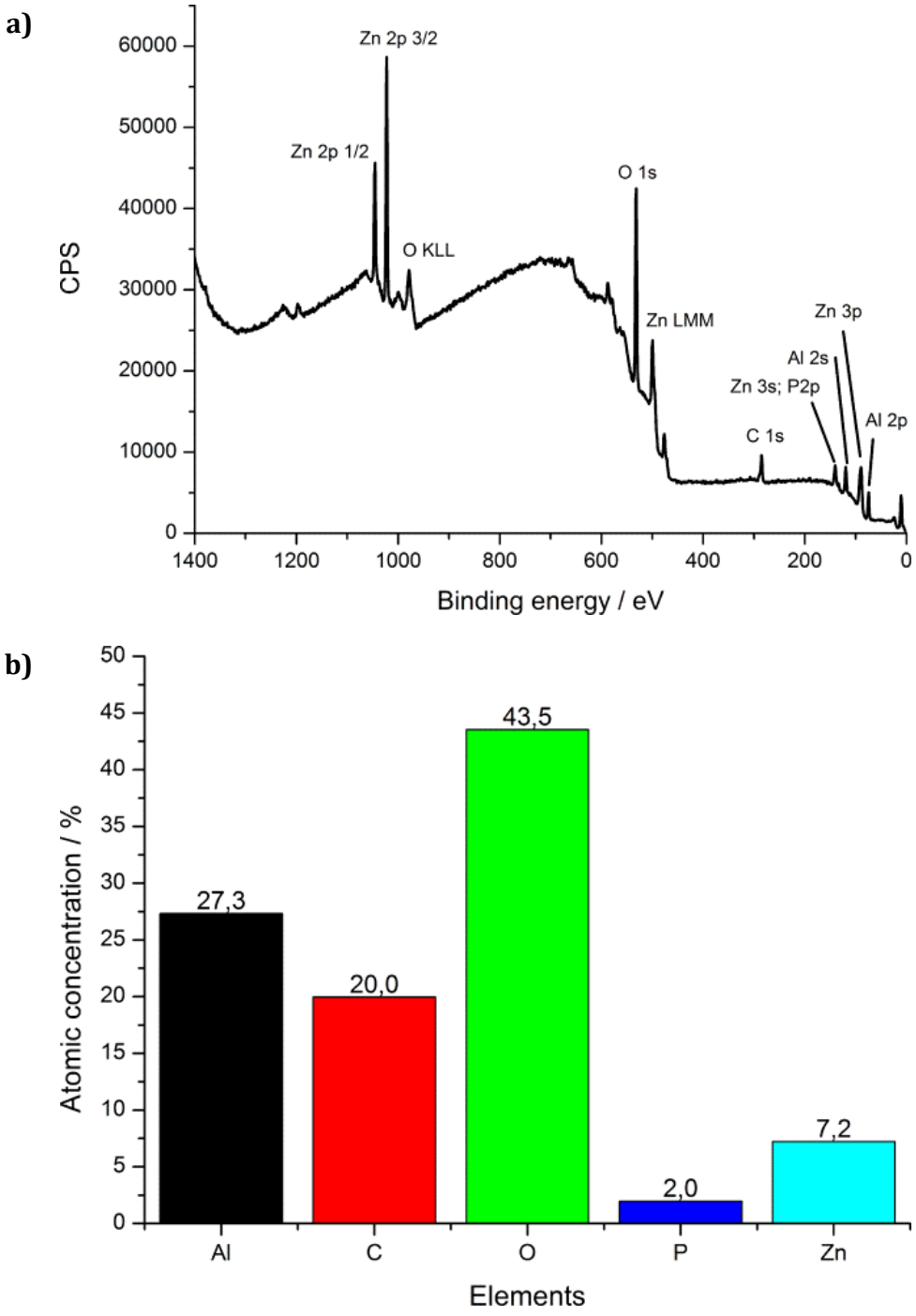

Figure 27. XPS survey (a) and atomic concentration (b) of skin-passed HDG steel

The XPS survey (Figure 27; a) and atomic concentrations (Figure 27; b) of HDG steel identifies the expected element aluminum, carbon, oxygen and zinc, but also minor contaminations of phosphorus.

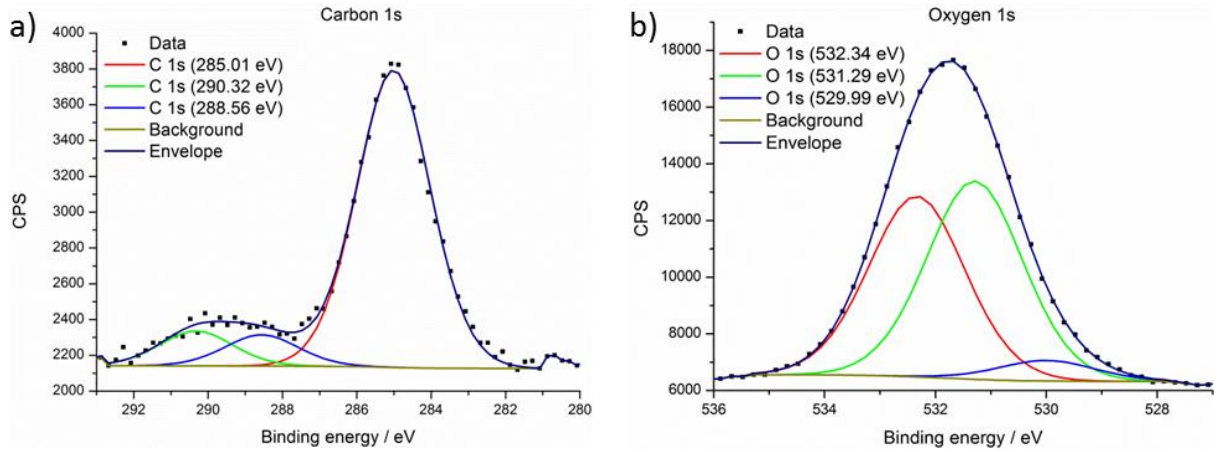

Figure 28. High-resolution XPS spectra of the *C 1s* (a) and *O 1s* (b) region of a skin-passed HDG reference sample

The *carbon 1s* high-resolution spectrum (Figure 28; a) gives the best fit with three peaks, where the lowest peak at 285.0 eV is assigned to hydrocarbons. The peak at 288.6 eV is assigned to –C-OH, -COC- and –C=O from an organic contamination layer. The third peak at 290.3 eV is assigned to metal carbonates or hydrocarbonates.

The *oxygen 1s* high-resolution spectrum (Figure 28; b) gives the best fit also with three peaks. The lowest peak at 530.0 eV is assigned as oxide, while the peak at 531.3 eV is assigned to oxyhydroxide. The third peak at 532.3 eV is assigned to –C-OH and –C=O from an organic contamination layer.

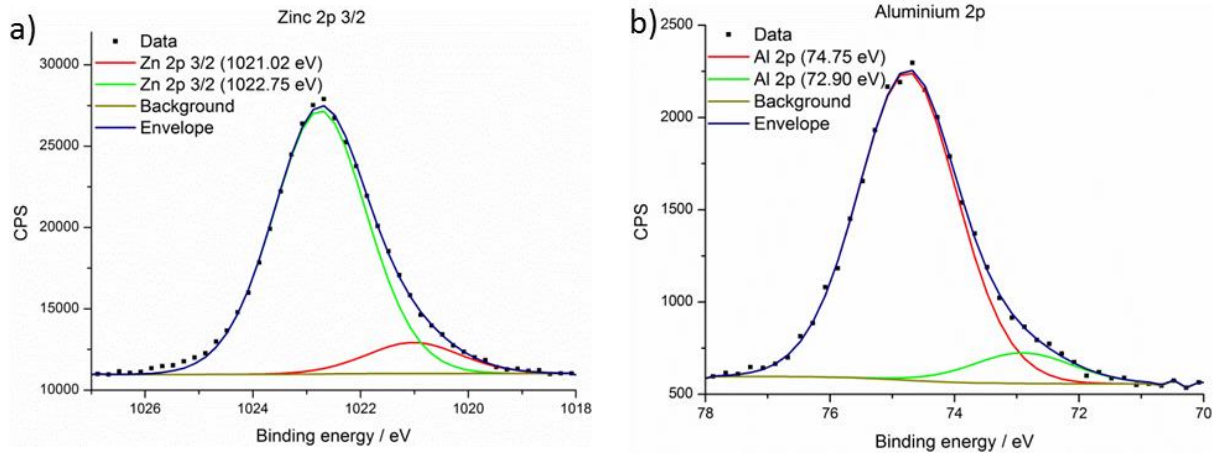

Figure 29. High-resolution XPS spectra of the *Zn 2p3/2* (a) and *Al 2p* (b) region of a skin-passed HDG reference sample

The *zinc 2p3/2* high-resolution spectrum (Figure 29; a) gives the best fit with two peaks, where the peak with the lowest binding energy at 1021.0 eV is assigned to metallic zinc. The second peak at 1022.8 eV is assigned to oxidic zinc.

The same assignment applies to the *aluminum 2p* high-resolution spectrum (Figure 29; b). The spectrum gives the best fit with two peaks, where the peak at the lowest binding energy at 72.9 eV is assigned to metallic aluminum while the second peak at 74.8 eV is assigned to oxidic aluminum.

In each case, the oxidic peak is the dominant part of the composition.

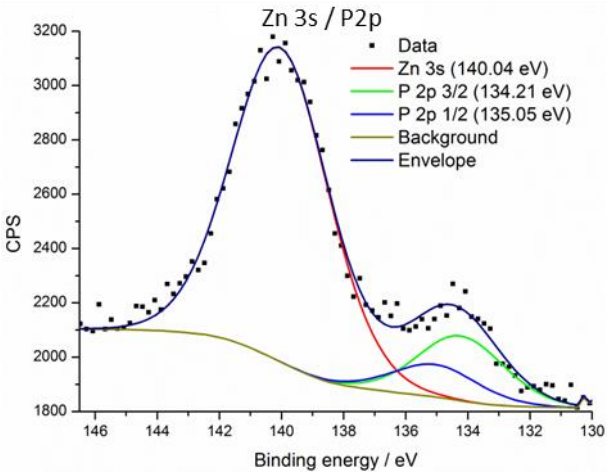

Figure 30. High-resolution XPS spectra of the Zn 3s / *P 2p* region of a skin-passed HDG reference sample

The high-resolution spectrum of the *Zn 3s / P 2p* region gives the best fit with three peaks, where the highest binding energy and dominating peak at 140.0 eV is assigned to zinc (*zinc 3s*). The two peaks at lower binding energies of 134.2 eV and 135.1 eV are spin-orbit coupled peaks of *phosphorus 2p* (*P 2p3/2* and *P 2p1/2*). They are assigned to a minor surface contamination (~2%; Figure 27; b) with phosphate.

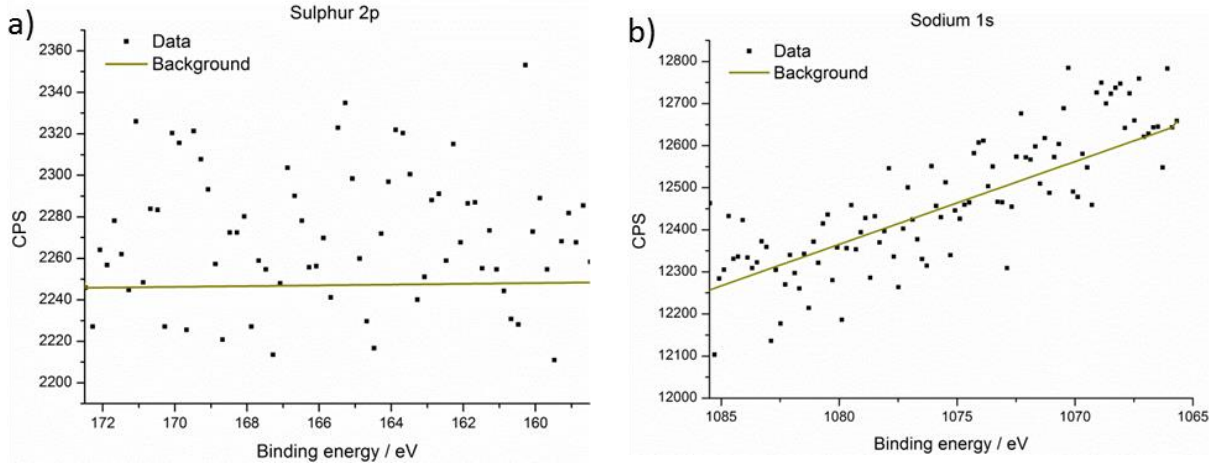

Figure 31. High-resolution XPS spectra of the *S 2p* (a) and *Na 1s* (b) region of a skin-passed HDG reference sample

The high-resolution spectra of the *sulphur 2p* region (Figure 31; a) and the *sodium 1s* region (Figure 31; b) verify the absence of both elements at the surface.

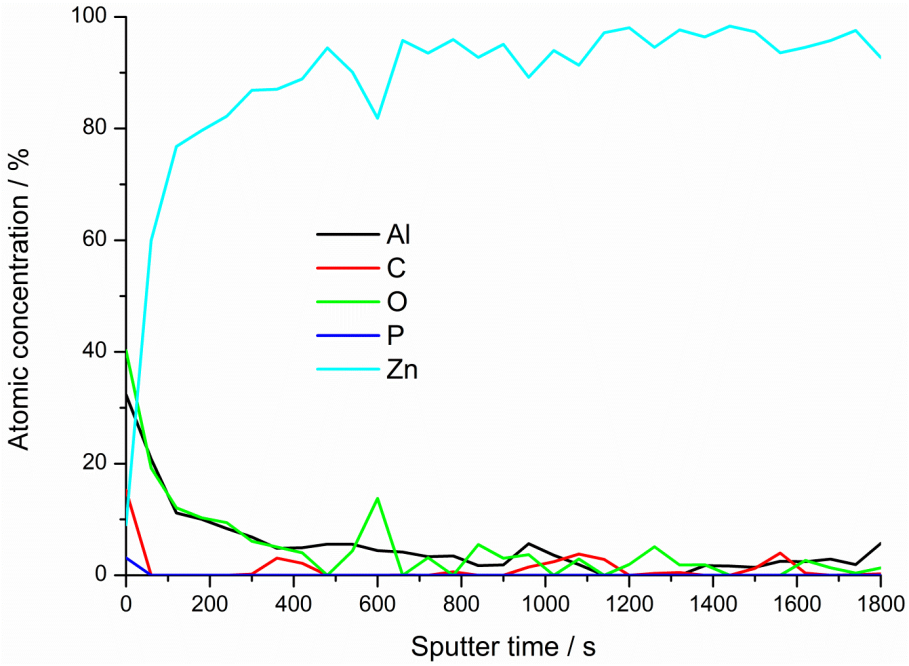

Figure 32. XPS depth profile of atomic concentrations of a skin-passed HDG reference sample

The depth profile (Figure 32) shows, that this contamination exists only in the first nanometers of the surface, and the main component is aluminum oxide.

Laser-Induced Breakdown Spectroscopy (LIBS)

Contrary to the XPS results (Figure 30), the LIBS element distribution (Figure 33) shows no presence of phosphorus. Therefore, the detection limit of LIBS is below the ~2% phosphate contamination detected by means of XPS. The HDG surface is also free of carbon and sulphur. Signals of oxygen and nitrogen are detected because of the measurement under atmospheric conditions. The spectra show the expected characteristics of a cleaned HDP sample handled under ambient air conditions.

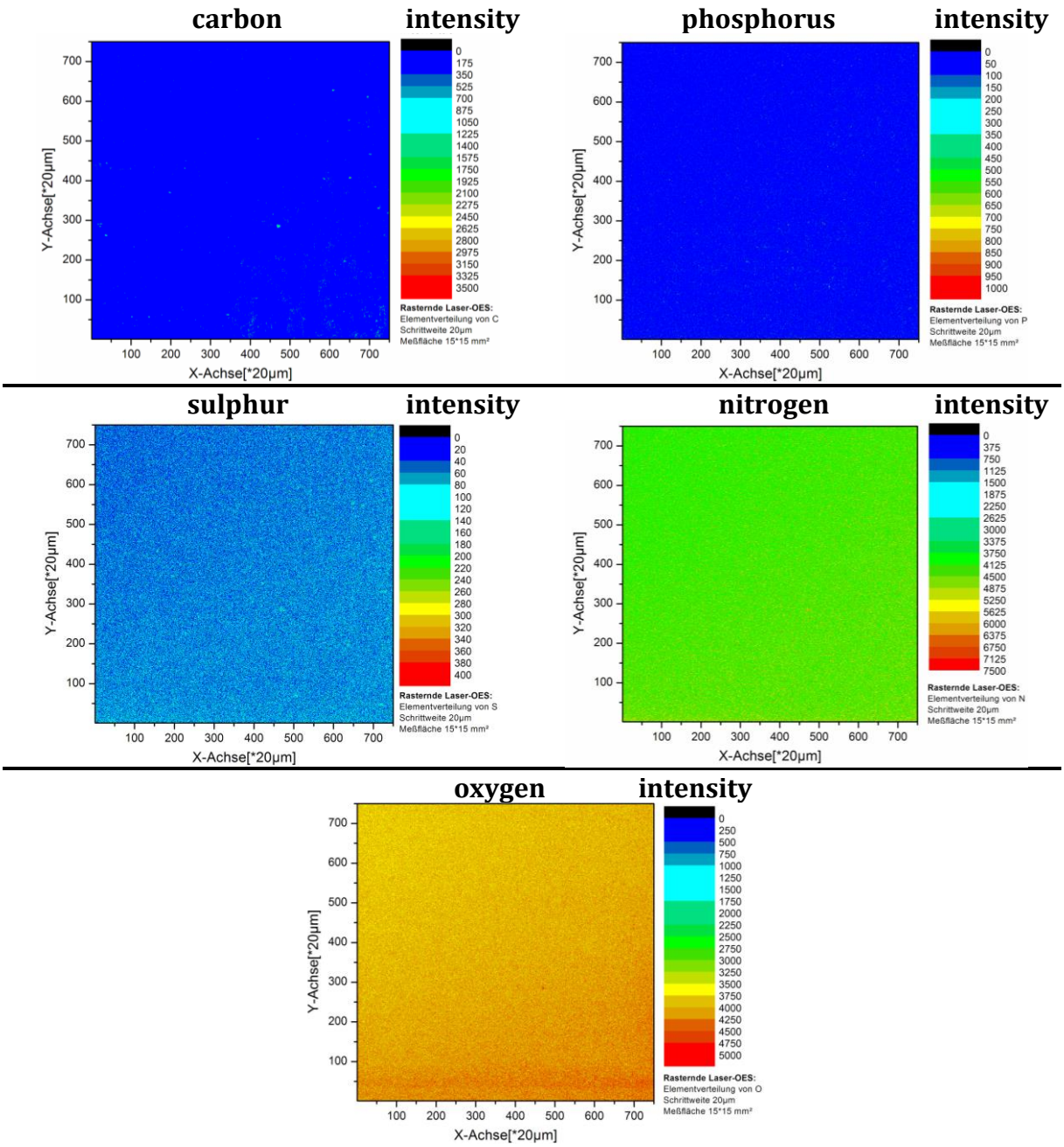

Figure 33. LIBS element distribution of skin-passed HDG

White light interferometry

The surface of this skin-passed HDG reference sample was analyzed via white light interferometry to observe wear induced morphological changes during the tribological treatment in chapter 5.1.4.1 (p. 111). The results are presented in form of 2D- and 3D-morphological maps and tables of roughness parameters (Figure 34).

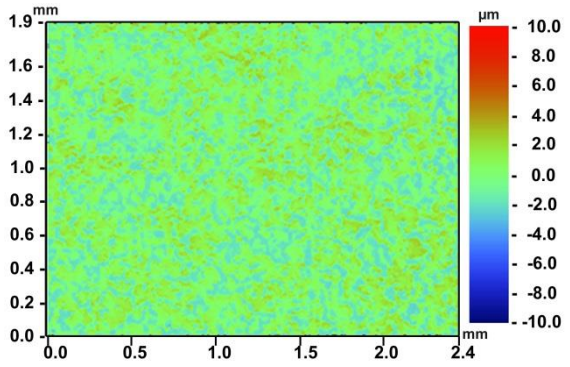

2D morphological map

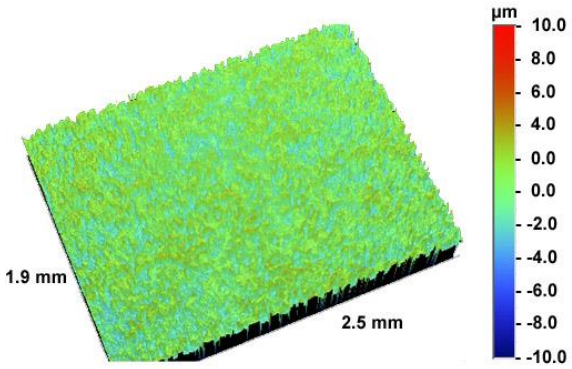

3D morphological map

Roughness parameters:			
R_z	6.88 µm	**R_a**	1.16 µm
R_p	4.82 µm	**R_q**	1.32 µm
R_t	8.39 µm	**Surface Area**	4.66 mm^2

Figure 34. Wight light interferometry morphological maps and roughness parameters of skin-passed HDG

The morphological maps and roughness parameters show a homogeneous rough surface with a mean roughness **R_a** of 1.16 µm.

This mean roughness is in the expected range from 0.857-1.629 µm for skin-passed HDG.[121]

Therefore, the samples with this purity and roughness can be used for further adsorption and tribological tests.

4.1.2.2 Non-skin-passed hot-dip galvanized steel (NSP-HDG)

X-ray photoelectron spectroscopy (XPS)

a)

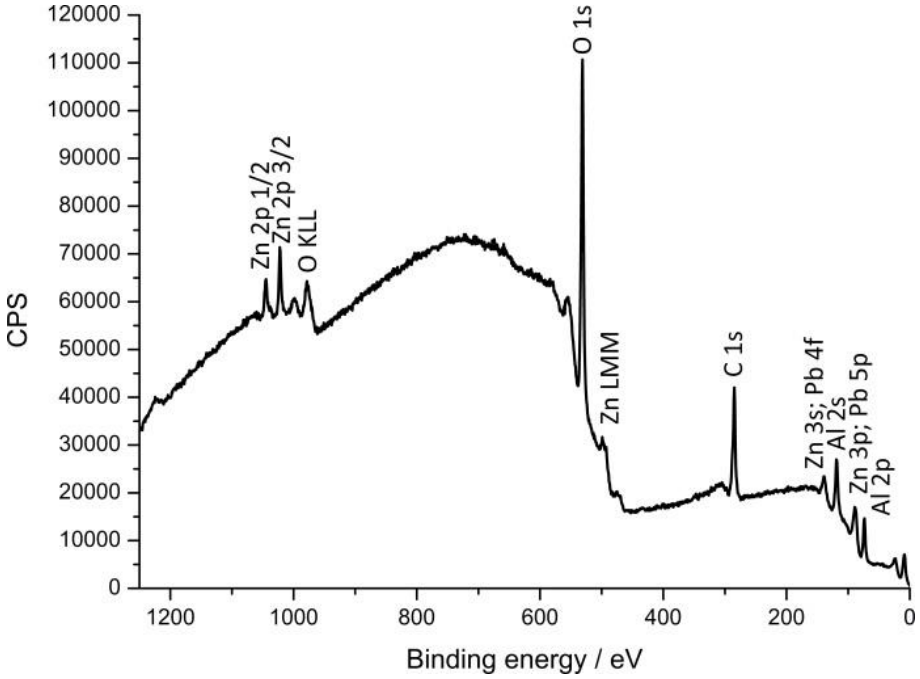

b)

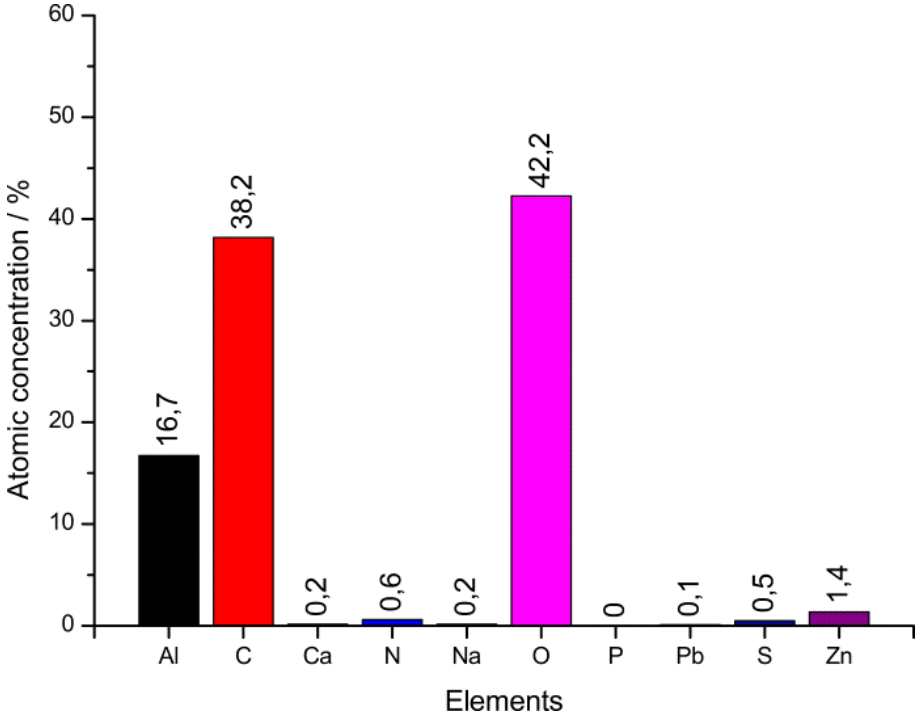

Figure 35. XPS survey (a) and atomic concentrations (b) of a NSP-HDG steel reference

The XPS survey of the NSP-HDG reference (Figure 35; a) reveals the expected elements for NSP-HDG like zinc, oxygen, carbon and alumina.

However, there is an unexpected signal at ~139 eV that indicates a contamination with lead. This contamination may originate from product changes in the hot-dip coating line because

the steel was purchased from field test runs and previous runs contained lead to get large zinc spangles.

The complete atomic concentrations (Figure 35; b) reveal additional small contaminations with calcium, sodium, nitrogen and sulfur at the edge of the detection limit. C1s, O1s, Al2p, Zn2p, P2p, S2p, Na1s, Ca2p and N1s high-resolution spectra of the HDG steel sample and their curve-fitting results are shown from Figure 36 to Figure 40.

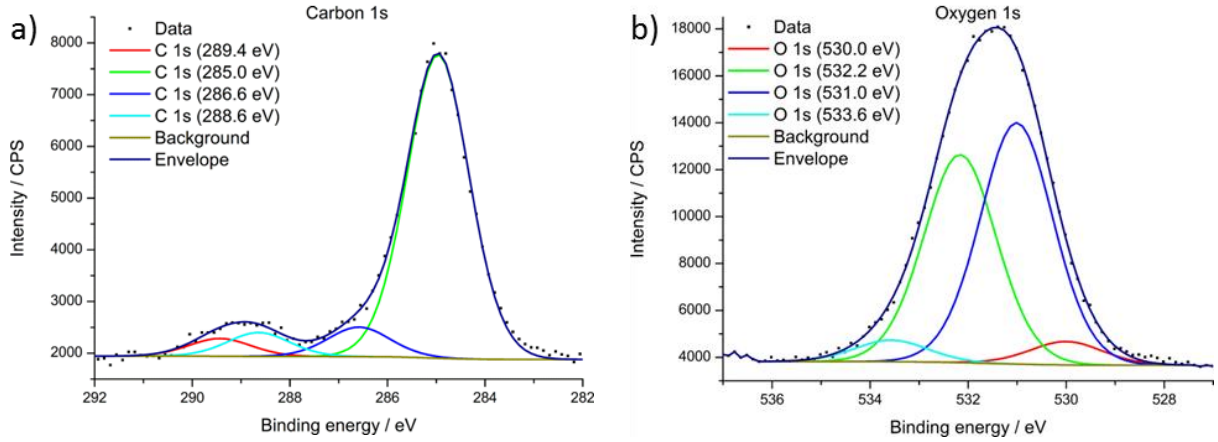

Figure 36. High-resolution XPS spectra of the *C 1s* (a) and *O 1s* (b) region of a NSP-HDG steel reference

The *carbon 1s* high-resolution spectrum (Figure 36; a) gives the best fit with four peaks, where the lowest peak at 285.0 eV is assigned to hydrocarbon. The peak at 286.6 eV is assigned to –C-OH or –COC- from the organic contamination layer and the peak at 288.6 eV is assigned to –C=O from the organic contamination layer, too. The fourth peak at 289.4 eV is attributable to metal carbonates or hydrocarbonates.

The *oxygen 1s* high-resolution spectrum (Figure 36; b) gives the best fit with four peaks, where the lowest peak at 530.0 eV is assigned to oxide and the peak at 531.0 eV is assigned to oxyhydroxide. The peaks at 532.2 eV and 533.6 eV are attributable to –C-O and –C=O from the organic contamination.

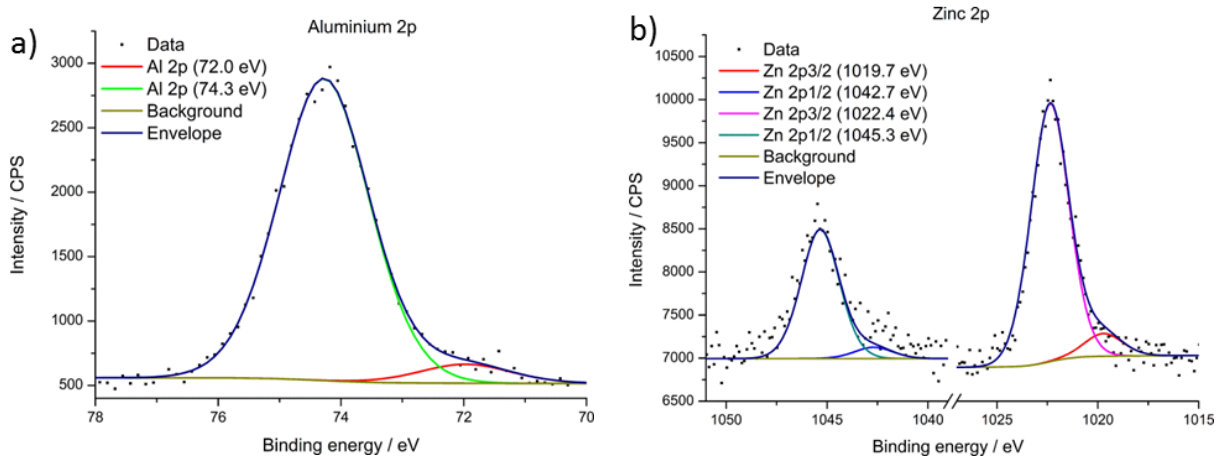

Figure 37. High-resolution XPS spectra of the *Al 2p* (a) and *Zn 2p* (b) region of a NSP-HDG steel reference

The high-resolution spectra of the metal surface components aluminum (Figure 37; a) and zinc (Figure 37, b) confirm the expected oxidic nature of these elements.

The *aluminum 2p* high-resolution spectrum (Figure 37; a) gives the best fit with two peaks, where the lowest peak at 72.0 eV is attributed to metallic aluminum and the peak at 74.3 eV is assigned to oxidic aluminum.

The *zinc 2p (*Figure 37*; b)* high-resolution spectrum is splitted into two spin-orbit components *Zn 2p3/2* and *Zn 2p1/2* with a difference of 22.9 eV. Both give the best fit with two peaks, where the lowest peak of *Zn 2p3/2* at 1019.7 eV is assigned to metallic zinc and the peak at 1022.4 eV is assigned to oxidic zinc.

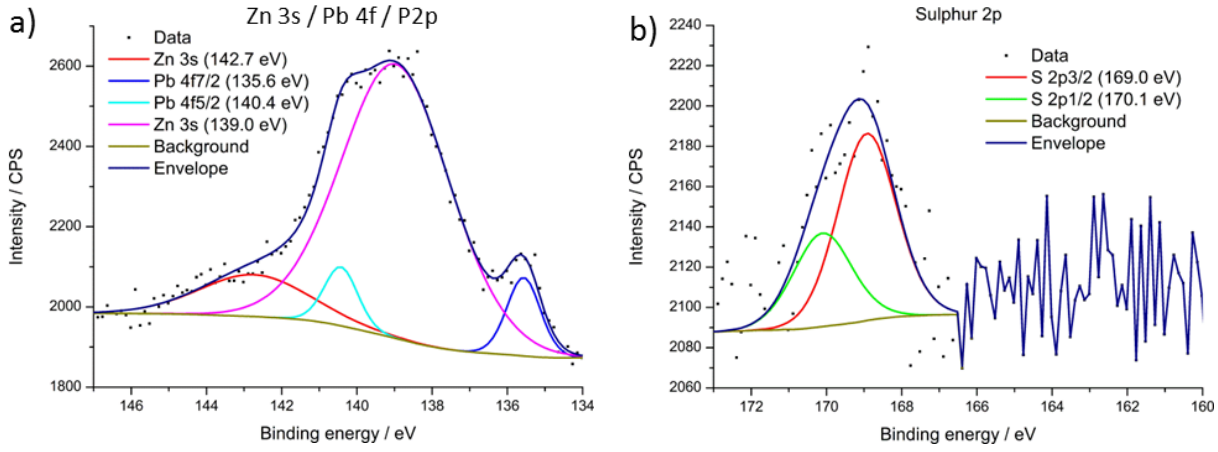

Figure 38. High-resolution XPS spectra of the *Zn 3s / Pb 4f / P 2p* (l.) and *S 2p* (b) region of a NSP-HDG steel reference

The *Zn 3s / Pb 4f / P 2p* high-resolution spectrum (Figure 38; a) is influenced by *lead 4f* peaks and a strong *zinc 3s* peak. The surface concentration of lead is very weak (~0.1 %), but a high relative sensitivity factor (22.7) of the *lead 4f* signal might deteriorate the

interpretation of phosphorus signals in this region. The spectrum gives the best fit with four peaks, where the lowest peak at 135.6 eV is assigned to the low energy spin-orbit component of metallic lead (*Pb 4f7/2*). The difference between both components is 4.8 eV, which allocates the *Pb 4f5/2* component to 140.4 eV. The peak at 139.0 eV is assigned to metallic zinc and the peak of 142.7 eV is assigned to oxidic zinc.

The *sulphur 2p* high-resolution spectrum (Figure 38; b) gives the best with two peaks, which are assigned as the spin-orbit components *S 2p3/2* at 169.0 eV and *S 2p1/2* at 170.1 eV of a high-oxidized sulphate contamination.

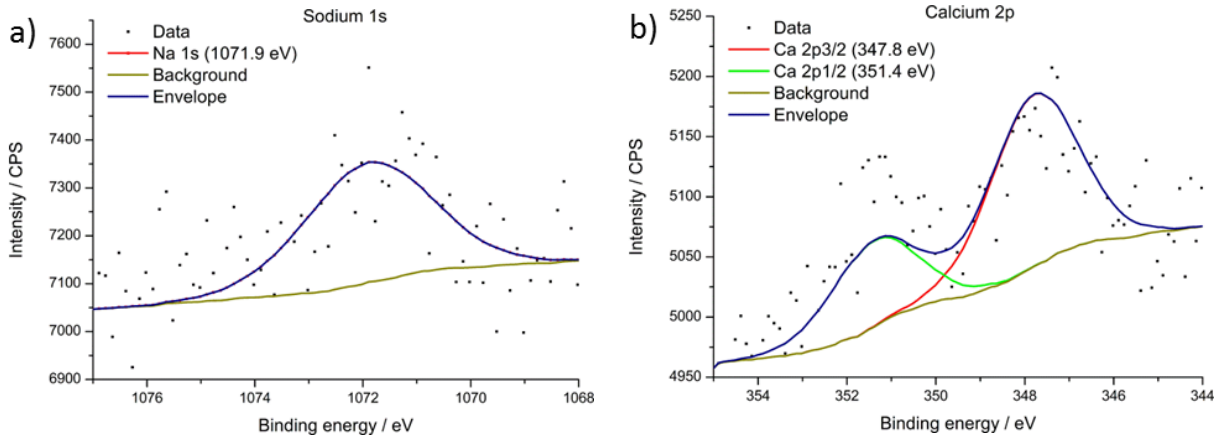

Figure 39. High-resolution XPS spectra of the *Na 1s* (a) and *Ca 2p* (b) region of a NSP-HDG steel reference

The minor contaminations of sodium (BE: 1071.9 eV) (Figure 39; a), calcium (BE: *2p3/2* 347.8 eV; *2p1/2* 351.4 eV) (Figure 39; b) and nitrogen (BE: 399.8 eV, 401.5 eV) (Figure 40) couldn`t be assigned to a specific species and their origin remains unknown. These signals shouldn`t interfere with further interpretation because of their small surface concentrations and binding energies.

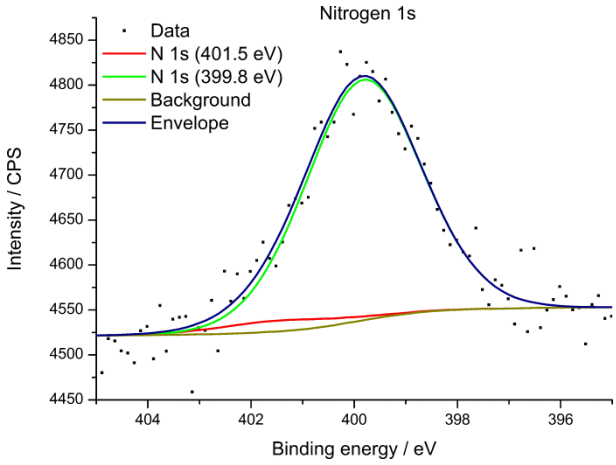

Figure 40. High-resolution XPS spectra of the *N 1s* region of a NSP-HDG steel reference

Raman spectroscopy

The zinc coated steel surface is not expected to be of pure metallic nature. The surface is in contact with atmospheric oxygen and thereby immediately oxidized.

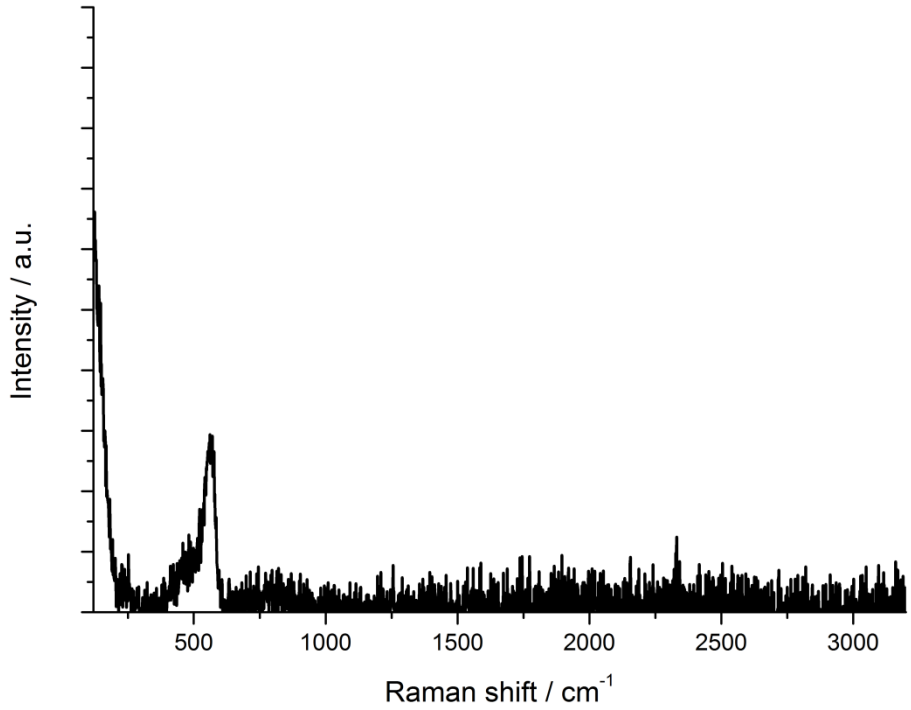

Figure 41. Raman spectrum of solvent cleaned NSP-HDG steel

The Raman spectrum (Figure 41) should reveal the vibrational modes of zinc oxide (ZnO). Based on the symmetry of ZnO, the following modes are known: 101 cm^{-1} (E_2), 437 cm^{-1} (E_2), 407 cm^{-1} (E_1 transverse), 380 cm^{-1} (A_1 transverse), 583 cm^{-1} (E_1 longitudinal) and 574 cm^{-1} (A_1 longitudinal).[122]

However, it is obvious that a hot-dipped surface is not a wurtzite crystal structure but hardly amorphous. This explains the absence of the mentioned peaks. The only peak at ~530 cm^{-1} can be assigned to a C-doped ZnO variant [123]. This can be explained by the incorporation of carbon during the hot-dipping process.

Important is, that the surface is free of detectable contaminations and is useable as reference for adsorption studies.

The NSP-HDG samples with this purity can be used for the tribological tests.

4.1.2.3 Zinc (Zn)

X-ray photoelectron spectroscopy (XPS)

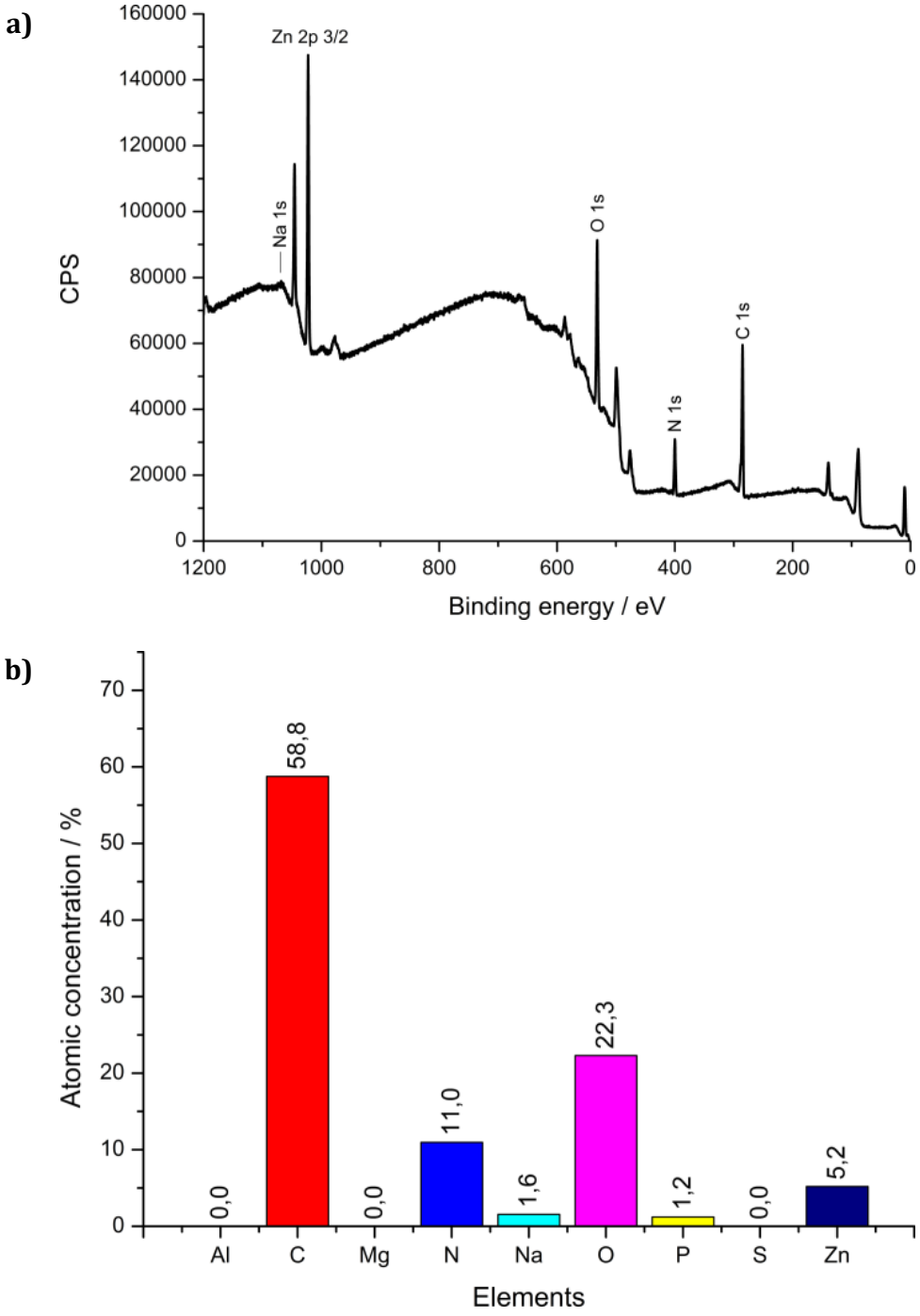

Figure 42. XPS survey (a) and atomic concentrations (b) of solvent cleaned Zn

The XPS survey spectrum (a) and the atomic composition (b) of fresh solvent cleaned zinc surface are shown in Figure 42. Strong signals of the expected elements carbon, oxygen and zinc are detected, implying that an oxide layer with a contamination of adventitious carbon through exposure to air is present. There are also small signals of sodium, nitrogen and phosphorus detectable. The nitrogen contamination is probably based on inclusions while

melting the zinc under nitrogen gas-stream. The sodium and phosphorus contamination is of unknown origin.

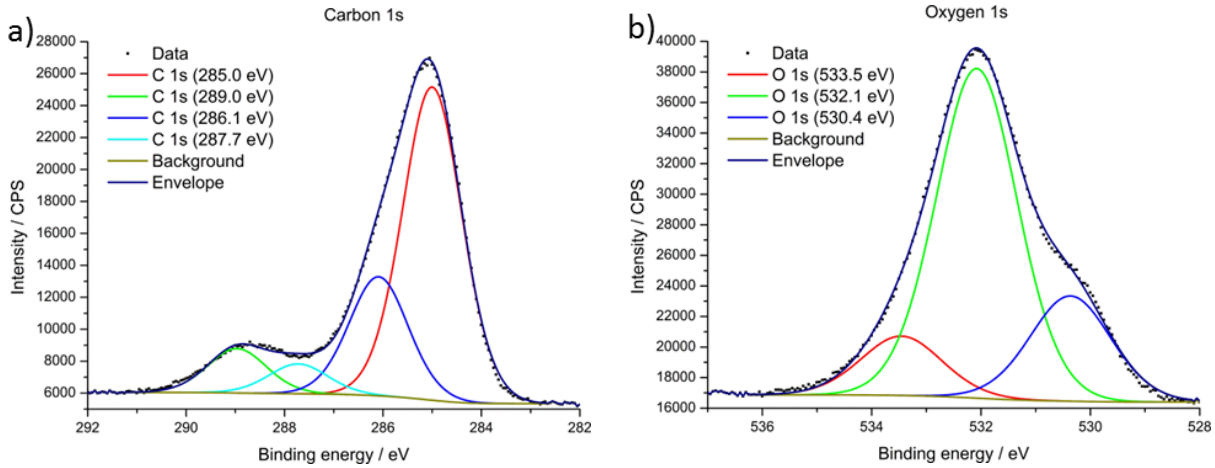

Figure 43. High-resolution XPS spectra of the *C 1s* (a) and *O 1s* (b) region of pure Zn

The *carbon 1s* high-resolution spectrum (Figure 43; a) gives the best fit with four separate peaks at 285.0 eV, 286.1 eV, 287.7 eV and 289.0 eV. The lowest peak at 285.0 eV is assigned to hydrocarbon and is used for the charge correction of the spectra. The peak at 286.1 eV is assigned to –C-OH or –COC- from the organic contamination layer and the peak of 287.7 eV is assigned to –C=O from the organic contamination layer, too. The fourth peak of 289.0 eV is attributable to metal carbonates or hydrocarbonates.

The *oxygen 1s* high-resolution spectrum (Figure 43; b) gives the best fit with three peaks at 530.4 eV, 532.1 eV and 533.5 eV. The lowest peak at 530.4 eV corresponds to an oxide based oxygen species, here probably zinc oxide. The peak at 532.1 eV is assigned to oxyhydroxide and the peak at 533.4 eV is attributable to –C-OH and –C=O from the contamination layer.

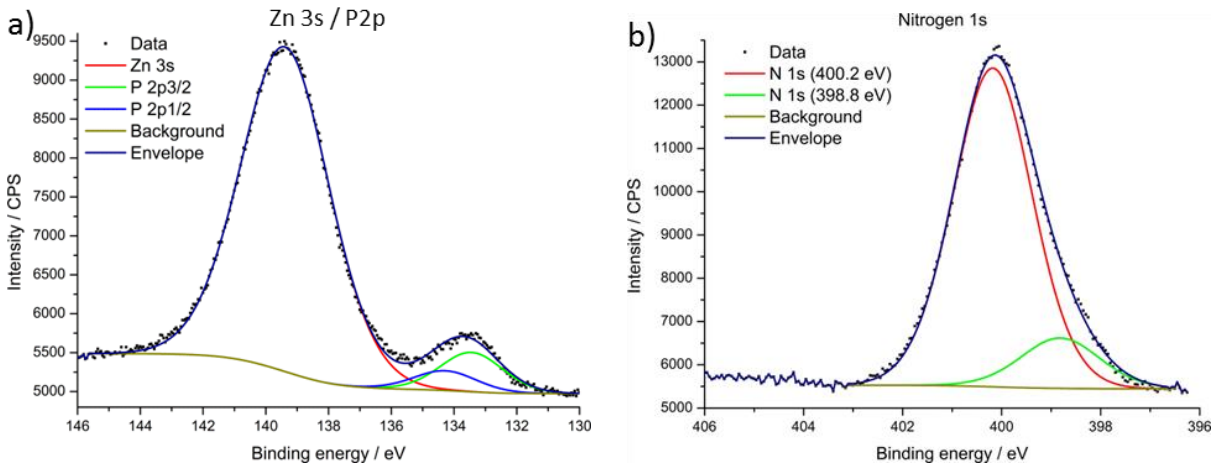

Figure 44. High-resolution XPS spectra of the *phosphorus 2p* (a) and *N 1s* (b) region of pure Zn

The high-resolution XPS spectra of the *Zn 3s / P 2p* region (Figure 44; a) in the range between 146-130 eV shows the signal of the *zinc 3s* orbital at 139.4 eV and the signal of the *phosphorus 2p* orbital which is separated in the two peaks *2p3/2* and *2p1/2* due to spin-orbit splitting. The peak at *2p3/2* (133.4 eV) is twice the size as the *2p1/2* (134.3 eV) peak. The two peaks are separated by 0.84 eV, which is used as constraint for fitting the phosphorus signal.

The *nitrogen 1s* high-resolution spectrum (Figure 44; b) gives the best fit with two peaks at 400.2 eV and 398.8 eV, which belongs to species originated by enclosed nitrogen during the melting process in the sample preparation, or aminogroup contaminations of unknown origin.

The zinc samples can be used for the adsorption tests, because the main reactive groups of the additives consist of phosphorus and sulphur. Therefore, the small contamination with phosphorus and the contamination with nitrogen shouldn`t influence the further characterizations strongly.

4.1.2.4 Zinc alloy (ZnAlMg)

X-ray photoelectron spectroscopy (XPS)

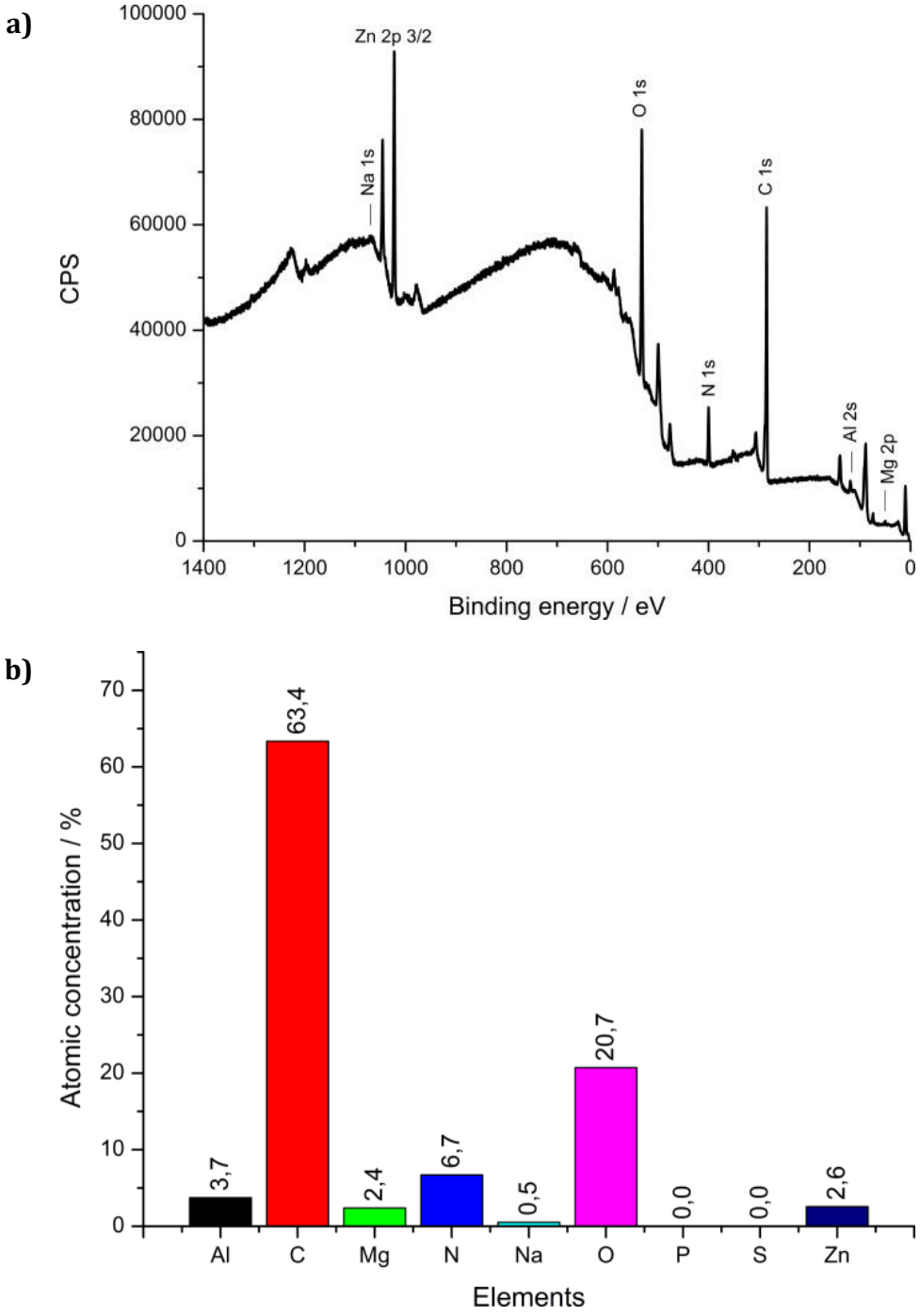

Figure 45. XPS survey (a) and atomic concentrations (b) of solvent cleaned zinc alloy

The XPS survey (a) of a fresh solvent cleaned zinc alloy sample is shown in Figure 45. Similar to the zinc sample (Figure 42) small contaminations of sodium and nitrogen are detectable on the surface. The expected signals of zinc, oxygen, carbon, aluminum and magnesium suggest an oxidized surface of aluminum, magnesium and zinc with a hydrocarbon contamination.

Also notable is the absence of the elements phosphorus and sulphur, which are key-elements of later adsorbed additives.

The atomic concentrations (b) evaluated out of this survey are also shown in Figure 45.

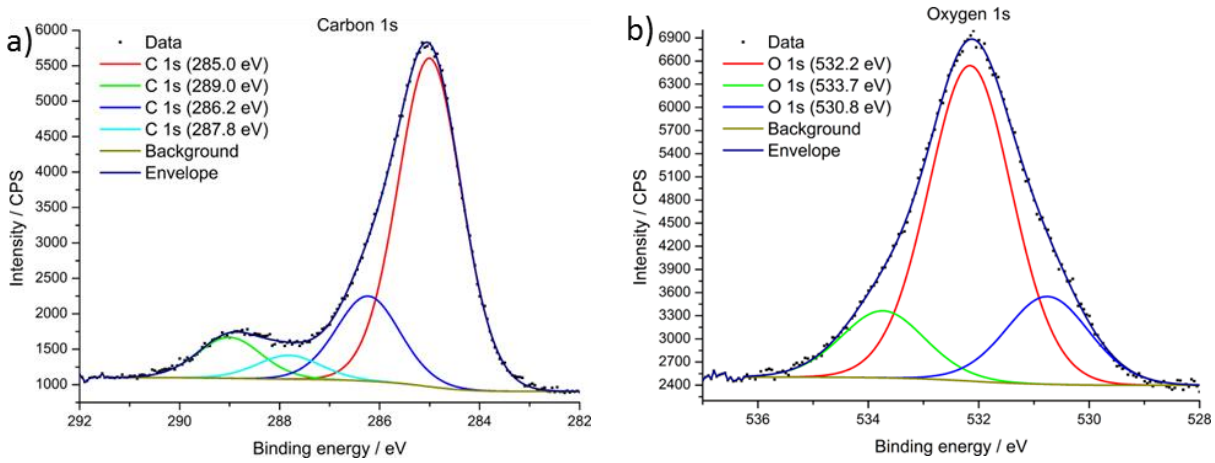

Figure 46. High-resolution XPS spectra of the *C 1s* (a) and *O 1s* (b) region of zinc alloy

C1s, O1s and N1s high-resolution spectra of the ZnAlMg-sample and their curve-fitting results are shown in Figure 46 and Figure 47.

The *carbon 1s* high-resolution spectrum (Figure 46; a) gives the best fit with four peaks, where the lowest peak at 285.0 eV is assigned to hydrocarbon. The peak at 286.2 eV is assigned to –C-OH or –COC- from the organic contamination layer and the peak at 287.8 eV is assigned to –C=O from the organic contamination layer, too. The fourth peak at 289.0 eV is attributable to metal carbonates or hydrocarbonates.

The *oxygen 1s* high-resolution spectrum (Figure 46; b) is best fitted with three peaks, where the peak with the lowest binding energy at 530.8 eV can be assigned to a combination of zinc, alumina, and magnesia oxides. The major peak at 532.2 eV can be assigned to oxyhydroxides while the peak with the highest binding energy of 533.7 eV is attributable to-C-OH and –C=O components from an adsorbed organic compound or an organic contamination.

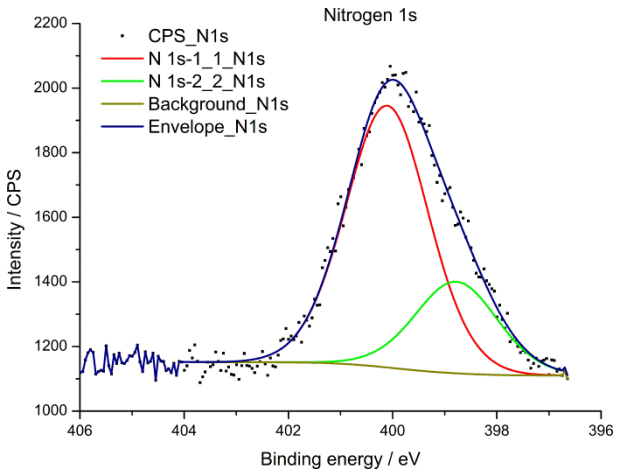

Figure 47. High-resolution XPS spectra of the *N 1s* region of zinc alloy

The *nitrogen 1s* high-resolution spectrum (Figure 47) gives the best fit with two peaks, which belongs to species originated by enclosed nitrogen during the melting process in the sample preparation.

The zinc alloy samples with this purity can be used for the adsorption tests.

4.1.3 Discussion

The reference measurements of the additives by means of GC-MS, IR- and Raman-spectroscopy demonstrate their purity and their usability for tribological studies without further purification. In addition, IR- and Raman-spectroscopy deliver useful spectra with additive characteristic peaks for the comparison with tribological treated surfaces. Because XPS measurements of the additives were not possible with the available equipment, the literature data provided by *Matsumuto* [124] of frozen additives is used for comparison.

The measurements of HDG provide reference data for the surface morphology and the chemical composition. WLI reveal a surface with homogenous roughness. Minor contaminations of phosphorus are found by XPS measurements, which can complicate the interpretation of phosphorus-containing additive adsorption processes. The XPS depth profile reveals that the first surface layers consist of aluminum and oxide followed by increasing zinc contents.

NSP-HDG steel shows minor contaminations with calcium, nitrogen, sodium and even lead and sulphur. Especially the last two elements occur in regions with expected additive adsorption, but a strong complication of the spectra is not suspected due to the small concentrations of both (S: 0.5 %; Pb: 0.1 %).

The reference measurements of pure zinc reveal surface contaminations with sodium, phosphorus and nitrogen of unknown origin. The interpretation of spectra with adsorbed phosphorus containing additives should not strongly be complicated by the phosphorus contamination, due to the small surface concentration of 1.2 %.

Contaminations on ZnAlMg substrates consist of small amounts of sodium and nitrogen and shouldn`t interfere with following spectra interpretation.

Consequently, it can be concluded that the reference measurements of additives and substrates confirm the needed purity and provide useful spectroscopic data for the comparison with following studies.

4.2 Adsorption on pure and technical substrates

Based on the reference measurements of additives and substrates, this chapter analyzes the adsorption processes (chapter 3.3.1; p. 28) of these additives on the surfaces. This chapter focuses on the adsorption processes of DTNPS and Irgalube TPPT as model substances for sulphur (DTNPS) and phosphorus-sulphur (Irgalube TPPT) additives on zinc surfaces. Therefore, the adsorption of the sulphur-based additive DTNPS and the sulphur- and phosphorus-based additive Irgalube TPPT on technical-grade NSP-HDG steel is characterized by XPS and ToF-SIMS. To support these results, the adsorption is also analyzed on laboratory-grade zinc and zinc alloy samples by means of XPS.

The results are assumed to support the interpretation of tribological generated layers in chapter 5 (p. 90).

Adsorption of further additives is shown in Appendix 12.1.

4.2.1 Adsorption on technical non-skin passed hot-dip galvanized steel (NSP-HDG)

4.2.1.1 Di-tert-nonyl polysulphide (DTNPS) / NSP-HDG

X-ray photoelectron spectroscopy measurements (XPS 2)

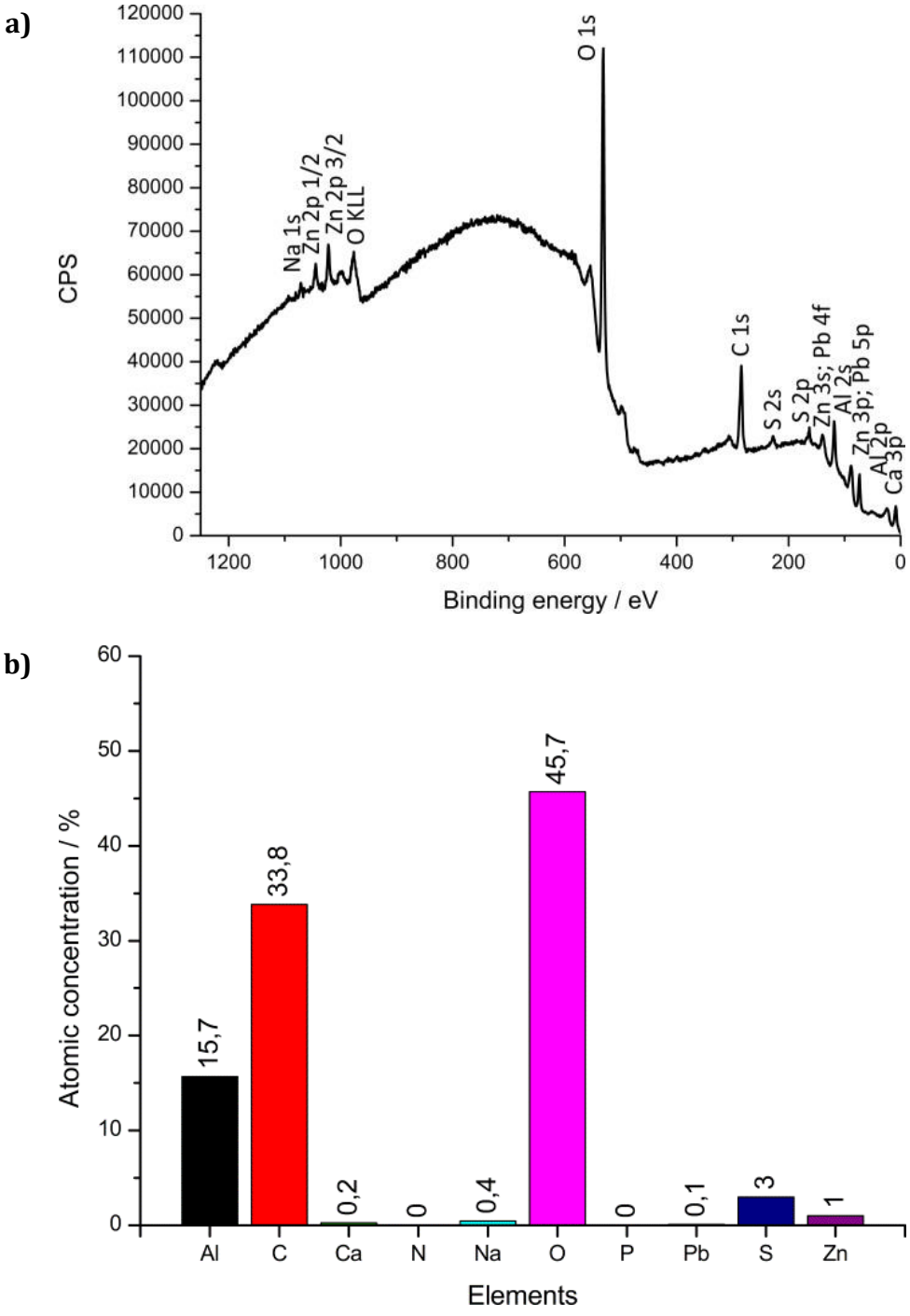

Figure 48. XPS survey (a) and atomic concentrations (b) of DTNPS on NSP-HDG steel

The XPS survey shown in Figure 48 reveals the expected elements estimated for coverage of HDG with DTNPS like zinc, oxygen, carbon, sulphur and alumina. Furthermore, minimal contaminations with sodium, calcium and lead are detectable as previously seen in the

reference measurements (chapter 4.1.2.2; p. 55). The atomic concentrations of the surface composition are also shown in Figure 48.

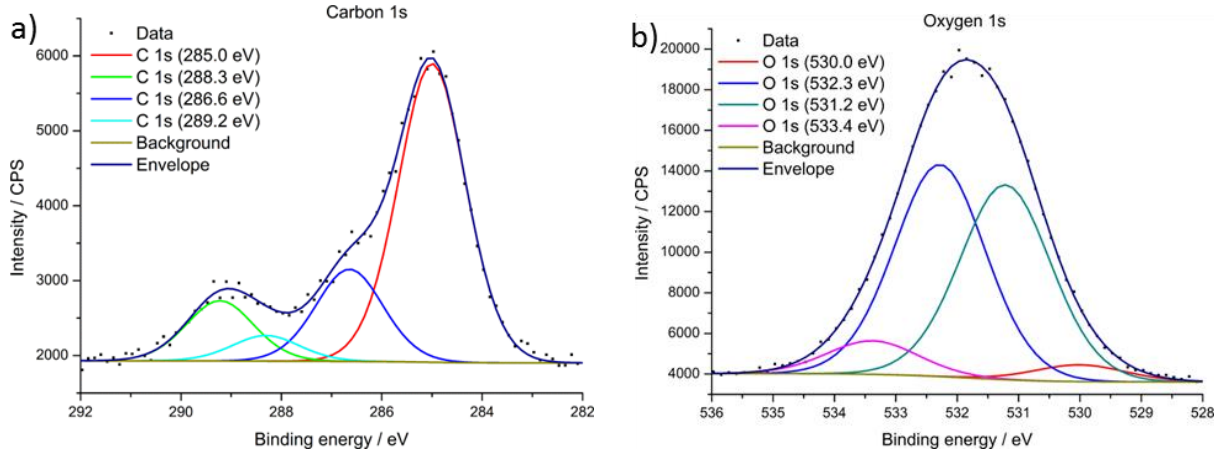

Figure 49. High-resolution XPS spectra of the *C 1s* (a) and *O 1s* (b) region of DTNPS on NSP-HDG steel

The *carbon 1s* high-resolution spectrum (Figure 49; a) gives the best fit with four peaks, where the lowest peak at 285.0 eV is assigned to hydrocarbon. The peak at 286.6 eV is assigned to -C-O- or -C-S- from an adsorbed organic compound. In addition, the peak at 288.3 eV can be assigned to -C=O or –C=S from an adsorbed organic compound. The fourth peak at 289.2 eV can be assigned to metal carbonates or hydrocarbonates.

The *oxygen 1s* high-resolution spectrum (Figure 49; b) gives the best fit with four peaks, where the peak at lowest binding energy at 530.0 eV is assigned to oxide and the peak at 531.2 eV is assigned to oxyhydroxide. The peaks at 532.3 eV and 533.4 eV contribute to -C-O- and -C=O components of an adsorbed organic compound or an organic contamination.

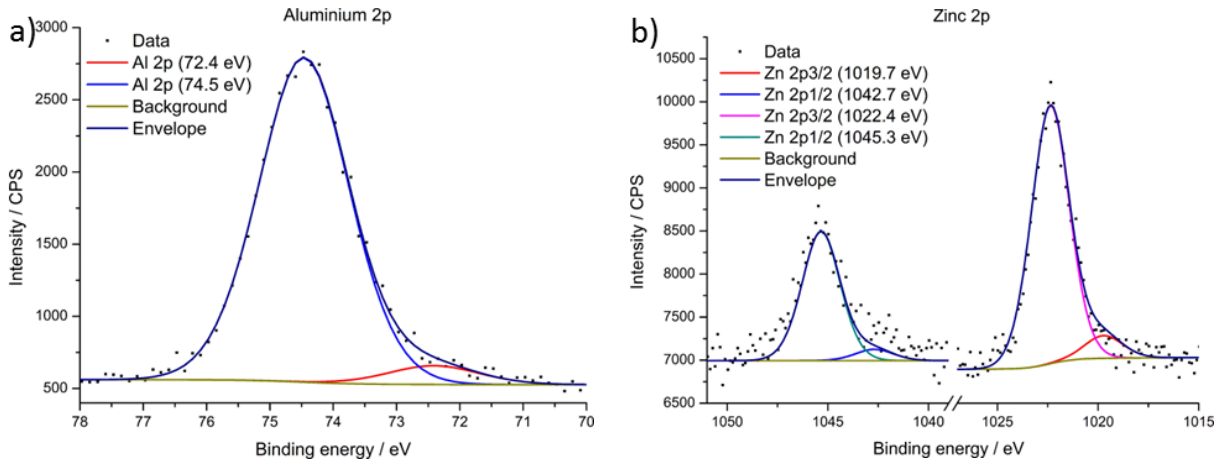

Figure 50. High-resolution XPS spectra of the *Al 2p* (a) and *Zn 2p* (b) region of DTNPS on NSP-HDG steel

The *aluminum 2p* high-resolution spectrum (Figure 50; a) gives the best fit with two peaks, where the lowest peak of 72.4 eV is assigned to metallic aluminum and the peak of 74.5 eV is assigned to oxidic aluminum.

The *zinc 2p* high-resolution spectrum (Figure 50; b) is splitted into two spin-orbit components *Zn 2p3/2* and *Zn 2p1/2* with a binding energy difference of 22.9 eV. Both give the best fit with two peaks, where the peaks of 1019.7 eV and 1042.7 eV are assigned to metallic zinc and the peaks of 1022.4 eV and 1045.3 eV are assigned to oxidic zinc.

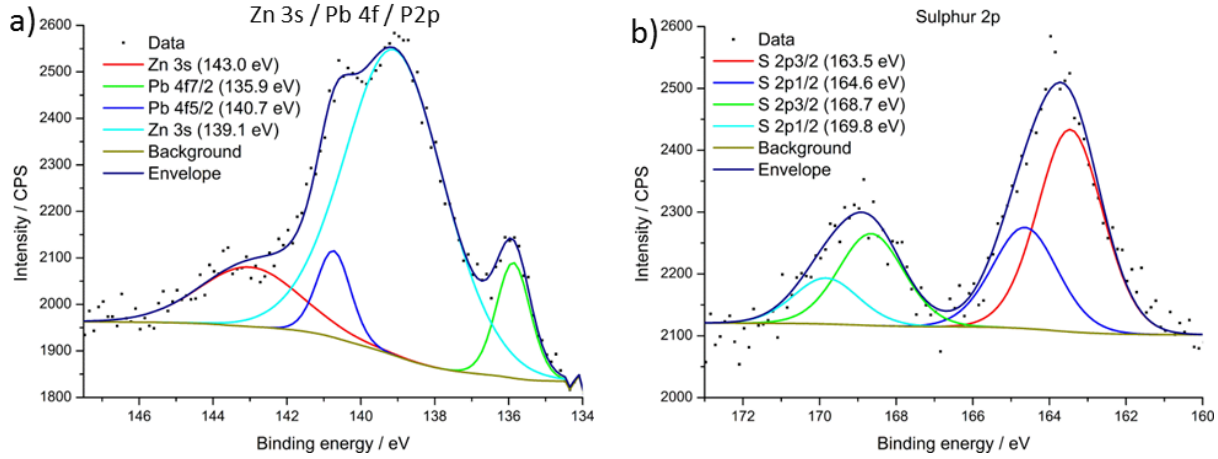

Figure 51. High-resolution XPS spectra of the *Zn 3s / Pb 4f / P 2p* (a) and *S 2p* (b) region of DTNPS on NSP-HDG steel

The *Zn 3s / Pb 4f / P 2p* high-resolution spectrum (Figure 51; a) is influenced by *lead 4f* peaks and a strong *zinc 3s* peak. The surface concentration of lead is very weak (~0.1 %), similar to the reference measurement of hot-dip galvanized steel (chapter 4.1.2.2, p. 55). However, the spectrum gives the best fit with four peaks, where the lowest peak of 135.9 eV is assigned to the low-energy spin-orbit component (*Pb 4f7/2*) of metallic lead. The

difference between both spin-orbit components of 4.8 eV allocates the high-energy component (*Pb 4f5/2*) to 140.7 eV. The peak of 139.1 eV is assigned to metallic zinc and the peak of 143.0 eV is assigned to oxidic zinc.

The *sulphur 2p* high-resolution spectrum (Figure 51; b) gives the best fit with two doublets. Similar to the reference measurement (Figure 38, r.; p. 57), a high-oxidized sulphate species is present (S 2p3/2: 168.7 eV; S 2p1/2: 169.8 eV). Additionally, a low binding energy sulphur species is detected (S 2p3/2: 163.5 eV; S 2p1/2: 164.6 eV) which can be assigned to a sulphide species.

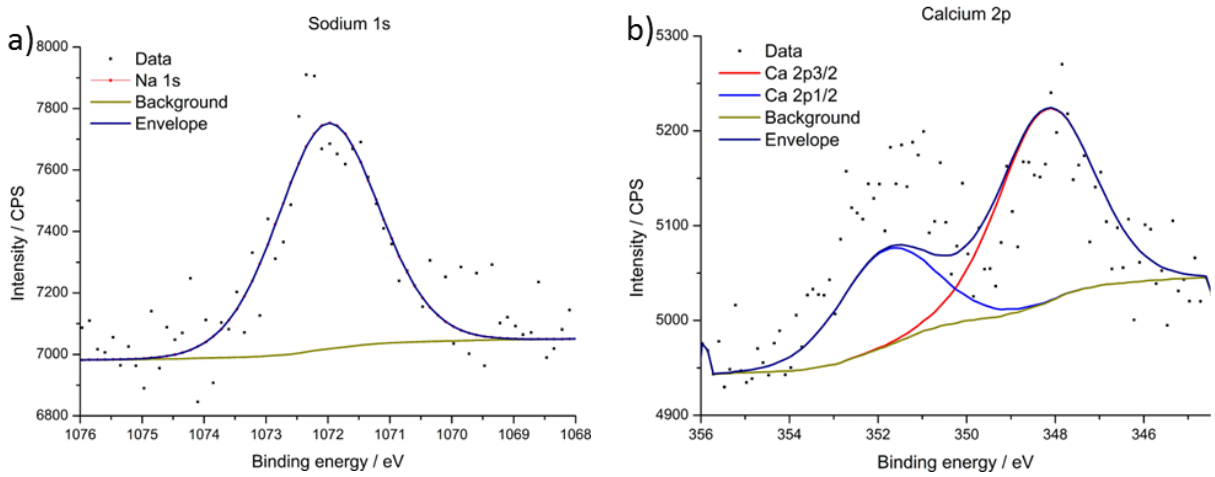

Figure 52. High-resolution XPS spectra of the *Na 1s* (a) and *Ca 2p* (b) region of DTNPS on NSP-HDG steel

The minor contaminations of sodium (Figure 52; a) and calcium (Figure 52; b) with surface concentrations of 0.4 % for sodium and 0.2 % for calcium cannot be assigned to specific species and their origin remains unknown.

Time of flight secondary ion mass spectrometry (ToF-SIMS)

The following image collection (Figure 53) presents the positive and negative ion images of DTNPS on NSP-HDG.

The negative ion images reveal that the fragments C_2HS^-, HS_2^- and $C_2S_2^-$ have the highest concentration of all sulphur-fragments on the surface. The fragment composition is followed by high amounts of fragments like $CH_3S_2^+$, C_2S^-, $C_{12}H_{15}O_3^-$ and S_4^-. The occurring of these fragments indicates the presence of monosulphides S^{2-}, disulphides S_2^{2-} and/or polysulphides S_n^{2-} as sulphur-species on the surface. In addition, no oxy-sulphur $S_xO_y^{z-}$ is revealed in the ion images.

In summary, the adsorption of DTNPS on NSP-HDG is confirmed due to XPS and ToF-SIMS analysis despite of the minor sulphur contamination on the reference (Figure 1; p. 57). The

XPS measurements (Figure 51; p. 69) reveal the presence of sulphides next to the sulphate contamination. These results are supported by the detection of mono-, di- and poly-sulphides on the surface by means of ToF-SIMS analysis (Figure 53; p. 71).

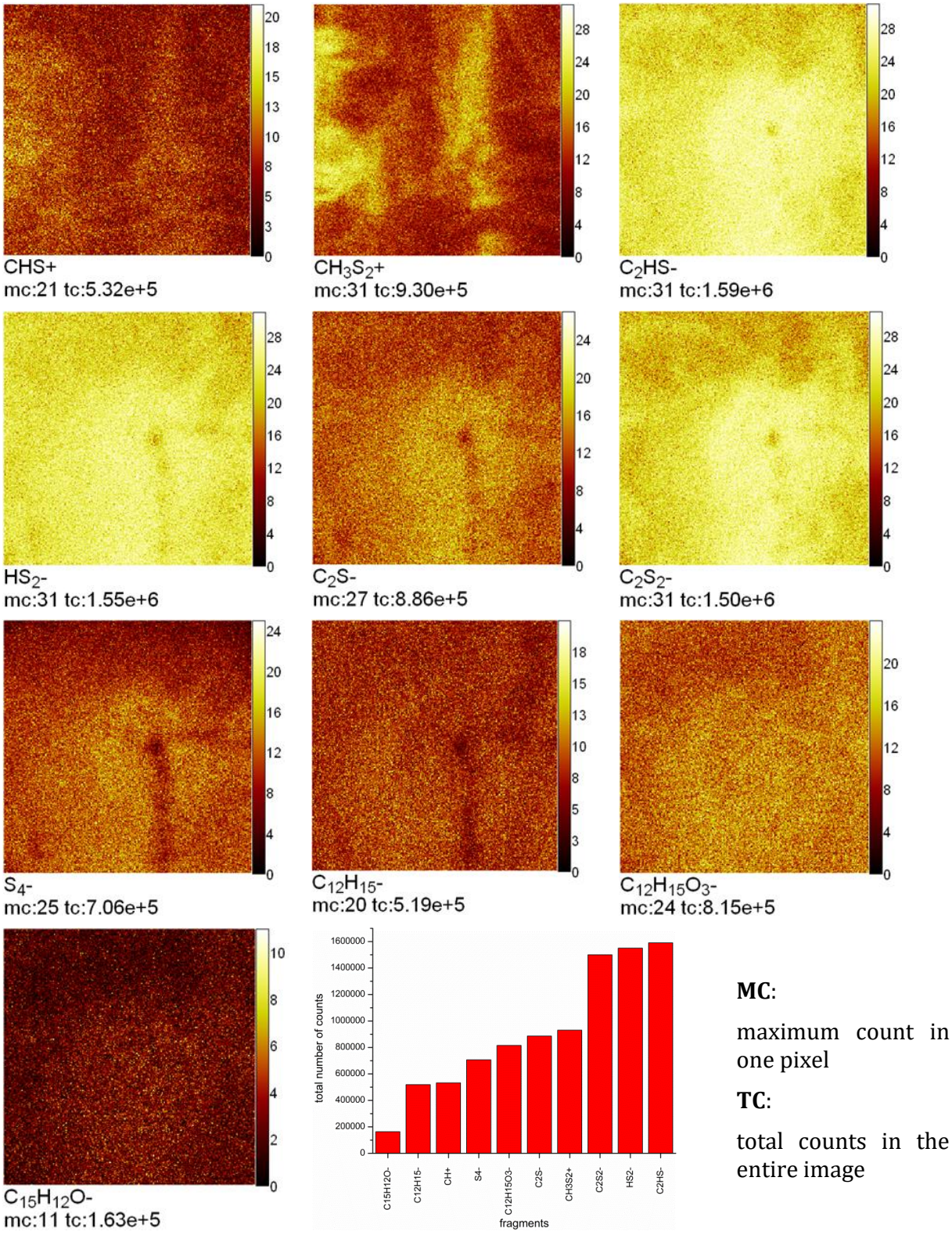

MC:

maximum count in one pixel

TC:

total counts in the entire image

Figure 53. ToF-SIMS ion images and total number of counts per fragment of DTNPS on NSP-HDG steel

4.2.1.2 Triphenylphosphorthionate / NSP-HDG

X-ray photoelectron spectroscopy (XPS)

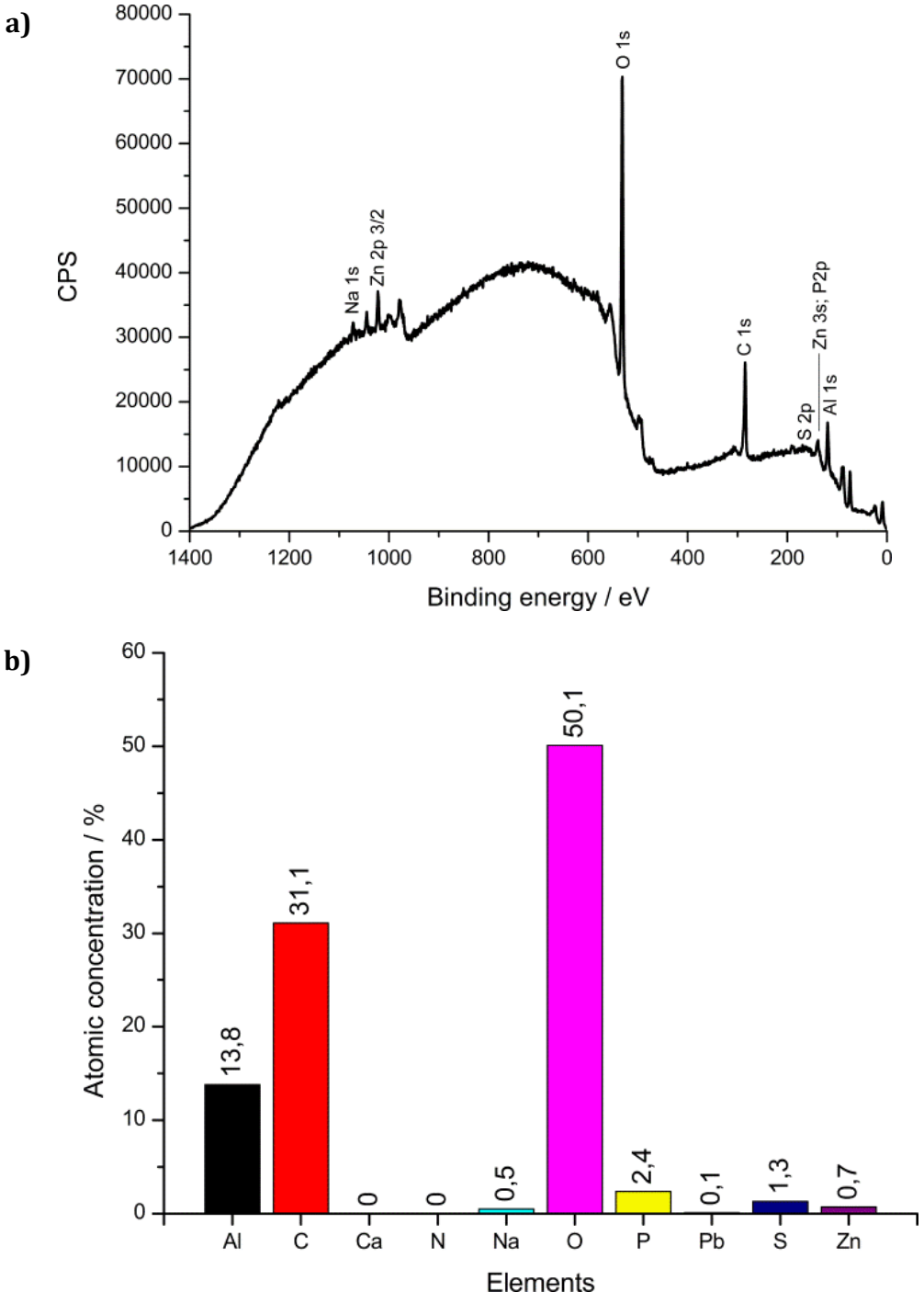

Figure 54. XPS survey (a) and atomic concentrations (b) of triphenylphosphorthionate on NSP-HDG steel

The XPS survey (Figure 54; a) shows the element signals of aluminum, carbon, sodium, oxygen, phosphorus, lead, sulfur and zinc. These signals correspond with the expected signals of adsorbed triphenylphosphorthionate on NSP-HDG. The atomic concentrations

(Figure 54; b) reveal that the additional elements sodium and lead are very small contaminations as previously seen in the reference measurements (chapter 4.1.2.2; p. 55).

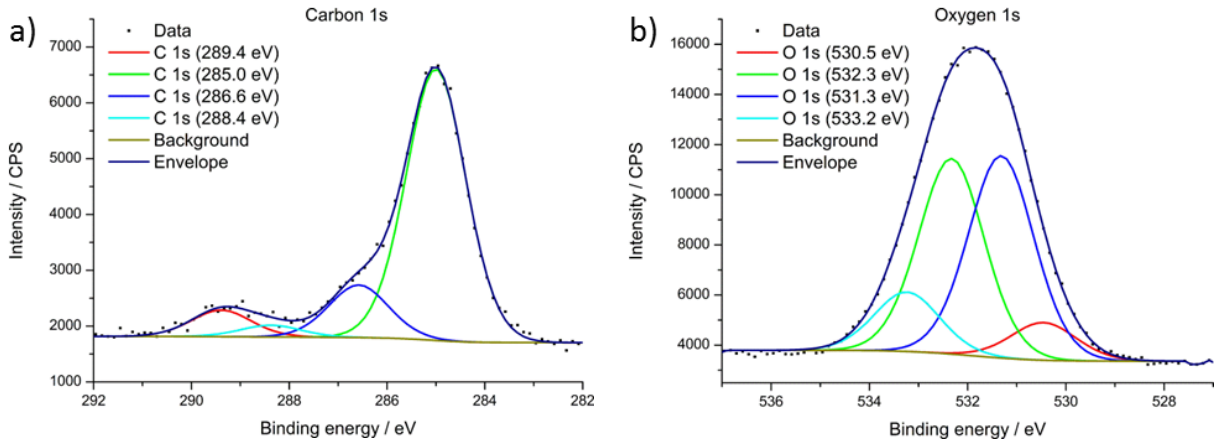

Figure 55. High-resolution XPS spectra of the *C 1s* (a) and *O 1s* (b) region of triphenylphosphorthionate on NSP-HDG steel

The *carbon 1s* high-resolution spectrum (Figure 55; a) gives the best fit with four peaks, where the peak with the lowest binding energy of 285.0 eV is assigned to aromatic or aliphatic hydrocarbons. The peaks at 286.6 eV and 288.4 eV can be assigned to oxygen-bounded carbon while the peak at 289.4 eV is contributed to metal carbonates and hydrocarbonates.

The *oxygen 1s* high-resolution spectrum (Figure 55; b) consists of three peaks where the peak at 530.5 eV can be assigned to metallic oxides. According to *Mangolini et al.* the peak at 531.3 eV can be assigned to "the oxygen in phosphates (PO_4^{3-}), sulphates (SO_4^{2-}) and to the terminating oxygen on polyphosphates (the so-called nonbridging oxygen, NBO)" [125]. The two peaks at 532.3 eV and 533.2 eV to oxygen in esters or ketones [125]. A contribution to the peak at 533.2 eV can derive from the bridging oxygen (BO) in polyphosphate chains and from the oxygen in C-**O**-P groups [125].

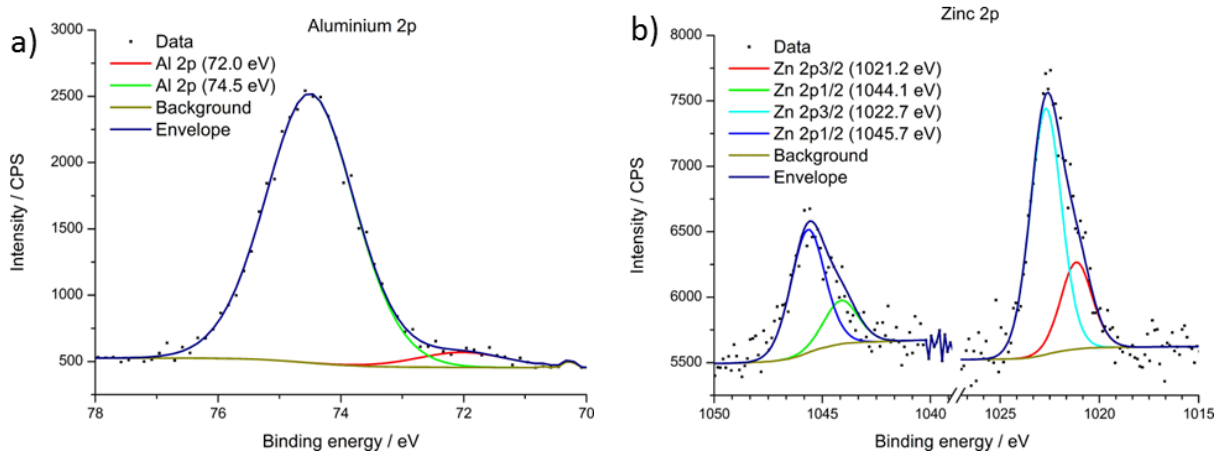

Figure 56. High-resolution XPS spectra of the *Al 2p* (a) and *Zn 2p* (b) region of triphenylphosphorthionate on NSP-HDG steel

The *aluminum 2p* high-resolution (Figure 56; a) spectrum turns out to contain two components. The minor component at 72.0 eV is assigned to metallic aluminum, while the major component at 74.5 eV is assigned to oxidic aluminum.

The *zinc 2p* high-resolution spectrum (Figure 56; b) gives the best fit with two doublets, due to spin-orbit coupling, with a binding energy difference of 22.9 eV. The minor component at 1021.2 eV (*Zn 2p3/2*) and 1044.1 eV (*Zn 2p1/2*) is assigned to metallic zinc. The major component at 1022.7 eV (*Zn 2p3/2*) and 1045.7 eV (*Zn 2p1/2*) is assigned to oxidic zinc.

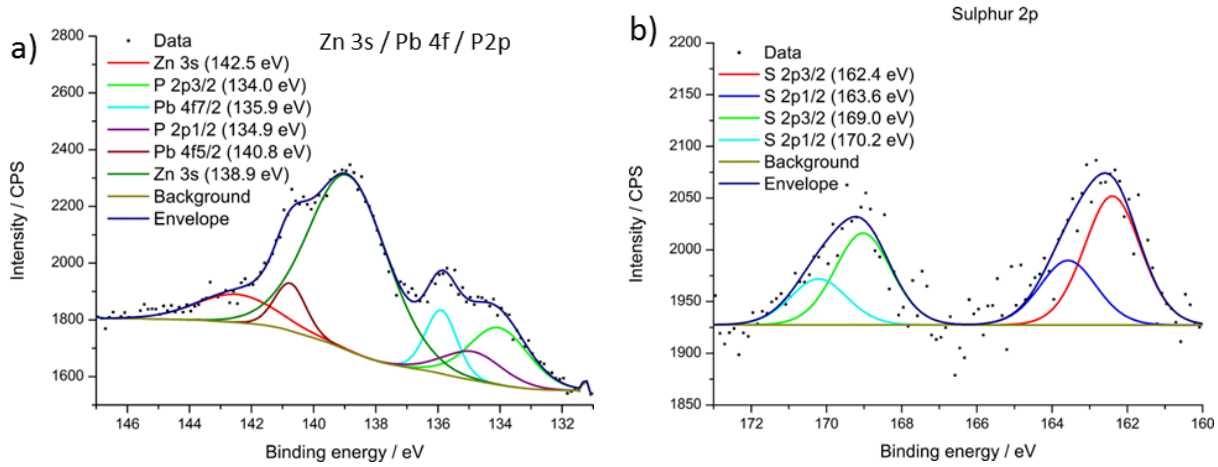

Figure 57. High-resolution XPS spectra of the *Zn 3s / Pb 4f / P 2p* (a) and *S 2p* (b) region of triphenylphosphorthionate on NSP-HDG steel

The *Zn 3s / Pb 4f / P 2p* high-resolution spectrum (Figure 57; a) gives the best fit with six peaks. This spectrum is highly influenced by the previously mentioned lead contamination. Nevertheless, due to the fixed spin-orbit coupling of *lead 4f* and *phosphorus 2,* it is possible to deconvolute the peaks. The lead contamination is detected at 135.9 eV (*Pb 4f7/2*) and at

140.8 eV (*Pb 4f5/2*) with a binding energy difference of 4.8 eV. The *zinc 3s* components at 138.9 eV and 142.5 eV can be assigned to metallic and oxidic zinc. The phosphorus 2p peaks have a binding energy difference of 0.84 eV, and their positions are detected at 134.0 eV (*P 2p3/2*) and 134.9 eV (*P 2p1/2*). These values are typical for multiple phosphate variants [125].

The *sulphur 2p* high-resolution spectrum (Figure 57; b) gives the best fit with two doublets, whose low binding energy component at 162.4 eV (*S 2p3/2*) and 163.6 eV (*S 2p1/2*) is assigned to sulphide-like sulphur. The lower intense component at higher binding energies of 169.0 eV (*S 2p3/2*) and 170.2 eV (*S 2p1/2*) is assigned to sulphates.

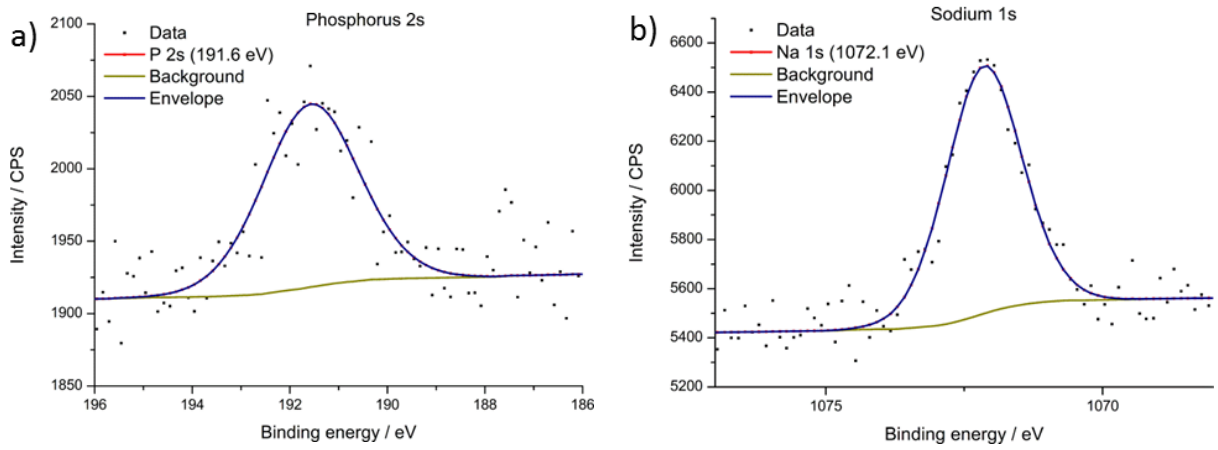

Figure 58. High-resolution XPS spectra of the *P 2s* (a) and *Na 1s* (b) region of triphenylphosphorthionate on NSP-HDG steel

The *phosphorus 2s* high resolution spectrum (Figure 58; a) gives the best fit with one peak at 191.6 eV which verifies the fitting of the *phosphorus 2p* signal with one component and is assigned to phosphate variants.

The minor sodium contamination (Figure 58; b) with a surface concentration of ~0.5 % and a binding energy of 1072.1 eV cannot be assigned to a specific species and the origin remains unknown.

Matsumoto [124] and *Heuberger* [126, 127] detect the sulphur component (S 2p3/2) of pure phosphorthionates by means of XPS at 163.3 eV and 162.6 eV respectively. *Heuberger* [126] also reported small amounts of an sulphide species after contact of an in-oil solution of partially butylated phosphorthionate on hardened 100Cr6 steel at room temperature. At higher temperatures [126] and at different contact pressures [127] *Heuberger et al.* detected only sulphate like species. *Mangolini et al.* [125] reported two sulphur species at higher binding energy which are assigned to sulphates and organic sulphoxides after the contact of

an iron-coated germanium ATR crystal in the presence of a solution of triphenylphosphorthionate in PAO for 18h at 423 K.

Because a sulphate species is present as contamination on the reference (Figure 38; p. 57), the sulphate signal of the adsorbed sample (Figure 57) is inconclusive. However, the presence of non-bridging and bridging oxygen species (Figure 55; p. 73), phosphate (Figure 57; p. 74) and sulphide (Figure 57; p. 74) confirm the successful adsorption of triphenylphosphorthionate on NSP-HDG steel. Furthermore, the results indicate a sulphide species of an unchanged molecule and thus a physisorption process.

4.2.2 Adsorption on zinc (Zn)

The adsorption studies of forming additives on pure substrates start with measurements on pure zinc (AES composition on p. 27).

4.2.2.1 Di-tert-nonyl polysulphide (DTNPS) / Zn

X-ray photoelectron spectroscopy (XPS)

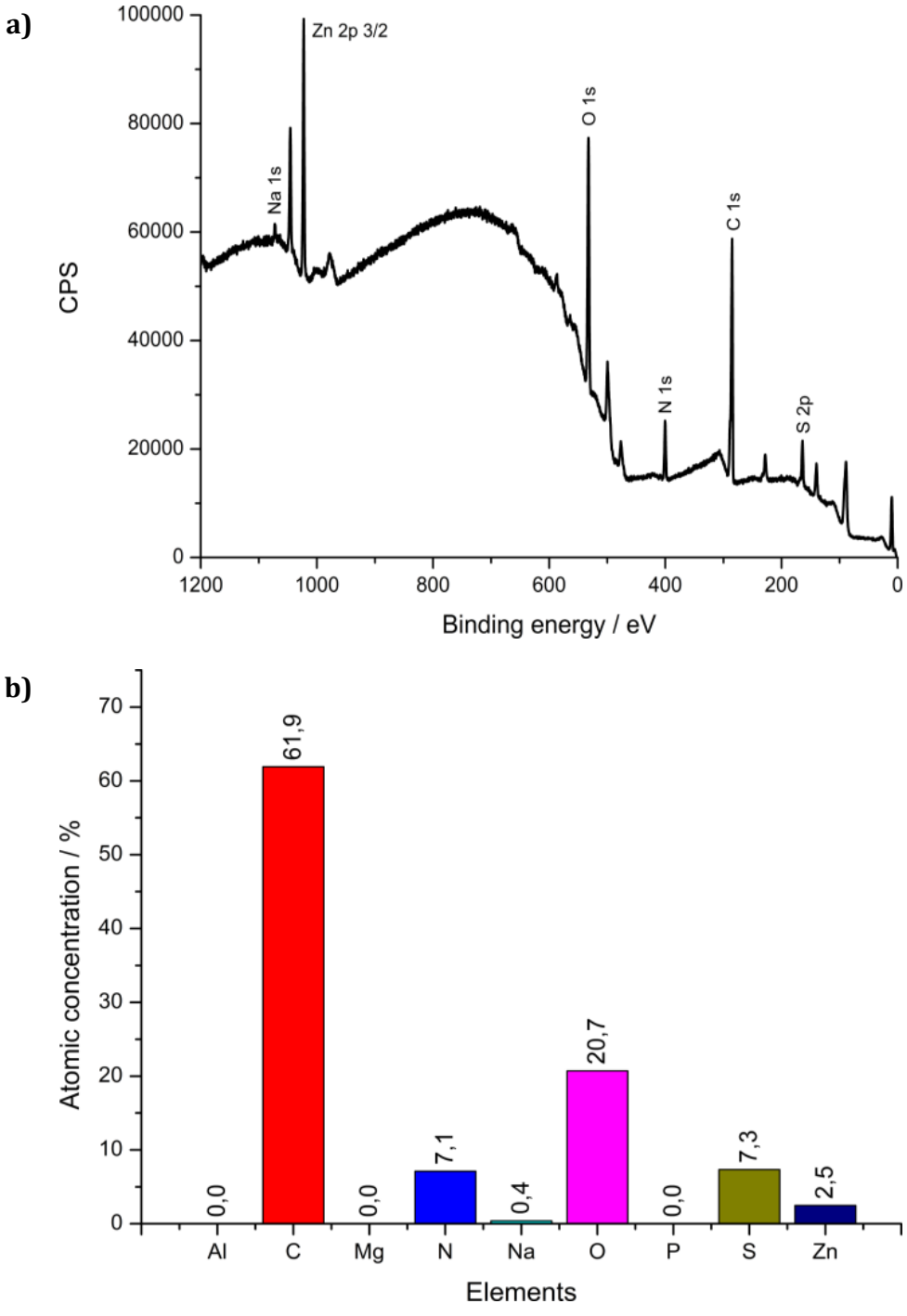

Figure 59. XPS survey (a) and atomic concentrations (b) of DTNPS on Zn

The XPS survey of DTNPS treated zinc in Figure 59 shows the expected signals of zinc, carbon, oxygen, and sulphur. Additional there are small contaminations of nitrogen and sodium as previously seen in the reference measurements (chapter 4.1.2.2; p. 55). The origin of the nitrogen contamination is described previously (chapter 4.1.2.3; p. 60). An overview with calculated atomic concentrations is given in Figure 59.

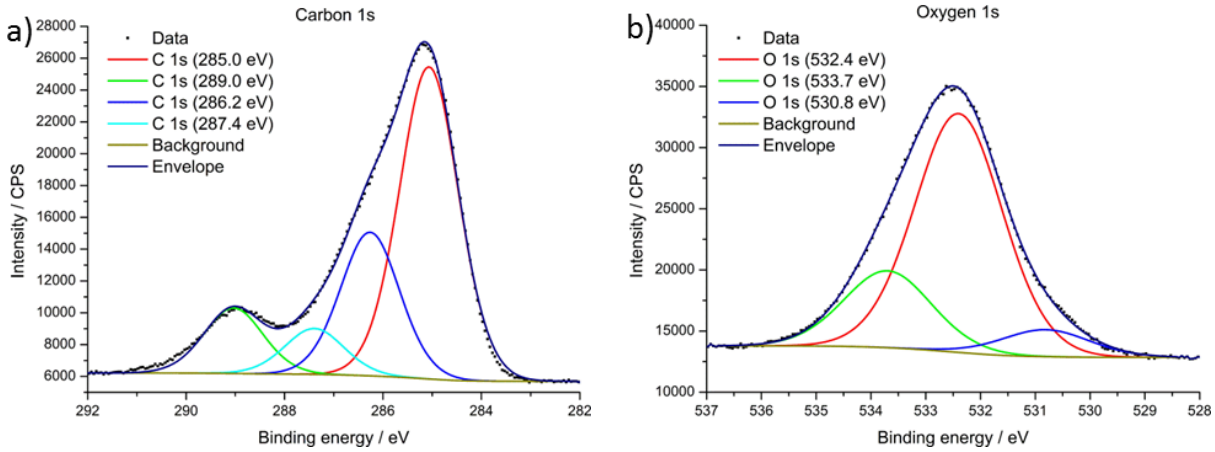

Figure 60. High-resolution XPS spectra of the *C 1s* (a) and *O 1s* (b) region of DTNPS on pure Zn

The *carbon 1s* high-resolution spectrum (Figure 60; a) gives the best fit with four peaks at 285.0 eV, 286.2 eV, 287.4 eV, and 289.0 eV. The peak at 285.0 eV assigns to aliphatic carbon and is used for the calibration of the spectra. The binding energy of the second peak is slightly increased to 286.2 eV compared to the reference and assigned to –C-O- or –C-S-. In addition, the relative intensity of this peak is increased. The peak at 287.4 eV is assigned to -C=O or –C=S while the peak of 289.0 eV is still assigned to metal carbonates or hydrocarbonates.

The *oxygen 1s* high-resolution spectrum (Figure 60; b) gives the best fit with three peaks at 530.8 eV, 532.4 eV, and 533.7 eV. The peak at 530.8 eV corresponds to an oxide based oxygen species, here probably zinc oxide and is decreased compared to the reference. The binding energy of the peak assigned to oxyhydroxide is increased to 532.4 eV compared to the reference. The peak of 533.7 eV is also increased in binding energy compared to the reference and assigned to –C-OH and –C=O from atmospheric organic contaminations.

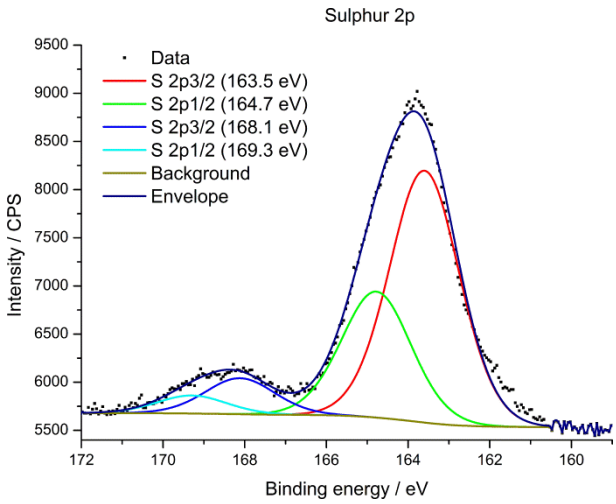

Figure 61. High-resolution XPS spectra of the *S 2p* region of DTNPS on Zn

The *sulphur 2p* high-resolution spectrum (Figure 61) gives the best fit with four peaks from two spin-orbit components with a binding energy difference of 1.2 eV. The peak pair at low binding energies (*S 2p3/2*: 163.5 eV and *S 2p1/2*: 164.7 eV) is assigned to a sulphur (II) component like thiol or sulphide. The peak pair at high binding energies (S 2p3/2: 168.1 eV and S 2p1/2: 169.3 eV) is attributed to an oxidized sulphur (VI) component like sulphate.

The absence of sulphur on the zinc reference (Figure 42; p. 60) and the clear identification of sulphur (II) and an oxidized sulphur component on this sample verifies the successful adsorption of DTNPS on pure zinc. Contrary to the adsorption of DTNPS on NSP-HDG in chapter 4.2.1.1 (p. 67), where the discussion of the sulphate species was inconclusive because of a sulphate contamination on the reference, the zinc alloy reference is sulphur-free. This indicates that next to the sulphide adsorption, a higher oxidized sulphate species is adsorbed on the surface. It remains unclear if these adsorption layers are physisorbed layers or chemisorbed layers with metal-sulphur bonds.

4.2.2.2 Triphenylphosphorthionate / Zn

X-ray photoelectron spectroscopy (XPS)

a)

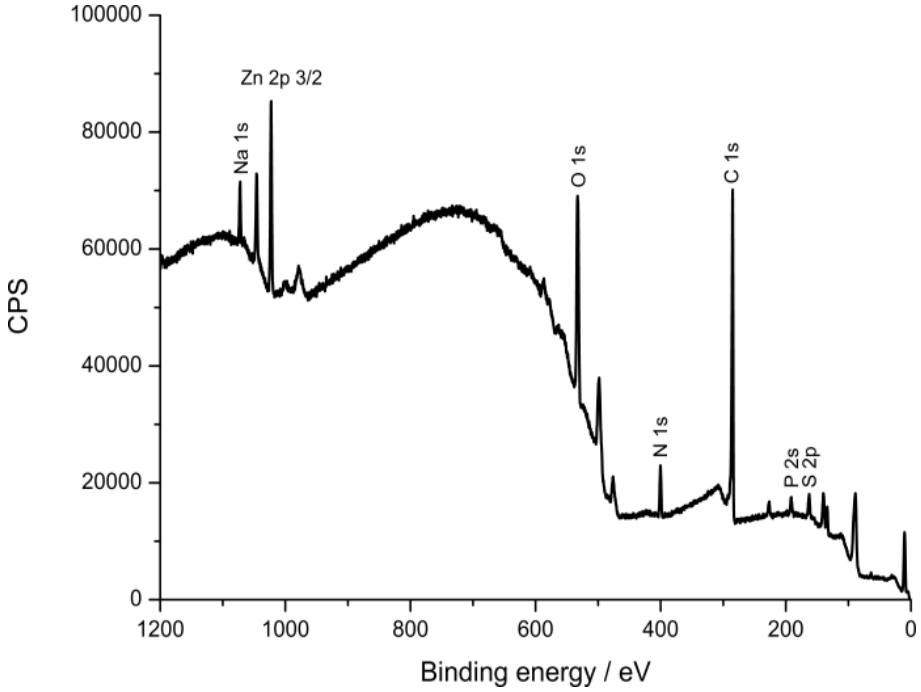

b)

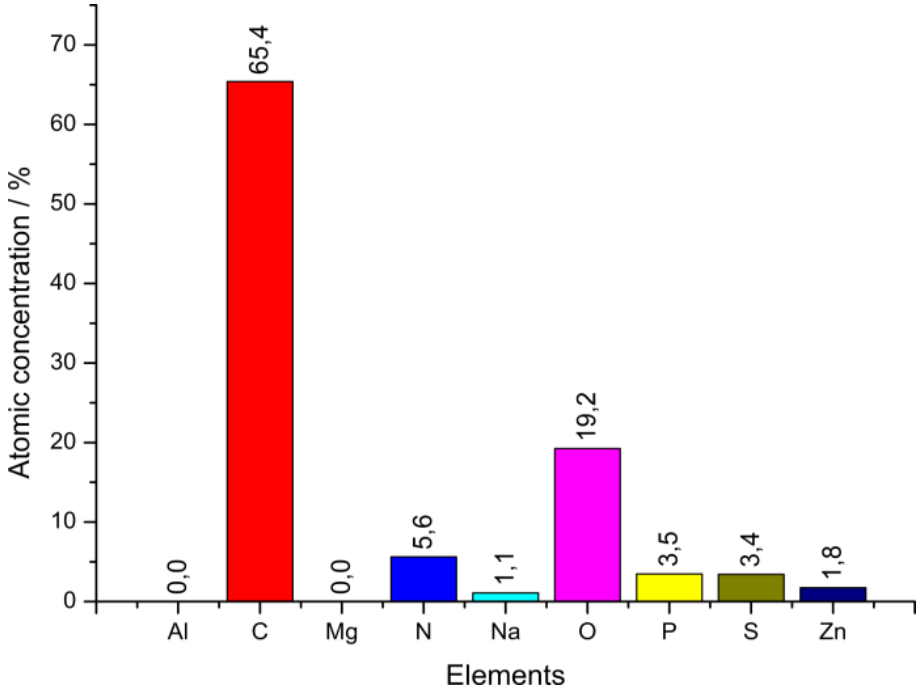

Figure 62. XPS survey (a) and atomic concentrations (b) of triphenylphosphorthionate on Zn

The XPS survey (Figure 62; a) of a triphenylphosphorthionate treated zinc sample also shows the previously described contaminations of sodium and nitrogen (chapter 4.1.2.3; p. 60). However, the more important signals of zinc, oxygen, carbon, sulphur and phosphorus are clearly detectable.

The survey indicates an oxidized zinc surface with coverage of triphenylphosphorthionate, which is specified by the following detail spectra. An overview of the atomic concentrations of the surface composition is also shown in Figure 62.

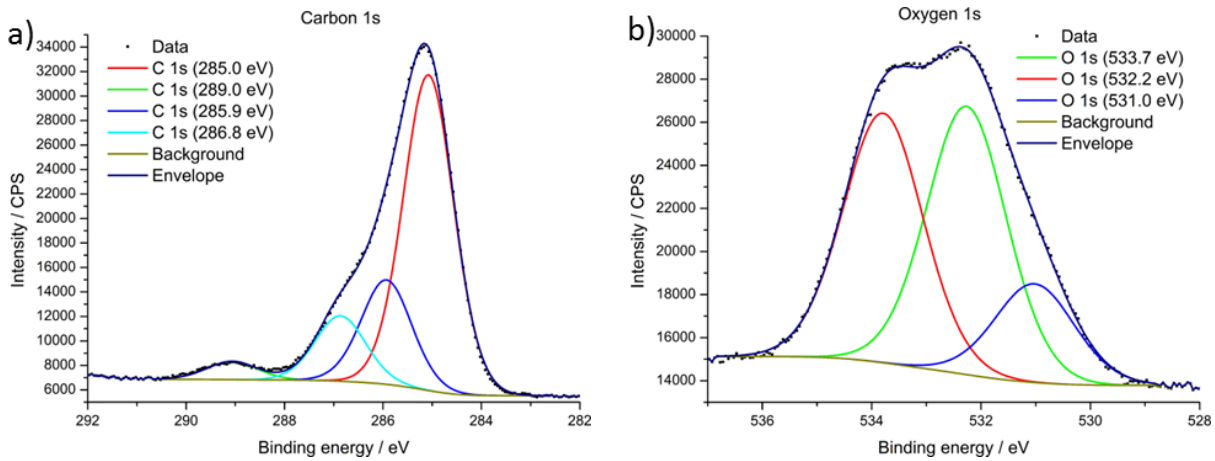

Figure 63. High-resolution XPS spectra of the *C 1s* (a) and *O 1s* (b) region of triphenylphosphorthionate on pure Zn

The *carbon 1s* high-resolution spectrum of triphenylphosphorthionate on pure zinc (Figure 63; a) gives the best fit with four peaks. The peak with the lowest binding energy and highest intensity of 285.0 eV is assigned to aromatic and aliphatic hydrocarbons. Compared to the reference the second and third lowest peaks are decreased to 285.9 eV and 286.8 eV and assigned to carbon bound to oxygen. The assignment of the fourth peak is still metal carbonates and hydrocarbonates.

The oxygen 1s high-resolution spectrum (Figure 63; b) is resolved into three peaks. Compared to the reference the peak at low binding energy (531.0 eV) is increased by 0.6 eV. The peak is still assigned to zinc oxide and the increase in binding energy is explained by the influence of an adsorbed organic compound. According to *Mangolini et al.* [125], the peak at 532.2 eV is assigned to "the terminating oxygen in polyphosphates (the so-called non-bridging oxygen, NBO)". In addition, an oxyhydroxide component might be part of this peak. Compared to the reference, the peak at 533.7 eV is increased in intensity and can be assigned to C-O- bonds of organic compounds. According to Mangolini et al. [125], "a contribution to the peak […] can derive from the oxygen that links phosphate groups in polyphosphate chains (the so-called bridging oxygen, BO) and from the oxygen in C–O–P groups."

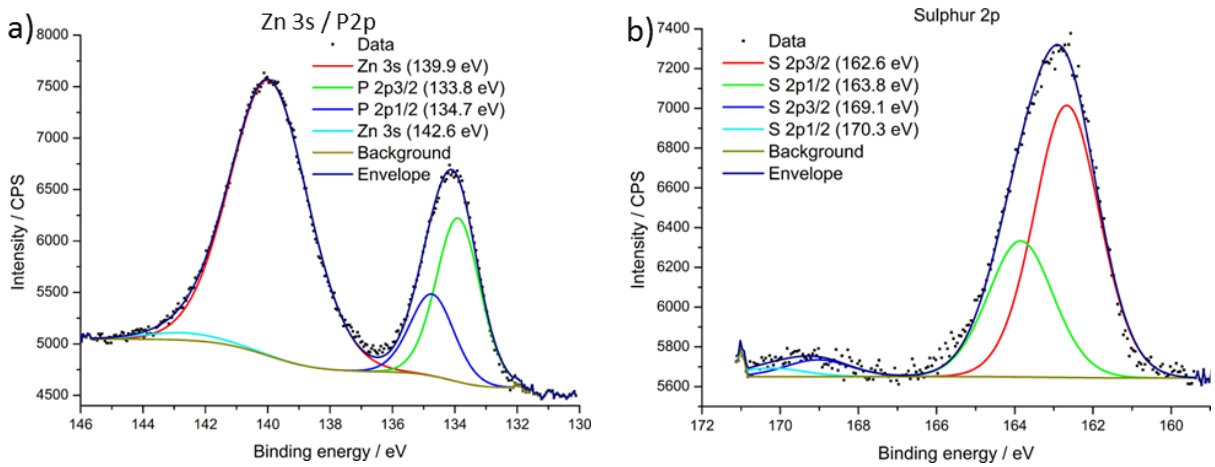

Figure 64. High-resolution XPS spectra of the *Zn 3s / P 2p* (a) and *S 2p* (b) region of triphenylphosphorthionate on pure Zn

The *Zn 3s / P 2p* high-resolution spectrum (Figure 64; a) gives the best fit with four peaks, where the two peaks at lowest binding energy can be assigned to the spin-orbit components of *phosphorus 2p*. This components (*P 2p3/2*: 133.8 eV; *P 2p1/2*: 134.7 eV) have a binding energy difference of 0.84 eV and can be assigned to phosphate. The two peaks at higher binding energies of 139.9 eV and 142.6 eV correspond to *zinc 3s* components.

The *sulphur 2p* high-resolution spectrum (Figure 64; b) gives the best fit with four peaks and consists of two spin-orbit pairs. The pair with the highest intensity and lowest binding energy (*S 2p3/2*: 162.6 eV; *S 2p1/2*: 163.8 eV) is fitted with a binding energy difference of 1.2 eV and can be assigned to a sulphur (II) species like sulphide. In addition, the pair at higher binding energies (*S 2p3/2*: 169.1 eV; *S 2p1/2*: 170.3 eV) is lower in intensity and can be assigned to sulphur (VI) species like sulphate.

Similar to the discussion in chapter 4.2.1.2 (p. 72) the detection of non-bridging and bridging oxygen species (Figure 63, b; p. 81), phosphate (Figure 64, a; p. 82) and sulphide (Figure 64, b; p. 82) confirm the successful adsorption of triphenylphosphorthionate on pure zinc. Additionally, the absence of any sulphur on the reference (Figure 45; p. 63) highlights the minor sulphate species (Figure 64, b; p. 82) on the adsorbed sample. This results correlate with the work of *Heuberger* [126] about the reaction of phosphorthionates with iron surfaces.

4.2.3 Adsorption on zinc alloy (ZnAlMg)

The adsorption studies of forming additives on pure substrates continue with measurements on zinc alloy (ZnAlMg) (AES composition on p. 27).

4.2.3.1 Di-*tert*-nonyl polysulphide / ZnAlMg

X-ray photoelectron spectroscopy (XPS)

a)

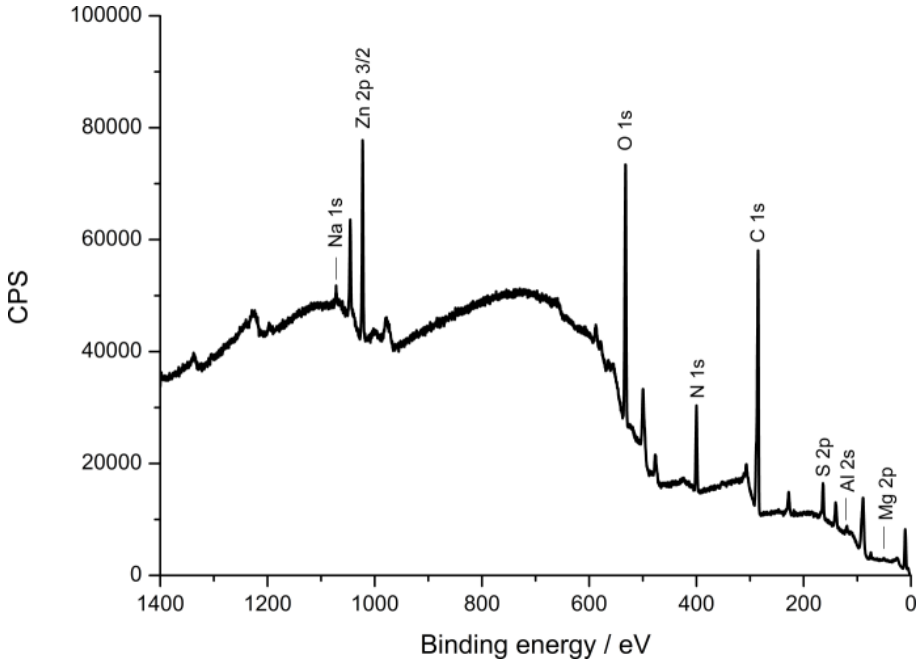

b)

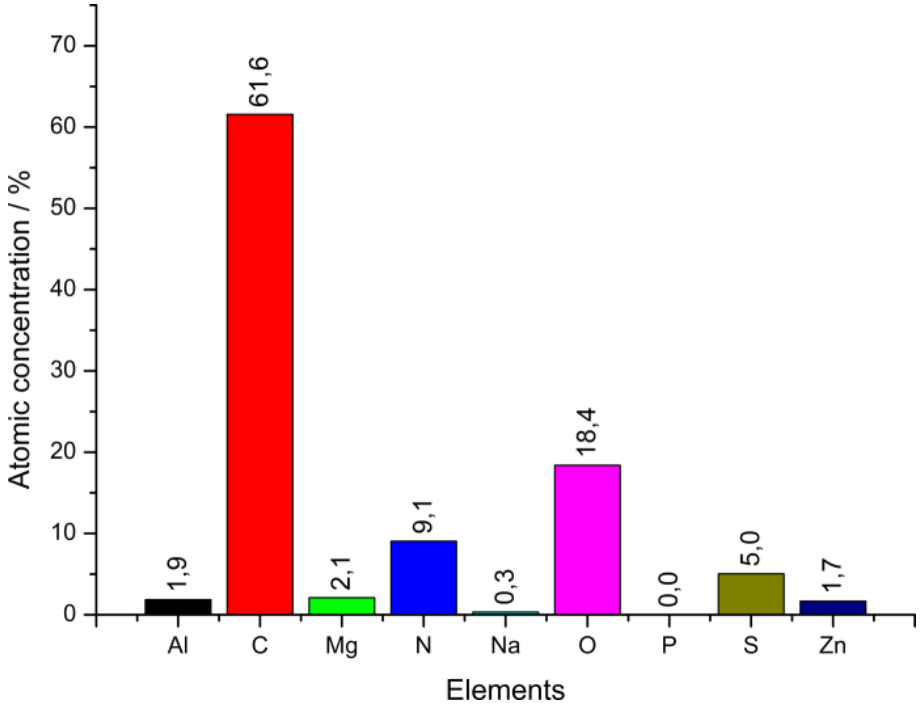

Figure 65. XPS survey (a) and atomic concentrations (b) of DTNPS on ZnAlMg

The XPS survey in Figure 65 shows the expected signals of zinc, aluminum, magnesium, carbon, oxygen and sulphur. In addition, there are small contaminations of sodium and nitrogen as previously seen in the reference measurements (chapter 4.1.2.4; p. 63). Detailed atomic concentrations are also shown in Figure 65.

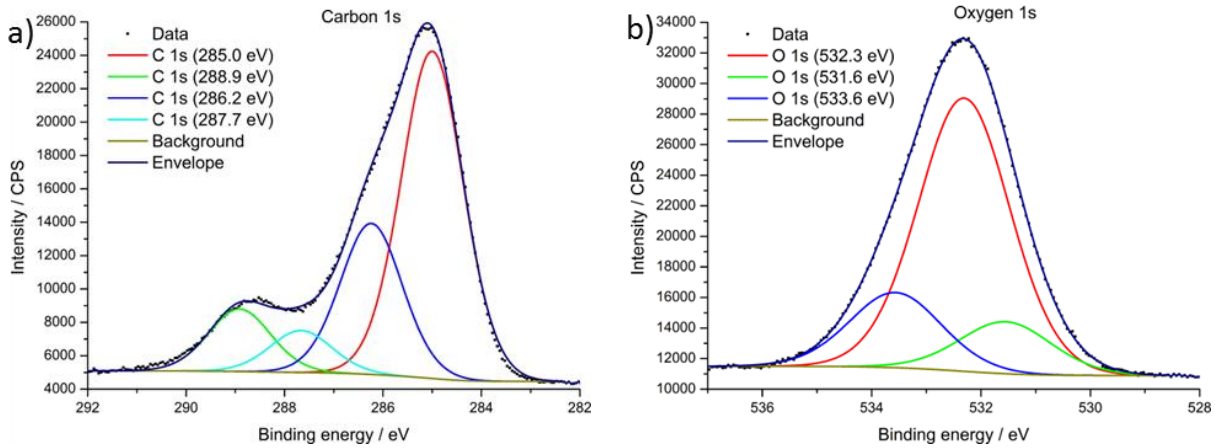

Figure 66. High-resolution XPS spectra of the *C 1s* (a) and *O 1s* (b) region of DTNPS on zinc alloy

The *carbon 1s* high-resolution spectrum (Figure 66; a) consists of four peaks, where the main peak at 285.0 eV can be assigned to hydrocarbons. The second peak at 286.2 eV can be assigned to -C-O- or –C-S- from an adsorbed organic compound. In addition, the peak at 287.7 eV can be assigned to –C=O or –C=S from an adsorbed organic compound while the peak at 288.9 eV can be assigned to metal carbonates or hydrocarbonates.

The *oxygen 1s* high-resolution spectrum (Figure 66; b) is fitted with three peaks, where the peak at lowest binding energy of 531.6 eV is assigned to oxide. The peaks at 532.3 eV and 533.6 eV contribute to –C-O- and –C=O components of an adsorbed organic compound or an organic contamination.

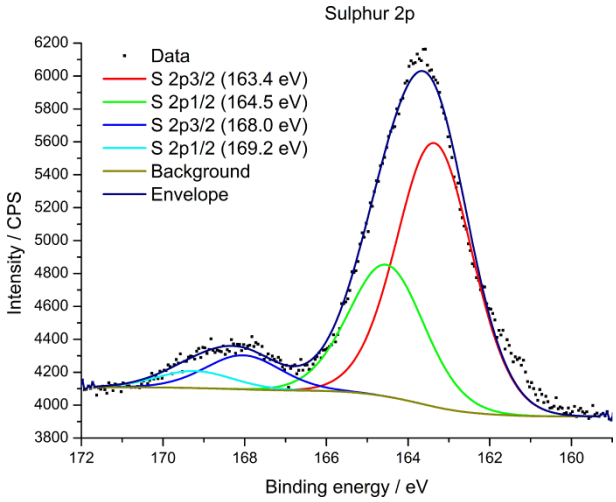

Figure 67. High-resolution XPS spectra of the *S 2p* region of DTNPS on zinc alloy

The *sulphur 2p* high-resolution spectrum gives the best fit with two pairs of spin-orbit components, where the pair at lowest binding energy (*S 2p3/2*: 163.4 eV; *S 2p1/2*: 164.5 eV) can be assigned to a sulphur (II) species like sulphide. The other pair (*S 2p3/2*: 168.0 eV; *S 2p1/2*: 169.2 eV) can be assigned to a sulphur (VI) species like sulphate.

The absence of sulphur on the zinc reference (Figure 42; p. 60) and the clear identification of sulphur (II) and an oxidized sulphur component on this sample verify the successful adsorption of DTNPS on zinc alloy. It remains unclear if these adsorption layers are a physisorbed layers or a chemisorbed layers with metal-sulphur bonds.

4.2.3.2 Triphenylphosphorthionate / ZnAlMg

X-ray photoelectron spectroscopy (XPS)

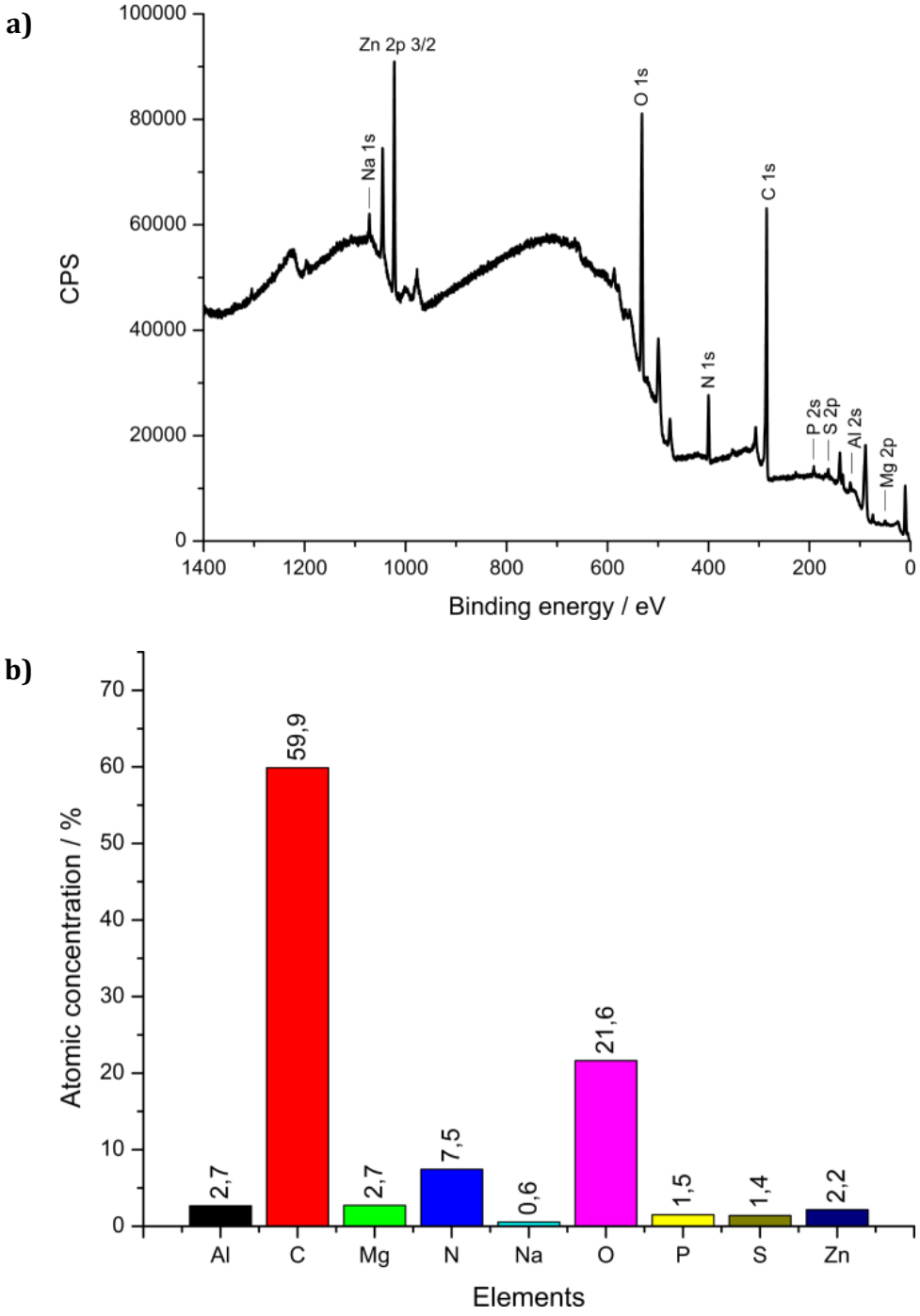

Figure 68. XPS survey (a) and atomic concentrations (b) of triphenylphosphorthionate on ZnAlMg

The XPS survey in Figure 68 shows the expected signals for a sample treated with triphenylphosphorthionate. The signals of zinc, oxygen, carbon, phosphorus, sulphur, aluminum and magnesium indicate an oxidized ZnAlMg-surface with a phosphorus and sulphur containing carbon layer. The detailed atomic concentrations of the surface are also shown in Figure 68.

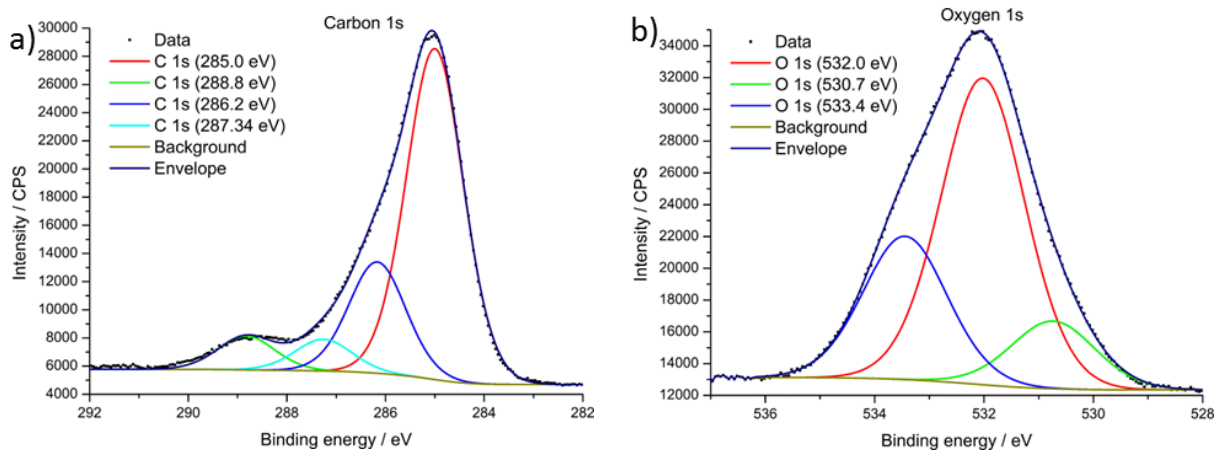

Figure 69. High-resolution XPS spectra of the *C 1s* (a) and *O 1s* (b) region of triphenylphosphorthionate on zinc alloy

The *carbon 1s* high-resolution spectrum (Figure 69; a) gives the best fit with four peaks, where the major peak at the lowest binding energy of 285.0 eV is assigned to aromatic and aliphatic hydrocarbons. The peaks at 286.2 eV and 287.3 eV can be assigned to oxygen-bounded carbon while the peak at 288.8 eV is contributed to metal carbonates and hydrocarbonates.

The *oxygen 1s* high-resolution spectrum (Figure 69; b) consists of three peaks where the peak at 530.7 eV can be assigned to oxides of zinc, alumina, and magnesia. The most intense peak at 532.0 eV and the peak at 533.4 eV, which is, compared to the reference, strongly increased are assigned accordingly to chapter 4.2.2.2 as non-bridging oxygen (NBO) and bridging oxygen (BO).

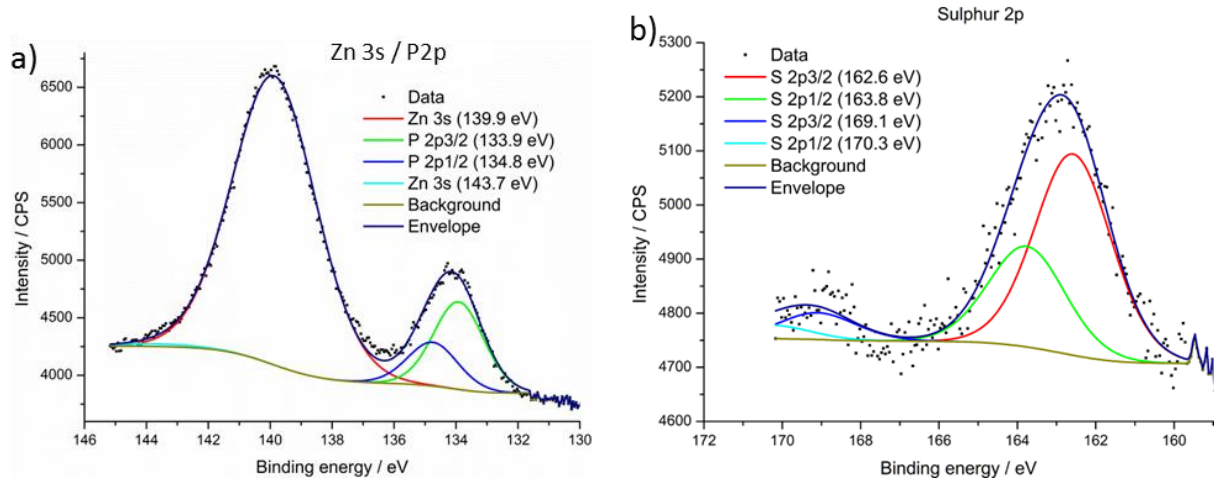

Figure 70. High-resolution XPS spectra of the *Zn 3s / P 2p* (a) and *S 2p* (b) region of triphenylphosphorthionate on zinc alloy

The *Zn 3s / P 2p* high-resolution spectrum (Figure 70; a) gives the best fit with four peaks consisting of a pair of *phosphorus 2p* spin-orbit component and two *zinc 3s* peaks. The

pair of *phosphorus 2p* peaks (*P 2p3/2*: 133.9 eV; *P 2p1/2*: 134.8 eV) can be assigned to phosphate, which would indicate an adsorption of triphenylphosphorthionate on the zinc alloy surface. In addition, one of the *zinc 3s* peaks is nearly zero and both can be assigned as surface near zinc components.

The *sulphur 2p* high-resolution spectrum (Figure 70; b) gives the best fit with four peaks and consists of two spin-orbit pairs. The pair with the highest intensity and lowest binding energy (*S 2p3/2*: 162.6 eV; *S 2p1/2*: 163.8 eV) is fitted with a binding energy difference of 1.2 eV and can be assigned to a sulphur (II) species like sulphide. In addition, the pair at higher binding energies (*S 2p3/2*: 169.1 eV; *S 2p1/2*: 170.3 eV) is lower in intensity and can be assigned to sulphur (VI) species like sulphate.

Similar to the discussion in chapter 4.2.1.2 (p. 72) the detection of non-bridging and bridging oxygen species (Figure 69, b; p. 87), phosphate (Figure 70, l; p. 87) and sulphide (Figure 70, b; p. 87) confirms the successful adsorption of triphenylphosphorthionate on pure zinc. Additionally, the absence of any sulphur on the reference (Figure 45; p. 63) highlights the minor sulphate species (Figure 70, b; p. 87) on the adsorbed sample similar to the adsorption on pure zinc in chapter 4.2.2.2 (p. 80).

4.3 Conclusions

The beginning of chapter 4 (and the corresponding appendix 12.1) presents the reference data of all used additives and substrates. These characterizations prove the purity of the additives DTNPS, Irgalube TPPT, Irgalube 349 and OBSS. Also, the surface of NSP-HDG, HDG, zinc and zinc alloy is characterized.

The main part of chapter 4 (and the corresponding appendix 12.1) shows by means of XPS and ToF-SIMS analysis that adsorbate layers of DTNPS, triphenylphosphorthionate and Irgalube 349 can be deposited on the surface of technical-grade non-skin passed hot-dip galvanized steel. It remains unclear whether the additives are chemisorbed or physisorbed.

Layers of DTNPS on NSP-HDG are identified through characteristic peaks of sulphides while characteristic peaks of bridging and non-bridging oxygen, phosphate and sulphide confirm the adsorption of triphenylphosphorthionate on this substrate.

The results are supported by XPS characterizations of the adsorbed layers on laboratory-grade zinc and zinc alloy samples. The cleaner surfaces allow the identification of minor high-oxidized sulphur species like sulphate next to the sulphides for both additives.

Layers of Irgalube 349 on NSP-HDG are identified through characteristic peaks of amine phosphate. The results are support by XPS characterizations of the adsorbed layers on laboratory grade zinc and zinc alloy samples.

In summary, these results, together with the reference measurements, are the basis for the interpretation of tribochemical reaction layers in chapter 5.

5 Reactivity of forming additives during the friction process on hot-dip galvanized steel

Based on the reference measurements and the characterization of the adsorbed additive layers on technical- and laboratory-grade zinc surfaces in chapter 4, this chapter describes the tribochemical performance of oil-based lubricants and their surface analysis.

In the beginning, an oil-free strip-drawing test is performed to gain basic knowledge about the tribochemical reactions on HDG steel surfaces. These results are followed by tribological studies about the use of this “dry”-lubrication layers as a pre-treatment before coil coating with oil.

The main part presents the tribological performance of oil-based additive systems by means of strip-drawing tests with increasing contact pressure followed by studies of morphological changes and the surface analytical characterization of build-up reaction layers.

Further knowledge about the influence of tribological conditions on the formation of tribochemical reaction layers is gained by multi frottement strip-drawing tests followed by surface analysis.

5.1 Results

5.1.1 Oil-free strip-drawing test

Oil-free strip drawing measurements were performed to gain basic knowledge about the additive reactions on HDG steel surfaces under tribological conditions. Therefore, additive layers on HDG were prepared by means of dip coating (chapter 3.3.2.1; p. 28) and oil-free strip-drawing tests (chapter 3.4.2.1; p. 31) with friction measurements on both sides were performed.

5.1.1.1 Additive layers on hot-dip galvanized steel

The adsorbed additive film is verified by means of wet chemical analysis (Figure 71+Figure 72) performed by the labs of TKSE. The analysis of the amounts of phosphorus on the zinc coated steel (Figure 71) gives clear verification only for Irgalube 349. The amounts of phosphorus for Irgalube TPPT as second phosphorus containing additive are only slightly above the HDG reference and on the same level as the phosphorus-free additive DTNPS. A possible explanation is the difference in the nature of

the phosphorus bond (phosphate for Irgalube 349 and thiophosphate for Irgalube TPPT), which could have influenced the sensitivity of the verification method. The amounts of additive were measured for both sides of the steel strip and are of the same amount.

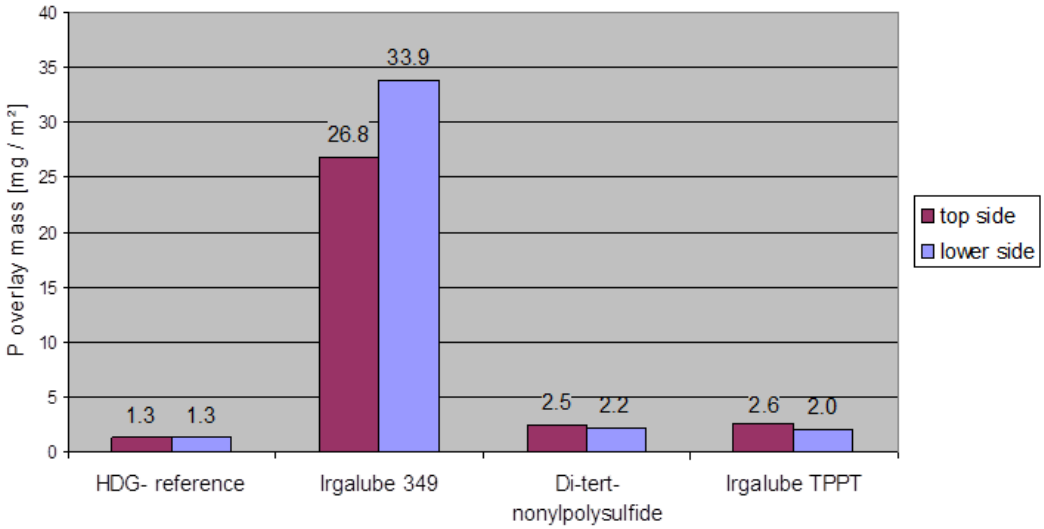

Figure 71. Wet chemical analysis of phosphorus mass in the film

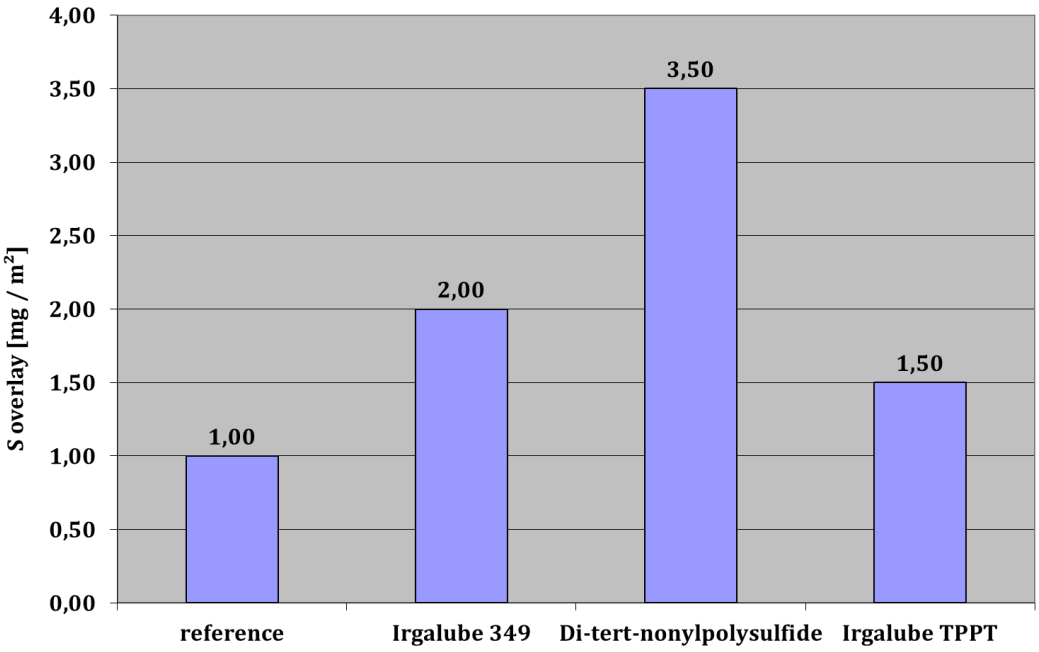

Figure 72. Wet chemical analysis of sulphur mass in the film

The amount of sulphur (Figure 72) was measured in an analogous way to the phosphorus method, but only for one side of the steel strip. The results are not as clear as for phosphorus, but the amount of sulphur on the DTNPS sample is nearly twice the amount of the sulphur-free samples. The sulphur containing Irgalube TPPT is not clearly identifiable because the measured amount of sulphur is below the amount of sulphur on the sulphur-free sample. The nature of the sulphur bond could have caused the lack of sulphur

sensitivity in this method. In addition, the lower amount of sulphur in the molecule (Irgalube TPPT, 9 w.-% S; DTNPS, 35-38 w.-% S) could have decreased the sensitivity below the detection limit.

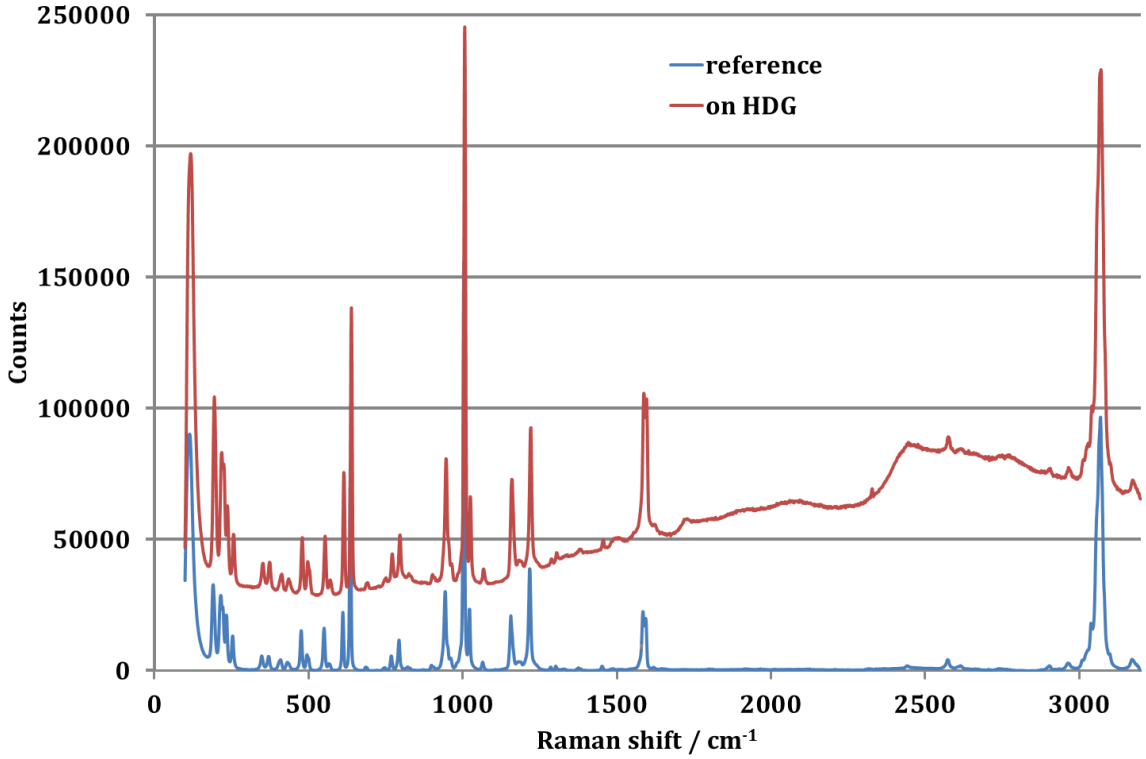

Figure 73. Raman spectra comparison of Irgalube TPPT reference (blue) and Irgalube TPPT on HDG (red)

Nevertheless, the Raman spectra comparison (Figure 73) of pure Irgalube TPPT and the Irgalube TPPT coated HDG strip obviously confirm the successful deposition. In addition, visible signs of additives are detectable on all stripes.

However, the additive film is not homogeneous. A signal to baseline mapping and comparison of the signal intensity in the wavenumber region from 2982 cm^{-1} to 3147 cm^{-1}, where the C-H stretching mode of the phenyl rings is located, reveals strong intensity differences (Figure 74; a). Full Raman spectra on selected points confirm the connection of single peaks to the spectrum of Irgalube TPPT (Figure 74; b). Few to no additive is detectable on the skin-passing marks (Figure 74; point/spectrum 3) while few additive intensity is measured next to the skin-passing marks (Figure 74; point/spectrum 2). The highest additive concentration is found in obvious crystalline spots of Irgalube TPPT (Figure 74; point/spectrum 1).

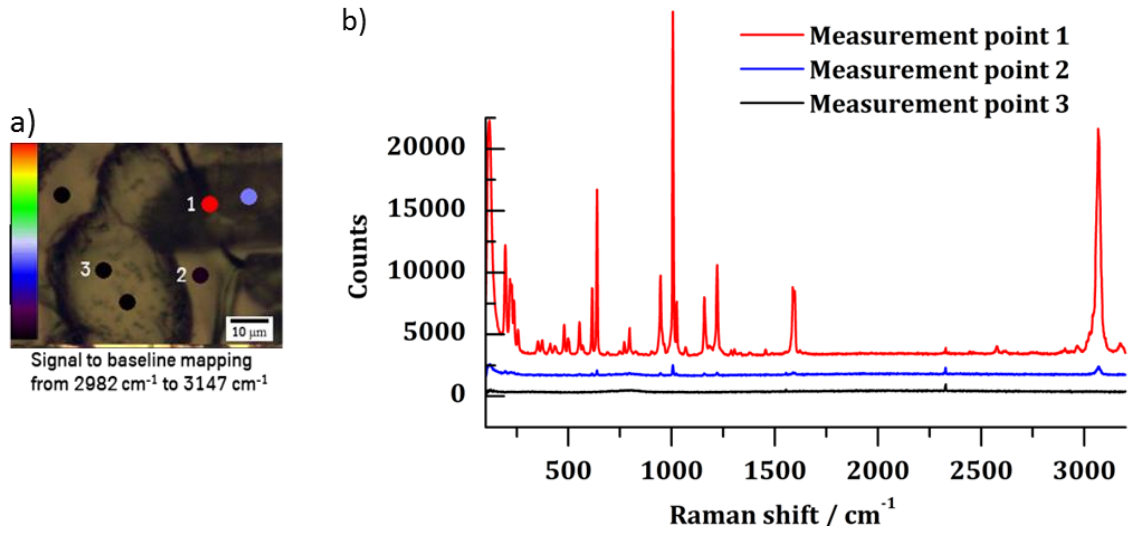

Figure 74. Single-point Raman mapping with intensity analysis of the C-H vibration area (a) and full Raman spectra of selected points (right) of Irgalube TPPT on HDG

A detailed mapping of such a crystalline spot is presented in Figure 75 with focus on the C-H vibration area. The streamline-mapping (b) and intensity analysis of the C-H vibration area shows concentrated amounts of additive. Complete spectra (c) of two selected points reveal the characteristic spectrum of Irgalube TPPT in the concentrated region (point 1) and a weak amount of additive next to the crystal (point 2).

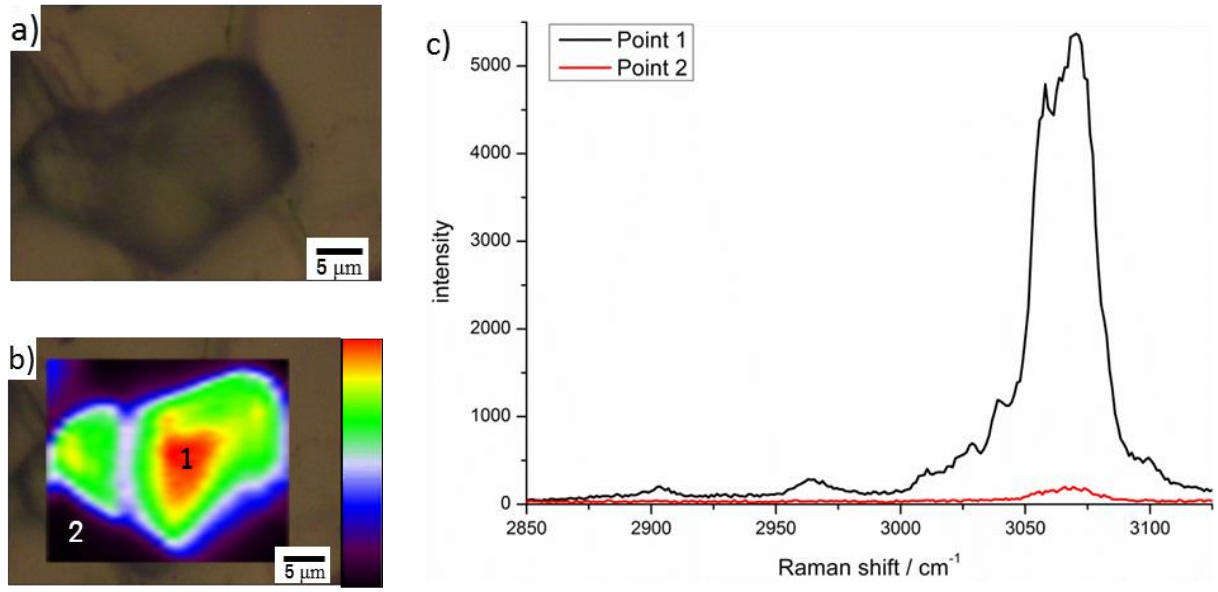

Figure 75. Crystalline additive spot (a) and streamline Raman imaging with intensity analysis of the C-H vibration area (b) and partial Raman spectra of selected points (c) of Irgalube TPPT on HDG

The successful adsorption of DTNPS is also verified by means of Raman-spectroscopy (Figure 76). Weak C-H vibrations of the additive can be identified in multiple

spots on the surface. They are detected both in and next to the skin-passing marks. The adsorption of DTNPS is more homogeneous than the adsorption of Irgalube TPPT.

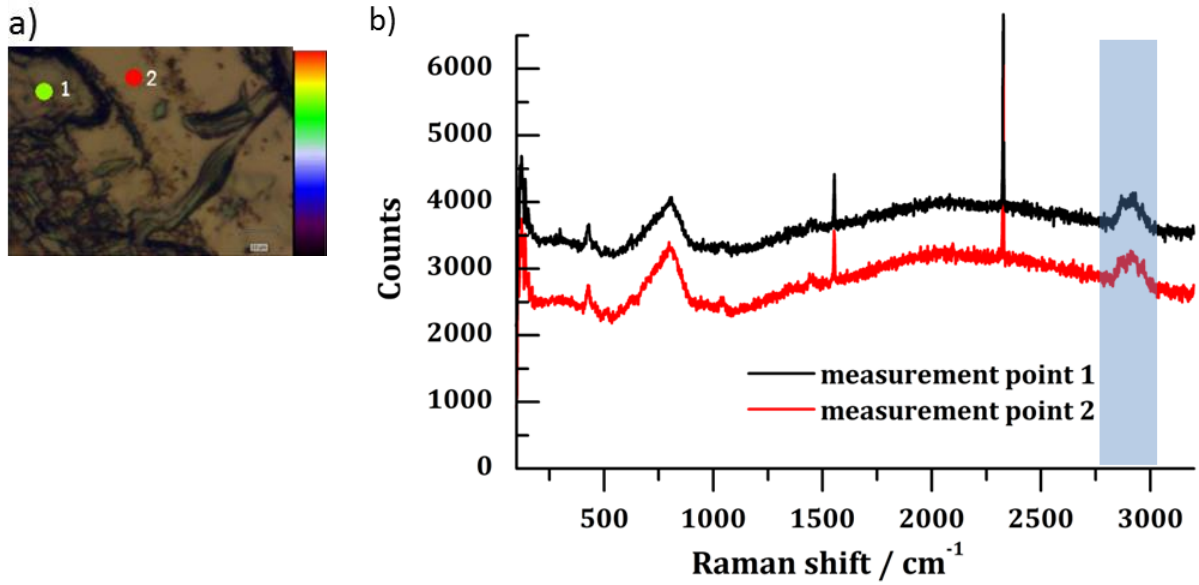

Figure 76. Single-point Raman mapping with intensity analysis of the C-H vibration area (a) and full Raman spectra of selected points (b) of DTNPS on HDG

Altogether, the comparison of visual impressions, wet-chemical film determination and Raman-spectroscopy confirms the successful deposition of Irgalube TPPT, DTNPS and Irgalube 349 (Appendix: Figure 151; p. 193) as layers on HDG.

5.1.1.2 Tribological measurements

The exemplary diagram of the strip-drawing results (Figure 77) presents the progression of distance, normal force and friction force on both sides of the steel sheets and of drawing force of an Irgalube TPPT coated steel strip at a normal force of 2000 N.

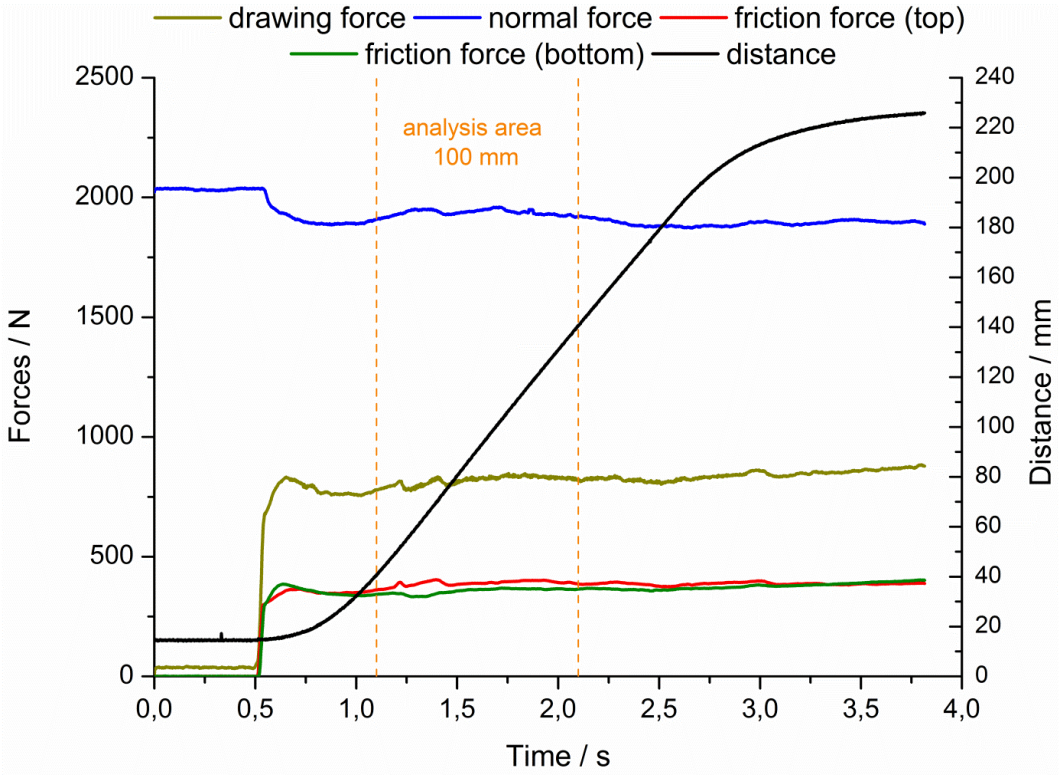

Figure 77. Exemplary diagram of strip-drawing test results with forces from both sides of Irgalube TPPT on HDG with a normal force of 2000 N

It can be noticed, that despite force control, the progression of the normal force is not constant. In addition, the progression of the friction forces of both sides is similar but not equal. These characteristics are also noticed in the force progressions of other additives and at higher contact pressures. The analysis area for the calculation of the coefficient of friction is a range of 100 mm in the middle of the run, because there is no influence of running-in or running-out effects.

The following charts (Figure 78) present the results of this calculation. For each additive, the coefficient of friction is given as linear gradient of the *force to normal force ratio* (Formula 7, p. 6). The results reveal only a minor difference between top and bottom side in the coefficient of friction. The coefficient of friction is generally low for all additives. With numbers of 0.16 for DTNPS, 0.18 for Irgalube TPPT and 0.17 for Irgalube 349 the coefficient of friction between the additives differentiates only slightly.

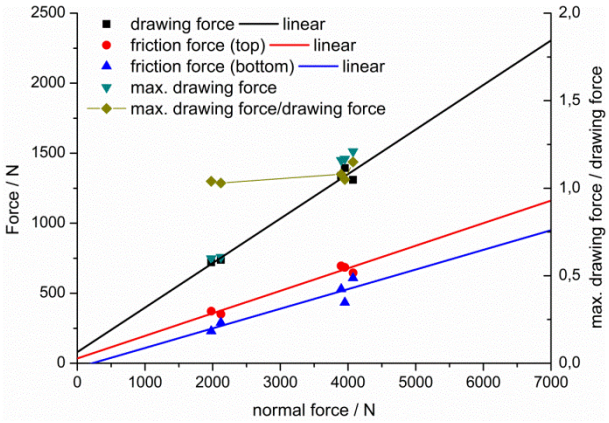

Friction force analysis of DTNPS

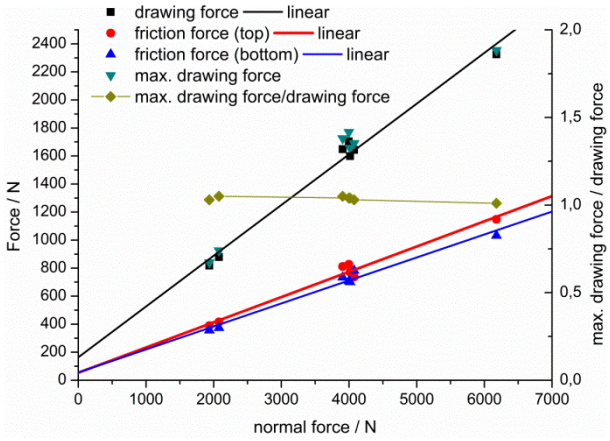

Friction force analysis of Irgalube TPPT

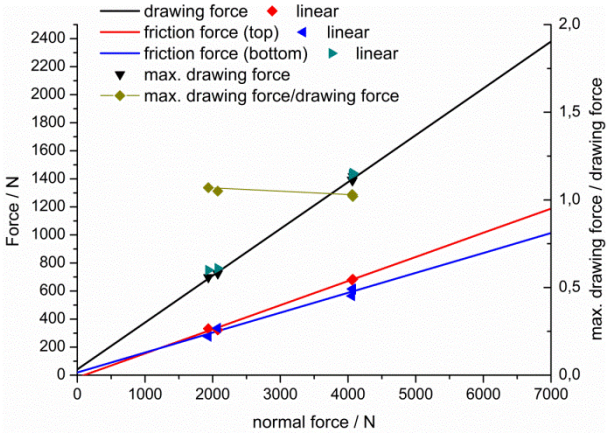

Friction force analysis of Irgalube 349

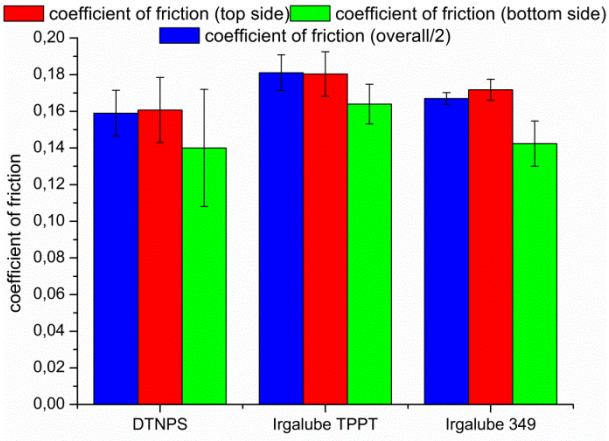

Calculated friction coefficient`s of Irgalube 349, Irgalube TPPT and DTNPS

Figure 78. Friction force analysis and calculated coefficient`s of friction for each additive film on HDG

However, for DTNPS and Irgalube 349 the calculation of the gradients is based on just two normal forces (2000 N and 4000 N). Higher normal forces were not possible due to heavy wear and stick-slip effects. Only Irgalube TPPT enabled normal forces of 6000 N without severe wear, which indicates the possibility of even higher normal forces.

Due to material limitations of the field test, from which the steel sheets were purchased, a change of substrate from HDG to non-skin-passed HDG (NSP-HDG) was necessary to perform additional measurements at higher normal forces with Irgalube TPPT.

With these conditions, even normal forces up to 16000 N were possible (Figure 79). Wear induced stick-slip effects occurred only at the end of the measurement.

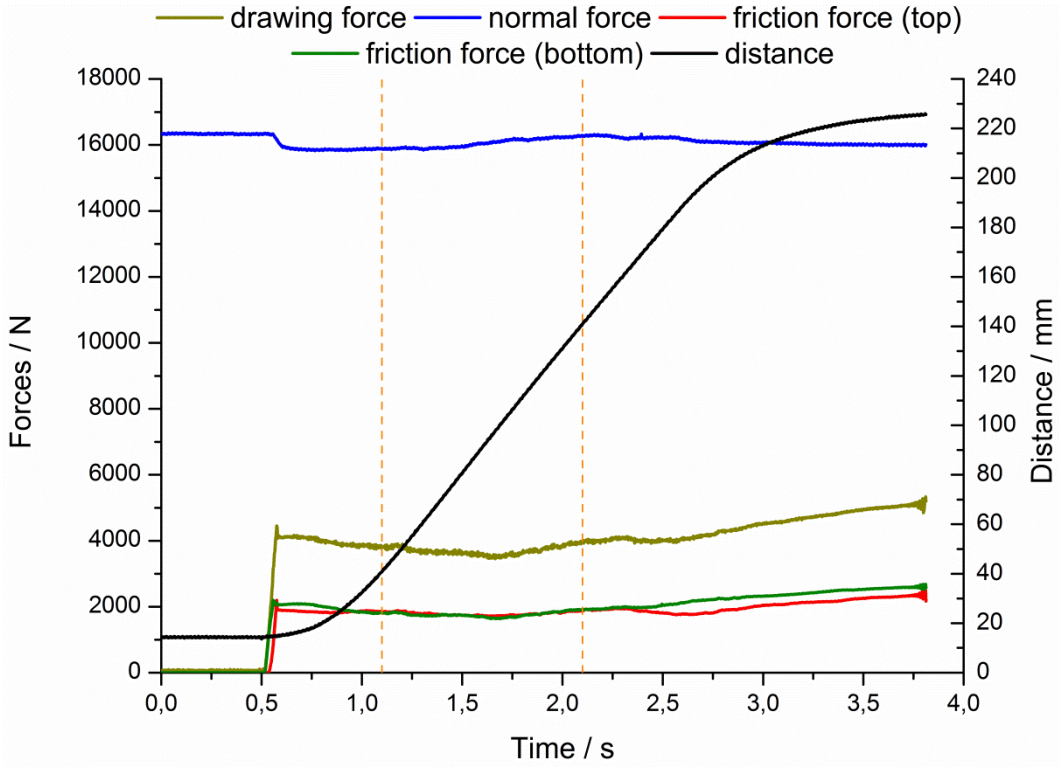

Figure 79. Exemplary diagram of strip-drawing test results with forces from both sides of Irgalube TPPT on NSP-HDG with a normal force of 16000 N

The friction force analysis of Irgalube TPPT on NSP-HDG (Figure 80) also gives the coefficient of friction as linear gradient of the *force to normal force ratio* (Formula 7, p. 6). Similar to the measurements on HDG, only minor differences between top and bottom side are detectable.

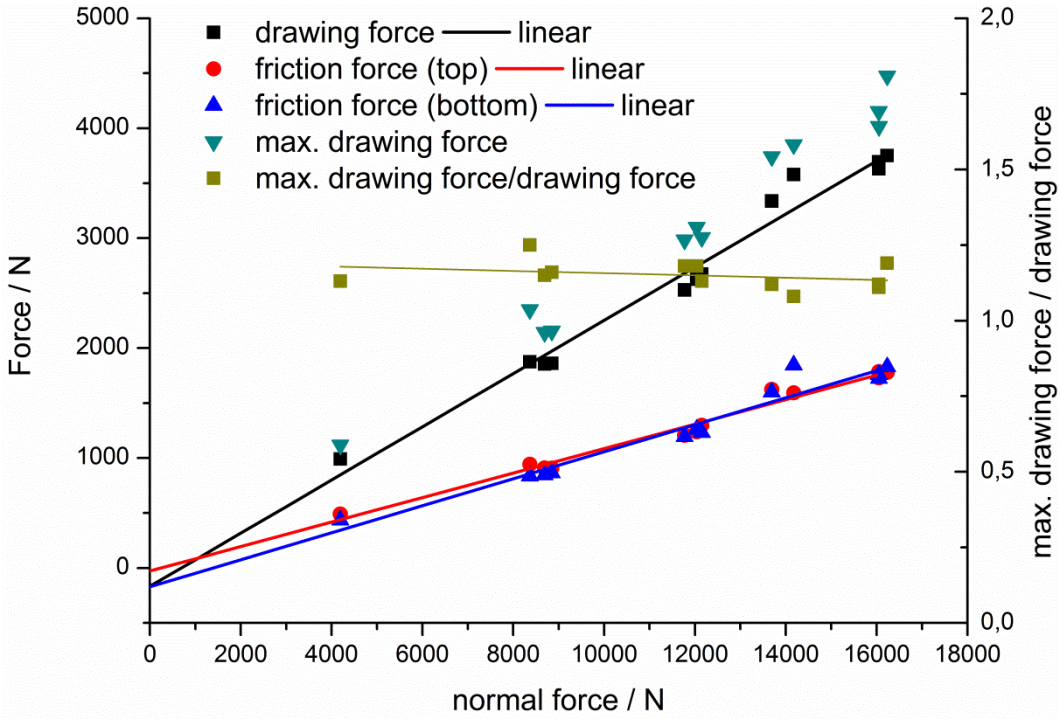

Figure 80. Friction force analysis of Irgalube TPPT on NSP-HDG

The coefficient of friction of Irgalube TPPT on NSP-HDG is with 0.12 significantly lower than on HDG (Figure 81).

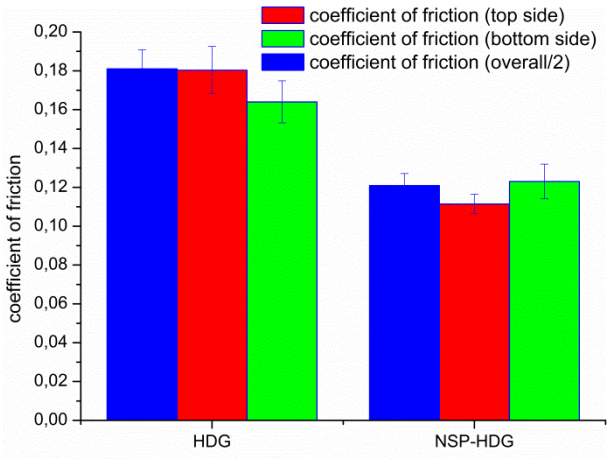

Figure 81. Comparison of the calculated coefficient of friction between HDG and NSP-HDG

5.1.1.3 Surface analysis

After the tribological test, samples were cut from the stripes to fit for surface analytical measurements. Therefore, only the area where the friction force analysis was performed was selected.

Microscope images and white light interferometry (WIL) were used to characterize the changes in surface morphology. Laser-Induced Breakdown Spectroscopy (LIBS) was used to

study the distribution of additive elements on the steel surface at different tribological conditions.

XPS analyses of these samples were not possible due to heavy gas release in the measurement-chamber.

The following chapter presents the surface analysis of tribological treated HDG samples with Irgalube TPPT and DTNPS. The surface analysis of Irgalube 349 is presented in the appendix 12.2.1 (p. 193).

The reference measurements of HDG are found in chapter 4.1.2.1 (p. 49) and in chapter 4.1.2.2 (p. 55) for NSP-HDG.

Irgalube TPPT

The surface analysis of tribologically treated Irgalube TPPT samples starts with the comparison of microscopic images at various magnifications (Figure 82).

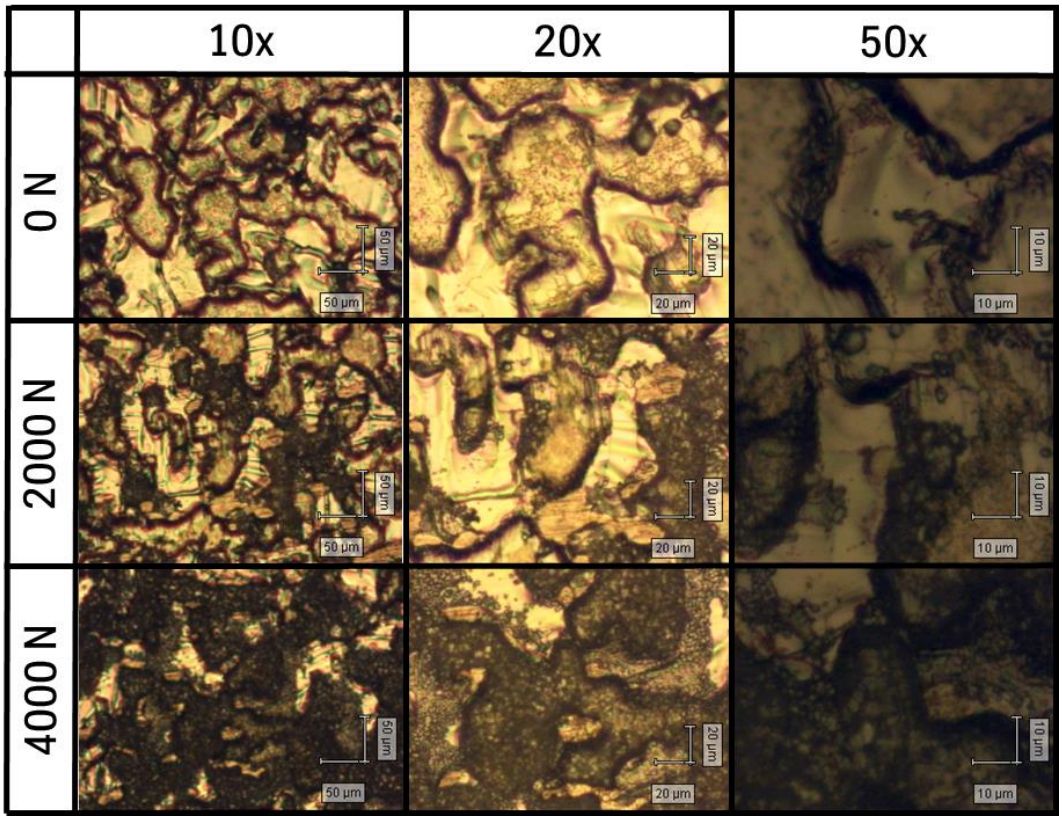

Figure 82. Microscope images of Irgalube TPPT coated HDG stripes at various conditions

The comparison reveals major changes of the HDG surface morphology. The images show broadening black spots with increased normal forces. It is likely, that these black spots have their origin in abrasive wear processes (cf. chapter 1.2; p. 3). This material transport process leads to a smoothening of the surface. In addition, the optical properties of the zinc oxide

layer might be changed so that the surface appears black.[128]

Irgalube TPPT

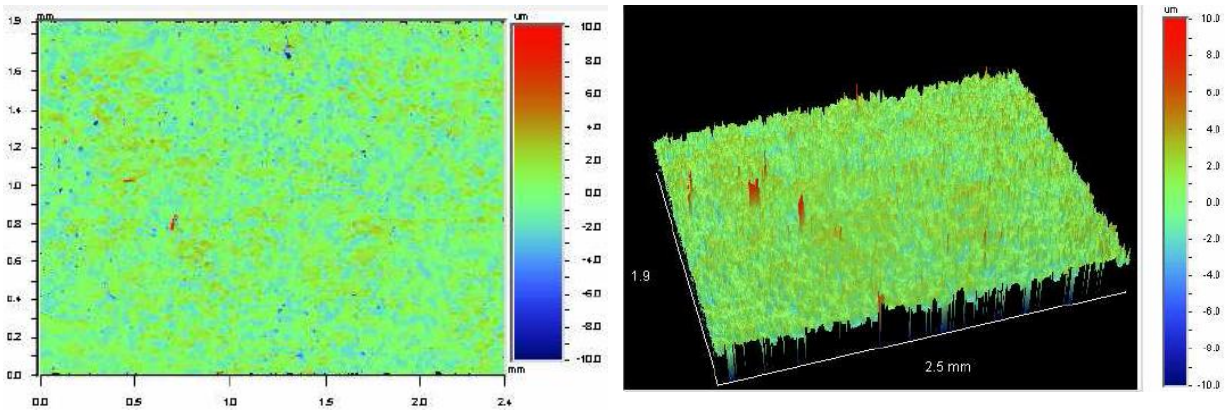

2000 N

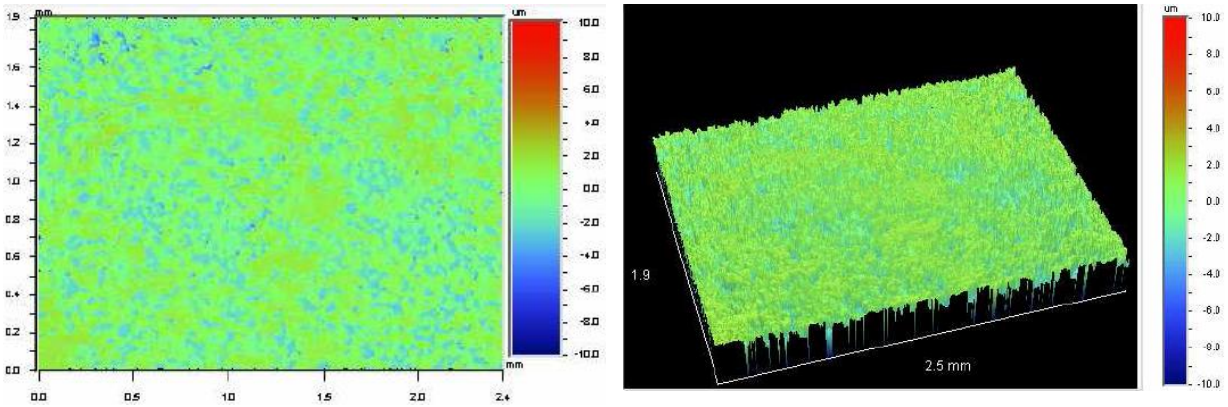

4000 N

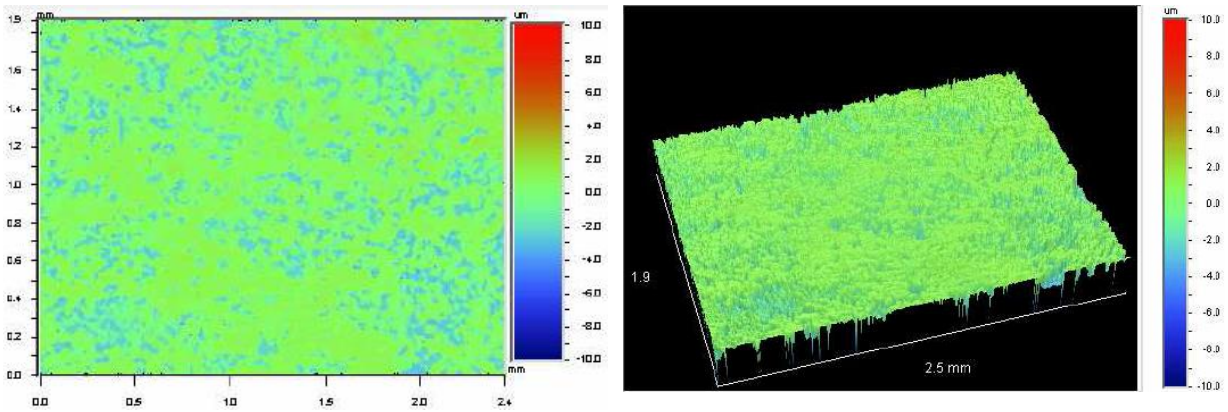

Figure 83. 2D- and 3D- morphological maps of Irgalube TPPT treated HDG samples before and after oil-free strip drawing

The 2D- and 3D-WIL images (Figure 83) and the roughness parameters (Table 4) confirm the smoothening of the surface.

Table 4. Roughness parameters of Irgalube TPPT samples after oil-free strip drawing

Roughness parameters:			
	0 N	**2000 N**	**4000 N**
R_z	20.35 µm	8.17 µm	7.79 µm
R_p	12.42 µm	3.47 µm	3.99 µm
R_t	25.00 µm	9.37 µm	9.96 µm
R_a	1.22 µm	1.18 µm	1.06 µm
R_q	1.43 µm	1.36 µm	1.25 µm
Surface Area	4.69 mm^2	4.67 mm^2	4.66 mm^2

The element distribution (Figure 84) measured by means of LIBS shows that the additive layer of Irgalube TPPT on HDG is inhomogeneous before the strip drawing. This inhomogeneity is even increased at higher normal forces of 2000 N. Especially the element distribution of phosphorus reveals areas of high and very low intensity. A similar distribution pattern is also visible in the element distributions of carbon and sulphur.

The homogeneity of the element distribution is then increased due to material displacement at the maximal normal force of 4000 N. The distributions of phosphorus, carbon and sulphur show few to no areas of very low element intensity.

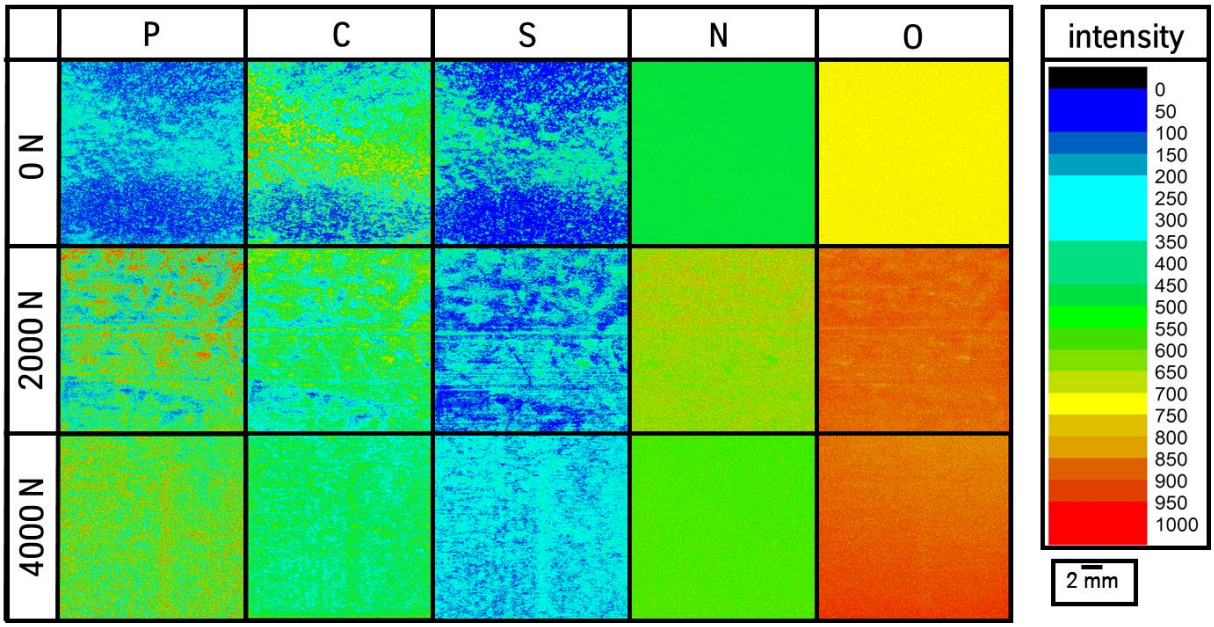

Figure 84. LIBS element distribution of Irgalube TPPT on HDG

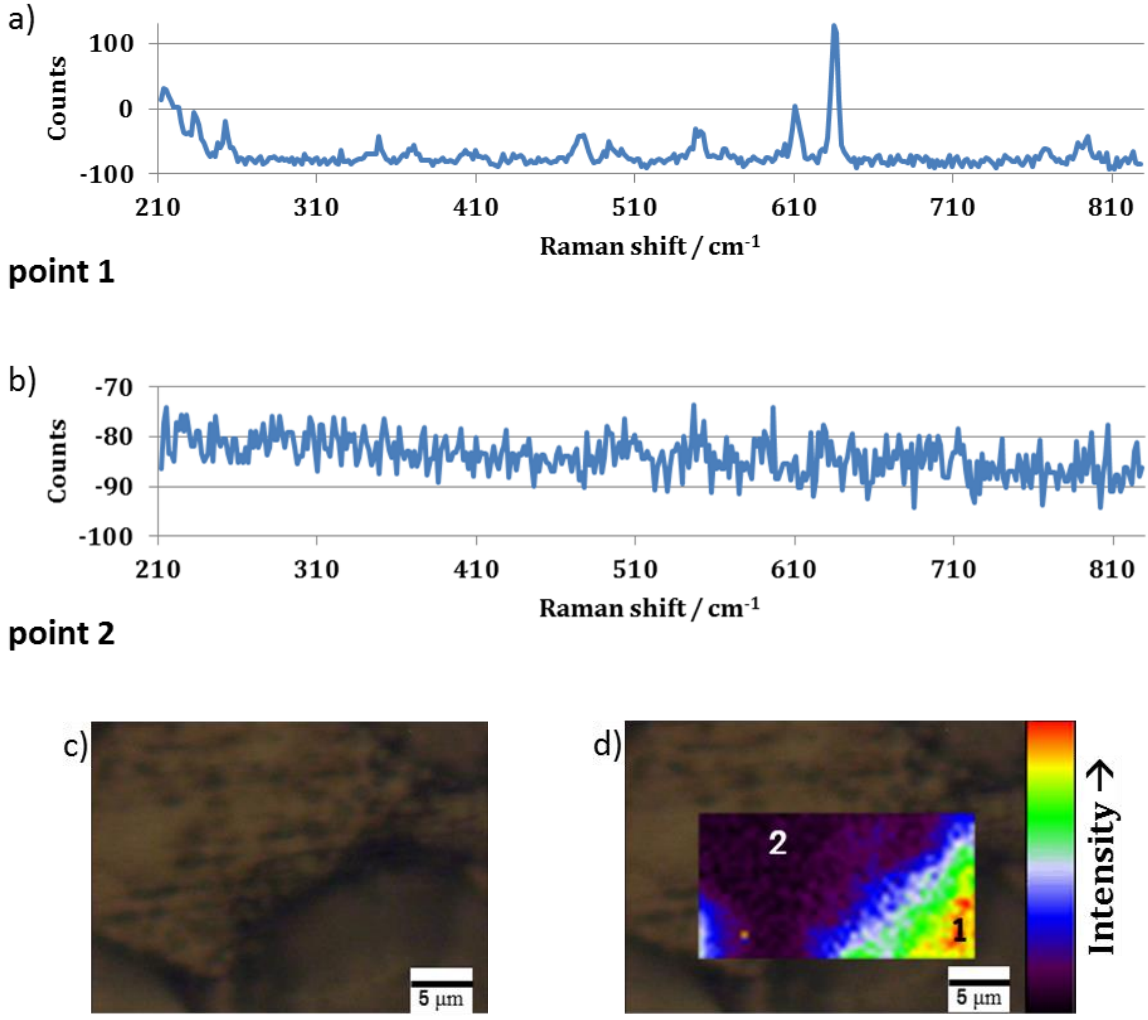

Figure 85. Raman streamline image of Irgalube TPPT coated HDG stripes after tribological treatment with 2000 N

The Raman imaging of Irgalube TPPT coated HDG stripes after normal forces of 2000 N (Figure 85) confirms the previously shown inhomogeneity of the layer. As seen in the reference measurements (Figure 25; p. 46) and in the confirmation of the adsorbed additive layers (Figure 73; p. 92), characteristic peaks of Irgalube TPPT can be detected. One of these peaks was used as analysis point for the streamline image (Figure 85). The intensity of this peak was analyzed over an area of ~10 µ x 25 µ. This analysis shows localized spots of additive as previously revealed by LIBS element distribution.

DTNPS

The comparison of microscope images (Figure 86) of DTNPS coated HDG strips before and after tribological treatment obviously shows differences in the surface morphology. Broad black spots and multi-colored areas are visible after the strip drawing with a contact force of 2000 N. A possible explanation for the black spots is the same as described for Irgalube TPPT. Abrasive wear processes and/or changes of optical parameters can explain those spots. The multi-colored areas could indicate the build-up of tribochemical reaction layers.

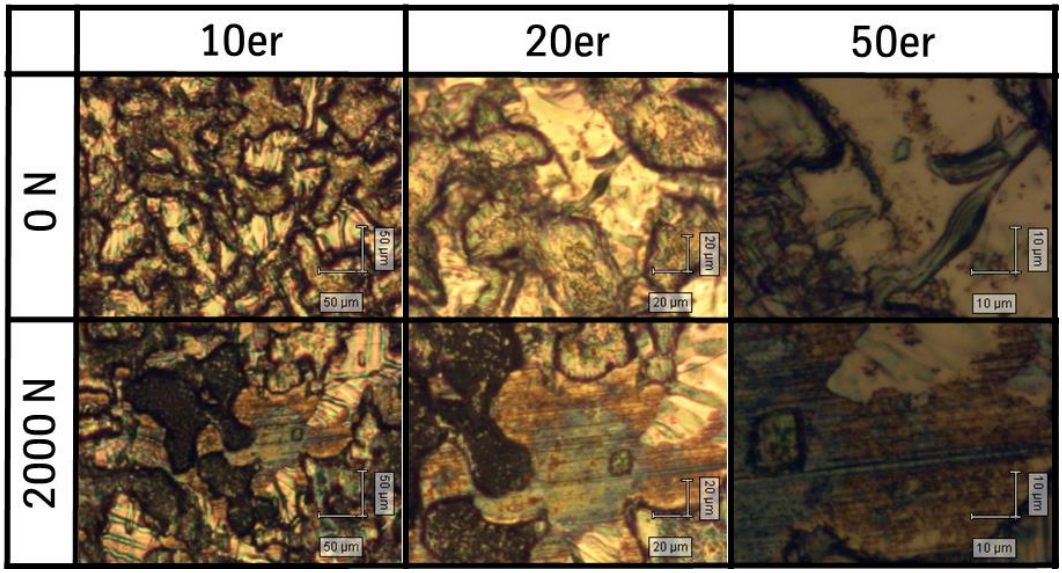

Figure 86. Microscope images of DTNPS coated HDG strips at various conditions

The 2D- and 3D-morphological maps (Figure 87), as well as the roughness parameters (Table 5; p. 105) confirm the occurring of wear at normal forces of 2000 N indicated by increasing parameters like the averaged depth of roughness (7.73 at 0 N up to 8,93 at 2000 N; Table 5; p. 105). At even higher contact forces (4000 N) the reduced roughness parameters indicate a smoothening of the surface possible due to material displacement.

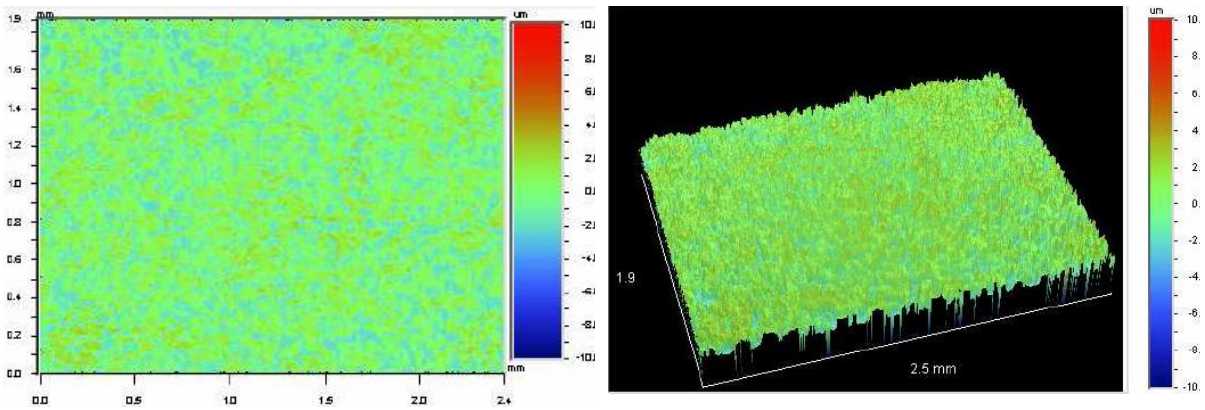

Di-*tert*-nonylpolysulfid

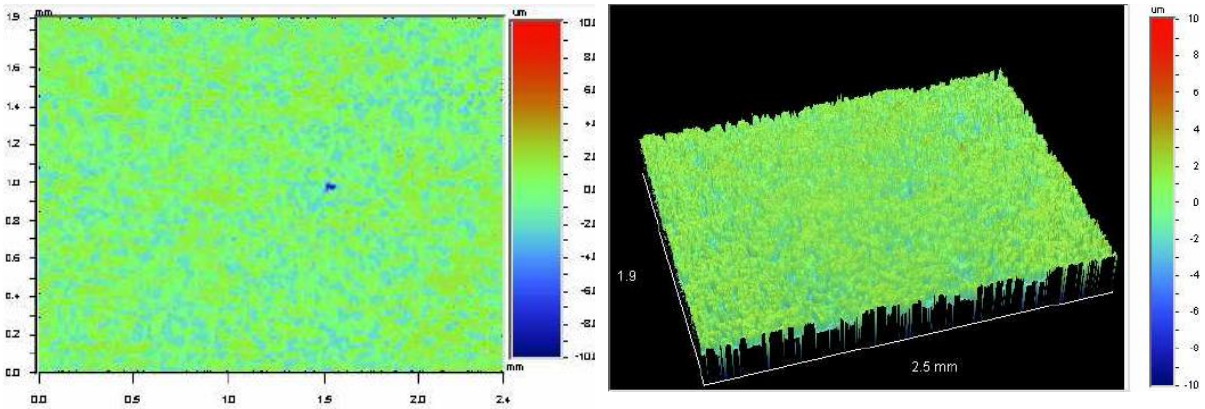

2000 N

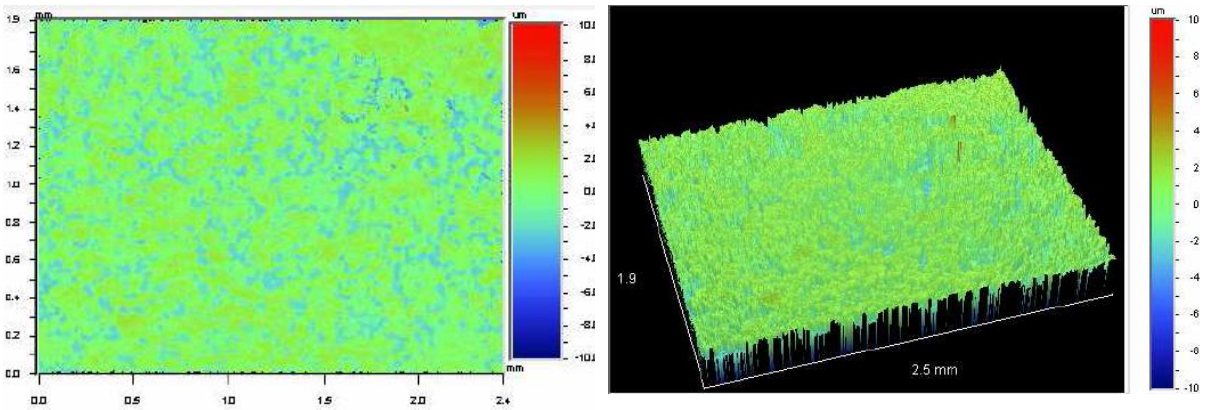

4000 N

Figure 87. 2D- and 3D- morphological maps of DTNPS treated HDG samples before and after oil-free strip drawing

Table 5. Roughness parameters of DTNPS samples after oil-free strip drawing

Roughness parameters:			
	0 N	**2000 N**	**4000 N**
R_z	7.73 µm	8.93 µm	8.87 µm
R_p	5.36 µm	4.54 µm	7.81 µm
R_t	9.57 µm	14.69 µm	12.58 µm
R_a	1.18 µm	1.21 µm	1.16 µm
R_q	1.33 µm	1.35 µm	1.35 µm
Surface Area	4.67 mm^2	4.67 mm^2	4.66 mm^2

The LIBS element distribution (Figure 88) reveals a homogeneous surface coverage of a sulphur additive. The distribution after tribological treatment shows a general reduction of carbon, with few areas where carbon is almost absent. The amount of sulphur is also decreased in these areas while a few spots of increased sulphur content are detectable.

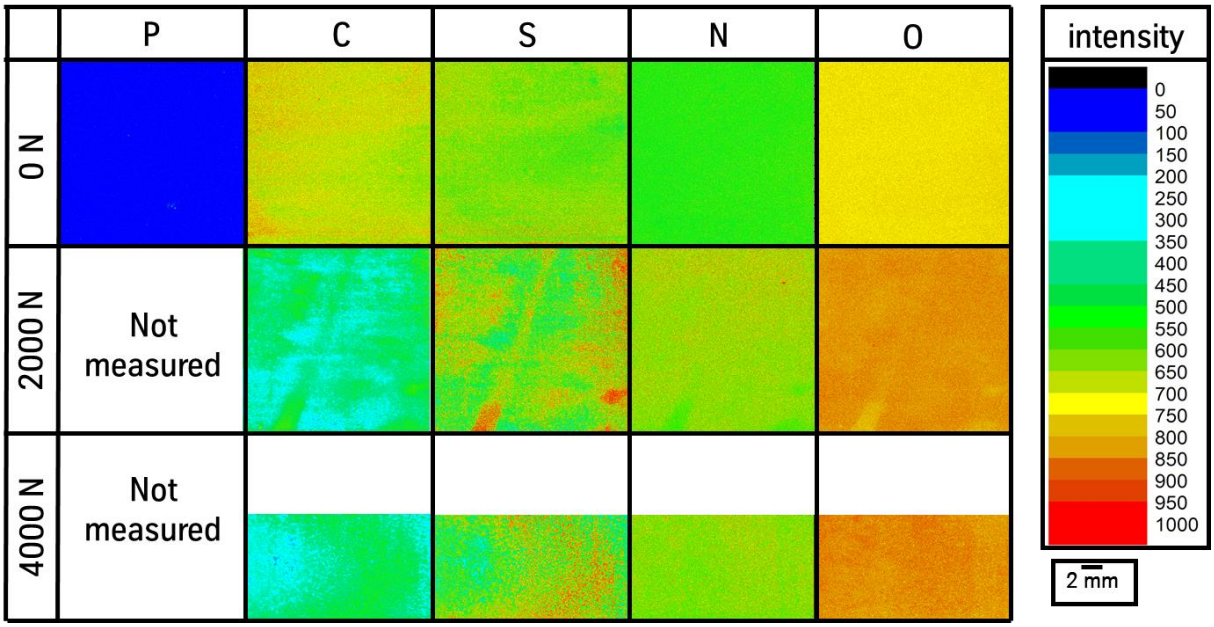

Figure 88. LIBS element distribution of DTPNS coated stripes at various conditions

The inhomogeneous surface composition after tribological treatment was confirmed by means of Raman spectroscopy (Figure 89). Full spectra were obtained at different spots of a sample after strip-drawing test with a contact force of 2000 N. The spectra were then compared with a reference measurement of pure DTNPS (Figure 21; p. 43). The obtained

spectra can be differentiated into two categories and the signal to baseline ratios of characteristic peak regions are used to create mappings.

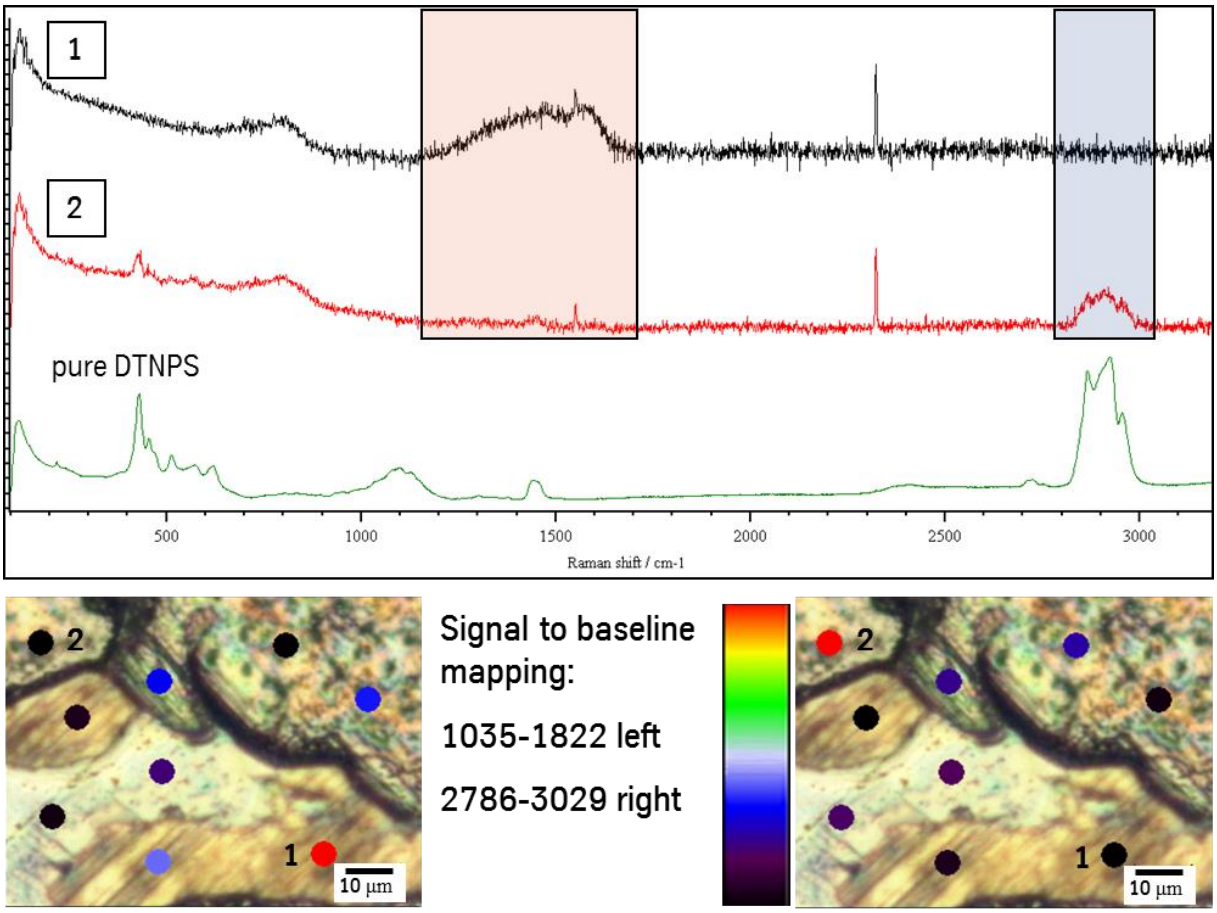

Figure 89. Raman single-point mapping of DTNPS coated HDG stripes after tribological treatment with 2000 N

One category contains spectra that reveal weak signals of DTNPS (Figure 89; spectrum 2). The signal to baseline ration in the region with C-H vibrations, between 2786 cm^{-1} and 3029 cm^{-1}, is used for the mapping.

The second category contained spectra where no additive signal is detectable (Figure 89, spectrum 1). These spectra show signals of sooty carbon in the region between 1035 cm^{-1} and 2822 cm^{-1}. The broad peak at lower wavenumbers is called D-band and is assigned to diamond-like (sp^3) carbon while the peak at higher wavenumber is called G-band and is assigned to graphite-like (sp^2) carbon.[129]

5.1.1.4 Discussion

The aim of this chapter was to gain basic knowledge about additive reactions on HDG under tribological conditions.

The preparation of oil-free additive films on HDG was successfully confirmed for the additives Irgalube TPPT, DTNPS and Irgalube 349 by means of wet-chemistry analysis and Raman spectroscopy.

Tribological treatment was performed by means of strip-drawing test with force measurement on both sides of the sample at various contact pressures. The best performing additive with the lowest COF was DTNPS with a COF of 0.16. Irgalube 349 and Irgalube TPPT also reached low COF with values of 0.17 and 0.18. While the friction force analysis for the additives DTNPS and Irgalube 349 was based on just two contact pressures (2000 N and 4000 N) due to the occurrence of stick-slip effects, the additive Irgalube TPPT enabled even normal forces of 6000 N without the occurrence of stick-slip effects. This makes Irgalube TPPT the best performing additive under wear-aspects and allowed further measurements at even higher contact pressures up to 16000 N. At this point, a change of substrate from skin-passed to non-skin-passed HDG was necessary. The additional measurement took place without the appearance of stick-slip effects and the friction force analysis revealed a lowered COF at 0.12.

For Irgalube TPPT, the ensuing microscopic and morphological characterization revealed the appearance and broadening of black spots with increasing contact pressure due to abrasive wear processes and/or changes of optical parameters. This result was underlined through decreasing roughness parameters indicating a smoothening of the surface. The surface analysis by the means of LIBS and imaging Raman spectroscopy revealed an inhomogeneous additive layer on the “non-contact” surface. With increasing contact pressure, the surface composition detected by means of LIBS remained inhomogeneous especially for the element phosphorus. The surface coverage got more homogeneous at higher contact pressures of 4000 N due to material displacement induced by abrasive wear processes. Despite *Najman et al.* [130] studied thermal and tribochemical films of related additives like diphenyl- and triphenylphosphates on AISI 52100 steel using a Plint high-frequency wear tester by means of XANES, and reported the buildup of Fe(II) polyphosphates, imaging Raman-spectroscopy in this work failed to reveal any tribochemical reaction products. The method allowed only the detection of localized spots of additive after the tribological treatment. *Landolt et al.* [131] also reported iron phosphates as reaction layer when they characterized zinc-free phoshphorus esters on 100Cr6 steel in a SRV machine by means of AES, XPS and SIMS. Various phosphorthionates were studied by *Heuberger et al.* [127] as thermal- and tribochemical-films by means of XPS on AISI 52100 steel using a ball-on-disc test. They reported thinner films of phosphorthionates than for ZnDTP and thermal decomposition of phosphorthionates around 150°C. Reaction

layers on the ball consisted of phosphates, sulphides and traces of sulphates, while on the disc mainly sulphates could be detected. They assumed that the oxidized layers were only possible on the disc, because the ball was under continuous tribological stress.

The high surface sensitivity of the synchrotron-based analysis method XANES, XPS and SIMS, compared to Raman spectroscopy could explain the undetected tribochemical layers. It is also possible that the differences in the tribological testing and the substrate prevent or change the buildup of (poly-) phosphate layers.

Microscopic photographs of tribologically treated DTNPS samples revealed also black spots, which can be explained in a similar way as for the Irgalube TPPT samples. The morphological characterization presented also a smoothening of the surface at high contact pressures but first showed an increase of roughness parameters during the "running-in" phase. Contrary to the Irgalube TPPT samples, the adsorption of DTNPS was more homogeneous as described by LIBS and Raman spectroscopy. The surface concentration of carbon and sulphur, detected by LIBS, decreased with increasing contact pressure with localized hotspots of sulphur. Raman spectroscopy confirmed that with increasing contact pressure, only localized spots of additive remain detectable. Again, no tribochemical reaction products were detectable but Raman spectroscopy revealed high amounts of sooty carbon on the surface.

For Irgalube 349, the microscopic imaging provided no black spots on the surface as described for the two other additives before. Maybe the corrosive protection attributes of Irgalube 349 prohibited changes of the oxide layer and therefore the assumed changes of the optical parameters. However, the morphological characterization showed also a smoothening of the surface with increasing contact pressure. The homogeneity of the additive layer appeared to be strong when described by the means of LIBS and looked more localized when characterized by the means of Raman spectroscopy. The higher surface resolution of Raman spectroscopy is an obvious explanation for this mismatch. With increasing contact pressure, both detection methods showed localization of the detected additive. Despite *Najman et al.* [130] also suggested a layered tribochemical film structure of Fe(II) polyphosphate and ammonium phosphate for Irgalube 349 on 52100 steel using a Plint high-frequency wear tester and characterization by means of XANES, no tribochemical reaction products could be detected in this work. It is possible that, similar to the Irgalube TPPT results, the differences in the surface analytical methods, tribological testing and the substrate prevent the detection of polyphosphate layers.

5.1.2 Base oil selection

The base oil selection was performed in combination with the characterization of the tribological performance of DPDS by means of strip drawing measurements with increasing contact pressure (Figure 90).

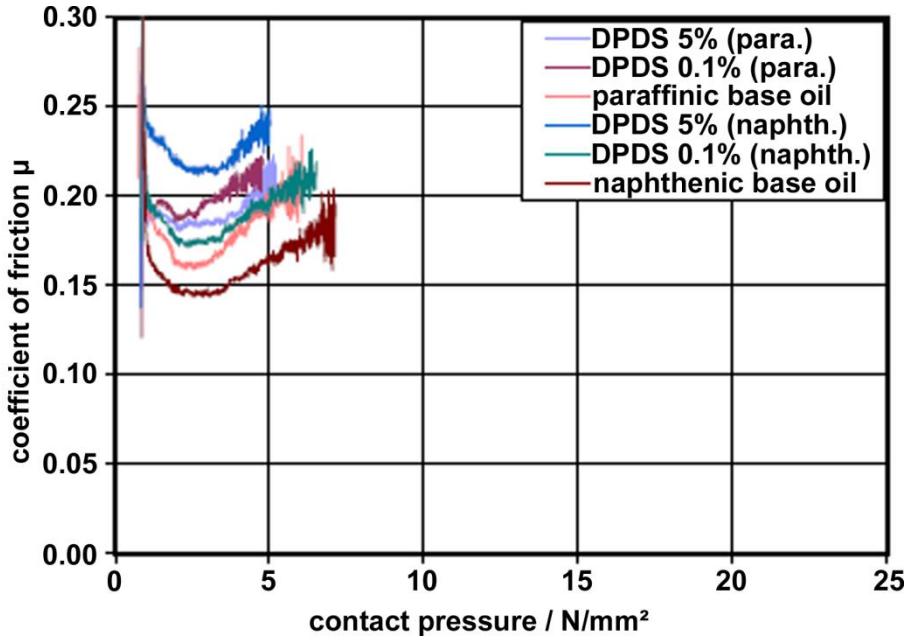

Figure 90. Base oil selection and tribological performance of DPDS

First, the addition of DPDS to naphthenic base oil increases the coefficient of friction. This effect is higher for 5 w.-% than for 0.1 w.-%. The coefficient of friction is also increased for the addition of DPDS to paraffinic base oil, while an additive concentration of 5 w.-% decreases the coefficient of friction back to an additive free level. These results are in contradiction to results presented by *Masuko et al.* [132] who reported the decreased wear rates with DPDS and di-benzyl disulphide (DBDS) under rolling conditions in a two-ball apparatus on high carbon chromium bearing steel and on carbon steel. Decreased wear rates with DPDS and DBDS were also reported by *Plaza et al.* [133, 134] in a four-ball test on AISI 52100 steel. Similar results with disulphides in a four-ball test with bearing steel were obtained by *Murakami et al.* [135] and *Sakai et al.* [136]. A direct comparison of these results is not recommended because of the different materials, tribological testing methods and higher temperature regions so that the corrosive reaction mechanism of DPDS as EP-additive [18] leads to higher COFs under the conditions applied in this thesis.

The comparison of paraffinic and naphthenic base oils reveals a lower coefficient of friction and a later beginning of stick-slip effects for the naphthenic base oil.

Therefore, all further oil-based tribological measurements were performed with naphthenic base oil.

5.1.3 Oil-based strip-drawing tests with adsorbed additives as pre-treatment

Building on the results of the oil-free strip-drawing test (chapter 5.1.1; p. 90), the tribological performance of adsorbed additives as pre-treatment was characterized. Therefore, adsorbed layers of DTNPS, Irgalube TPPT and Irgalube 349 were prepared on HDG strips by means of dip coating and coil coated with naphthenic base oil (chapter 3.3.2.2; p. 29). These samples were compared with reference measurements of an additive-free naphthenic base oil and the reference pre-lube PL 3802-39S. The tribological performance was characterized by means of strip-drawing test with increasing contact pressure (chapter 3.4.2.2; p. 32).

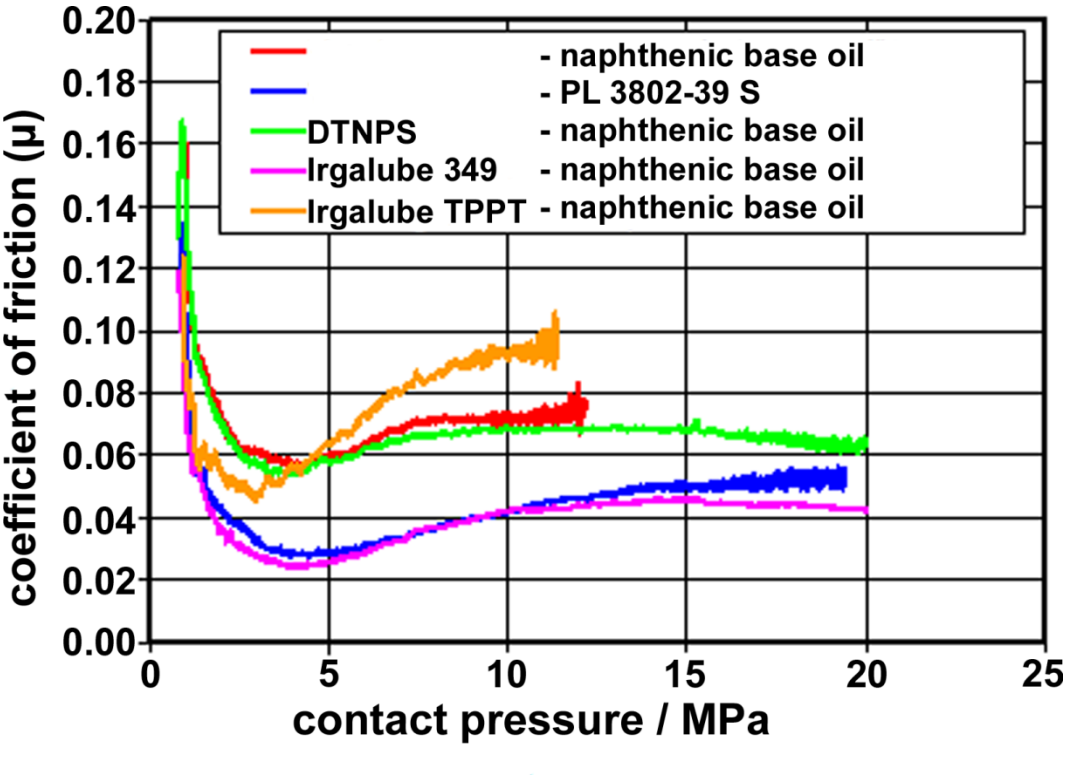

Figure 91. Comparison of friction coefficient gradients of adsorbed additives as pre-treatment

The comparison of friction coefficient gradients (Figure 91) shows that the pre-treatment with Irgalube TPPT has the worst performance and a deteriorating effect despite the best performance in the oil-free environment (chapter 5.1.1.2; p. 95). The coefficient of friction for Irgalube TPPT is higher than of pure naphthenic base oil and even the occurring of stick-slip effects starts earlier. The pre-treatment with DTNPS shows in the beginning similar characteristics as pure naphthenic base oil but while the base oil stops at ~12 MPa due to

stick-slip effects, DTNPS continues with decreasing coefficient of friction up to the maximum of 20 MPa. The coefficient of friction nearly reaches the performance of the full-developed PL 3802-39S with a coefficient of friction of ~0.06. An even better performance is achieved by the pre-treatment with Irgalube 349. The coefficient of friction is almost over the complete contact pressure range below PL 3802-39S and the sample reaches the maximum contact pressure of 20 MPa without the occurring of stick-slip effects.

The results show, that the pre-treatment with selected additives like DTNPS and Irgalube 349 can be a foundation to develop lubricants with low friction and suitable anti-wear parameters. Due to limited measurement capabilities, surface characterization techniques were only used for the analysis of tribochemical layers in chapter 5.1.4 and 5.1.5. Therefore, no surface analysis of the samples in this chapter was performed.

5.1.4 Oil-based strip-drawing with increased pressure

The main part of chapter 5 is the tribological and surface analytical characterization of additive systems diluted in oil and coated on hot-dip galvanized steel (chapter 3.3.2.3; p. 29). The tribological characterization was performed by means of strip-drawing test with increasing contact pressure (chapter 3.4.2.2; p. 32). XPS (chapter 3.4.8.1; p. 38), ToF-SIMS (chapter 3.4.6; p. 35) and imaging Raman spectroscopy (chapter 3.4.4; p. 33) were selectively used to study the chemical composition of the surface. After further screening tests, DTNPS and OBSS were selected due to their diverse tribological performance to deepen the knowledge of the tribochemical reaction mechanism of sulphur-based additives.

5.1.4.1 Tribological and morphological results

Strip drawing test results

Tribological measurements depend heavily on the environmental parameters. Possible differences in temperature and humidity therefore enable the comparison of friction coefficients only for each respective test series. Qualitative comparisons of additive effects between different test series are still possible.

While the base oil selection (chapter 5.1.2; p. 109) was performed in addition with the tribological characterization of DPDS, Figure 92 shows an additional test series with various sulphur and phosphorus based additives and an oil coverage of 1.0 g/m^2.

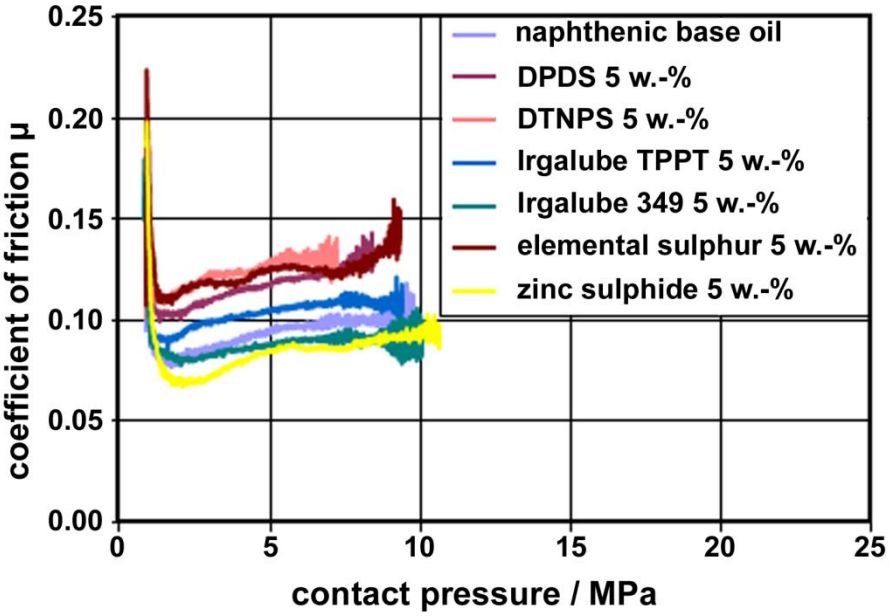

Figure 92. Comparison of friction coefficient gradients of additives in naphthenic base oil on HDG

The friction coefficient gradients of the tested additives vary in their amount of friction. Zinc sulphide and Irgalube 349 have a lower coefficient of friction than the pure base oil. DPDS and DTNPS show a similar coefficient of friction like elemental sulphur and have all together the worst friction performance in this test series. A coefficient of friction only slightly higher than the pure base oil shows the sulphur and phosphorus based Irgalube TPPT. All additives show poor anti-wear performance with stick-slip effects occurring at the half contact pressure range around 10 MPa.

Therefore, further test series (Figure 93+Figure 94) were performed with additional additives and higher oil coverage of 1.5 g/m^2.

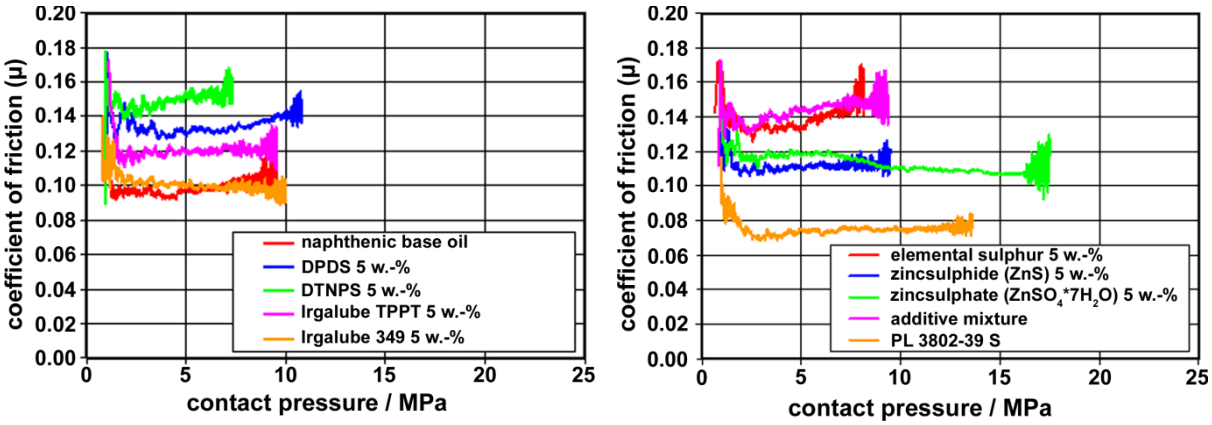

Figure 93. Comparison of friction coefficient gradients of additives in naphthenic base oil on HDG with higher oil films of 1.5 g/m^2

The friction coefficient gradients with oil films of 1.5 g/m^2 (Figure 93) show similar trends to the gradients with oil films of 1.0 g/m^2 (Figure 92). Organic sulphur additives like DPDS

and DTNPS, together with elemental sulphur show the worst friction performance of this test series with coefficients of friction higher than 0.13. Also the performance of an "additive mixture" (DPDS, DTNPS, Irgalube TPPT, Irgalube 349, elemental sulphur, zinc sulphide and zinc sulphate; 5 w.-% in each case) is dominated by the three sulphur additives and shows also a coefficient of friction of 0.14. While Irgalube 349 and zinc sulphide show a better performance than the base oil with oil coverage of 1.0 g/m^2 (Figure 92), their performance in this test series is equal to the pure base oil at its best. The best friction and increased anti-wear performance is shown by the fully developed pre-lube PL 3802-39S with a friction coefficient below 0.08 and the occurring of stick-slip effects around 13 MPa. An even better anti-wear performance is presented by zinc sulphate as additive. While the friction coefficient of ~0.11 is higher than the base oil, stick-slip effects arise around 17 MPa.

A similar test series with oil films of 1.5 g/m^2 was performed with additional sulphur based additives to characterize the important influence of sulphur on the tribological performance (Figure 94). The performance of various different concentrations of Irgalube 349 which presented the best behavior as pre-treatment (Figure 91) was also studied.

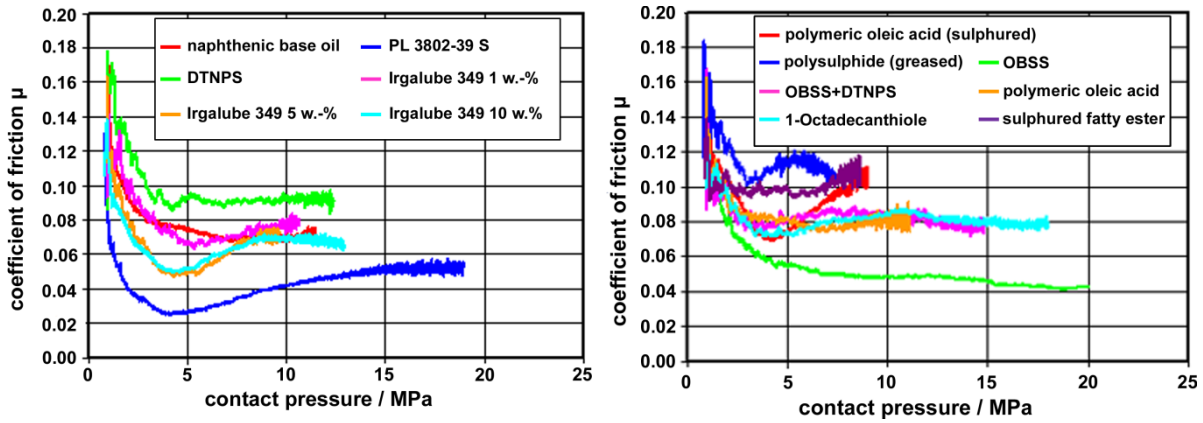

Figure 94. Comparison of friction coefficient gradients of various additives in naphthenic base oil on HDG

This test series (Figure 94) shows again that one of the worst tribological performances is presented by DTNPS with a coefficient of friction of ~0.09 and the occurring of stick-slip effects at ~12 MPa. The pure base oil itself runs with friction coefficients around 0.07 and stick-slip effects starts around 11 MPa. The best performances next to the fully developed PL 3802-39S is demonstrated by OBSS with friction coefficients permanently decreasing down to 0.04 and without stick-slip effects. A combination of both additives (OBSS+DTNPS) with five weight-percent each shows an increased performance compared to pure DTNPS. The coefficient of friction is decreased down to the level of pure base oil and the occurring of stick-slip effects is delayed up to 15 MPa. Additives with similar gradients but even later

occurring of stick-slip effects are polymeric oleic acid (~11 MPa) and 1-Octadecanthiole (~18 MPa). Other additional sulphur-base additives like sulphured and non-sulphured polymeric oleic acid and a greased polysulphide have higher coefficients of friction and earlier occurring of stick-slip effects than the pure base oil. The concentration variations of Irgalube 349 reveal that the performance of all three concentrations doesn`t vary significantly from the performance of the pure base oil. The lowest concentration of 0.1 w.-% shows a similar coefficient of friction than the base oil and a slightly decreased stick-slip behavior. The higher concentrations of 5 w.-% and 10 w.-% show an identical running-in phase with lowered coefficients of friction than the base oil. After the running-in phase the coefficient of friction increases back to the level of pure base oil and stick-slip occurs slightly earlier for 5 w.-% and slightly later for 10 w.% than the pure base oil.

Because in the previous test-series the additive OBSS runs up to maximum contact pressure of 20 MPa with low coefficients of friction and without stick-slip effects, it was necessary to start an additional test series with the maximum contact pressure raised to 80 MPa (Figure 95).

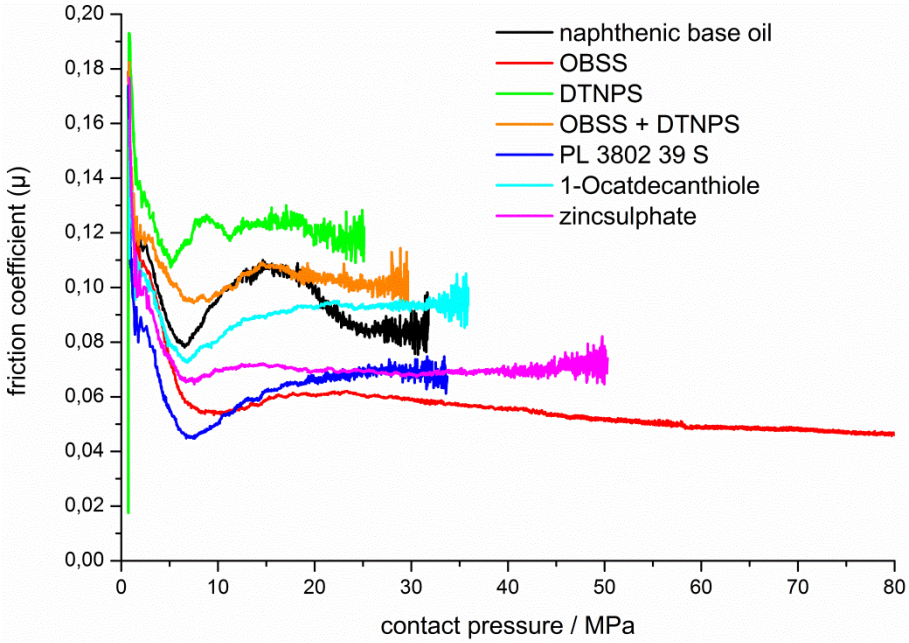

Figure 95. Comparison of friction coefficient gradients of additives in naphthenic base oil on HDG with an increased maximum contact pressure of 80 MPa

As mentioned before, the tribological behavior is heavily influenced by environmental and instrumental parameters. The fourfold increase of the maximum contact pressure also quadruples the increasing-rate of the contact pressure. In addition, the tool was changed to achieve the higher contact pressures (tool surface changed from 1200 mm^2 to 600 mm^2). Therefore, the quantitative results of this test series vary from the previous test series while the qualitative categorization remains comparable.

The pure base oil as reference ends with the occurring of stick-slip effects around 31 MPa with a coefficient of friction of ~0.08. Worsened coefficient of friction and earlier occurring of stick-slip effects are again shown the combination of DTNPS and OBSS (COF: 0.10; stick-slip: ~29 MPa). 1-Octadecanthiole again shows a delay of stick-slip effects (~35 MPa) but a slightly increased coefficient of friction of ~0.09 compared to the pure base oil.

A significantly improved anti-wear performance with stick-slip effects at ~50 MPa is presented by zinc sulphate as additive. While Figure 93 shows zinc sulphate with a similar anti-wear performance but increased coefficient of friction compared to the base oil, the higher increasing-rate leads to a slightly decreased COF compared to the base oil. The anti-wear performance is even better than the fully developed PL 3802-39S and the COF is on the same level.

The worst tribological performance is shown again by DTNPS (highlighted in Figure 96). The COF of DTNPS as additive is increased from ~0.08 up to ~0.12 compared to the pure base oil. Also stick-slip effects occur earlier at ~25 MPa compared to ~31 MPa for the pure base oil.

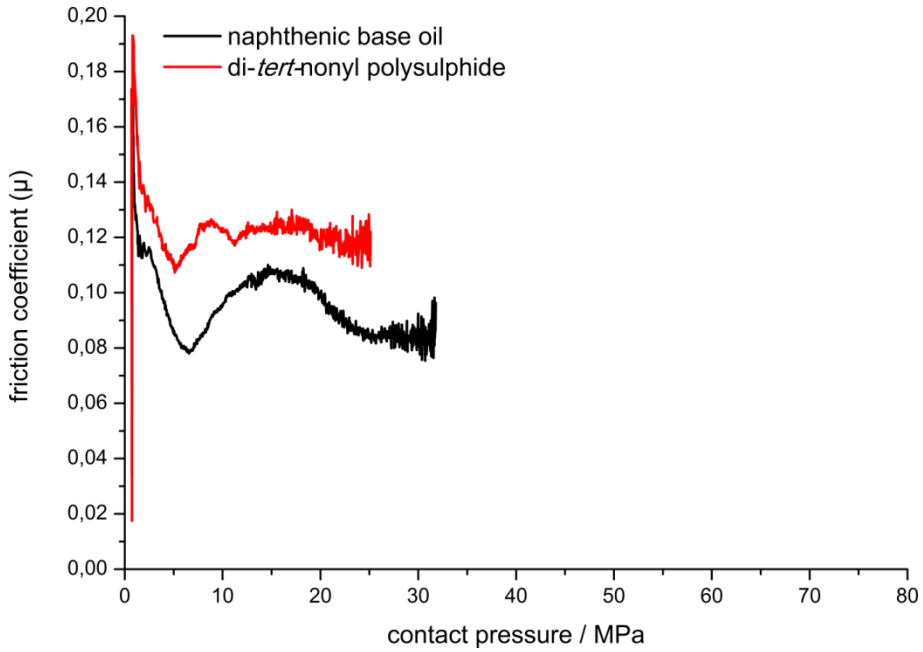

Figure 96. Comparison of friction coefficient gradients of naphthenic base oil and DTNPS solved in naphthenic base oil

The best tribological performance is again demonstrated by OBSS as additive (highlighted in Figure 97). The COF is with ~0.06 from the beginning the lowest of this test series and even decreases with higher contact pressures down to ~0.05. Outstanding is the absence of stick-slip effects over the whole drawing range up to the maximum contact pressure of 80 MPa.

Both, the worst (DTNPS) and the best (OBSS) additive, are highlighted because they are selected for detailed surface analysis.

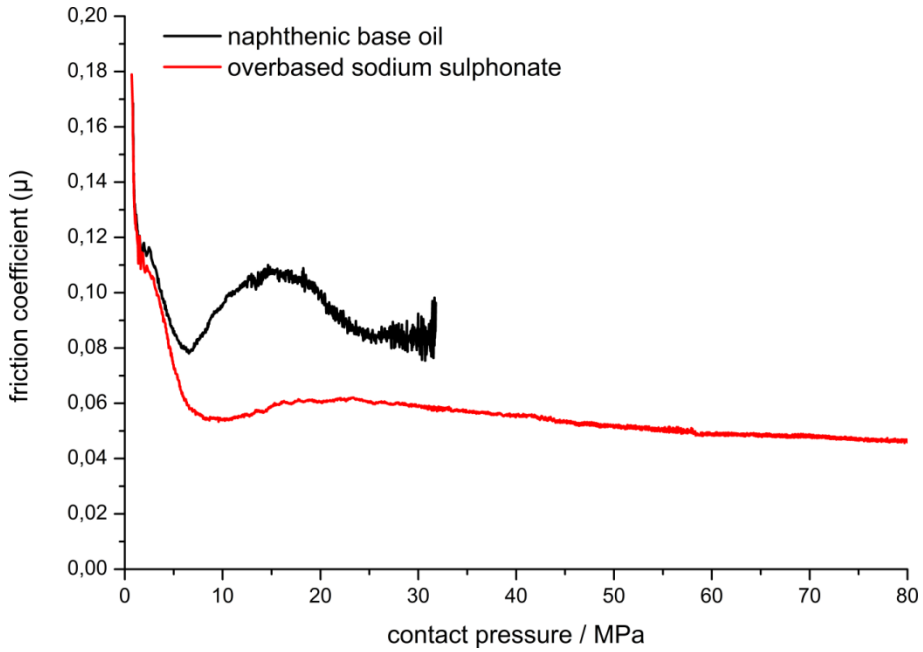

Figure 97. Comparison of friction coefficient gradients of naphthenic base oil and OBSS solved in naphthenic base oil

Figure 98 shows an exemplary presentation of the samples that were cut out of the steel strips after the tribological treatment (chapter 3.3.2.3; p. 29).

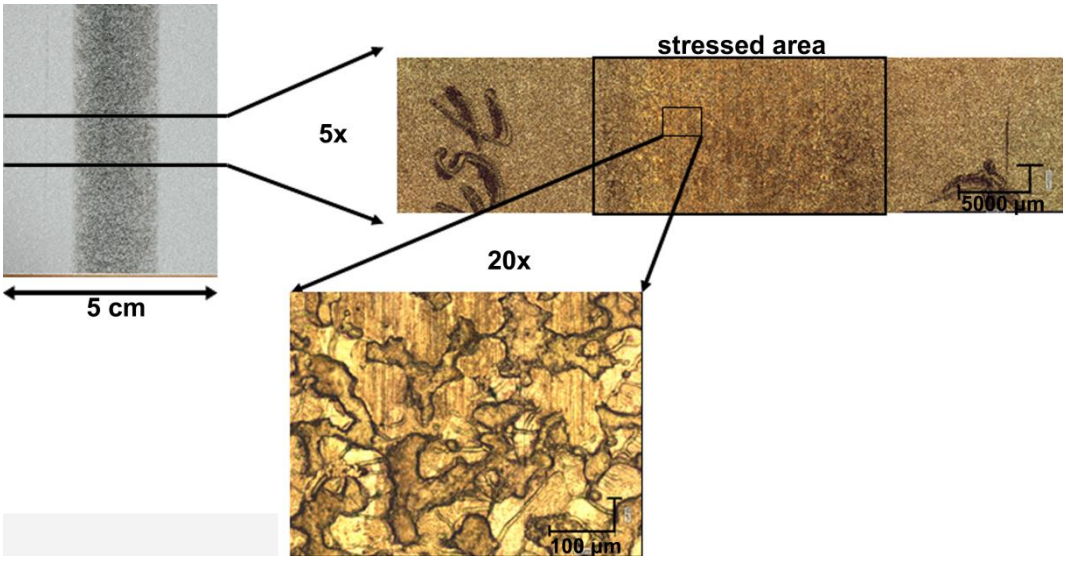

Figure 98. Exemplary presentation of cut and magnified zinc-coated steel sheet

White light interferometry results and roughness parameters

The surfaces of selected tribological treated samples (low and high contact pressure) were analyzed via white light interferometry to observe wear induced morphological changes.

The results are presented in form of 2D- and 3D-morphological maps and roughness parameters and compared to the results of the reference (Figure 34, p. 54).

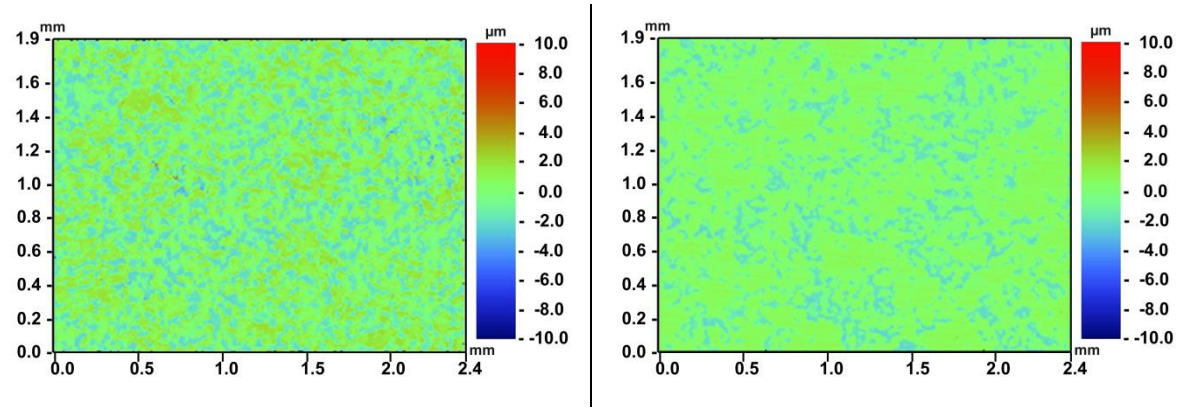

2D morphological map

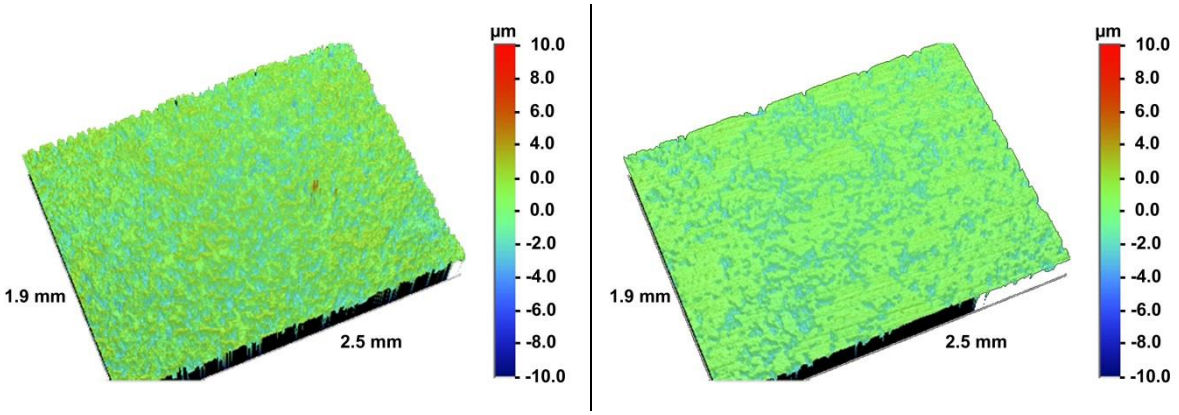

3D morphological map

Roughness parameters:				Roughness parameters:			
R_z	11.88 µm	R_a	1.23 µm	R_z	4.89 µm	R_a	0.74 µm
R_p	7.68 µm	R_q	1.39 µm	R_p	2.81 µm	R_q	0.88 µm
R_t	28.07 µm			R_t	5.89 µm		
Surface Area	4.67 mm^2			**Surface Area**	4.60 mm^2		

Figure 99. Wight light interferometry morphological maps and roughness parameters of OBSS samples with low (~4 MPa) (left) and high (~76 MPa) (right) contact pressure

The comparison of morphological maps and roughness parameters (see chapter 1.2 Fundamentals of tribology, p. 3) of an area on the untreated reference sample and areas with low and high contact pressure on OBSS samples reveals a roughening of the surface in the beginning of the strip drawing test correlating with high coefficients of friction in this phase. In the later phase of the strip drawing, higher contact pressures obviously yield to a smoothening of the surface due to wear effects.

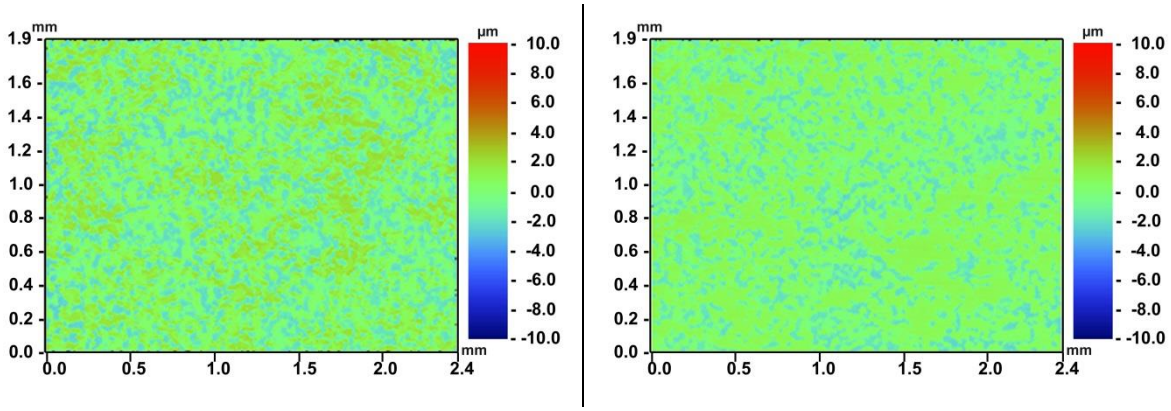

2D morphological map

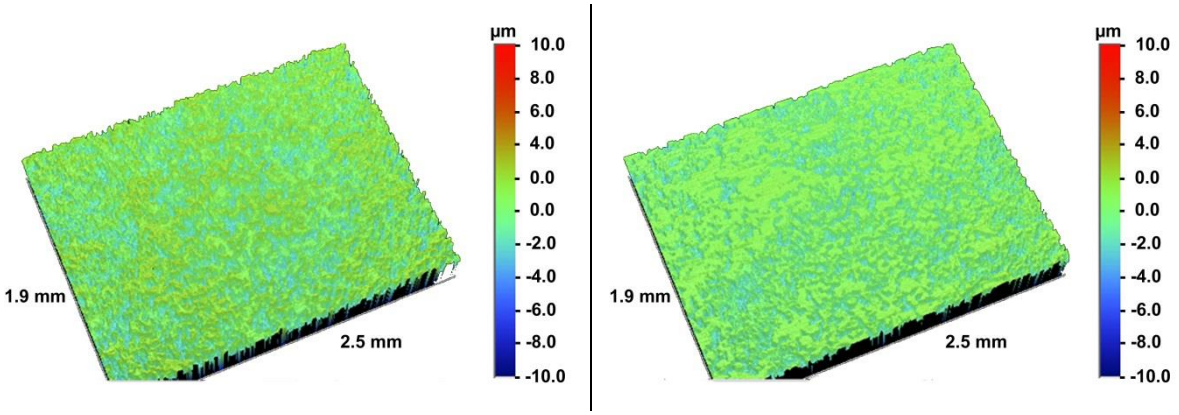

3D morphological map

Roughness parameters:				Roughness parameters:			
R_z	6.36 µm	R_a	1.21 µm	R_z	5.08 µm	R_a	0.93 µm
R_p	3.88 µm	R_q	1.38 µm	R_p	2.79 µm	R_q	1.05 µm
R_t	7.92 µm			R_t	6.72 µm		
Surface Area		4.66 mm²		**Surface Area**		4.62 mm²	

Figure 100. Wight light interferometry morphological maps and roughness parameters of DTNPS samples with low (~4 MPa) (left) and high (~36 MPa) (right) contact pressure

The comparison of morphological maps and roughness of an area on the untreated reference sample and areas with low and high contact pressure on DTNPS samples reveals nearly unchanged surface morphology in the beginning of the strip-drawing test. The coefficient of friction is high as with OBSS in this phase of the strip drawing. However, the absence of surface roughening indicates improved anti-wear characteristics of this additive under the starting conditions. With increasing contact pressure (here 36 MPa) a smoothening of the surface is observable similar to OBSS.

5.1.4.2 Surface analysis

After presenting the tribological performance of various additives and the morphological analysis of selected sulphur-based additives, this part reports the corresponding surface-chemical analysis results.

Imaging Raman spectroscopy

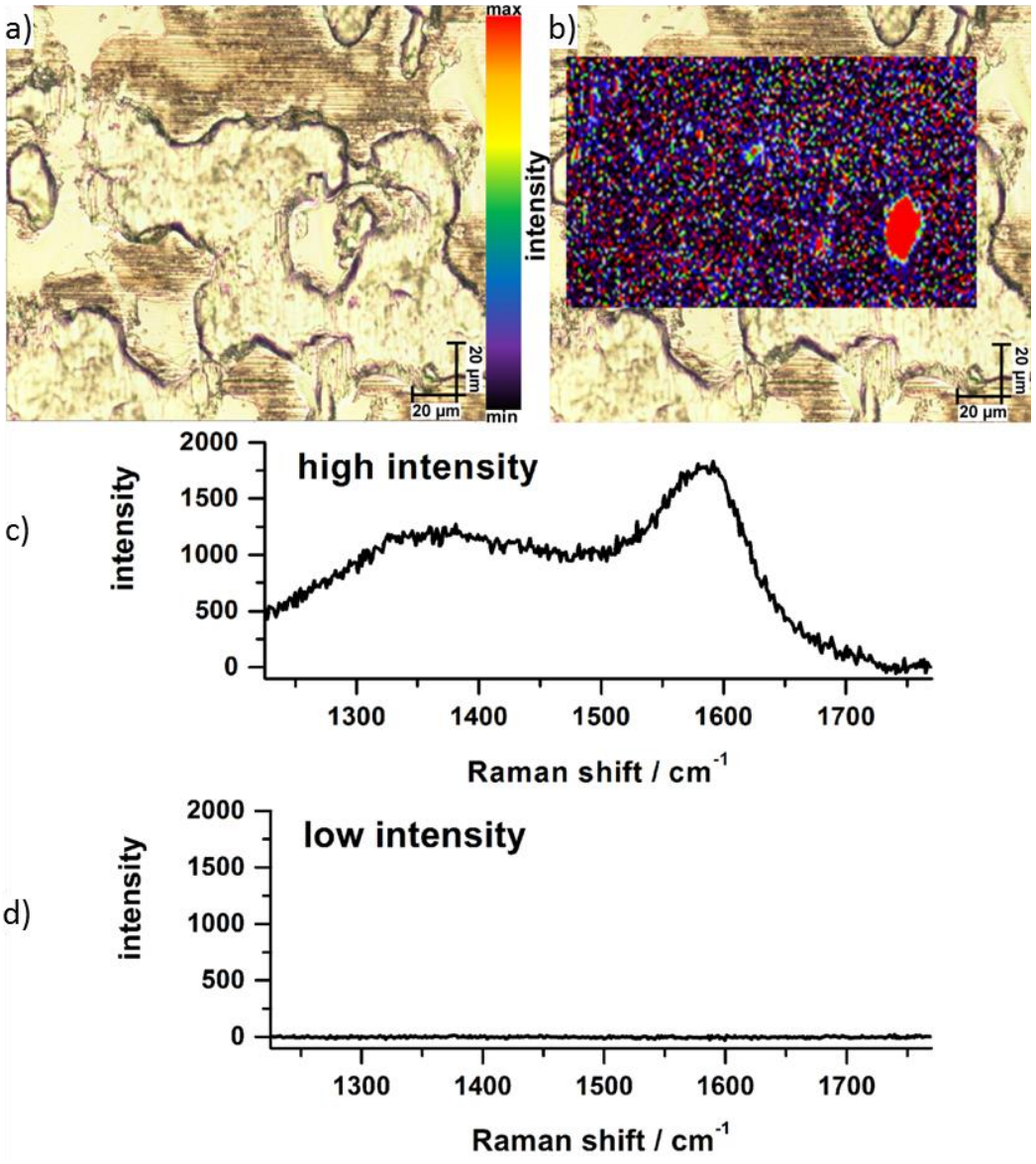

Figure 101. G-Band imaging Raman spectra of naphthenic base oil after strip drawing test with 44 MPa

Figure 101 shows a white-light image (a) and a streamline mapping (b) of a pure base oil sample stressed with 44 MPa at 50-times magnification. The mapping virtualizes the Raman spectroscopic intensity of the G-band (graphitic carbon). The figure also shows the corresponding partial Raman spectra at the lowest and highest intensity. The mapping reveals that only localized spots of sooty carbon can be detected. The broad peak at lower

wavenumbers is called D-band and is assigned to diamond-like (sp^3) carbon while the peak at higher wavenumber is called G-band and is assigned to graphite-like (sp^2) carbon.[129, 137]

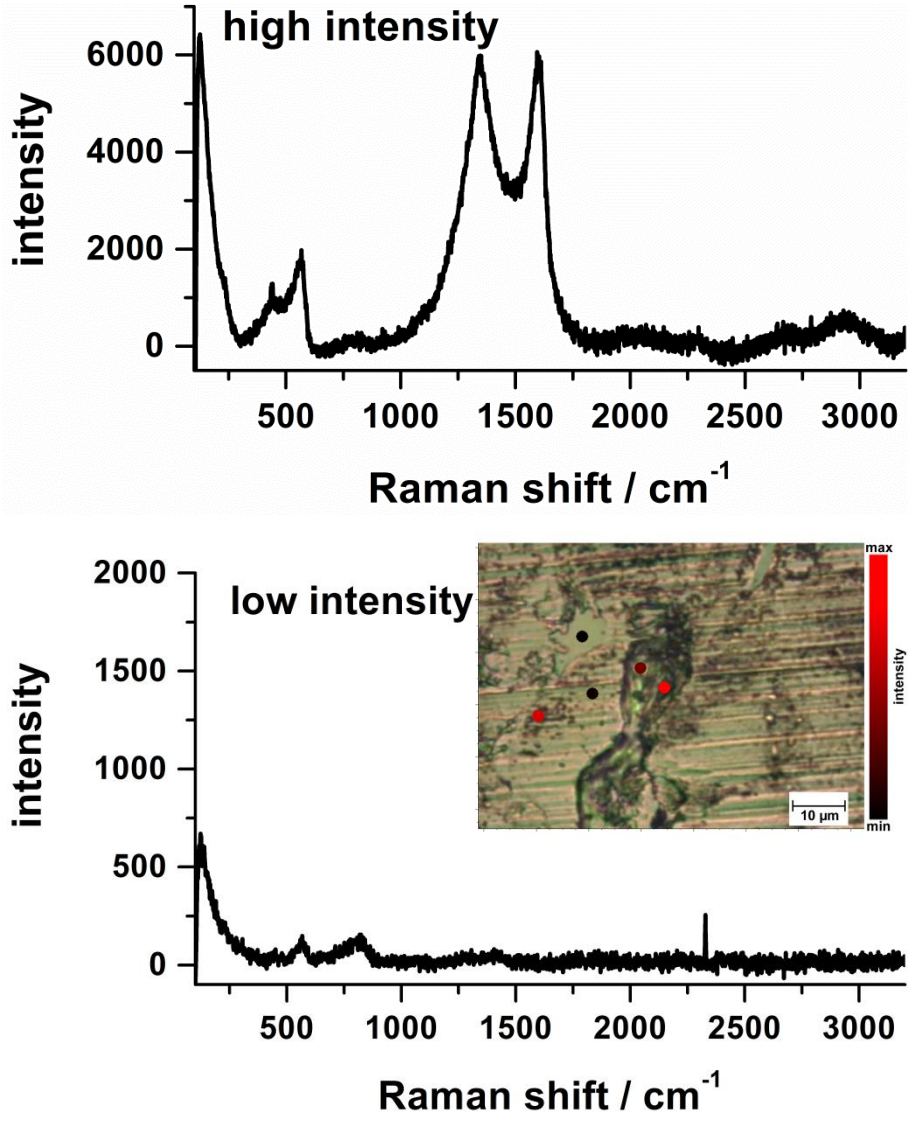

Figure 102. G-Band imaging Raman spectra of OBSS after strip drawing test with 60 MPa

Figure 102 shows similar results for the OBSS additive systems. It presents a single point mapping of the G-band (graphitic carbon) signal-intensity detected with Raman spectroscopy on the sample after the tribologically treatment with 60 MPa. The obtained spectra show the D- and G-band of carbon-based reaction products only in localized spots with varying signal intensity. Some spots show a high intensity of both signals, while other spots reveal none of these components. No sulphur-based reaction products can be detected with this method.

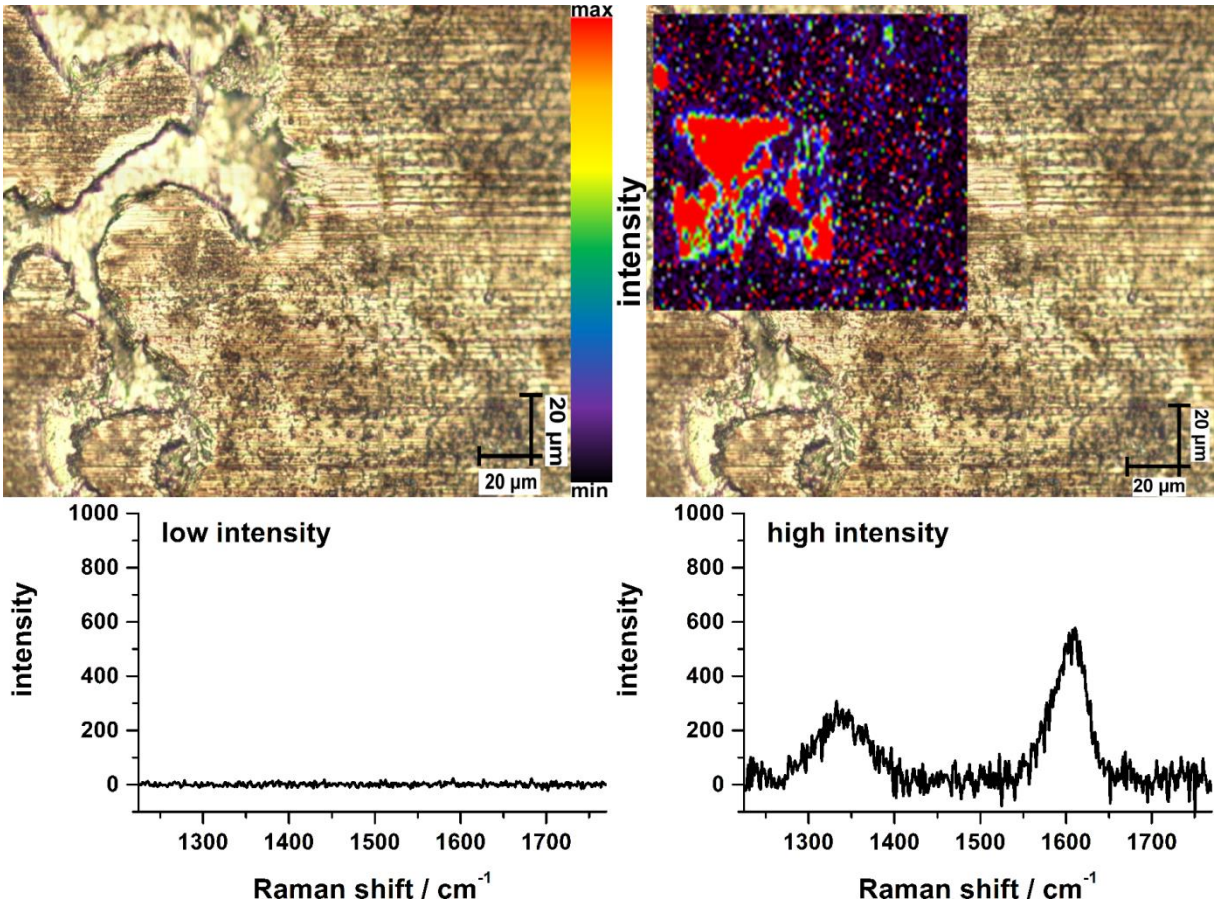

Figure 103. G-Band imaging Raman spectra of DTNPS in naphthenic base oil after strip drawing test with 12 MPa

Imaging Raman spectroscopy of the second sulphur-based additive system DTNPS also shows comparable results as the two previously shown measurements. Figure 103 also presents an intensity mapping of the G-band signal obtained by means of streamline imaging Raman spectroscopy. The G- and D-band of sooty carbon is again only detectable in localized spots. No signals of sulphur-based reaction products are detectable.

The surface analysis of tribologically stressed oil-based additive systems by means of imaging Raman spectroscopy was difficult as shown in the previous three systems. The measurements gained no hints of additive-based reaction products. This means either, that no homogenous reactions layers were formed or that the chemical sensitivity of the used system and parameters was not specific enough to obtain these results. While it is previously shown that additives and reaction products were detectable under oil-free conditions, very thin reaction layers like monolayers may have been below the detection limit. It is also possible that additive-based reaction products were only formed in localized spots. In that case, it is likely, that these spots were missed during the measurements despite areas of at least 100 µm^2 are analyzed. The detection of sooty carbon in localized spots illustrates this problem. Full spectra measurements were possible only in a focused

operating mode and were time consuming. The streamline imaging mode on the other hand enabled the analyses of larger areas but was limited to a wavelength band of around 500 cm^{-1} and consumed several hours of measurement time due to the large scanned areas. Another explanation of the absence of reaction-product peaks is the development of large fluorescence backgrounds that could have masked very weak Raman signals.

The localized spots of sooty carbon could be formed due to several possible reasons. A laser-induced decomposition of oil or additive residues could be one reason. However, that a thermal effect of the laser is unlikely due to the high heat conductivity of the HDG sheets, this effect could be ruled out because reference measurements with varying laser power and laser time revealed no degradation of additive signals. *Uy et al.* [138] described the formation of similar carbon layers out of aged engine oils under high frequency reciprocating rig (HFRR) tribological conditions on AISI 52100 steel (American Iron and Steel Institute). That means, that the here reported layers could be formed from soot particles that are already present in the oil, or that the oil partly decomposes and generates soot particles. These layers form in the naphthenic base oil systems and in the two sulphur-based additive systems like OBSS and DTNPS respectively. The formation conditions reveal no systemic trend because the layers were not detectable on every sample and the contact pressure varied.

In summary, it was not possible to detect additive-based reaction products by means of Raman spectroscopy under these conditions. However, localized spots of sooty carbon were detected on all three analyzed systems.

X-ray photoelectron spectroscopy (XPS)

OBSS

The XPS results are reported in form of survey spectra, atomic concentrations of the surface, depth profiles of atomic concentrations, high-resolution detail-spectra and the run of atomic concentrations out of survey data versus the strip-drawing contact pressure. The HDG reference data are reported in chapter 4.1.2.1 (p. 49).

Figure 104 shows the surveys of the HDG reference and tribologically stressed samples of the OBSS additive system. They include an area without any contact pressure (non-contact) and samples with increasing contact pressure (4 MPa, 20 MPa, 36 MPa, 52 MPa, 68 MPa and 76 MPa). The reported contact pressures are the median values corresponding to cut steel sheets with a deviation of ±4 MPa. In contrast to the HDG reference data, the unstressed and

stressed samples of the OBSS additive system reveal an additional signal of sodium. Also notable is the absence of any sulphur signal.

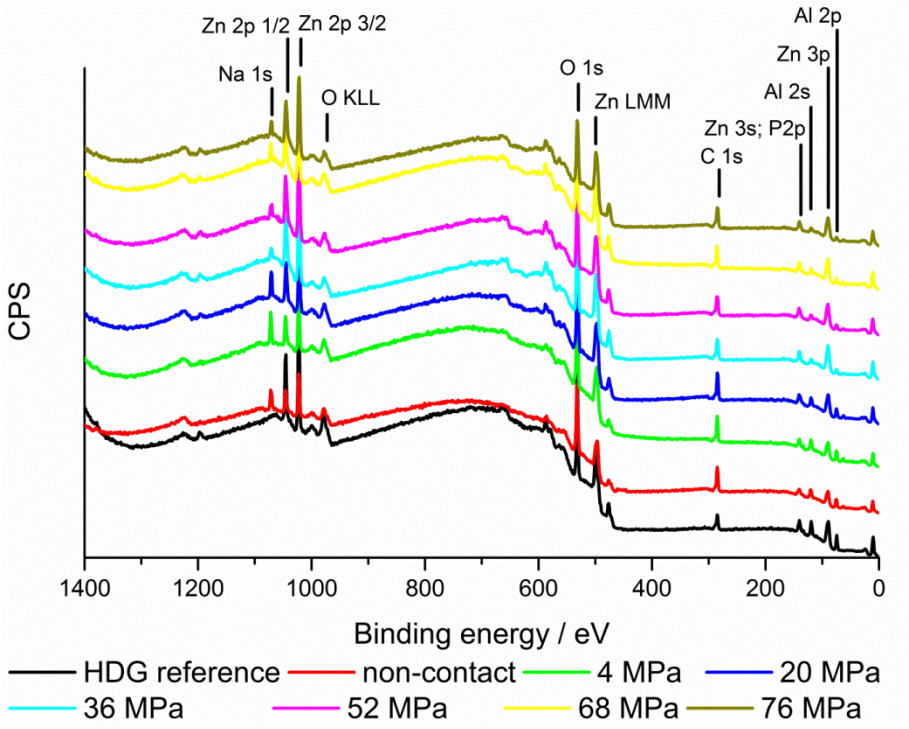

Figure 104. XPS-survey comparison of OBSS samples with different contact-pressures

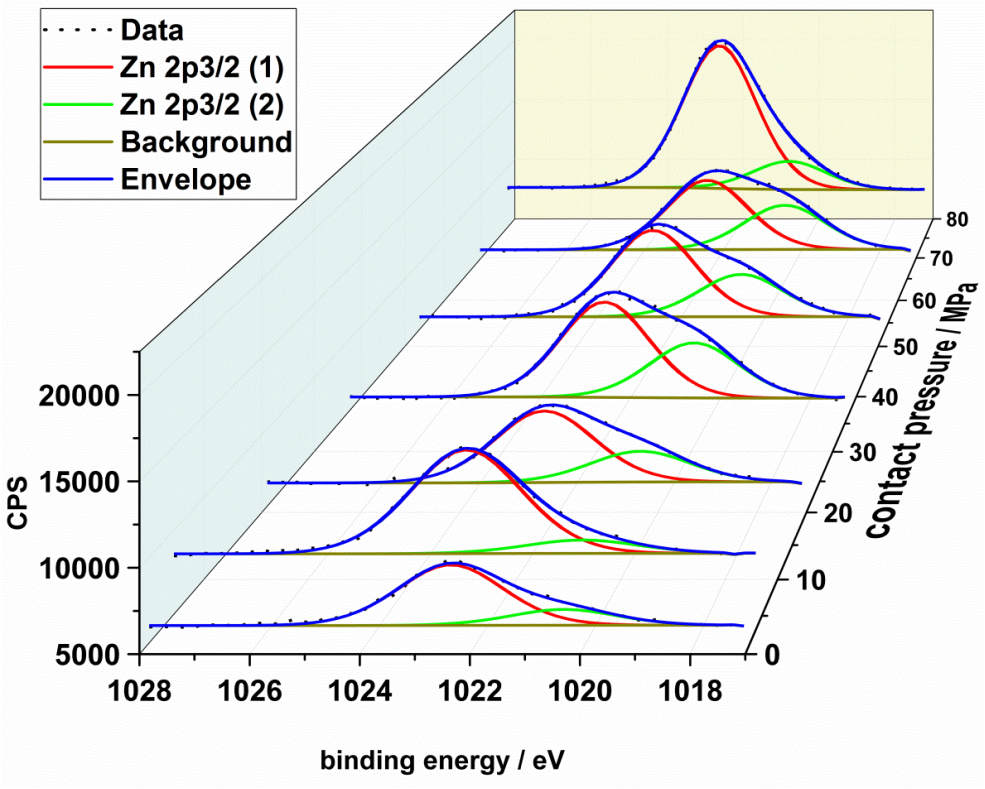

Figure 105. High-resolution XPS spectra of the *Zn 2p3/2* region of the OBSS additive system on HDG at various contact pressures

Table 6. Fit parameters of the high-resolution XPS spectra of the *Zn 2p3/2* region of the OBSS additive system on HDG at various contact pressures

Contact pressure (MPa)	Metallic zinc			Oxidic zinc		
	Position (eV)	FWHM	% Conc.	Position	FWHM	% Conc.
0	1020,3	2,3	20,8	1022,3	2,3	79,3
4	1020,3	2,4	11,5	1022,4	2,4	88,6
20	1020,4	2,4	30,1	1022,3	2,4	69,9
36	1020,3	2,3	36,6	1022,3	2,3	63,4
52	1020,3	2,3	32,9	1022,4	2,3	67,1
68	1020,2	2,4	38,9	1022,2	2,4	61,1
76	1020,6	2,3	16,5	1022,4	2,3	83,5

Figure 105 shows the high-resolution XPS spectra of the *zinc 2p 3/2* region of the OBSS additive system on HDG in correspondence to the contact pressure of the strip drawing test. The spectra give the best fit with two components where the peak with the lowest binding energy is assigned to metallic zinc (component 2) while the peak with the higher binding energy is assigned to oxidic zinc (component 1). The corresponding parameters of the fitting are listed in Table 6.

The data reveal a qualitative increase of metallic zinc with increasing contact pressure while the oxidic component decreases. Despite the possible runaway at the highest contact pressure, the results correspond with the decreasing coefficient of friction (Figure 97; p. 116) and are explainable with a smoothening of the surface and the abrasion of the oxide layer.

Figure 106 shows the high-resolution XPS spectra of the *aluminum 2p* region of the OBSS additive system on HDG in correspondence to the contact pressure of the strip-drawing test. The corresponding fit parameters are listed in Table 7. The spectra give the best fit with two components where the peak with the lowest binding energy is assigned to metallic aluminum (component 2) while the peak with the higher binding energy is assigned to oxidic aluminum (component 1).

The data reveal, except for the 76 MPa sample, an increase of the metallic and a decrease of the oxidic component. This corresponds, similar to the zinc components, to a smoothening of the surface and the abrasion of the oxide layer.

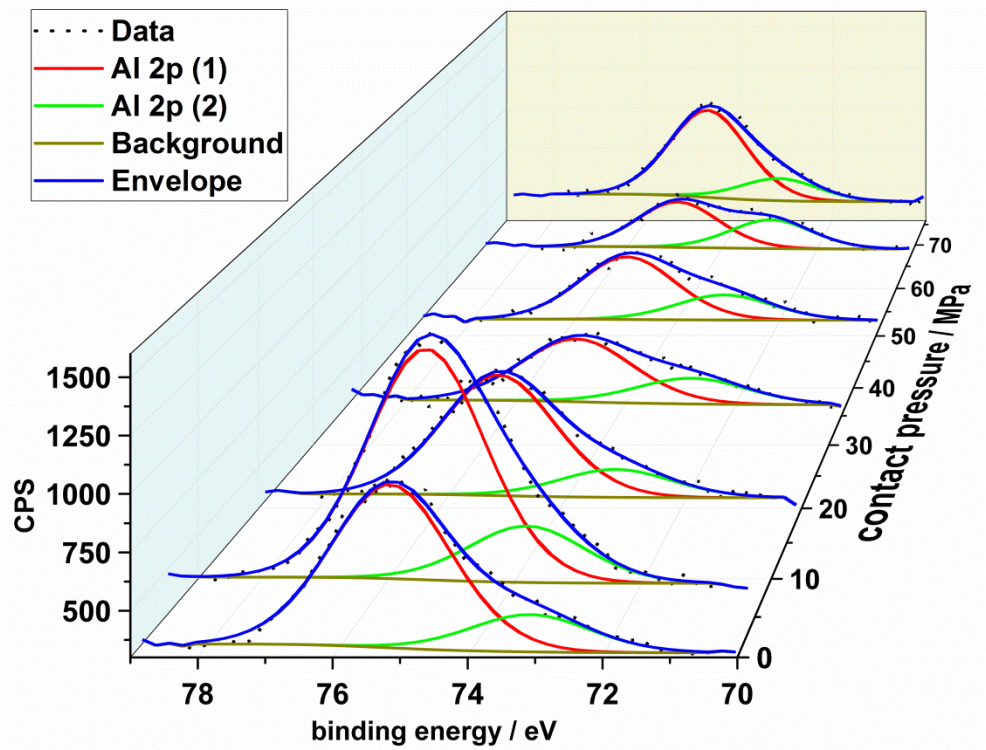

Figure 106. High-resolution XPS spectra of the *Al 2p* region of the OBSS additive system on HDG at various contact pressures

Table 7. Fit parameters of the high-resolution XPS spectra of the *Al 2p* region of the OBSS additive system on HDG at various contact pressures

Contact pressure (MPa)	Metallic aluminum			Oxidic aluminum		
	Position (eV)	FWHM	% Conc.	Position	FWHM	% Conc.
0	73,1	2,1	18,6	75,1	2,1	81,4
4	73,4	2,1	19,7	74,9	2,1	80,3
20	73,1	2,2	18,8	75,0	2,2	81,2
36	72,7	2,4	29,1	74,8	2,4	70,9
52	73,0	2,2	28,6	74,9	2,2	71,4
68	72,9	2,0	38,8	74,9	2,0	61,2
76	73,1	2,0	20,3	74,7	2,0	79,7

Figure 107 shows the high-resolution XPS spectra of the *carbon 1s* region of the OBSS additive system on HDG in correspondence to the contact pressure of the strip-drawing test. The corresponding fit parameters are listed in Table 8 (p. 127). The spectra give the best fit with four components where the hydrocarbon signal is referenced to 285.0 eV (component 2). Two oxygen bound carbon components are detected at higher binding energies, where the signal around 288 eV is assigned to a –C-OH, -C-O-C or –C=O component (component 1). The signal at the highest binding energy around 289 eV corresponds to metallic carbons or metallic hydrocarbons. The peak with the lowest binding energy ~283.4 eV can be assigned to graphitic (sp^2) carbon (component 3). This result contributes to the detection of sooty carbon by the means of imaging Raman spectroscopy on various tribologically stressed samples.

With increasing contact pressure, a decrease of hydrocarbons (component 1) and oxygen-bound carbon (component 1) can be observed. Otherwise, an increase of the amount of (hydro-) carbonates and graphitic carbon is detected with increasing contact pressure.

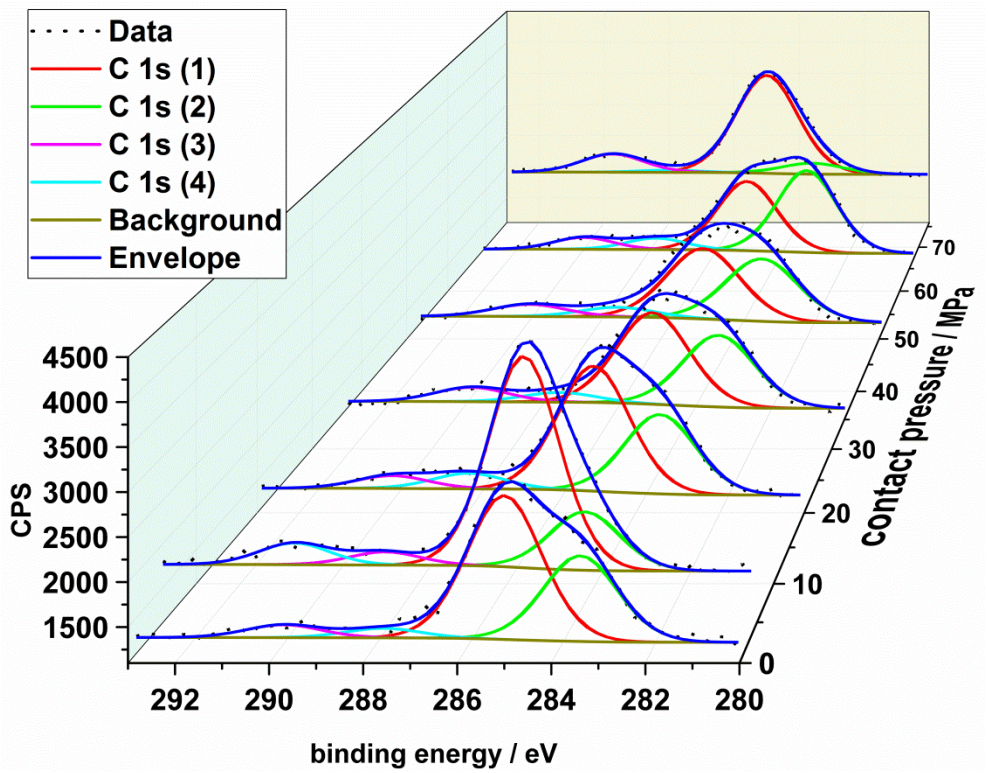

Figure 107. High-resolution XPS spectra of the *C 1s* region of the OBSS additive system on HDG at various contact pressures

Figure 108 shows the high-resolution XPS spectra of the *oxygen 1s* region of the OBSS additive system on HDG in correspondence to the contact pressure of the strip-drawing test. The corresponding fit parameters are listed in

Table 9 (p. 127). The spectra give the best fit with four components where the peak at the lowest binding energy at ~529.1 eV is assigned to metallic oxides. A peak corresponding to hydroxides of aluminum, sodium and zinc is found at ~530.4 eV. The largest peak at ~531.9 eV can be assigned to carbonates and hydro carbonates. The fourth and smallest peak at ~534.7 eV can be assigned to organic contaminations.

The data reveal an increase of the metallic oxide and metallic hydroxide oxygen components with increasing contact pressure while the components corresponding to (hydro-) carbonates and organic contaminations decrease.

Table 8. Fit parameters of the high-resolution XPS spectra of the *C 1s* region of the OBSS additive system on HDG at various contact pressures

Contact pressure (MPa)	graphitic carbon (sp^2)			hydrocarbons (sp^3)			C-O- or C=O			(hydro-) carbonates		
	Position (eV)	FWHM	Conc. %	Position (eV)	FWHM	Conc. %	Position (eV)	FWHM	% Conc.	Position (eV)	FWHM	% Conc.
0	283,4	1,9	34,0	285,0	1,9	57,1	288,0	1,8	4,3	289,7	1,9	5,1
4	283,7	1,8	19,2	285,0	1,8	69,4	288,0	2,0	6,7	290,0	1,8	7,1
20	283,4	2,0	34,1	285,0	2,0	53,8	287,4	2,2	5,1	289,8	2,0	5,5
36	283,3	2,2	38,3	285,0	2,2	48,9	287,4	2,4	6,3	289,7	2,2	7,6
52	283,4	2,4	40,4	285,0	2,4	45,5	287,7	2,1	6,5	289,8	2,4	7,9
68	283,2	2,1	47,0	285,0	2,1	39,7	288,0	2,2	1,7	289,9	2,1	6,8
76	283,6	2,2	8,4	285,0	2,2	75,8	288,0	1,8	4,3	289,7	2,2	14,1

Table 9. Fit parameters of the high-resolution XPS spectra of the *O 1s* region of the OBSS additive system on HDG at various contact pressures

Contact pressure (MPa)	metal oxides			hydroxides (Al, Na, Zn)			(hydro-) carbonates			organic contamination		
	Position (eV)	FWHM	Conc. %	Position (eV)	FWHM	Conc. %	Position (eV)	FWHM	% Conc.	Position (eV)	FWHM	% Conc.
0	529,1	2,4	3,1	530,2	2,4	24,8	531,9	2,4	70,0	535,3	2,4	2,1
4	529,4	2,3	2,2	530,6	2,3	26,3	531,9	2,3	68,1	535,8	2,3	3,5
20	529,4	2,5	7,8	530,3	2,5	26,6	531,9	2,5	63,5	534,8	2,5	2,1
36	529,1	2,5	6,7	529,9	2,5	24,3	531,7	2,5	69,1	533,6	2,5	0,0
52	529,1	2,5	7,7	530,3	2,5	39,1	532,0	2,5	52,6	534,1	2,5	0,7
68	529,1	2,2	17,7	530,5	2,2	41,4	532,1	2,2	38,6	533,7	2,2	2,3
76	528,8	2,2	2,9	530,7	2,2	35,6	532,0	2,2	59,0	535,5	2,2	2,5

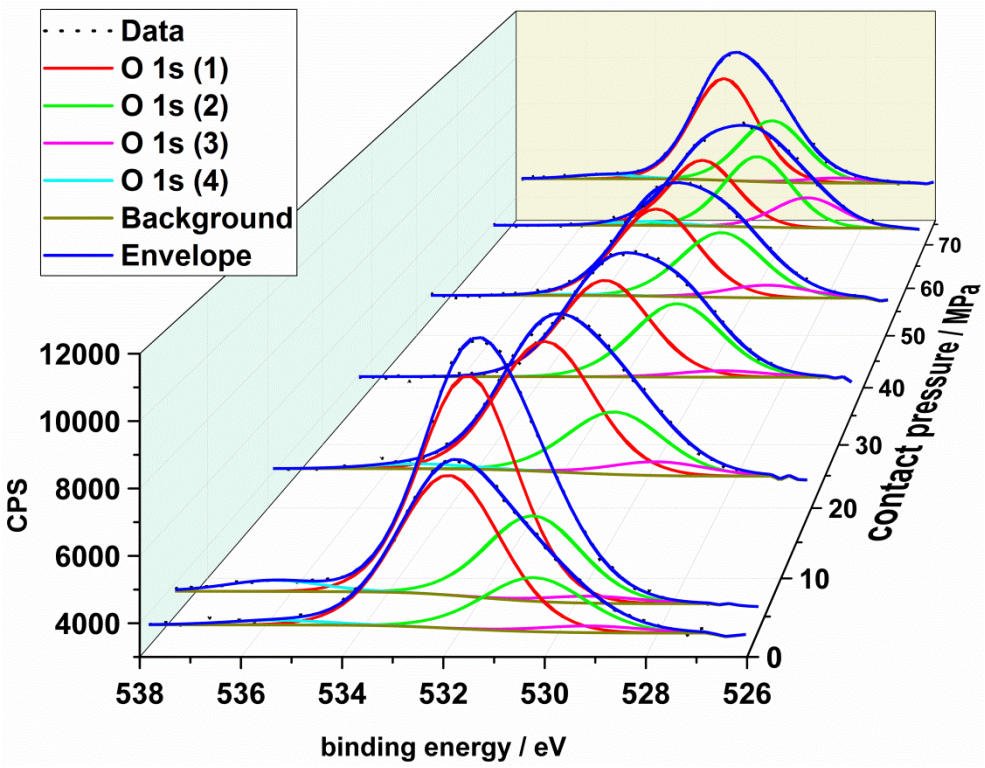

Figure 108. High-resolution XPS spectra of the *O 1s* region of the OBSS additive system on HDG at various contact pressures

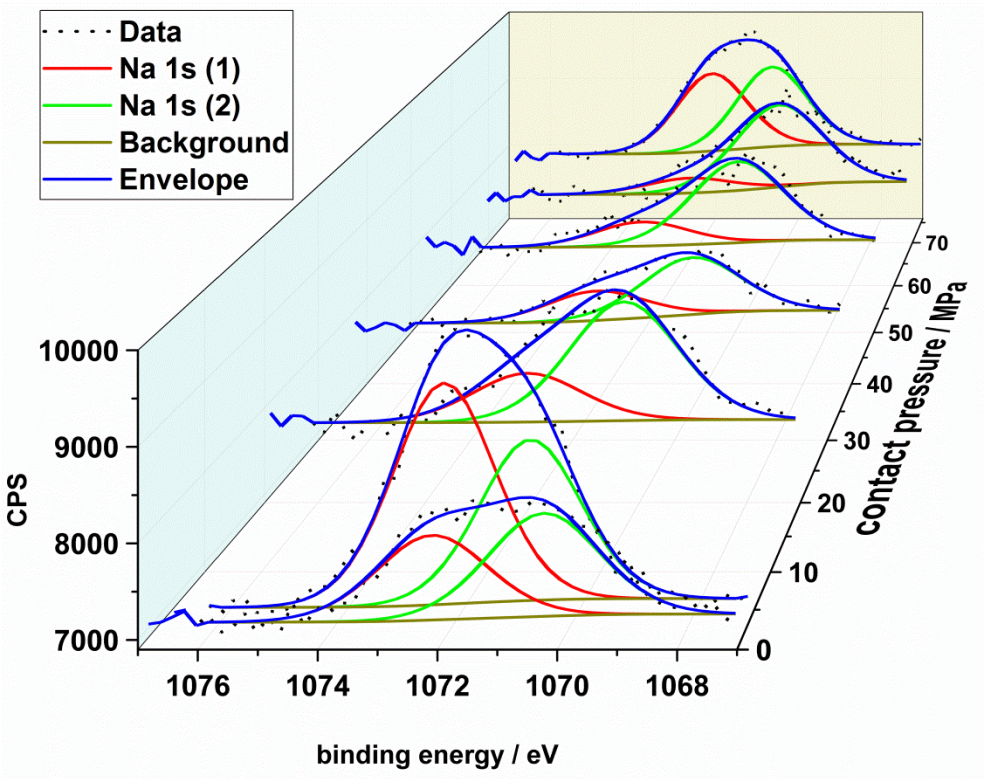

Figure 109. High-resolution XPS spectra of the *Na 1s* region of the OBSS additive system on HDG at various contact pressures

Figure 109 shows the high-resolution XPS spectra of the *sodium 1s* region of the OBSS additive system on HDG in correspondence to the contact pressure of the strip-drawing test. The corresponding fit parameters are listed in Table 10. The spectra give the best fit with two components where the peak at the lowest binding energy at ~1070.3 eV is assigned to sodium carbonate and the peak around 1072.1 eV correspond to sodium hydroxide and sodium hydrogen carbonate.

The data reveal an increase of amount of the sodium carbonate component with increasing contact pressure despite a possible runaway at the highest contact pressure. Diametrically the amount of the sodium hydroxide and/or sodium hydrogen carbonate decreases.

Table 10. Fit parameters of the high-resolution XPS spectra of the *Na 1s* region of the OBSS additive system on HDG at various contact pressures

Contact pressure (MPa)	Na_2CO_3			$NaOH$ / $NaHCO_3$		
	Position (eV)	FWHM	% Conc.	Position	FWHM	% Conc.
0	1070,2	2,2	54,9	1072,1	2,2	45,1
4	1070,8	2,0	42,1	1072,2	2,0	57,9
20	1070,3	2,4	70,9	1072,1	2,4	29,1
36	1070,0	2,3	66,0	1072,0	2,3	34,0
52	1070,0	2,4	77,1	1072,1	2,4	22,9
68	1070,0	2,4	84,6	1072,1	2,4	15,4
76	1070,6	2,0	50,7	1072,1	2,0	49,3

Because the analysis of the high-resolution XPS spectra in correspondence with the contact pressure of the strip-drawing test describes only the changes of proportions of element components, it is necessary to combine these results with the overall changes of element concentration. It is possible that the amount of an element component partially increases while the surface concentration of this element decreases.

The surface analysis of the OBSS samples via XPS, shown in Figure 110, reveals the changes of atomic concentrations in correspondence with the contact pressure of the strip-drawing test. It is obvious that the increase in the atomic concentration of carbon between the reference and the “non-contact” state at zero MPa results of adsorbed residues of the oil coating. The metallic oxide layer is covered with an adsorption layer as seen by the decrease of zinc, aluminum and oxygen. In contrast to the reference, sodium is detectable on all other samples. In combination with the high-resolution spectra, it is obvious to assume the presence of an adsorbed OBSS additive layer.

With increasing contact pressure, the element distribution reveals a decrease of aluminum and an increase of zinc with a change of the dominating element around 40 MPa contact pressure. This change corresponds to the previously described abrasion of the oxide layer

and smoothening of the surface. The amount of sodium slightly decreases with increasing contact pressure and indicates a reduction of the additive on the surface. The runaways at the highest contact pressure probably originate from the stopping process of the strip-drawing test. The sample with the highest contact pressure is also the sample where the tool stops and remains in contact with the surface. The time needed to remove the steel strip from the strip-drawing device is only a few minutes but this is probably enough to influence the susceptible surface composition.

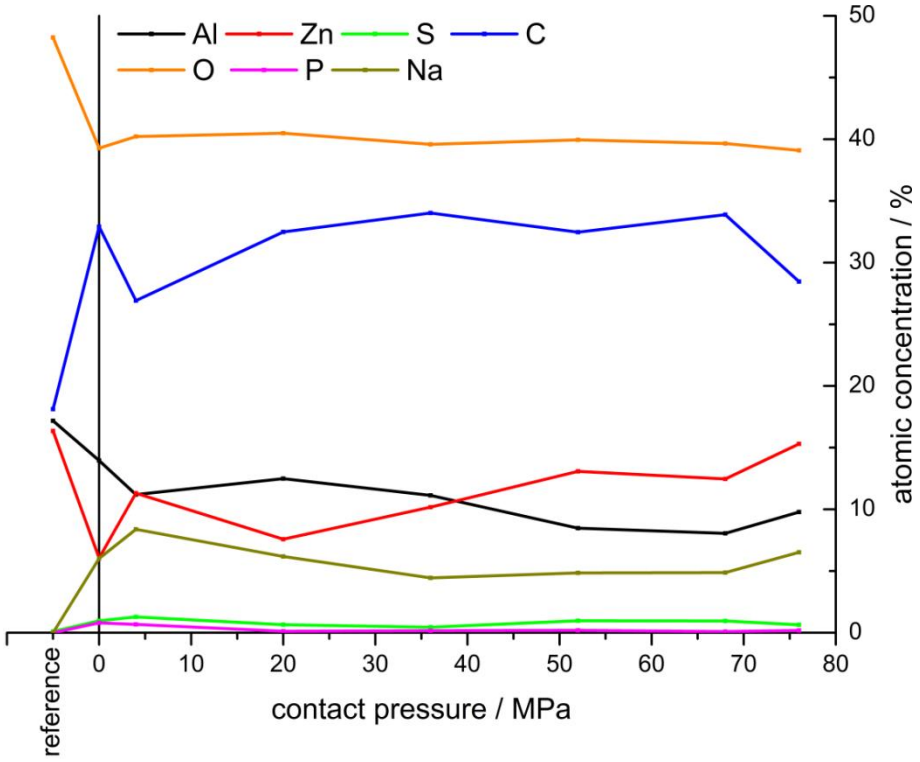

Figure 110. Atomic concentration trend of OBSS sample over increasing contact pressures

DTNPS

Figure 111 shows the surveys of the HDG reference and tribologically stressed samples of the DTNPS additive system. They include an area without any contact pressure (non-contact) and samples with increasing contact pressure (4 MPa, 20 MPa and 36 MPa). The reported contact pressures are the median values corresponding to cut steel sheets with a deviation of ±4 MPa. In contrast to the HDG reference data and to the OBSS samples, the unstressed and stressed samples of the DTNPS additive system reveal an additional signal of sulphur.

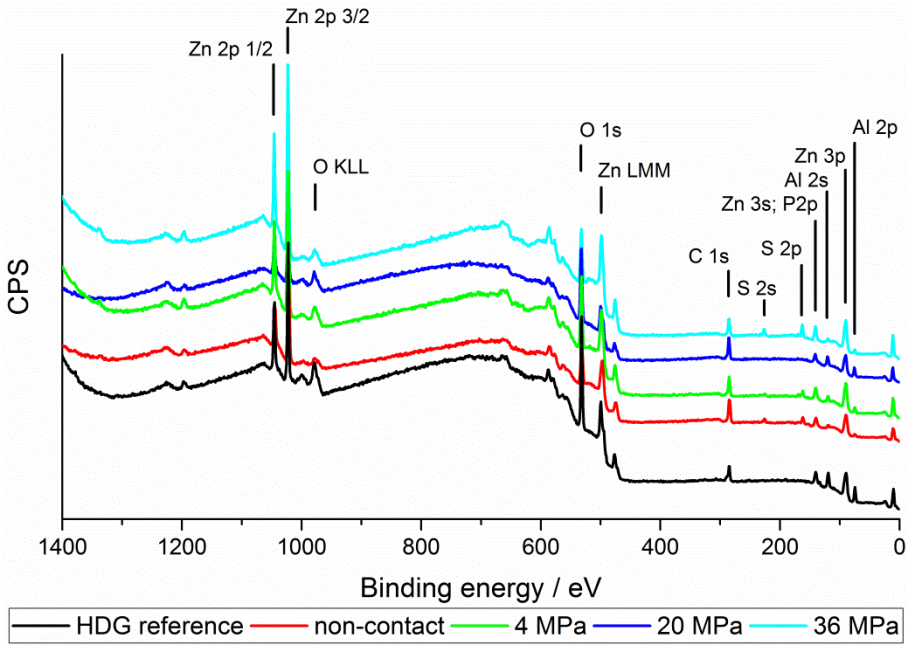

Figure 111. XPS-survey comparison of DTNPS samples with different contact-pressures

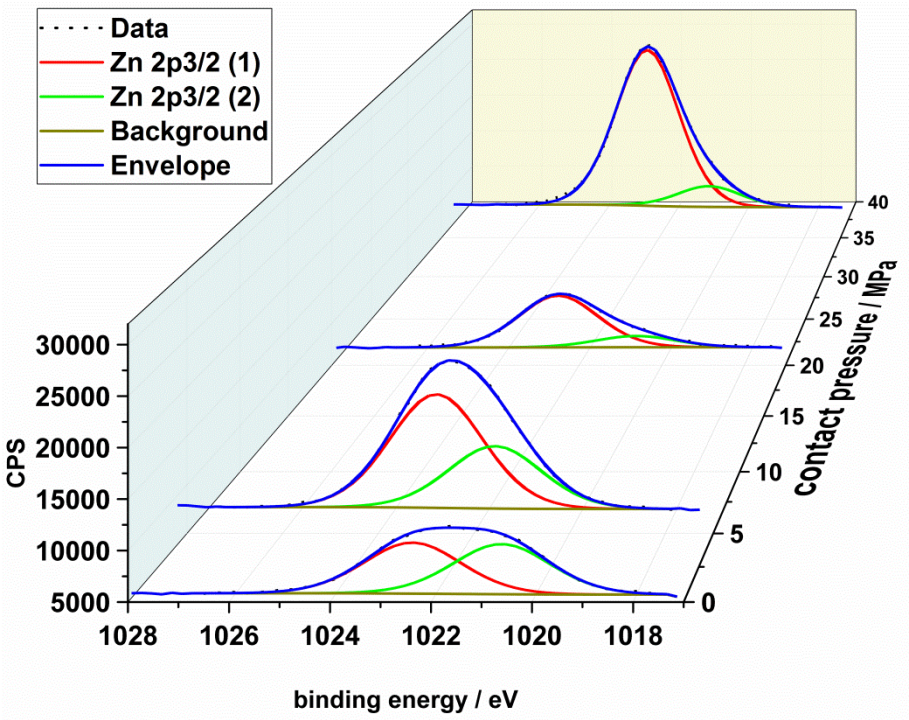

Figure 112. High-resolution XPS spectra of the *Zn 2p3/2* region of the DTNPS additive system on HDG at various contact pressures

The high-resolution XPS spectra of the *zinc 2p3/2* region of the DTNPS additive system on HDG in correspondence to the contact pressure of the strip drawing-test is presented in Figure 112 (p. 131). The corresponding fit parameters are listed in Table 11 (p. 132). The spectra gives the best fit with two components where the component with the lowest binding energy at ~1020.8 eV is assigned to metallic zinc and the component with the

highest binding energy at ~1022.5 eV can be assigned to oxidic zinc. Contrary to the OBSS additive system (Figure 105; p. 123), these results show a decrease of the metallic zinc component and an increase of the oxidic zinc component with rising contact pressure. This could mean, that the abrasive wear and therefore the removal of oxide layers is higher in the DTNPS system.

Table 11. Fit parameters of the high-resolution XPS spectra of the *Zn 2p3/2* region of the DTNPS additive system on HDG at various contact pressures

Contact pressure (MPa)	Metallic zinc			Oxidic zinc		
	Position (eV)	FWHM	% Conc.	Position (eV)	FWHM	% Conc.
0	1020,6	2,3	49,6	1022,4	2,3	50,4
4	1021,4	2,3	35,5	1022,6	2,3	64,5
20	1020,6	2,3	17,9	1022,5	2,3	82,1
36	1020,7	2,1	11,7	1022,5	2,1	88,3

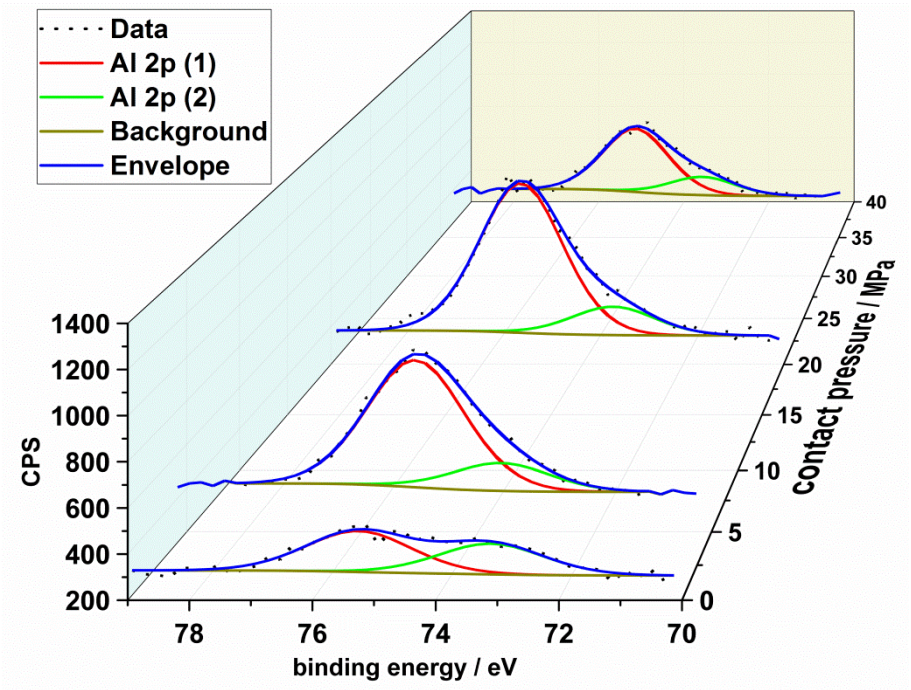

Figure 113. High-resolution XPS spectra of the *Al 2p* region of the DTNPS additive system on HDG at various contact pressures

A similar effect is observed in the high-resolution XPS spectra of the aluminum 2p region of the DTNPS additive system in HDG in correspondence to the contact pressure of the strip-drawing test (Figure 113; p. 132). These spectra also give the best fit with two components where the lower binding component at ~73.3 eV is assigned to metallic aluminum while the higher binding component at ~75,0 eV is assigned to oxidic aluminum. The corresponding fit parameters are listed in Table 12 (p. 133).

Table 12. Fit parameters of the high-resolution XPS spectra of the *Al 2p* region of the DTNPS additive system on HDG at various contact pressures

Contact pressure (MPa)	Metallic aluminum			Oxidic aluminum		
	Position (eV)	FWHM	% Conc.	Position (eV)	FWHM	% Conc.
0	73.1	2.0	42.8	75.3	2.0	57.2
4	73.5	1.9	17.9	74.9	1.9	82.1
20	73.4	2.0	16.0	75.2	2.0	84.0
36	73.2	1.8	22.4	74.7	1.8	77.6

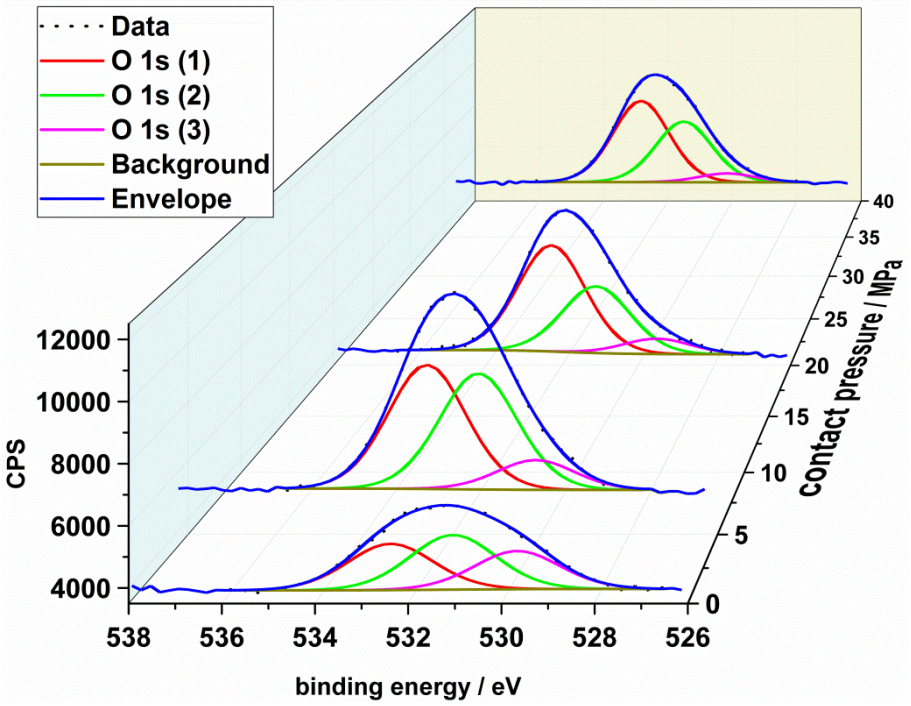

Figure 114. High-resolution XPS spectra of the *O 1s* region of the DTNPS additive system on HDG at various contact pressures

Figure 114 shows the XPS high-resolution spectra of the *oxygen 1s* region of the DTNPS additive system on HDG in correspondence to the contact pressure of the strip-drawing test. The corresponding fit parameters are listed in Table 13. The spectra give the best fit with three components where the lowest binding component at ~529.7 eV can be assigned to metal bound oxides. The component at ~531.1 eV is assigned to metal bound oxyhydroxides and the highest binding component at ~532.35 eV can be assigned to oxygen bound to carbon and sulphur. The diagram reveals a decrease of the oxide component with increasing contact pressure while the amount of the oxyhydroxide component remains nearly unchanged. The share of the carbon- and sulphur-bound oxygen rises with increased contact pressure.

Table 13. Fit parameters of the high-resolution XPS spectra of the *O 1s* region of the DTNPS additive system on HDG at various contact pressures

Contact pressure (MPa)	Metal oxides			Metal oxyhydroxides			-C-O-; -C=O; -S=O		
	Position (eV)	FWHM	% Conc.	Position	FWHM	% Conc.	Position	FWHM	% Conc.
0	529.7	2.2	27.5	531.0	2.2	39.3	532.4	2.2	33.3
4	530.0	2.1	11.0	531.2	2.1	43.0	532.4	2.1	46.0
20	529.5	2.1	8.2	531.1	2.1	35.5	532.3	2.1	56.4
36	529.7	2.0	5.9	531.0	2.0	40.3	532.3	2.0	53.8

The XPS high-resolution spectra of the *carbon 1s* region of the DTNPS additive system on HDG in correspondence with the contact pressure (Figure 115) gives the best fit with four components for all but one contact pressures. The spectra at the maximum contact pressure of 36 MPa gives the best fit with only two components. In all cases, the component with the lowest binding energy at ~283.5 eV can be assigned to a graphitic (sp^2) carbon species. Also in all cases, the component at 285.0 eV is assigned to hydrocarbon (sp^3). Small amounts of a C-O and/or C=O oxygen bound carbon species can be detected on the first three samples and correspond to the peak at ~287.3 eV. The highest binding component is also detected in only small amounts at ~289.4 eV and can be assigned to (hydro-) carbonates. The corresponding fit parameters are listed in Table 14 (p. 135).

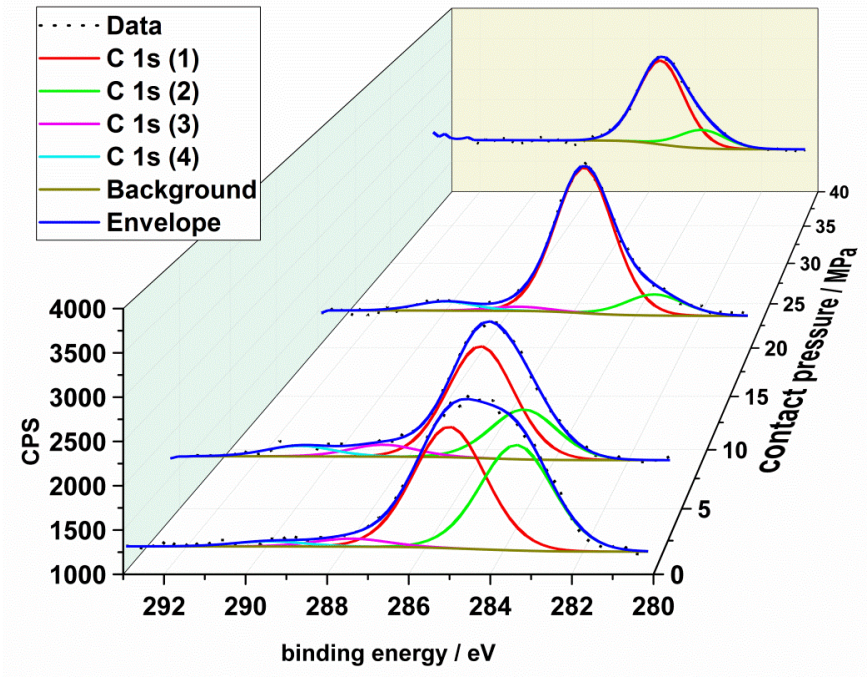

Figure 115. High-resolution XPS spectra of the *C 1s* region of the DTNPS additive system on HDG at various contact pressures

The trend shows a decrease of graphitic carbon while the amount of hydrocarbon's increases.

Table 14. Fit parameters of the high-resolution XPS spectra of the *C 1s* region of the DTNPS additive system on HDG at various contact pressures

Contact pressure (MPa)	graphitic carbon (sp^2)			hydrocarbons (sp^3)			C-O- or C=O			(hydro-) carbonates		
	Position (eV)	FWHM	Conc. %	Position (eV)	FWHM	Conc. %	Position (eV)	FWHM	% Conc.	Position (eV)	FWHM	% Conc.
0	283.4	2.1	43.9	285.0	2.1	50.6	287.4	2.1	3.3	289.4	2.1	2.1
4	283.9	2.0	27.1	285.0	2.0	60.7	287.5	2.0	6.5	289.6	2.0	5.8
20	282.9	2.1	11.7	285.0	2.1	80.8	287.0	2.1	2.3	289.2	2.1	5.1
36	283.6	1.9	17.9	285.0	1.9	82.1						

Table 15. Fit parameters of the high-resolution XPS spectra of the *S 2p* region of the DTNPS additive system on HDG at various contact pressures

Contact pressure (MPa)	Sulphide						Sulphate					
	S 2p			S 2p			S 2p			S 2p		
	Position (eV)	FWHM	Conc. %	Position (eV)	FWHM	Conc. %	Position (eV)	FWHM	% Conc.	Position (eV)	FWHM	% Conc.
0	161.2	2.5	45.2	162.3	2.5	44.2	168.0	2.5	5.3	169.1	2.5	5.2
4	161.4	2.5	38.2	162.6	2.5	37.4	168.1	2.5	12.4	169.3	2.5	12.1
20	162.1	2.5	29.1	163.3	2.5	28.5	168.5	2.5	21.4	169.7	2.5	21.0
36	161.9	2.2	44.6	163.0	2.2	43.7	168.3	2.2	5.9	169.5	2.2	5.8

The high-resolution XPS spectra of the *sulphur 2p* region gives the best fit with four component consisting of two pairs of spin-coupled 2p 3/2 and 2p 1/2 peaks (Figure 116). The corresponding fit parameters are listed in Table 15 (p. 135). The pair at binding energies around 162 eV can be assigned to a sulphide component while the pair at higher binding energies around 169 eV is assigned to a sulphate component.

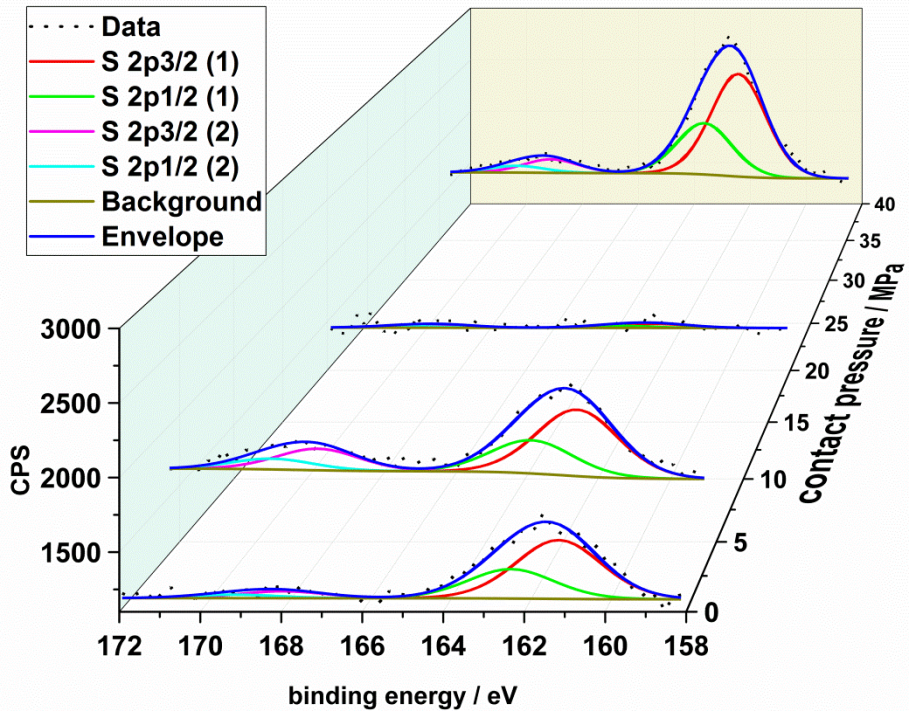

Figure 116. High-resolution XPS spectra of the *S 2p* region of the DTNPS additive system on HDG at various contact pressures

Similar to the methodology at OBSS, it is necessary to combine the gained high-resolution results with the overall changes of element concentration.

The trend of atomic concentration on DTNPS samples with increasing contact pressure is presented in Figure 117. Similar to the OBSS samples, the strong increase in the atomic concentration of carbon from the reference to the "non-contact" state, is obviously correlated to an adsorbed DTNPS layer. The metallic oxide surface is covered by an adsorption layer of DTNPS as seen by the decrease of aluminum and oxygen and the increase of carbon and sulphur. This oil based adsorption layer is comparable to results gained from the high-sensitive adsorption study presented in chapter 4.2.1.1 (p. 67).

With beginning contact pressure the strong amount of carbon drops sharply and remains then steady with increasing contact pressure at an amount around ~30 %. The carbonic part of the DTNPS adsorption layer starts to be abraded and the sulphurous part remains on the surface. The XPS depth profiles presented in Figure 118 supports this result.

Both figures reveal a decrease of sulphur with progressing contact pressure.

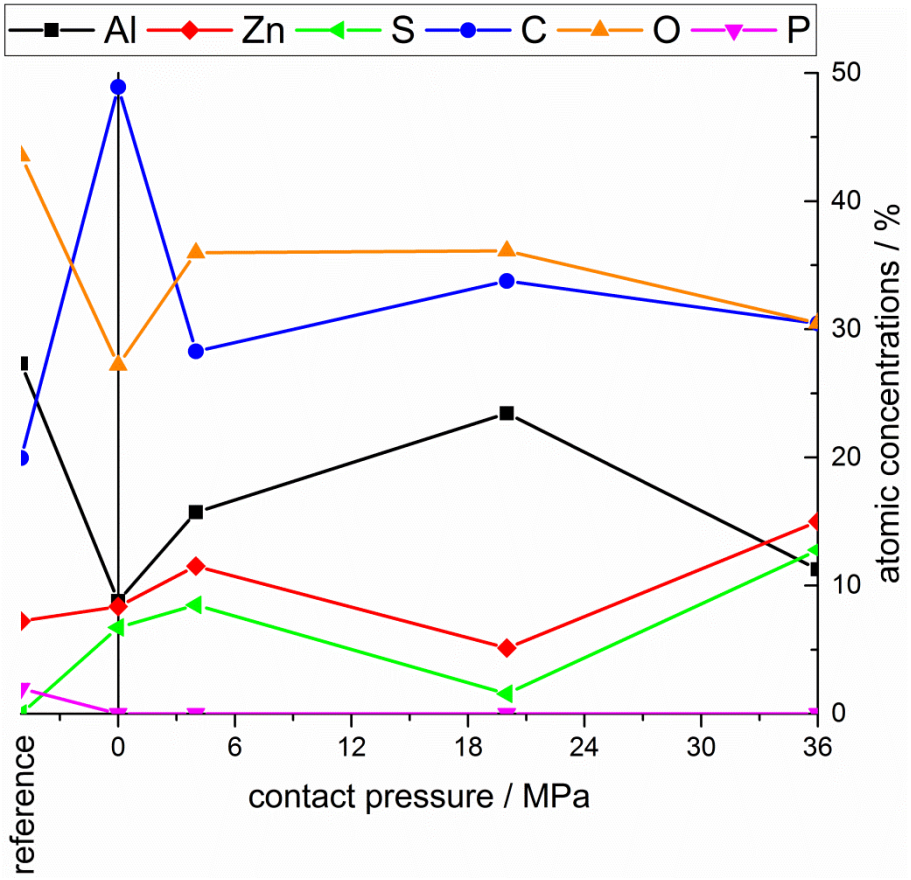

Figure 117. Atomic concentration trend of DTNPS sample over increasing contact pressures

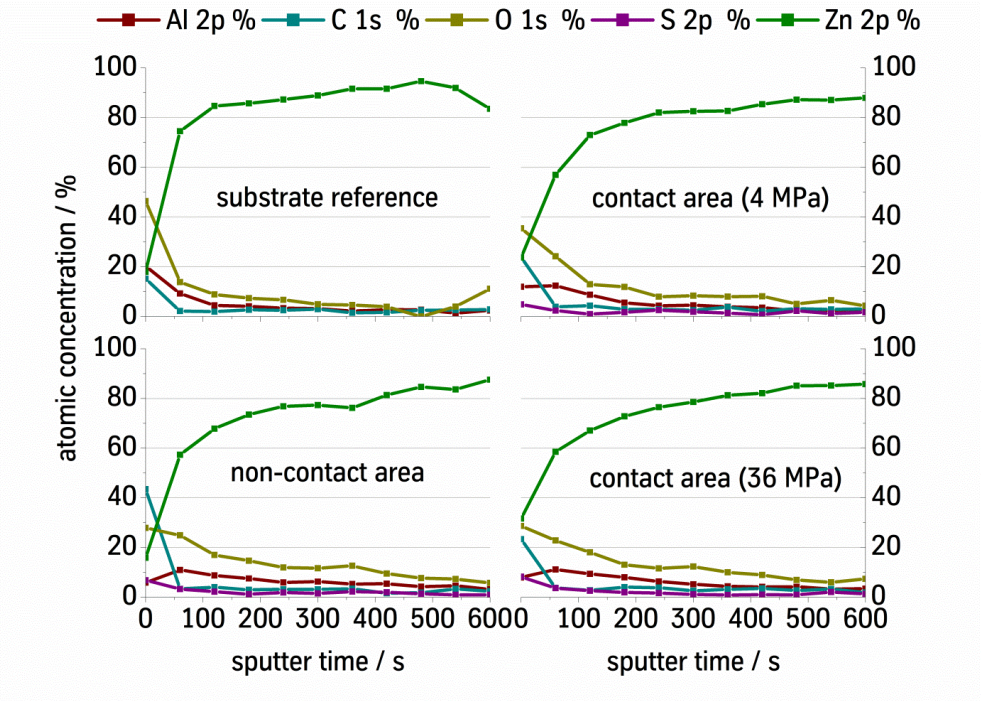

Figure 118. XPS depth profile of DTNPS samples at different contact pressures

The trend of decreasing sulphur amount with increasing contact pressure seems contradicted by the high-contact pressure sample with 36 MPa. The amount of sulphur on this sample even exceeds the “non-contact” stage. However, similar to the OBSS sample it has to be noted that the results are distorted by the characteristics of the last sample because the strip-drawing tool remains longer in contact with the surface than on all other samples.

Time of flight Secondary Ion Mass spectrometry (ToF-SIMS)

To supplement the XPS results and to reveal further details of the chemical surface composition, additional samples treated with high contact pressure were compared to untreated samples via ToF-SIMS analysis.

The severe surface disruption due to the high contact pressures complicates the ToF-SIMS measurements because the ionization probability of secondary ions strongly depends on the underlying matrix.

OBSS

The analysis reveals that the intensity of zinc-containing fragments like Zn, ZnOH, ZnH_2O, Zn_3O_3H, Zn_4O_4H as well as Al, AlH, AlH_2O, AlH_2O_2 and several organic fragments like C_xH_y and C_xH_yO is more intense on the tribologically treated sample.

The nature of this increased intensity could be an obvious higher surface coverage of these fragments. However, matrix-differences through higher oxygen ratios on the surface or removal of primary contaminations are also possible explanations.

Lower signal intensities of fragments like $C_xH_ySO_3Na_2$ are observed on the tribologically treated sample in comparison to the untreated sample.

No hints of any sodium-sulphonate reaction products with the zinc-layer are detectable on the tribologically treated sample.

DTNPS

The XPS measurements of tribologically treated DTNPS samples revealed a decrease of sulphides and an increase of sulphates. To back up these results and to disclose the metallic or organic nature of these sulphur variants, the surfaces were also analyzed via ToF-SIMS.

The tribologically treated sample reveals higher sulphur signals (S and S_2) than the untreated sample. Also, the intensity of sulphuroxid SO is increased on the loaded sample.

In addition, the signals of all detected zinc sulphides (ZnS, ZnS_2, ZnS_2H, ZnS_3) are more intensive on this sample. The same intensity-distribution is observed for the zinc sulphates (ZnSO and ZnSOH). All these sulphides and sulphates have strong congruency with the theoretically calculated isotopic distributions of the zinc isotopes with mass units of 64, 66, 67, 68 and 70.

Furthermore, additional fragments with higher masses than the nominally mass are found on the tribologically treated sample. Maybe, these fragments are organic sulphides like $C_xH_ySO_3$. The most likely identified molecules $C_8H_{17}SO_3$ and $C_9H_{19}SO_3$ have also strong congruency with the theoretically calculated isotopic distribution.

5.1.4.3 Discussion

As mentioned before, tribological measurement are heavily influenced by environmental and experimental parameters for example temperature, humidity, materials and concentrations.

Therefore, the chapter started with a screening of the tribological performance of promising additives as in-oil solution at different oil films by means of a strip drawing with increasing contact pressure. With oil coverage of 1.0 g/m^2, the screening was dominated by the poor anti-wear performance. Stick-slip effects occurred with all additives at contact pressures of 10 MPa at its best. Only zinc sulphide and Irgalube 349 performed better than the pure base oil at this oil coverage while Irgalube TPPT had a slightly higher COF. The three sulphur based additive DPDS, DTNPS and elemental sulphur showed the worst performance at this oil coverage and at the increased oil coverage of 1.5 g/m^2. These three additives also dominated the performance of an additive mixture (DPDS, DTNPS, Irgalube TPPT, Irgalube 349, elemental sulphur, zinc sulphide and zinc sulphate; 5 w.-% each) at oil coverage of 1.5 g/m^2 witch resolved in a high COF and the occurrence of stick-slip effects below 10 MPa. The best friction and an increased anti-wear performance was obtained from fully developed pre-lube PL 3802-39S. The additive zinc sulphate presented an even better anti-wear performance with the occurrence of stick-slip effects as late as 17 MPa.

While Forbes [139] described DPDS as the worst sulphur additive in a range of mono- and disulphides on a four-ball machine with EN 31 steel balls, this work identified DPDS as the best organo-sulphur additive with a performance comparable to elemental sulphur. The positive effect of sulphides, described by *Bowden and Taylor* [140], is not visible under the studied conditions on HDG because the COF is higher than the pure base oil.

A successional test series with additional sulphur additives at oil films of 1.5 g/m² was performed due to the recognized importance of sulphur additives. A polymeric oleic acid, a sulphured polymeric oleic acid, a greased polysulphide and a sulphured fatty ester achieved only the performance of the pure base oil or worse. The additive 1-Octadecanthiole reached a COF similar to the pure base oil and nearly doubled the maximum contact pressure. A concentration variation of the sulphur-free additive Irgalube 349 showed that a concentration of 1 w.-% is not enough to improve the tribological performance in comparison to the pure base oil. A reduced COF could be achieved with 5 w.-% of this additive while an additional increase up to 10 w.-% didn`t change the COF but improved the anti-wear behavior slightly. Also notable is the mixture of DTNPS and OBSS, which resulted in a COF comparable to the pure base-oil, but a delay of stick-slip effects late as 15 MPa. The only additive that reached the maximum contact pressure of 20 MPa was OBSS. It also had the lowest COF together with the fully developed pre-lube PL 3802-39S.

This overwhelming performance directed to an additional test-series with the maximum contact pressure increased up to 80 MPa. As result of this raise of contact pressure, the increasing-rate also quadruples and therefore the quantitative results of this test series varied from the previous ones. However, DTNPS still performed worse than the pure base oil, which indicated that the qualitative categorization of the additives remained comparable. The mixture of DTNPS and OBSS also had a COF higher than the pure base oil. The COF for 1-Octadecanthiole remained on the same level than the pure base oil but the anti-wear performance was only slightly better compared to the doubled maximum contact pressure in the previous test series. The only additives with a better COF than the pure base oil were PL 3802-39S, zinc sulphate and OBSS. While the pre-lube fell short with anti-wear performance, zinc sulphate nearly doubled the maximum contact pressure before the occurrence of stick-slip effects. OBSS not only had the lowest COF, it also progressed up to the highest contact pressure of 80 MPa without the occurrence of stick-slip effects.

Thereafter, the best (OBSS) and the worst (DTNPS) additive were selected for detailed surface analysis. Imaging Raman spectroscopy revealed localized spots of sooty carbon after tribological treatment on samples with the pure base oil, the OBSS additive system and the DTNPS additive system. As described before (p. 122) it is likely, that the detected layers were formed from soot particles that are already present in the oil, or that the oil partly decomposed and generated soot particles. No tribochemical reaction products could be detected by the means of imaging Raman spectroscopy.

Dabo et al. [141] studied amorphous and crystalline overbased calcium sulphonates in a lithium complex grease on AISI 52100 steel using a SRV friction and wear tester and characterized the tribochemical layers by means of FTIR, SEM and XPS. They indicated the importance of carbonates for the tribological behavior of this tribosystem.

The detailed, contact-pressure resolved XPS analysis in this work revealed for OBSS on HDG a decrease of metallic oxide and an increase of sodium carbonate with increasing contact pressure. No sulphur components were detectable by the means of XPS analysis. The ToF-SIMS analysis on the other side revealed a decrease of organic-sulphonate with increasing contact pressure but couldn`t deliver any details of the carbonate layer.

The similar analysis for DTNPS showed a change from sulphides to sulphates in combination with a decrease of metallic zinc and aluminum on the surface. The ToF-SIMS analysis confirmed the presence of both components on the surface. In addition, with this method it was possible to identify both components as zinc-bound.

5.1.5 Multi frottement strip-drawing tests

This chapter describes the tribological performance and surface analytical results of the multi frottement strip-drawing test (chapter 3.4.2.2; p. 32). The sample preparation is reported in chapter 3.3.2.3 (p. 29). This test was performed to study the reaction of selected additives under challenging tribological conditions and to produce thicker reaction layers. The selected additives were again the sulphur additive DTNPS, the phosphorus-sulphur additive Irgalube TPPT compared with the base oil and a fully developed pre-lube PL 3802-39S. These layers were characterized by means of ToF-SIMS surface analysis (chapter 3.4.6; p. 35).

5.1.5.1 Tribological performance

The tribological performance is characterized by friction force analysis (Figure 119; left). The coefficient of friction (COF) of each run is determined halfway of the drawing distance over a range of 20 mm. This analysis is performed five times for each variant and the results are averaged (Figure 119: right).

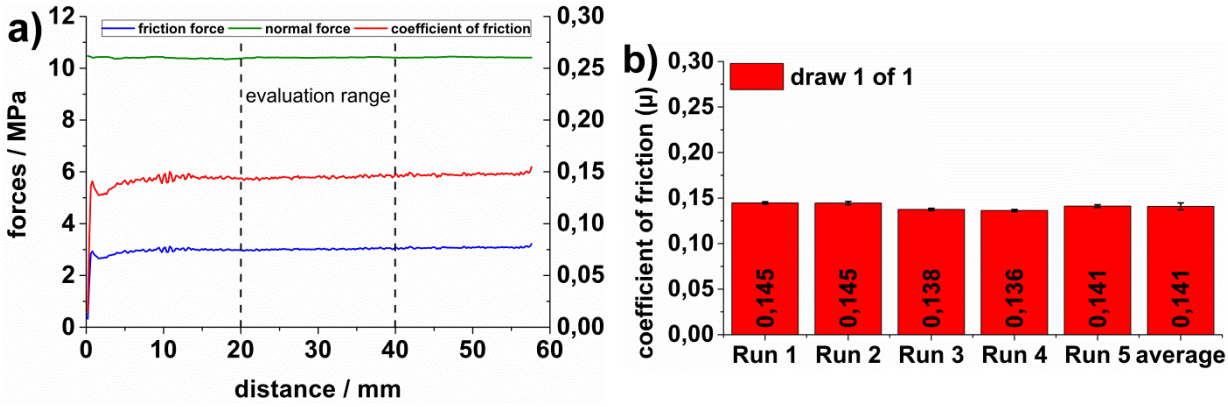

Figure 119. Exemplary friction force analysis of Run 1 (a) and COF report (b) of a one draw multi-frottement strip-drawing test with 2 w.-% DTNPS as additive at 10 MPa

Figure 119 presents an exemplary friction force analysis (a) of a one-draw multi-frottement strip-drawing test with 2 w.-% DTNPS as additive in naphthenic base oil with a contact pressure of 10 MPa. The gradients reveal a short running-in period of ~5 mm followed by stable forces over the complete drawing distance. It is also notable that the complete measurement is performed without the appearance of stick-slip effects. These stable charts result in an averaged COF with very low standard deviation (b).

The comparison of the averaged coefficient`s of friction after one-draw at a contact pressure of 10 MPa for the selected additives is reported in Figure 120. The results reveal, that the fully developed pre-lube PL 3802-39S has the lowest COF with 0.106 while the pure base oil

as reference reaches a COF of 0.130. The adding of 2 w.-% of DTNPS as additives increases this value slightly up to 0.141 and the adding of 2 w.-% of Irgalube TPPT leads to a reduction down to 0.125. Therefore, both additives have only minimal influence on the friction performance under these mild conditions.

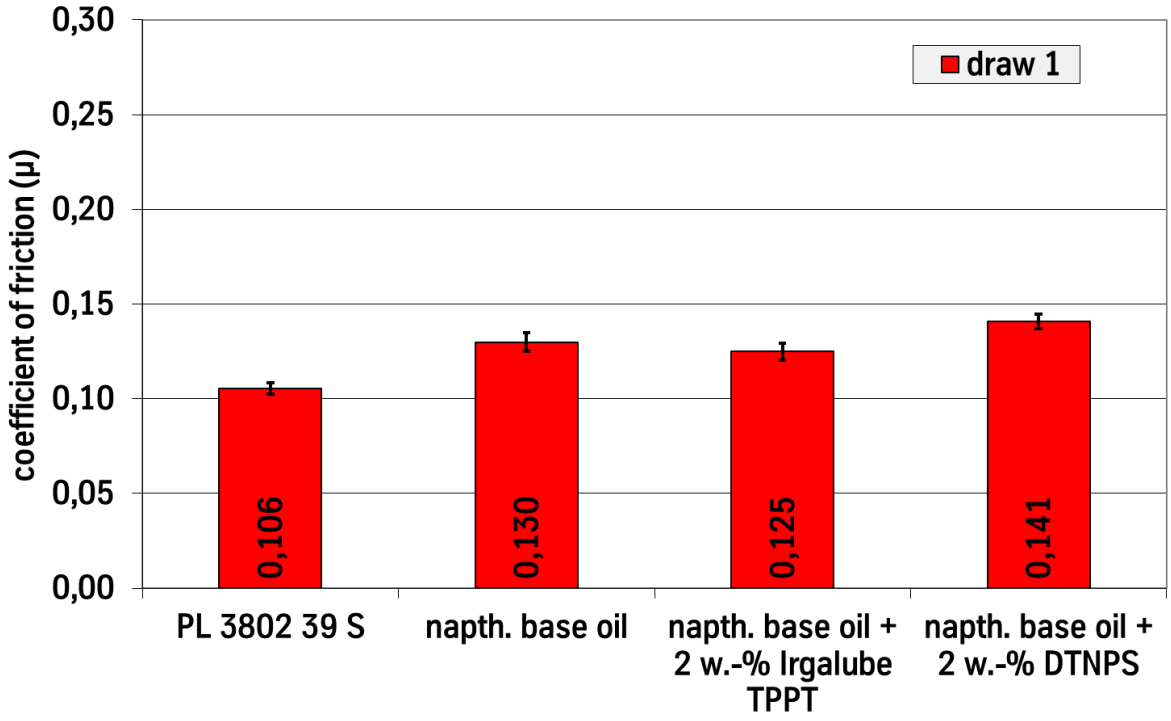

Figure 120. Comparison of COF after one draw at 10 MPa

While the standard deviation of a one draw test is very low (Figure 119), it increases strongly with repeated draws (Figure 121). The exemplary friction force analysis of a selected run with 2 w.-% DTNPS at a contact pressure of 10 MPa reveals disturbed gradients at the end of draw two and during the complete draw three. This disturbance means the appearance of stick-slip effects. The averaged COF of the first of three draws is with 0.136 on the same level as the comparable draw with 0.141 in the previous test (Figure 119). The COF levels of each run show the same qualitative progression rise for each draw. In addition, the quantitative values are comparable and the averaged COF step from 0.136 for the first draw, over 0.170 for the second draw up to 0.207 for the third draw. As mentioned before, the standard deviation is heavily increased for draw two and three.

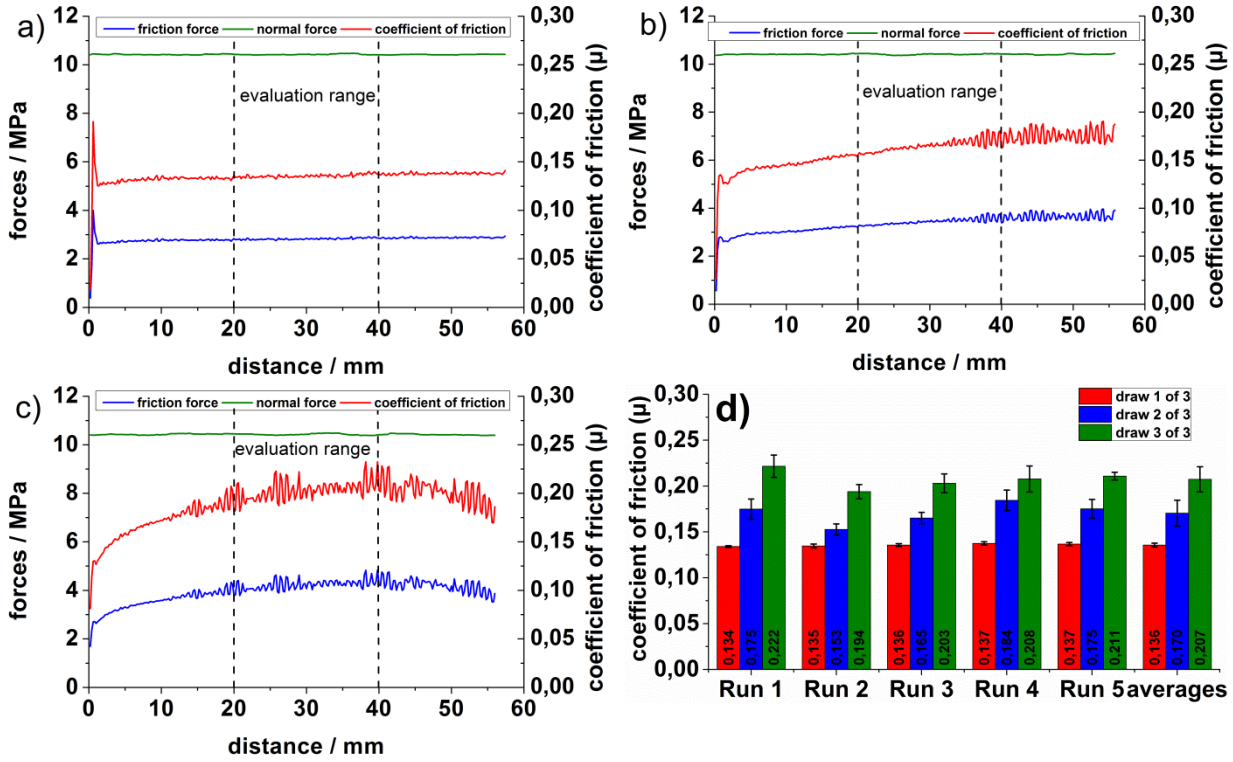

Figure 121. Exemplary friction force analysis of Run 3 (a; draw 1; b; draw 2; c; draw 3) and COF report (d) of a three draw multi-frottement strip-drawing test with 2 w.-% DTNPS as additive at ten MPa

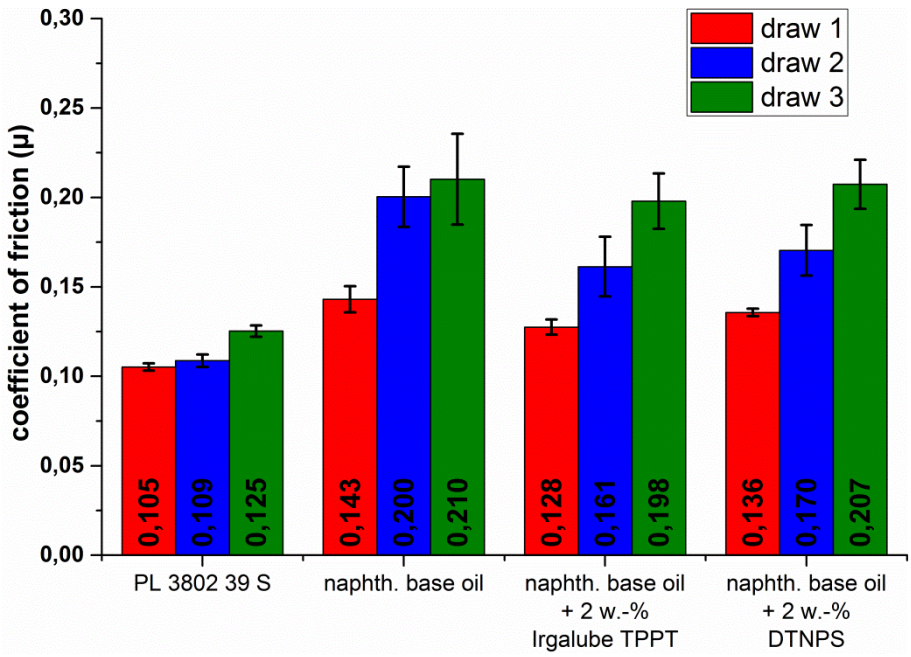

Figure 122. Comparison of COF after three draws at 10 MPa

Figure 122 shows the averaged COF comparison of the selected additive systems after three draws at ten MPa. As expected, the averaged COF of the first draw of all additive systems is comparable to the previous reported test (Figure 120). The best results are again obtained by the fully developed pre-lube PL 3802-39S. It is notable that the standard deviation is very

low for each draw of this additive system. The COF increases only slightly from 0.105 to 0.109 when progressing from the first to the second draw. The increase of COF for the third draw is greater, with a final value of 0.125. In comparison, the COF increase of each draw is higher and the standard deviation is bigger for the DTNPS additive system as presented in Figure 121. The same effect is visible for the pure base oil and the Irgalube TPPT additive system therefore no further differentiation is possible. Only the heavily increased COF for the second step of the pure base oil stands out.

Due to the strong stick-slip effects for the pure base oil and the DTNPS and Irgalube TPPT additive system, the contact pressure for the five draw test has to be reduced from 10 MPa down to 5 MPa. Only the pre-lube system was again measured with a contact pressure of 10 MPa.

Figure 123 shows the expected reduction of stick-slip effects of a five draw multi frottement strip-drawing test with 2 w.-% DTNPS as additive with reduced contact pressure of 5 MPa. The quantitative COF values of this measurement cannot be compared to the previous series with 10 MPa, but the qualitative trends remain comparable. Obvious is the absence of stick-slip effects and therefore smaller standard deviations for each draw. The overall trend is the increase of COF at each draw. However, the increase is much smaller than in the previous test due to the reduced contact pressure. The COF increases from 0.137 in the first draw, up to 0.157 in the fifths draw.

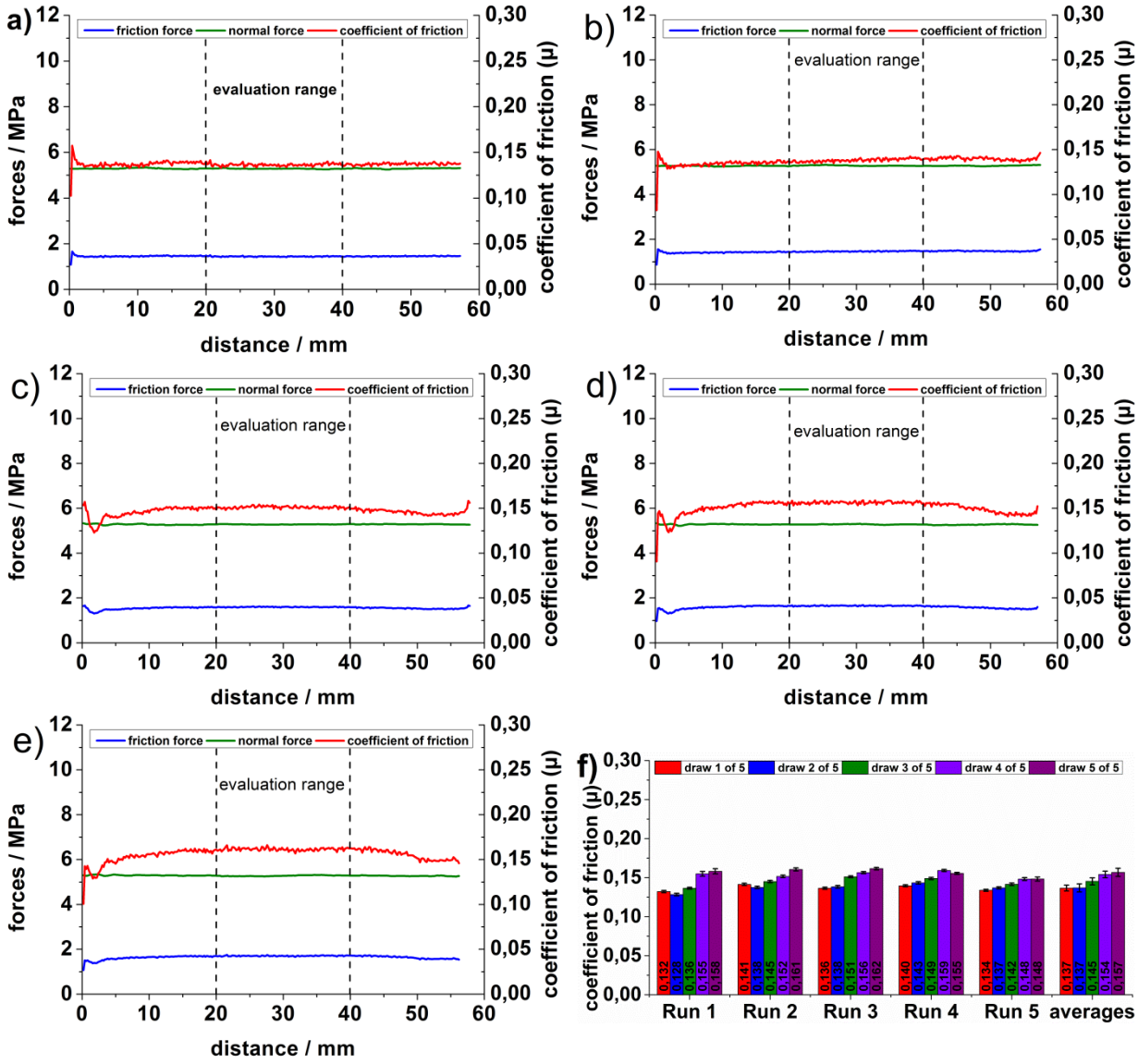

Figure 123. Exemplary friction force analysis of Run 3 (a: draw 1; b: draw 2; c: draw 3; d: draw 4; e: draw 5) and COF report (f) of a five-draw multi-frottement strip-drawing test with 2 w.-% DTNPS as additive at 5 MPa

The overall comparison between the selected additive systems for the five-draw multi frottement strip drawing test is split due to the reduced contact pressure for the pure base oil and the DTNPS and Irgalube TPPT additive systems. Figure 124 shows the averaged COF for the test at 10 MPa on the left side and for the other systems at 5 MPa on the right side. It reveals that the fully developed pre-lube system is nearly on the same COF level as the other systems despite the doubled contact pressure. The COF increases from 0.106 for the first draw, up to 0.204 for the fifths draw. Notable is the raising of standard deviation with each draw due to increased wear effects. The pure base oil as reference presents a steady increase of the COF for each draw with medium standard deviations. It raises from 0.131 for the first draw, up to 0.181 for the fifths draw. The addition of DTNPS or Irgalube TPPT both reduces the increase rate and the maximum COF after the fifths draw. While the COF of the

first draw is on the same level as the pure base oil (Irgalube TPPT: 0.127; DTNPS: 0.137), the COF of the fifths draw only raises up to 0.155 for Irgalube TPPT and to 0.151 for DTNPS in the fifths draw.

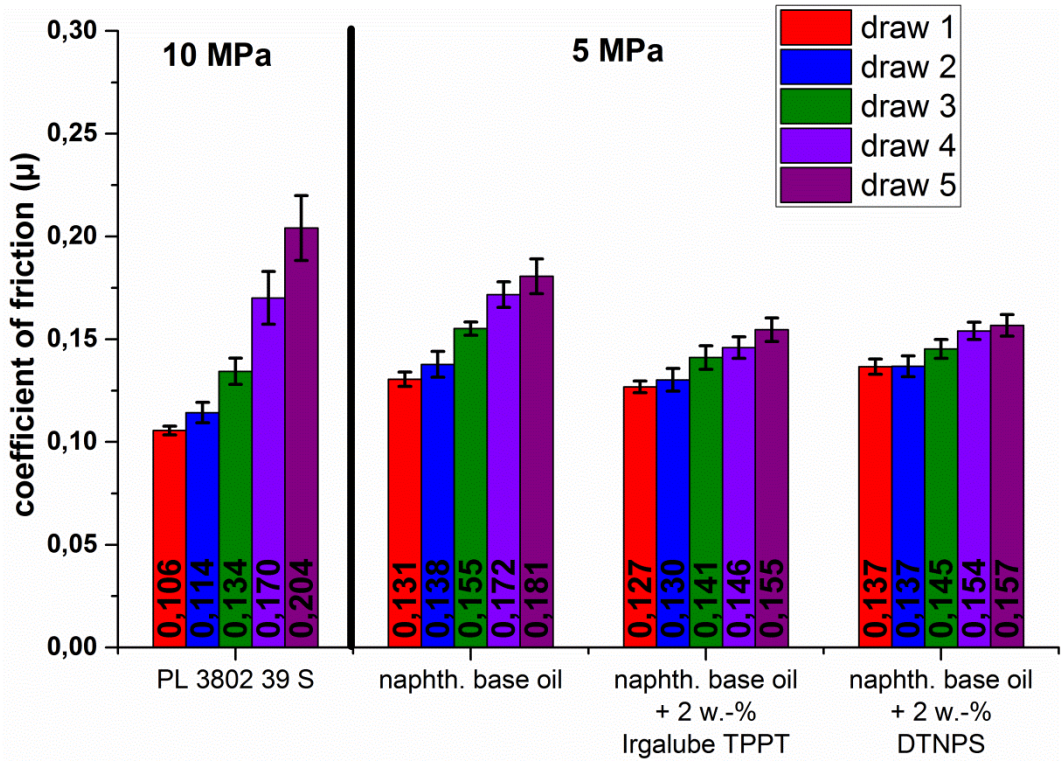

Figure 124. Comparison of COF after three draws at 10 MPa and 5 MPa

In summary, the fully developed pre-lube PL 3802-39S shows the best performance in all test series. Up to three draws, it diminishes the raise of the COF with repeated draws and prevents wear effects. In the five-draw test, the COF levels are nearly on the same level as the other tested system despite the doubled contact pressure. The addition of Irgalube TPPT to naphthenic base oil decreases the COF slightly for one draw while the addition of DTNPS increases it slightly. The three-draw test allows no differentiation between these three systems because of strong wear effects displayed by stick-slip effects. An influence of the additive is only visible at the five-draw test. The COF of both additive systems (Irgalube TPPT: 0.155; DTNPS: 0.157) is significantly reduced at the fifths draw in comparison to the pure base oil (0.181). Both additive systems are nearly on the same level with slightly lower COF for the Irgalube TPPT additive system.

5.1.5.2 Surface analysis

The analysis of chemical composition of the surface was performed by means of ToF-SIMS (chapter: 3.4.6; p. 35). Therefore, samples with the highest amount of repeated draws (5) were compared with samples without tribological treatment.

The comparison of samples with and without tribological treatment of pure naphthenic base oil reveal, that higher signals of zinc, zinc hydride, zinc hydroxide and zinc oxide are detectable on the stressed surface. The operator interprets this increase in signal intensity as effects of the matrix change due to the tribological treatment. The sample without tribological treatment reveals higher intensities of aluminum, aluminum hydride, calcium, iron, iron hydride, phosphate and sulphate. Both effects could also be explained by abrasive wear effects, in which the outermost layer of aluminum hydroxide and contaminations are rubbed of and zinc-rich layers are exposed. No reaction products of the base oil with the HDG surface are detectable.

The analyses of samples of the fully developed pre-lube PL 3802-39S show similar results as the analysis of the base oil. On the stressed sample higher intensities of zinc, zinc hydride, zinc oxide and zinc hydroxide are detectable. The operator interprets this increase in signal intensity also as effects of the matrix change due to the tribological treatment. The comparison between stressed and unstressed samples shows a stressed region without reaction products.

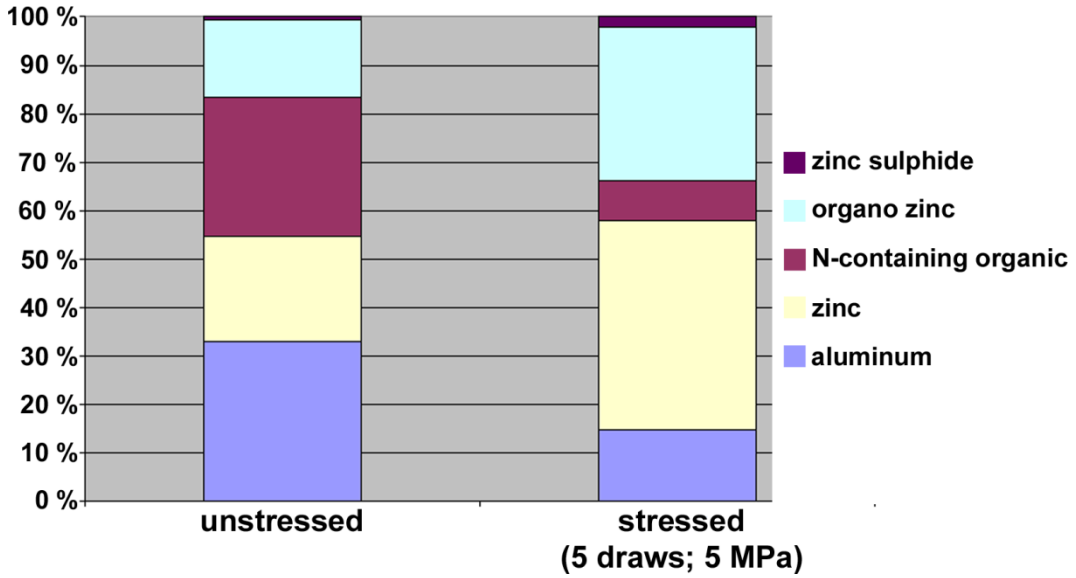

Figure 125. Intensity variations of essential fragment categories of Irgalube TPPT in naphthenic base oil before and after multi-frottement test with five draws at 5 MPa

The ToF-SIMS surface analysis of samples treated with Irgalube TPPT in naphthenic base oil shows similar to the two previous results higher signal intensities of aluminum, aluminum oxide, calcium, sulphur, sulphur oxide and N-containing organics on the unstressed sample. Next to increased signal intensities of zinc, zinc oxide and zinc hydroxide the tribological treated sample also reveals increased signals of possible reaction products like zinc sulphide and organo-zinc components. The intensity variations of essential

fragment categories are visualized in Figure 125. The corresponding fragment signals of each category are listed in Table 16.

Table 16. Fragment signals of essential fragment categories of Irgalube TPPT

zinc, zinc hydride	$Zn^{\oplus}$, $Zn_2^{\oplus}$, $ZnH^{\oplus}$, $ZnH^{\ominus}$
zinc oxide	$ZnO^{\oplus}$, $Zn_2O_2^{\oplus}$, $Zn_3O_3^{\oplus}$; $Zn_4O_4^{\oplus}$; $Zn_5O_5^{\oplus}$, $ZnOH^{\ominus}$, $ZnO_2H^{\ominus}$
zinc hydroxide	$ZnOH^{\oplus}$, $Zn_2O_2H^{\oplus}$, $Zn_3O_3H^{\oplus}$, $Zn_4O_4H^{\oplus}$, $Zn_5O_5H^{\oplus}$, $ZnOH^{\ominus}$, $ZnO_2H^{\ominus}$
zinc sulphide	$ZnS^{\ominus}$
organo zinc	$CH_2Zn^{\oplus}$, $CH_3Zn^{\oplus}$
sulphur, sulphur oxide & hydroxide	$S^{\oplus}$, $S^{\ominus}$, $SH^{\ominus}$, $SO^{\ominus}$, $SO_2^{\ominus}$, $SOH^{\ominus}$
aluminum, aluminum hydroxide	$Al^{\oplus}$, $AlH^{\oplus}$, $AlO_2^{\ominus}$, $AlO_2H^{\ominus}$
N-containing organic	$CH_4N^{\oplus}$
calcium	$Ca^{\oplus}$, $CaOH^{\oplus}$

The ToF-SIMS evaluation of samples treated with DTNPS in naphthenic base oil reveals higher intensities for aluminum and aluminum oxide on the unstressed sample. This result is identic with the evaluation of the other additive systems. Additional, the unstressed sample shows an increased signal intensity for molecular sulphur.

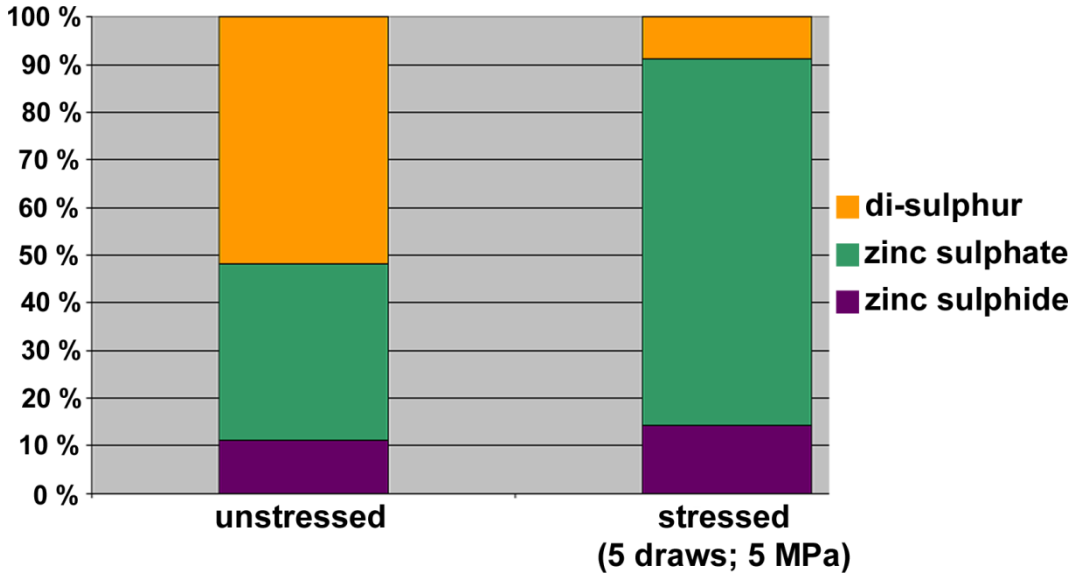

Figure 126. Intensity variations of essential fragment categories of DTNPS in naphthenic base oil before and after multi-frottement test with five draws at 5 MPa

However, the stressed sample shows higher intensities of zinc, zinc oxide, zinc hydroxide, zinc sulphide, zinc sulphate and elemental sulphur.

The comparison of the essential fragment categories is visualized in Figure 126 and the corresponding fragment signals are listed in Table 17.

Table 17. Fragment signals of essential fragment categories of DTNPS

zinc, zinc hydride	$Zn^{\oplus}$, $Zn_2^{\oplus}$, $ZnH^{\oplus}$
zinc oxide, zinc hydroxid	$Zn_2O^{\oplus}$, $Zn_3O^{\oplus}$, $Zn_2OH^{\oplus}$, $Zn_2O_2H^{\oplus}$, $Zn_4O_4H^{\oplus}$, $ZnO^{\ominus}$, $ZnO_2^{\ominus}$, $ZnOH^{\ominus}$
sulphur, sulphur oxide	$S^{\oplus}$, $HS^{\oplus}$, $SO^{\oplus}$, $S^{\ominus}$, $SO^{\ominus}$
zinc sulphide	$ZnS^{\oplus}$, $ZnSH^{\oplus}$, $ZnS^{\ominus}$, $ZnSH^{\ominus}$, $ZnS_2^{\ominus}$
zinc sulphate	$ZnSO^{\ominus}$, $ZnSOH^{\ominus}$, $ZnSO_2^{\ominus}$, $ZnSO_2H^{\ominus}$, $Zn_2SO^{\oplus}$, $Zn_2SOH^{\oplus}$
aluminum, aluminum hydride, aluminum oxide	$AlH^{\oplus}$, $AlOH^{\oplus}$, $Al_2^{\oplus}$, $Al^{\ominus}$, $AlH^{\ominus}$, $AlO_2^{\ominus}$
di-sulphur	$S_2^{\ominus}$

In summary, the characterization of the fully developed pre-lube system reveals no indications of possible tribologically induced reaction products.

The characterization of the pure base oil also gives no hints of possible reaction products.

The intensity variations of aluminum species on the unstressed sample and zinc species on the stressed sample can be explained du to stress induced matrix changes. Another explanation is the removal of the outermost aluminum layer due to wear effects and the exposure of zinc-rich layers.

The Irgalube TPPT additive system shows increased intensities for zinc sulphide (ZnS) and organo-zinc species on the stressed sample.

The characterization of the fourth additive system with DTNPS also reveals possible tribologically induced reaction products. The increased intensities of zinc sulphide and zinc sulphate on the stressed sample point to this conclusion. However, the intensity of the di-sulphur signal is reduced due to the tribological treatment. This effect hints to the conclusion, that this DTNPS fragment is essentially involved in the further formation of zinc sulphide and zinc sulphate.

5.1.5.3 Discussion

This chapter studied the reaction of selected additives under more challenging conditions than the conditions in chapter 5.1.4. The COF of PL 3802-39S, naphthenic base oil and mixtures of Irgalube TPPT and DTNPS in naphthenic base oil (each 2 w.-%) for one, three and five draws were detected. The contact pressure during the drawing was 10 MPa expect for naphthenic base oil and the two mixtures in the five-draw measurement due to strong stick-slip effects during the three-draw measurement. In the experiments with multiple draws, the tool was pushed back to the starting point between two draws with a contact pressure of 1 MPa.

The fully developed pre-lube PL 3802-39S showed the best performance with the lowest COF in all three test-series. The addition of the additives Irgalube TPPT and DTNPS to naphthenic base oil displayed a differentiation between these additive systems only for the five-draw test. The COF at the first draw was similar in all three systems but Irgalube TPPT and DTNPS reduced the COF significantly up to the fifths draw.

The surface analysis was performed by means of ToF-SIMS for all four systems at an unstressed sample and at a sample with five repeated draws. The comparison of unstressed and stressed samples revealed no possible reaction products for the systems with naphthenic base oil and for the pre-lube PL 3802-39S. However, reaction products like zinc sulphide and organo-zinc components could be identified on the stressed samples of the Irgalube TPPT sample. The surface analysis of the DTNPS systems also revealed reaction products due to increased intensities of zinc sulphide and zinc sulphate.

In summary, it was possible to identify tribologically induced reaction products like metal-bound sulphur-species for both additive systems.

5.2 Conclusions

Based on the characterization of layers of forming additives on laboratory and technical-grade zinc-alloys, this chapter presented the occurrence and the characterization of tribological layers on HDG.

The preparation of oil-free additive films on HDG was successfully confirmed for the additives Irgalube TPPT, DTNPS and Irgalube 349. The tribological tests by means of strip-drawing showed that DTNPS and Irgalube 349 only reached a contact pressure of 4000 N because of heavy stick-slip effects while Irgalube TPPT showed the lowest COF and reached even contact pressures of 16000 N. The succeeding microscopic, morphological and surface analytical characterizations showed a smoothening of the surface for all three additive systems und the appearance of black spots for the additive systems with Irgalube TPPT and DTNPS. These black spots could have their origin in abrasive wear processes due to the material transport that smoothed the surfaces or in changes of the optical parameters of the oxide layer. The surface analysis revealed a homogenization of additive concentrations for the additive system Irgalube TPPT with increasing contact pressure. Contrary results were obtained by this method for the additive system DTNPS, where the homogeneity was high at the beginning and overall additive concentrations decreased at increased contact pressures with localized spots of sulphur. The homogeneity appeared even stronger for the additive system Irgalube 349 in the beginning and looked localized with increased contact pressure.

No tribochemical reaction products could be detected for all three additive systems but the high resolution of the imaging-Raman spectroscopy allowed the detection of localized spots of remaining additive after the tribological treatment. With this method, it was also possible to identify high amounts of the D- and G-bands of sooty carbon on the surface of the DTNPS additive systems. These sooty carbons could originate from the decomposition of the hydrocarbon side chain of the additive. For the Irgalube 349 additive system, it was also possible to detect remaining spots of additive after the tribological treatment.

During the base oil selection, it was recognized that an additive with a short sulphur chain like DPDS increased the COF with increasing concentrations under the studied conditions despite contradicting reports under different conditions. The base-oil with the lowest COF was used for all further oil-based tribological measurements.

The use of adsorbed additives as pre-treatment showed improved performance in an oil-based strip-drawing test for the additive systems DTNPS and Irgalube 349 compared to the naphthenic base oil. Stick-slip effects were prevented for both additive systems and Irgalube 349 even performed with an lowered COF comparable to the fully developed PL 3802-39S. The additive systems with Irgalube TPPT, which showed the best performance under oil-free conditions, ended with a higher COF than the base oil and similar stick-slip characteristics. These results, in particular the increased performance of the Irgalube 349 additive system, indicated that adsorbed additives as pretreatment could be the foundation for the development of tribological systems with improved characteristics.

The main part characterized the tribological behavior of various oil-based additive systems by means of strip-drawing tests with increasing contact pressure. The screening of additive systems revealed the influence of the oil-coverage with increased performance at higher coverages und the heavy depending of the nature of the additive systems. Sulphur-based additive systems were identified as important reactive structure but the results also varied heavily depending on the specific molecule. While the additive systems with OBSS, zinc sulphide and the sulphur-free Irgalube 349 improved the tribological performance compared to the base oil, the additive systems with DPDS, DTNPS and elemental sulphur showed the worst results in all tests and even dominated the performance of additive mixtures. Therefore, the tribological characteristics of DTNPS as one of the worst and OBSS as one of the best additives were studied in detail and succeeded by surface analytical measurements to reveal tribochemical reaction products. With imaging Raman spectroscopy, it was possible to detect soot particles on the surface of the OBSS and the DTNPS additive systems as well as on the reference with pure base-oil after the strip-

drawing tests. While the soot particles in the oil-free tests could originate from the decomposition of the additives, here the decomposition of the oil or the presence of the particles from the beginning is more likely.

The detailed contact-pressure resolved XPS analysis enabled the identification of tribochemical reaction products. For the OBSS additive system, no sulphur components could be detected. The main reaction products were sodium based carbonates and hydrogen carbonates. The contact-pressure resolved measurements revealed a decrease of metallic oxides on the surface with increasing contact pressure and confirmed the presence of soot particles due to an increase of graphitic carbon with increasing contact pressure. At the same time, an increase of sodium carbonates could be detected. The sodium to carbonate ratios indicate a conversion from sodium hydrogen carbonate ($NaHCO_3$; ratio: 1:1) to sodium carbonate (Na_2CO_3; ratio: 1:1) which could be responsible for the low COF without the appearance of stick-slip effects. Additionally the ToF-SIMS analysis revealed the decreasing of organic-sulphonate on the surface with increasing contact pressure.

For the DTNPS additive system, sulphur based tribochemical reaction products could be detected by means of high-resolution XPS analysis. With increasing contact pressure, a transformation from sulphides to sulphates in combination with a decrease of metal concentrations on the surface was revealed. With ToF-SIMS analysis, it was possible to further identify both components as zinc-bound. Therefore, it could be confirmed that the sulphides and sulphates are not residues of the oil-based additive but tribochemical reaction products that formed during the strip-drawing test.

Furthermore, selected additives (Irgalube TPPT, DTNPS) were studied as in-oil solutions under more challenging tribological conditions by means of multi-frottement strip-drawing tests and compared to the performance of the fully developed pre-lube PL 3802-39S and the naphthenic base oil. The best performance was shown by the pre-lube PL 3802-39S with the lowest COF in the complete test series. For the pre-lube, it was also possible to run the five-draw test with doubled contact pressure than for the oil-solutions. An effect from the addition of the additives to naphthenic base could only be detected in the five-draw test, were the addition lowered the COF significantly compared to the base oil. The two additives couldn`t be significantly differentiated in all tests.

The surface analysis of the highest stressed samples couldn`t reveal any tribochemical reaction products for the systems with naphthenic base oil and the pre-lube. However, the build-up of zinc sulphide and zinc sulphate layers was confirmed by means of ToF-SIMS for

the DTNPS system. In addition, it was possible to identify zinc sulphide and organo-zinc compounds as reaction products of the Irgalube TPPT system.

6 Overall conclusions and outlook

The reaction mechanism of forming additives in tribological conditions was studied by correlating friction and wear information with surface analysis.

First, various analytical methods (GC-MS, DRIFT, Raman spectroscopy) were used to obtain characteristic reference information of the selected tribological additives. The selected additives were sulphur-based additives like DTNPS and OBSS, a phosphorus-based additive like Irgalube 349, and the phosphorus- and sulphur-based additive Irgalube TPPT. XPS, LIBS, WLI and Raman spectroscopy were used to gain similar characteristic reference information of the used zinc substrates. The zinc surfaces were laboratory-grade zinc and zinc alloy as well as technical-grade HDG and NSP-HDG. The analyses confirmed their purity and supplied important information for the characterization of adsorbed layers and tribochemical products.

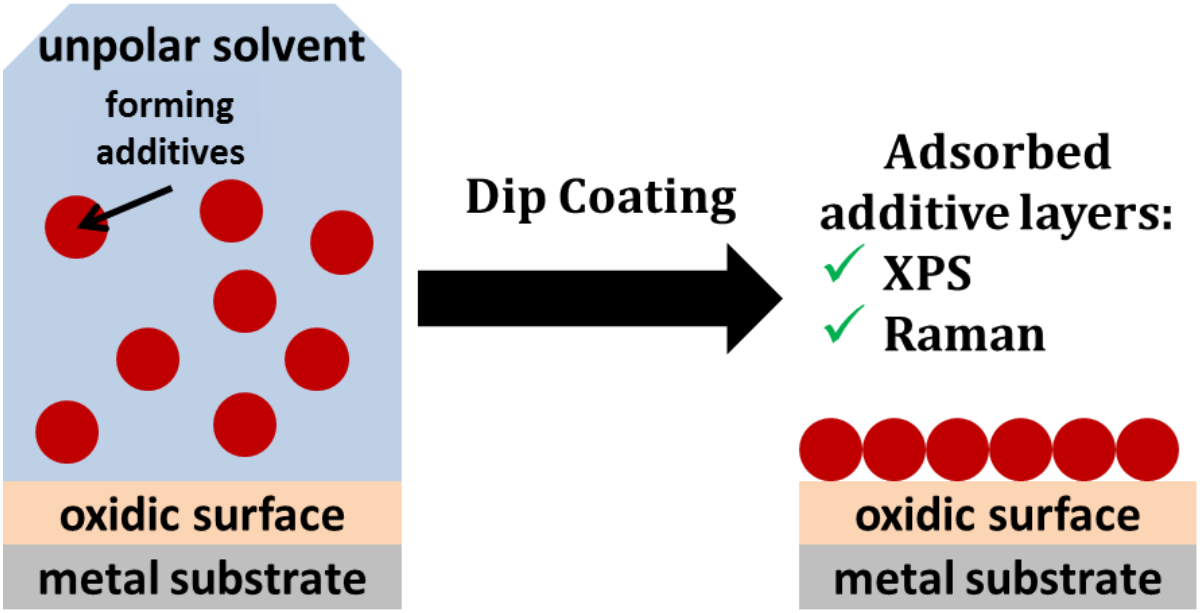

Figure 127. Interfacial adsorption processes on zinc alloys (schematic overview)

Adsorption films of DTNPS, Irgalube TPPT and Irgalube 349 were successfully prepared by means of dip coating on technical-grade NSP-HDG. The adsorbed layer of Irgalube 349 was confirmed by means of XPS analysis via a characteristic peak of amine phosphate while characteristic peaks of sulphide identified the DTNPS adsorption layer. Strong peaks of bridging and non-bridging oxygen along with signals of phosphate and sulphide confirmed the presence of adsorption layers of Irgalube TPPT on NSP-HDG.

These results were supported via the characterization of adsorption layers on laboratory-grade zinc surfaces. The cleaner surfaces allowed the detection of minor high-oxidized sulphur species like sulphates next to the sulphides for the additive systems with Irgalube TPPT and DTNPS.

In the main part of this thesis, the tribological reaction of selected additives was studied by means of strip-drawing tests to replicate the tribological performance of these additive systems in the holder region while deep-drawing a cup.

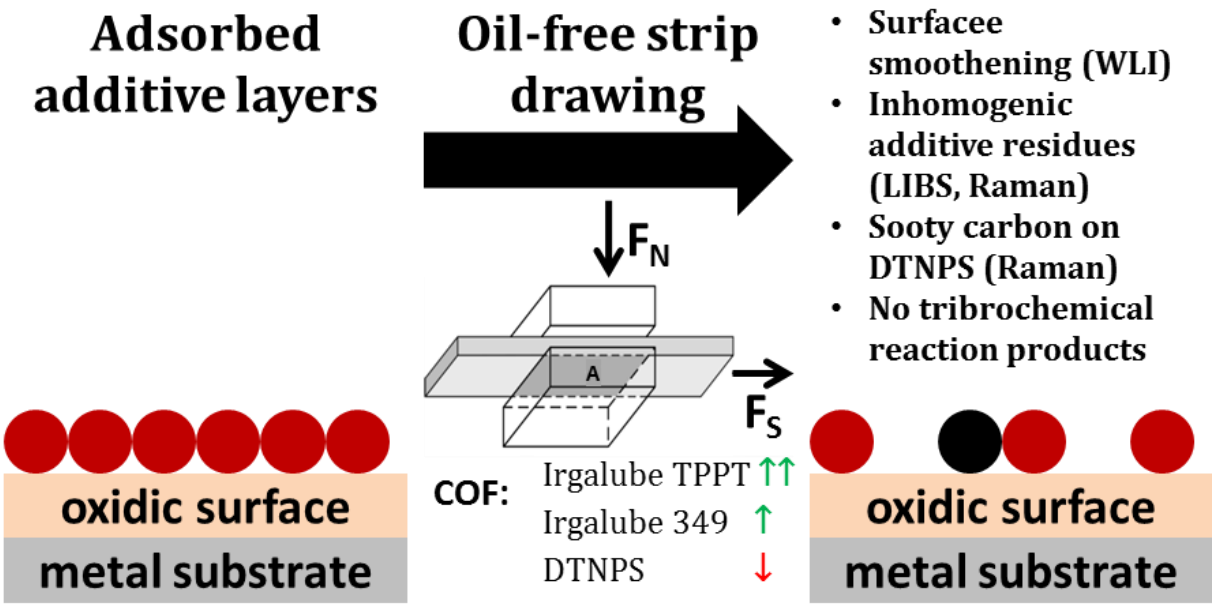

Figure 128. Reactivity of adsorbed forming additives under oil-free tribological conditions (schematic overview)

Building on the results of the adsorption layers, oil-free additive systems on HDG were prepared, confirmed by surface analysis and tribologically tested by means of strip-drawing tests with constant contact pressure. The strong influence of the surface morphology was studied by means of WLI and a smoothening of the surfaces due to material transport processes could be revealed. While no reaction products could be detected for all studied systems, it was possible to identify remaining spots of additive and high amounts of sooty carbon which could originate from the decomposition of the hydrocarbon side chains of the additives.

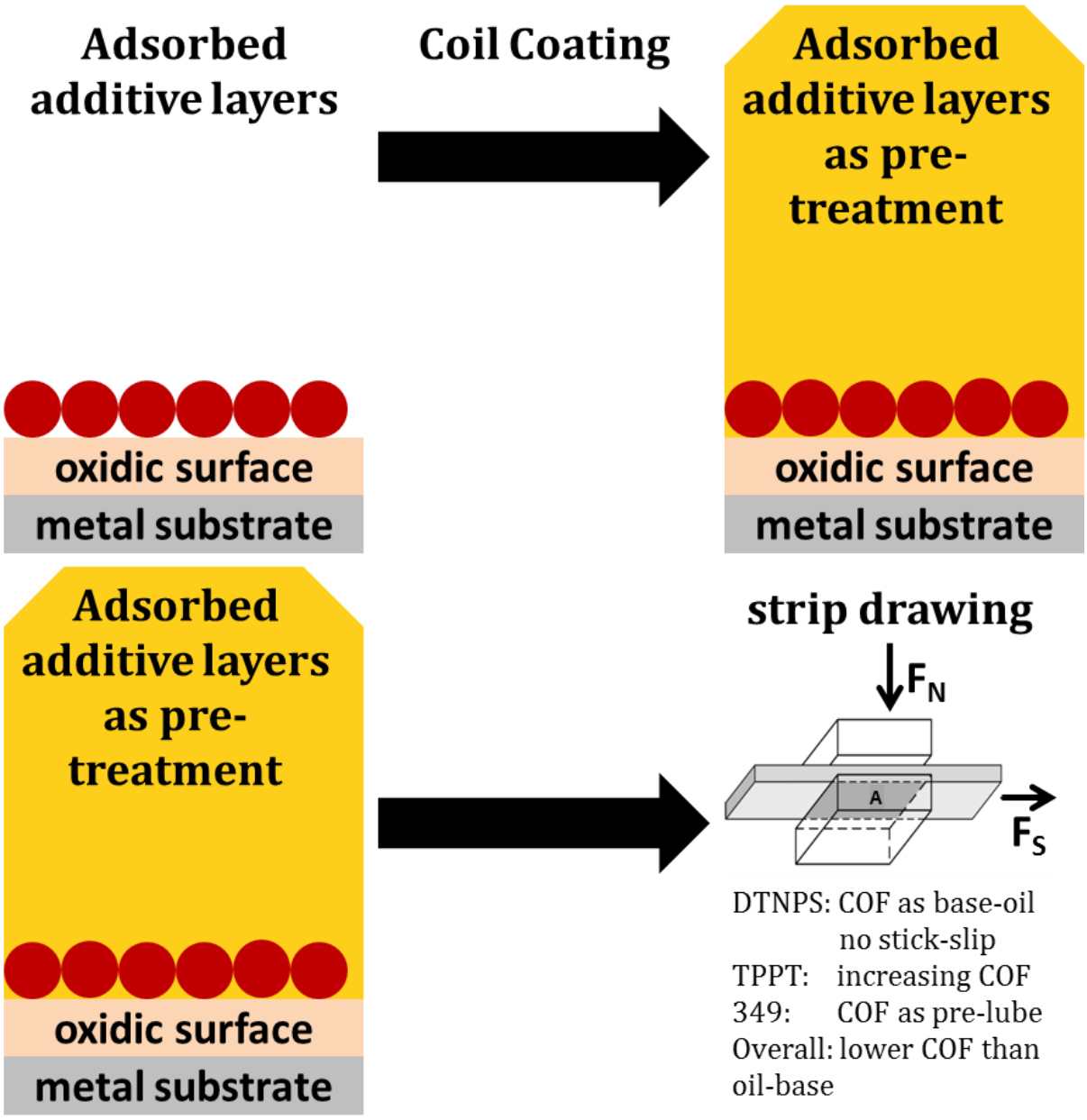

Figure 129. Reactivity of adsorbed forming additives as pre-treatment under tribological conditions (schematic overview)

The use of these additive systems as pre-treatment before the coating with a base oil, improved the tribological performance of all studied additive systems in comparison with the pure base oil system. All systems showed no occurrence of sticks-slip effects and the additive Irgalube 349 even performed with a COF lower than the fully developed pre-lube PL 3802-39S.

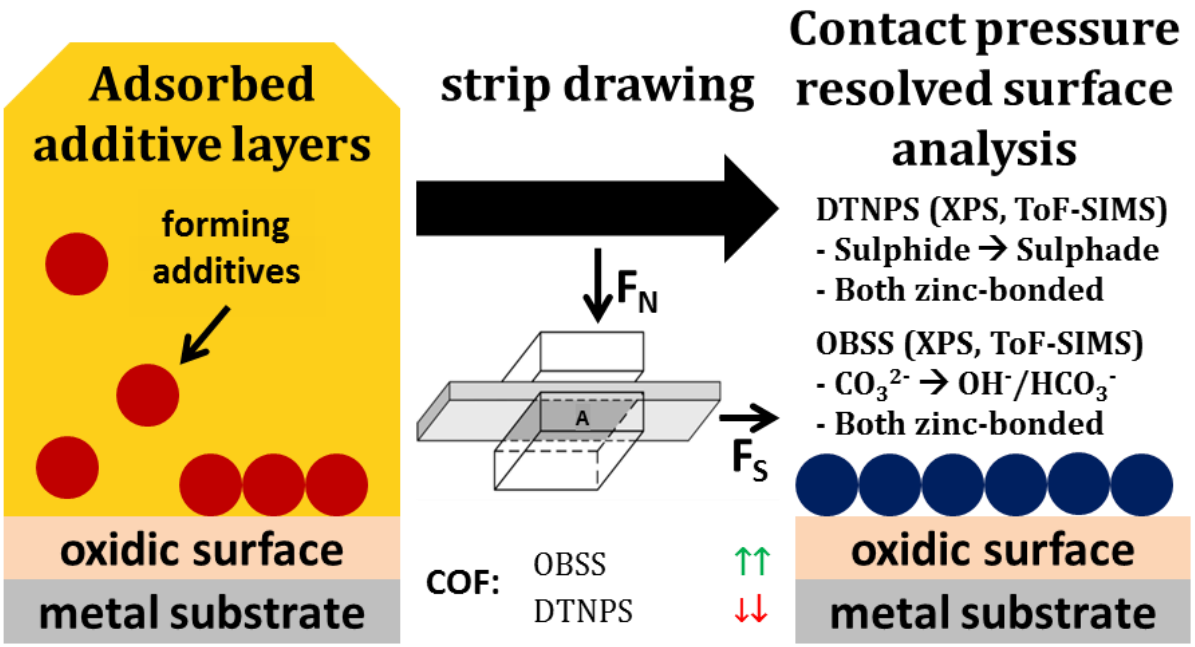

Figure 130. Reactivity of oil-based forming additives under tribological conditions (schematic overview)

A broad screening of tribological additives identified sulphur-based additives as promising reactive species. The specific nature of the molecule still had important influence on their performance. Strip-drawing tests with increasing contact pressure were used to generate contact pressure resolved samples for further surface analysis. By means of XPS analysis, it was possible to identify tribochemical reaction products for the systems with OBSS and DTNPS. For the OBSS samples, no sulphur based reactions products could be found, but the analysis with XPS and ToF-SIMS enabled the identification of an increase of sodium carbonates with increasing contact pressure. Sulphur-based reaction products were identified on contact-pressure resolved samples of the DTNPS additive system. It was possible to reveal the change from sulphide to sulphate species with increasing contact pressure. Furthermore, the nature of these reaction products could be identified as metal-bound. Under even more tribologically challenging conditions performed by means of multi frottement strip-drawing tests, it was possible to confirm the build-up of zinc sulphide and zinc sulphate for the DTNPS system and to reveal zinc sulphide and organo-zinc species as reaction products for the Irgalube TPPT additive system.

In order to deepen the understanding of these results, *in lubro* characterizations by means of Raman spectroscopy, supported by means of *ex situ* XPS and ToF-SIMS analysis, of tribochemical films created in an oil-based pin-on-disc-like system with low contact pressures and high numbers of repetitions could be used.

7 Tables

8 Figures

9 Formulas

10 Abbreviations and Symbols

°C	degree Celsius
μ	friction coefficient
μ_e	dipole moment
μm	micrometre
μm^2	square micrometre
2D	two-dimensional
3D	three-dimensional
A	surface area
A.D.	Anno Domini
AAS	atomic absorption spectroscopy
AES	auger electron spectroscopy
AFM	atomic force microscopy
AISI	american iron and steel institute
Al_2O_3	aluminum oxide
amu	atomic mass unit
ATR	attenuated total reflection
BE	binding energy
BO	bridging oxygen
CCD	charge-coupled device
cm^{-1}	inverse centimetre
COF	coefficient of friction
CSI	coherence scanning interferometry
CVD	chemical vapor deposition
DBDS	di-benzyl disulphide
DLC	diamond-like carbon
DPDS	diphenyldisulphide
DRIFTS	Diffuse reflectance infrared Fourier transform spectroscopy
DTNPS	di-*tert*-nonyl polysulphide
EDX	energy-dispersive X-ray spectroscopy
EG	electrogalvanization
EN31	chrome steel
EP	extreme pressure
ESCA	Electron Spectroscopy for Chemical Analysis
eV	electron volt
FFM	friction force microscopy
FIB	focus ion beam
F_N	normal force
F_R	friction force
F_S	strip-drawing force
FTIR	fourier transform infrared spectroscopy
F_{tot}	total drawing force
g	gram

GC-MS	gas chromatography - mass spectrometry
HDG	hot-dip galvanization
HFRR	high-frequency reciprocating rig
hν	photon energy
ICP	inductively coupled plasma
ICP-OES	inductively coupled plasma - optical emission spectrometry
IR	infrared spectroscopy
Irgalube TPPT	triphenylphosphorthionate
KE	kinetic energy
keV	kilo electron volt
kg	kilogram
l	lenght
l_g	connected lenght
LIBS	laser-induced breakdown spectroscopy
LIPS	laser-induced plasma spectroscopy
LSS	laser spark spectroscopy
m	meter
m/z	mass to charge ratio
m^2	square metre
min.	minute
mm	millimetre
mm^2	square millimetre
MoDTC	molybdenum dithiocarbamate
MPa	megapascal
mPa	millipascal
N	Newton (kg m s^{-2})
NBO	nonbridging oxygen
NMR	nuclear magnetic resonance spectroscopy
nN	nano Newton
NSP	non-skin passed
OBSS	overbased sodium sulphonate
OES	optical emission spectroscopy
p	surface pressure
PAO	poly-alpha-olefine
ppm	parts per million
PVD	physical vapor deposition
q	vibration coordinate
QCM	quartz crystall microbalance
R_a	arithmetic roughness index
R_{max}	maximal depth of roughness
R_p	averaged smoothing depth
R_q	square mean roughness index
R_t	depth of roughness
R_v	averaged scoring depth

R_z	averaged depth of roughness
s	second
SEM	scanning electron microscopy
SERS	Surface-enhanced Raman spectroscopy
SFA	surface force apparatus
SO	sulphuroxide
SRV	german: Schwingung-Reibung-Verschleiß; oscillation-friction-wear
STM	scanning tunneling microscopy
TEM	transmission electron microscopy
TGA	thermogravimetric analysis
THF	tetrahydrofuran
TKSE	thyssenkrupp Steel Europe AG
ToF	time-of-flight
TOF-SIMS	time-of-flight secondary-ion mass spectrometry
UHV	ultra-high vacuum
UTFI	ultrathin film interferometry
VDA	Verband der Automobilindustrie e. V (german); German Association of the Automotive Industry
w.-%	weight percentage
WLI	white light interferometry
XANES	X-ray absorption near edge structure spectroscopy
XAS	X-ray absorption spectroscopy
XPS	X-ray photoelectron spectroscopy
XRF	X-ray fluorescence spectroscopy
ZMG	zinc-magnesium coated
ZnDTP	zinc dialkyl dithiophosphate
ZnO	zinc oxide
α	molecular polarizability
φs	work function

11 Bibliography

1. Dowson, D., *History of tribology*. 2 ed. 1998, London: Professional Engineering Pub. xxiv, 768.
2. Bartz, W.J., *Zur Geschichte der Tribologie*. 1988, Ehningen bei Böblingen: Expert. 148.
3. Popov, V.L., *Kontaktmechanik und Reibung: Ein Lehr- und Anwendungsbuch von der Nanotribologie bis zur numerischen Simulation*. 2009, Berlin; Heidelberg: Springer-Verlag Berlin Heidelberg.
4. Mortier, R.M., M.F. Fox, and S.T. Orszulik, *Chemistry and Technology of Lubricants*. 2010, Dordrecht: Springer Netherlands. Online-Ressource.
5. Bhushan, B. and B.K. Gupta, *Handbook of tribology: Materials, coatings, and surface treatments*. 1991, New York: McGraw-Hill. 1 v. (various.
6. Mang, T., *Lubricants and lubrication*. 2., completely rev. and extended ed. ed. 2007, Weinheim: WILEY-VCH Verlag GmbH. 850.
7. Czichos, H. and K.-H. Habig, *Tribologie Handbuch: Reibung und Verschleiss : Systemanalyse, Prüftechnik, Werkstoffe und Konstruktionselemente*. 1992, Weisbaden: Vieweg. [1 v.].
8. Suh, N.P., *Fundamentals of tribology: Proceedings of the international conference; Cambridge - Mass., June 1978*. 1980, Cambridge - Mass: MIT Press. XX, 1206.
9. Macherauch, E. and H.-W. Zoch, *Praktikum in Werkstoffkunde : 95 ausführliche Versuche aus wichtigen Gebieten der Werkstofftechnik*. 12., überarb u. erw. Aufl. 2014 ed. 2014, Wiesbaden: Springer Fachmedien Wiesbaden.
10. Volk, R., *Rauheitsmessung : Theorie und Praxis*. 2., überarb. Aufl. H1 - D35 WFC2199(2)+3 ed. Praxis : Messwesen. 2013, Berlin [u.a.]: Beuth.
11. Schuler, *Handbuch der Umformtechnik*. 1996, Berlin ;, New York: Springer. xx, 565.
12. Wagoner, R.H. and J.L. Chenot, *Fundamentals of metal forming*. 1997, New York: Wiley. xiv, 389.
13. Iliuc, I., *Tribology of thin layers*. 1980, Bucureşti; Amsterdam ;, New York; New York: Editura Academiei Republicii Socialiste România; Elsevier Scientific Pub. Co.; distribution for the U.S.A. and Canada, Elsevier/North Holland. ix, 225.
14. Butt, H.-J., K. Graf, and M. Kappl, *Physics and chemistry of interfaces*. Third, rev. and enl. ed ed. 2013, Weinheim: Wiley-VCH. 461 S.
15. Butt, H.-J. and M. Kappl, *Surface and interfacial forces*. Physics textbook. 2010, Weinheim: Wiley-VCH. 1 online resource (xv, 421).
16. Hudson, J.B., *Surface science: An introduction*. 1998, New York: J. Wiley & Sons. xii, 321.
17. Nilsson, A., L. Pettersson, and J.K. Nørskov, *Chemical bonding at surfaces and interfaces*. 1st ed ed. 2008, Amsterdam; Oxford: Elsevier. 1 online resource (xii, 520.
18. Bartz, W.J., *Additive für Schmierstoffe*. Reihe Tribotechnik. 1990, Hannover. 318.
19. Forbes, E.S., *Antiwear and extreme pressure additives for lubricants.* Tribology, 1970. **3**(3): p. 145–152.
20. Papay, A.G., *Antiwear and extreme-pressure additives in lubricants.* Lubrication Science, 1998. **10**(3): p. 209–224.
21. Marder, A.R., *The metallurgy of zinc-coated steel.* Progress in Materials Science, 2000. **45**(3): p. 191–271.

22. Feliu, S. and V. Barranco, *XPS study of the surface chemistry of conventional hot-dip galvanised pure Zn, galvanneal and Zn-Al alloy coatings on steel.* Acta Materialia, 2003/10/20/. **51**(18): p. 5413–5424.

23. Fink, N., B. Wilson, and G. Grundmeier, *Formation of ultra-thin amorphous conversion films on zinc alloy coatings: Part 1. Composition and reactivity of native oxides on ZnAl (0.05%) coatings.* Electrochimica Acta, 2006. **51**(14): p. 2956–2963.

24. Asgari, H., M.R. Toroghinejad, and M.A. Golozar, *On texture, corrosion resistance and morphology of hot-dip galvanized zinc coatings: The 4th International Workshop on Basic Aspects of Nonequilibrium Plasmas Interacting with Surfaces; Negative ions, their function & designability, and 4th EU-Japan Joint Symposium on plasma Processes - 4th BANPIS.* Applied Surface Science, 2007/6/15/. **253**(16): p. 6769–6777.

25. Dillen, R., et al., *From Substrate to Coating: Micro- and Surface Analysis Techniques for the Development of Steel Products.* Microchimica Acta, 2004/04/01/. **145**(1): p. 29–39.

26. Hosking, N.C., et al., *Corrosion resistance of zinc-magnesium coated steel.* Corrosion Science, 2007/9//. **49**(9): p. 3669–3695.

27. Dutta, M., A.K. Halder, and S.B. Singh, *Morphology and properties of hot dip Zn-Mg and Zn-Mg-Al alloy coatings on steel sheet.* Surface and Coatings Technology, 2010. **205**(7): p. 2578–2584.

28. Lostak, T., et al., *Zr-based conversion layer on Zn-Al-Mg alloy coated steel sheets: insights into the formation mechanism.* Electrochimica Acta, 2014. **137**(Supplement C): p. 65-74.

29. Schuhmacher, B., et al., *Innovative steel strip coatings by means of PVD in a continuous pilot line: process technology and coating development.* Proceedings of the 29th International conference on Metallurgical Coatings and Thin Films, 2003. **163–164**(0): p. 703–709.

30. O'Brien, S., et al., *Zinc oxide thin films: Characterization and potential applications: Proceedings of the EMRS 2009 Spring Meeting Symposium H: Synthesis, Processing and Characterization of Nanoscale Multi Functional Oxide Films II.* Thin Solid Films, 2010. **518**(16): p. 4515–4519.

31. Zabinski, J., et al., *Lubricious zinc oxide films: synthesis, characterization and tribological behaviour.* Journal of Materials Science, 1997/10/01/. **32**(20): p. 5313–5319.

32. Shibli, S.M.A., R. Manu, and S. Beegum, *Studies on the influence of metal oxides on the galvanic characteristics of hot-dip zinc coating.* Surface and Coatings Technology, 2008/2/1/. **202**(9): p. 1733–1737.

33. Le, H.R. and M.P.F. Sutcliffe, *Measurements of friction in strip drawing under thin film lubrication.* Tribology International, 2002. **35**(2): p. 123-128.

34. Hivart, P. and J.-P. Bricout, *Influence of cleaning pretreatments on tribological properties of zinc phosphated steels.* Industrial Lubrication and Tribology, 2003. **55**(2): p. 90–96.

35. Hörnström, S.E., et al., *A surface study of the chemical pretreatment before coil coating of hot dip zinc-coated steel.* Surface and Interface Analysis, 1992. **19**(1-12): p. 121–126.

36. Bajat, J.B., et al., *The influence of zinc surface pretreatment on the adhesion of epoxy coating electrodeposited on hot-dip galvanized steel.* Progress in Organic Coatings, 2007/3/1/. **58**(4): p. 323–330.

37. Carlsson, P., U. Bexell, and M. Olsson, *Friction and wear mechanisms of thin organic permanent coatings deposited on hot-dip coated steel.* Wear, 2001. **247**(1): p. 88–99.

38. Carlsson, P., U. Bexell, and M. Olsson, *Tribological performance of thin organic permanent coatings deposited on 55%Al-Zn coated steel -- influence of coating composition and*

thickness on friction and wear: 13th International Conference on Wear of Materials. Wear, 2001. **251**(1-12): p. 1075–1084.

39. Carlsson, P., U. Bexell, and M. Olsson, *Tribological behaviour of thin organic permanent coatings deposited on hot-dip coated steel sheet -- a laboratory study.* Surface and Coatings Technology, 2000/10/23/. **132**(2-3): p. 169–180.

40. Mitterer, C., et al., *A comparative study on the evaluation of the tribological behaviour of polymer/zinc coated steel sheets.* Wear, 1997. **210**(1-2): p. 88–95.

41. Ohnesorge, M., et al., *Additivanalytik in Schmierstoffen: Teil 1: Charakterisierung aller Bestandteile eines Modellschmieröls und Übersichtsanalyse.* Tribologie + Schmierungstechnik, 2009. **56**(3): p. 18–24.

42. Ash, D.C., et al., *Viscosity measurement of industrial oils using the droplet quartz crystal microbalance.* Measurement Science and Technology, 2003. **14**(11): p. 1955–1962.

43. Schumacher, R., et al., *Über die Tribofragmentierung von Verschleißschutzadditiven und die oberflächenanalytische Charakterisierung der gebildeten Reaktionsschichten*, in *Proc. 5th Intern Coll. "Additives for Lubricants and Operational Fluids"*. 1986: Esslingen. p. 3.9-1 - 3.9-19.

44. Martin, J.M. and T. Le Mogne, *Interpretation of friction and wear of ceramics in terms of surface analysis.* Surface and Coatings Technology, 1991. **49**(1–3): p. 427–434.

45. Smith, G.C., *Surface analytical science and automotive lubrication.* Journal of Physics D: Applied Physics, 2000. **33**(20): p. R187.

46. Martin, J.M. and M. Belin, *New trends in analytical tribology.* Thin Solid Films, 1993. **236**(1-2): p. 173–179.

47. Bongaerts, J.H.H., et al., *In situ confocal Raman spectroscopy of lubricants in a soft elastohydrodynamic tribological contact.* Journal of Applied Physics, 2008/07/01/. **104**(1): p. 014913-10.

48. Yablon, D.G., et al., *Atomic Force Microscopy and Raman Spectroscopy Investigation of Additive Interactions Responsible for Anti-Wear Film Formation in a Lubricated Contact.* Tribology Transactions, 2006. **49**(1): p. 108–116.

49. Rossi, A., et al., *Surface analytical studies of surface-additive interactions by means of in situ and combinatorial approaches.* Wear, 2004. **256**(6): p. 578–584.

50. Fuller, M.L.S., et al., *Solution decomposition of zinc dialkyl dithiophosphate and its effect on antiwear and thermal film formation studied by X-ray absorption spectroscopy.* Tribology International, 1998. **31**(10): p. 627–644.

51. Nicholls, M., et al., *The contribution of XANES spectroscopy to tribology.* Canadian Journal of Chemistry, 2007. **85**(10): p. 816–830.

52. Pereira, G., et al., *Chemical and mechanical analysis of tribofilms from fully formulated oils Part 1 – Films on 52100 steel.* Tribology - Materials, Surfaces & Interfaces, 2007. **1**(1): p. 48–61.

53. Pereira, G., et al., *Chemical and mechanical analysis of tribofilms formed from fully formulated oils Part 2 – Films on Al–Si alloy (A383).* Tribology - Materials, Surfaces & Interfaces, 2007. **1**(2): p. 105–112.

54. Najman, M.N., M. Kasrai, and G.M. Bancroft, *X-ray Absorption Spectroscopy and Atomic Force Microscopy of Films Generated from Organosulfur Extreme-Pressure (EP) Oil Additives.* Tribology Letters, 2003. **14**(4): p. 225–235.

55. Rosset, E., H.J. Mathieu, and D. Landolt, *A new experimental technique for the study of the surface reactions of extreme pressure additives at elevated temperatures.* Wear, 1984. **94**(2): p. 125–133.

56. De Barros, M.I., et al., *Friction reduction by metal sulfides in boundary lubrication studied by XPS and XANES analyses.* Wear, 2003. **254**(9): p. 863–870.

57. Mathieu, H.J., D. Landolt, and R. Schumacher, *Electron Spectroscopy of Reaction Layers Formed Under Different Wear Test Conditions.* Surface and Interface Analysis, 1986. **9**: p. 477–492.

58. Schumacher, R., et al., *Auger electron spectroscopy study on reaction layers formed under Reichert wear test conditions in the presence of extreme pressure additives.* Tribology International, 1980. **13**(6): p. 311–317.

59. Heuberger, R.C., A. Rossi, and N.D. Spencer, *XPS study of the influence of temperature on ZnDTP tribofilm composition.* Tribology Letters, 2007. **25**(3): p. 185–196.

60. Hipler, F., et al., *Chemie gegen Reibung und Verschleiß: Untersuchung molekularer Wirkungsmechanismen von Schmierstoffadditiven.* Materialwissenschaft und Werkstofftechnik, 2000. **31**(9): p. 872–877.

61. Liang, P., et al., *Tribological performances of heterocyclic-containing ether and/or thioether as additives in the synthetic diester.* Lubrication Science, 2009. **21**(3): p. 111–121.

62. Grün, F., et al., *Tribometrie von Grenzschichten in grossflächigen Kontakten: Methodik zur Erzeugung von Tribofilmen und begleitende Analytik.* Tribologie + Schmierungstechnik, 2010. **57**(1): p. 5–11.

63. Kar, P., P. Asthana, and H. Liang, *Formation and Characterization of Tribofilms.* Journal of Tribology, 2008/10/00/. **130**(4): p. 042301–042306.

64. Gunst, U., et al., *Tribosurface and lubricant characterization by ToF-SIMS.* Surface and Interface Analysis, 2004. **36**(8): p. 1231–1235.

65. Dauchot, G., et al., *Application of ToF-SIMS surface analysis to tribochemistry in metal forming processes: Tribology in Manufacturing Processes.* Wear, 2006. **260**(3): p. 296–304.

66. Evans, R.D., et al., *Transmission Electron Microscopy of Boundary-Lubricated Bearing Surfaces. Part I: Mineral Oil Lubricant.* Tribology Transactions, 2004. **47**(3): p. 430–439.

67. Evans, R.D., et al., *Transmission Electron Microscopy of Boundary-Lubricated Bearing Surfaces. Part II: Mineral Oil Lubricant with Sulfur- and Phosphorus-Containing Gear Oil Additives.* Tribology Transactions, 2005. **48**(3): p. 299–307.

68. Reichelt, M., et al., *Elektronenmikroskopische und Rastersonden-Untersuchungen des Verschleißschutzes durch Reaktionsschichten in langsam laufenden Wälzlagern.* Tribologie + Schmierungstechnik, 2005. **52**(2): p. 18–23.

69. Ratoi, M., et al., *Mechanisms of oiliness additives.* Tribology International, 2000. **33**(3–4): p. 241–247.

70. Stadler, A., et al., *Surface analysis of different boundary layers on steel discs formed in a lubricated tribocontact during laboratory test compared with field application.* Surface and Interface Analysis, 2008/03/01/. **390**(6): p. 1527–1535.

71. Canter, N. *NANOTRIBOLOGY: The science of thinking small*. Tribology & Lubrication Technology 2004 29.03.2014]; Available from: http://www.highbeam.com/doc/1P3-643410581.html.

72. Bhushan, B., *Nanotribology, nanomechanics and nanomaterials characterization.* Philosophical Transactions of the Royal Society A: Mathematical, Physical and Engineering Sciences, 2008/04/28. **366**(1869): p. 1351–1381.

73. Hölscher, H., A. Schirmeisen, and U.D. Schwarz, *Principles of atomic friction: from sticking atoms to superlubric sliding.* Philosophical Transactions of the Royal Society A:

Mathematical, Physical and Engineering Sciences, 2008/04/28. **366**(1869): p. 1383–1404.

74. Bouzigues, C.I., et al., *Using surface force apparatus, diffusion and velocimetry to measure slip lengths.* Philosophical Transactions of the Royal Society A: Mathematical, Physical and Engineering Sciences, 2008. **366**(1869): p. 1455–1468.

75. Krim, J. and R. Chiarello, *Sliding friction measurements of molecularly thin films.* Journal of Vacuum Science and Technology A, 1991/07/00. **9**(4): p. 2566–2569.

76. Krim, J., *Progress in Nanotribology: Experimental Probes of Atomic Scale Friction.* Comments in Condensed Matter Physics, 1995. **17**(5): p. 263–280.

77. Krim, J., *Resource Letter: FMMLS-1: Friction at macroscopic and microscopic length scales.* American Journal of Physics, 2002. **70**(9): p. 890.

78. Krim, J., *Atomic-Scale Origins of Friction.* Langmuir, 1996/01/01/. **12**(19): p. 4564–4566.

79. Spikes, H., *Nanotribology and Nanoadditives*, in *17th international colloquium tribology 2010*. 2010, Currans Associates: Red Hook, NY. p. 34–44.

80. Bhushan, B., ed. *Springer handbook of nanotechnology, third revised and extended edition*. 3rd rev. and extended ed ed. 2010, Springer: Heidelberg; New York. 1 online resource.

81. Tambe, N.S. and B. Bhushan, *Nanoscale friction and wear maps.* Philosophical Transactions of the Royal Society A: Mathematical, Physical and Engineering Sciences, 2008. **366**(1869): p. 1405–1424.

82. Gitis, N., et al., *Integrierte SPM für Nano-Tribologische Charakterisierung von Oberflächen.* Tribologie + Schmierungstechnik, 2007. **54**(1): p. 47–51.

83. Abdelmaksoud, M., J.W. Bender, and J. Krim, *Bridging the Gap between Macro- and Nanotribology: A Quartz Crystal Microbalance Study of Tricresylphosphate Uptake on Metal and Oxide Surfaces.* Physical Review Letters, 2004/04/27/. **92**(17): p. 176101.

84. Gwenin, C.D., et al., *Viscoelastic change following adsorption and subsequent molecular reorganisation of a nitroreductase enzyme on a gold surface: A QCM study.* Sensors and Actuators B: Chemical, 2007. **126**(2): p. 499–507.

85. Zhuang, H., et al., *Effects of Interface Slip and Viscoelasticity on the Dynamic Response of Droplet Quartz Crystal Microbalances.* Analytical Chemistry, 2008/10/01/. **80**(19): p. 7347–7353.

86. Persson, B.N.J., *Sliding friction.* Surface Science Reports, 1999. **33**(3): p. 83–119.

87. Mak, C. and J. Krim, *Quartz-crystal microbalance studies of the velocity dependence of interfacial friction.* Physical Review B, 1998. **58**(9): p. 5157–5159.

88. Krim, J. and A. Widom, *Damping of a crystal oscillator by an adsorbed monolayer and its relation to interfacial viscosity.* Physical Review B, 1988. **38**(17): p. 12184-12189.

89. Krim, J., D.H. Solina, and R. Chiarello, *Nanotribology of a Kr Monolayer: A Quartz-Crystal Microbalance Study of Atomic-Scale Friction.* Physical Review Letters, 1991. **66**(2): p. 181–185.

90. Dayo, A. and J. Krim, *Electrical Resistivity and quartz microbalance studies of sliding friction in Xe/Ag(111)*, in *8th International Conference on Vibration at Surfaces*. 1996: Birmingham.

91. Borovsky, B., B.L. Mason, and J. Krim, *Scanning tunneling microscope measurements of the amplitude of vibration of a quartz crystal oscillator.* Journal of Applied Physics, 2000/10/01/. **88**(7): p. 4017–4021.

92. Daly, C. and J. Krim, *Applications of a combined scanning tunneling Microscope and quartz microbalance*, in *Atomic Force Microscopy/Scanning Tunneling Microscopy*, S.H. Cohen, M.L. Lightbody, and M.T. Bray, Editors. 1994, Plenum Press: New York. p. 303–311.

93. Krim, J., *QCM tribology studies of thin adsorbed films.* nanotoday, 2007. **2**(5): p. 38–43.

94. Johannsmann, D., *Viscoelastic, mechanical, and dielectric measurements on complex samples with the quartz crystal microbalance.* Physical Chemistry Chemical Physics, 2008. **10**(31): p. 4516.

95. Liese, D., *Oil properties*. 2008: Dortmund.

96. Galsworthy, J., S. Hammond, and D. Hone, *Oil-soluble colloidal additives.* Current Opinion in Colloid & Interface Science, 2000. **5**(5–6): p. 274-279.

97. Kern, W., *The Evolution of Silicon Wafer Cleaning Technology.* Journal of The Electrochemical Society, 1990. **137**(6): p. 1887-1892.

98. Hübschmann, H.-J., *Handbook of GC/MS: Fundamentals and applications*. 2nd, completely rev. and updated ed ed. 2009, Weinheim: Wiley-VCH. xvii, 719.

99. Totten, G.E., *Handbook of Lubrication and Tribology: Volume I Application and Maintenance*. Vol. 1. 2006: CRC Press.

100. de Groot, P., *Coherence Scanning Interferometry*, in *Optical Measurement of Surface Topography*, R. Leach, Editor. 2011, Springer Berlin Heidelberg: Berlin, Heidelberg. p. 187-208.

101. Schrader, B. and D. Bougeard, *Infrared and Raman spectroscopy: Methods and applications*. 1995, Weinheim; New York: VCH. xx, 787.

102. Kudelski, A., *Analytical applications of Raman spectroscopy.* Talanta, 2008. **76**(1): p. 1–8.

103. Lewis, I.R. and H.G.M. Edwards, *Handbook of Raman spectroscopy: From the research laboratory to the process line*. Practical spectroscopy. 2001, New York: Marcel Dekker. xiii, 1054.

104. Salzer, R. and H.W. Siesler, *Infrared and Raman spectroscopic imaging*. 2009, Weinheim: Wiley-VCH. xx, 510.

105. Günzler, H. and H.-U. Gremlich, *IR-Spektroskopie: Eine Einführung*. 4 ed. 2003, Weinheim: Wiley-VCH. XIII, 352 S.

106. Benninghoven, A., *Chemische Analyse von anorganischen und organischen Oberflächen und von dünnen Schichten mit der statischen Flugzeit-Sekundärionen-Massenspektrometrie (TOF-SIMS).* Angewandte Chemie, 1994. **106**(10): p. 1075–1096.

107. Cremers, D.A. and L.J. Radziemski, *Handbook of Laser-Induced Breakdown Spectroscopy*. Second edition ed. 2013, Oxford, UK: John Wiley & Sons Ltd. 1 online resource.

108. Kuss, H.-M., H. Mittelstaedt, and G. Mueller, *Inclusion mapping and estimation of inclusion contents in ferrous materials by fast scanning laser-induced optical emission spectrometry.* Journal of Analytical Atomic Spectrometry, 2005. **20**(8): p. 730-735.

109. Moulder, J.F. and J. Chastain, *Handbook of X-ray photoelectron spectroscopy: A reference book of standard spectra for identification and interpretation of XPS data*. 1995, Eden Prairie; Minn.: Physical Electronics. 261.

110. Lin-Vien, D., et al., *The Handbook of infrared and raman characteristic frequencies of organic molecules*. 1991, San Diego: Academic Press. 503.

111. Trofimov, B.A., L.M. Sinegovskaya, and N.K. Gusarova, *Vibrations of the S-S bond in elemental sulfur and organic polysulfides: a structural guide.* Journal of Sulfur Chemistry, 2009. **30**(5): p. 518–554.

112. Allum, K.G., et al., *The vibrational spectra of some dialkyl and diaryl disulphides and of di-n-butyl diselenide.* Spectrochimica Acta Part A: Molecular Spectroscopy, 1968. **24**(7): p. 927–941.

113. Bastian, E.J. and R.B. Martin, *Disulfide vibrational spectra in the sulfur-sulfur and carbon-sulfur stretching region.* The Journal of Physical Chemistry, 1973. **77**(9): p. 1129–1133.

114. Colthup, N.B., L.H. Daly, and S.E. Wiberley, *Introduction to infrared and Raman spectroscopy.* 1975.

115. Mangolini, F., A. Rossi, and N.D. Spencer, *Reactivity of Triphenyl Phosphorothionate in Lubricant Oil Solution.* Tribology Letters, 2009. **35**(1): p. 31–43.

116. Stobart, S.R., *Characteristic vibrational frequencies of compounds containing main-group elements*, in *Spectroscopic Properties of Inorganic and Organometallic Compounds: Volume 6*, N.N. Greenwood, Editor. 1973, The Royal Society of Chemistry. p. 245-308.

117. Tavacoli, J.W., et al., *Effect of Water on Overbased Sulfonate Engine Oil Additives.* Langmuir, 2008. **24**(8): p. 3807-3813.

118. Said, E.Z., I.H. Al-Wahaib, and H.H. Nima, *Infrared spectrophotometric determination of the alkalinity of overbased petroleum sulphonates.* Analyst, 1987. **112**(4): p. 499-500.

119. Giasson, S., et al., *Study of boundary film formation with overbased calcium sulfonate by PM-IRRAS spectroscopy.* Thin Solid Films, 1994. **252**(2): p. 111–119.

120. Palermo, T., et al., *Study of deposit and friction films of overbased calcium sulphonate by PM-IRRAS spectroscopy.* Lubrication Science, 1996. **8**(2): p. 119-127.

121. Liu, X., et al., *Influence of Surface Roughness of Galvanized Steel Sheet on Self-lubricated Coating.* Journal of Iron and Steel Research, International, 2014. **21**(3): p. 342-347.

122. Damen, T.C., S.P.S. Porto, and B. Tell, *Raman Effect in Zinc Oxide.* Physical Review, 1966. **142**(2): p. 570–574.

123. Manikandan, E., G. Kavitha, and J. Kennedy, *Epitaxial zinc oxide, graphene oxide composite thin-films by laser technique for micro-Raman and enhanced field emission study.* Ceramics International, 2014. **40**(10, Part A): p. 16065-16070.

124. Matsumoto, K., *Surface Chemical and Tribological Investigations of Phosphorus-Containing Lubricant Additives*, in *Swiss Federal Institute of Technology*. 2003, Eidgenössische Technische Hochschule: Zürich.

125. Mangolini, F., A. Rossi, and N.D. Spencer, *Tribochemistry of Triphenyl Phosphorothionate (TPPT) by In Situ Attenuated Total Reflection (ATR/FT-IR) Tribometry.* The Journal of Physical Chemistry C, 2012. **116**(9): p. 5614-5627.

126. Heuberger, R.C., *Combinatorial Study of the Tribochemistry of Anti-Wear Lubricant Additives*. 2007, Eidgenössische Technische Hochschule: Zürich.

127. Heuberger, R.C., A. Rossi, and N.D. Spencer, *Reactivity of alkylated phosphorothionates with steel: a tribological and surface-analytical study.* Lubrication Science, 2008. **20**(2): p. 79–102.

128. Hoshino, K., et al., *Effect of Al-based Oxide Layer on Frictional Properties of Hot-dip Galvanized Steel Sheets.* ISIJ International, 2017. **57**(5): p. 895-904.

129. Lu, C.-J., et al., *Nano-tribological investigations of carbon overcoats: Correlation with Raman spectra.* Thin Solid Films, 1995. **268**(1-2): p. 83–90.

130. Najman, M.N., et al., *Study of the Chemistry of Films Generated from Phosphate Ester Additives on 52100 Steel Using X-ray Absorption Spectroscopy.* Tribology Letters, 2002. **13**(3): p. 209–218.

131. Landolt, D., H. Mathieu, and R. Schumacher. *Surface reactivity of anti-wear additives*. in *Analytical proceedings*. 1993: Royal Society of Chemistry.

132. Masuko, M., K. Akatsuka, and H. Okabe, *Effect of sulphur-type extreme-pressure additives on wear in rolling-sliding contact.* Lubrication Science, 1989. **2**(1): p. 45–61.

133. Plaza, S., L.R. Comellas, and L. Starczewski, *Tribochemical reactions of dibenzyl and diphenyl disulphides in boundary lubrication.* Wear, 1997. **205**(1-2): p. 71–76.

134. Plaza, S., *Some Chemical Reactions of Organic Disulfides in Boundary Lubrication.* A S L E Transactions, 1987. **30**(4): p. 493–500.

135. Murakami, T., et al., *Lubricating Performance of Organic Sulfides Under Repeated Rubbing Conditions.* Tribology Transactions, 1985. **28**(3): p. 363–373.

136. Sakai, T., T. Murakami, and Y. Yamamoto, *Lubricating Performance of Organic Sulfides Under Repeated Rubbing Conditions. Part II: Effect of Additive Concentration.* Tribology Transactions, 1991. **34**(2): p. 215–222.

137. Hu, L., et al., *Structural changes in soot particles induced by diode laser irradiation.* Carbon, 2006/8//. **44**(9): p. 1725–1729.

138. UY, D., et al., *Characterization of anti-wear films formed from fresh and aged engine oils: 16th International Conference on Wear of Materials.* Wear, 2007. **263**(7-12): p. 1165–1174.

139. Forbes, E.S., *The load-carrying action of organo-sulphur compounds-A review.* Wear, 1970/2//. **15**(2): p. 87–96.

140. Bowden, F.P. and D. Tabor, *Reibung und Schmierung fester Körper*. 1959, Berlin: Springer Berlin Heidelberg. 1 online resource (440.

141. Liu, D., et al., *Tribological behavior of amorphous and crystalline overbased calcium sulfonate as additives in lithium complex grease.* Tribology Letters, 2012. **45**(2): p. 265-273.

12 Appendix

12.1 Interfacial adsorption processes on zinc alloys

12.1.1 Reference measurements

Diphenyldisulphide

GC-MS

The gas chromatography of diphenyldisulphide shows the high purity of this additive because there is only one peak with a retention time of 9.5 minutes (Figure 131; left). The corresponding mass-spectrometry (Figure 131; right) of this fraction has as the strongest signal the molecule-peak [M+] at m/z=218. An additional peak at m/z=109 belongs to the sulfur-bridge split molecule fragment.

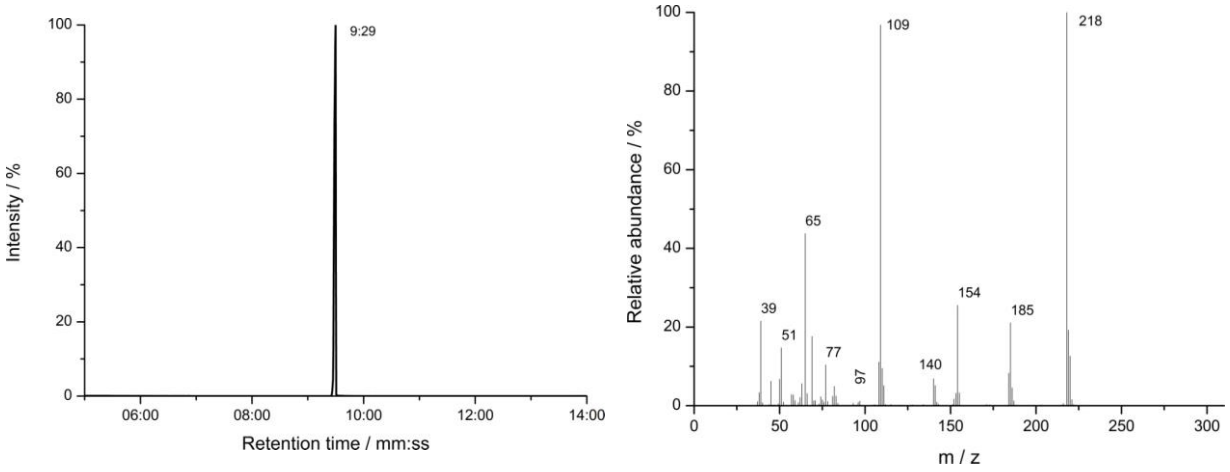

Figure 131. Gas chromatography spectrum (left) and mass spectrum at retention time of 9:29 (mm:ss) of diphenyldisulphide

Diffuse reflectance infrared Fourier transform spectroscopy (DRIFTS)

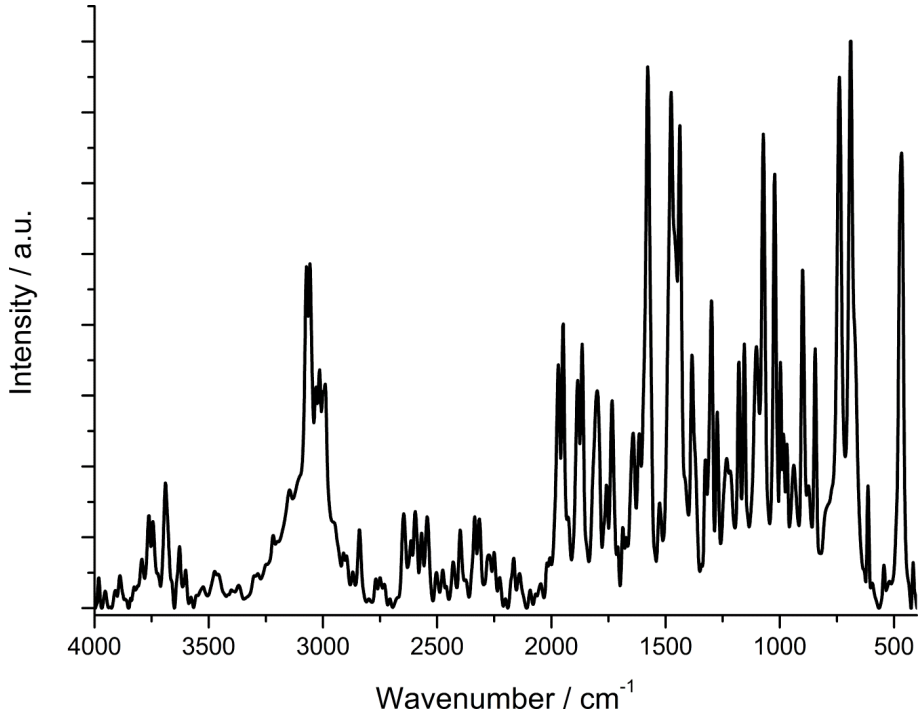

Figure 132. DRIFT spectrum pure of diphenyldisulphide with KBr

Raman spectroscopy

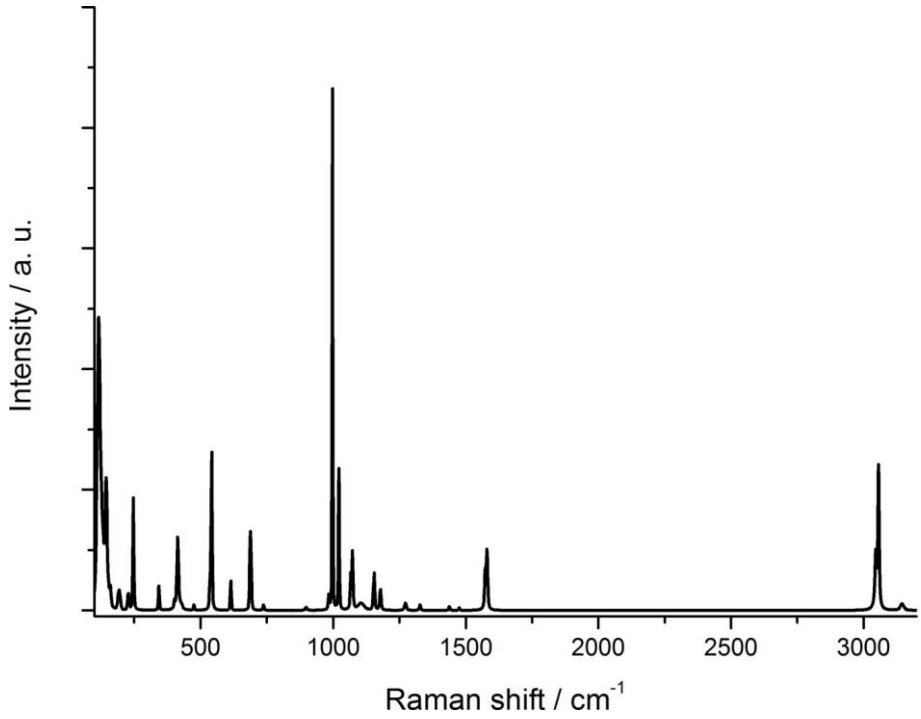

Figure 133. Raman spectra of solid diphenyldisulphide

Irgalube 349

GC-MS

The GC-spectrum of Irgalube 349 shows an intensive broad peak around a retention time of 12.2 minutes. The corresponding mass spectrum reveals multiple peaks in the higher mass range, each with a distance of m/z=14 which indicates alkyl chain fragments with different chain lengths. The peaks at m/z=44 and m/z=57 are suggested as possible amine fragments.

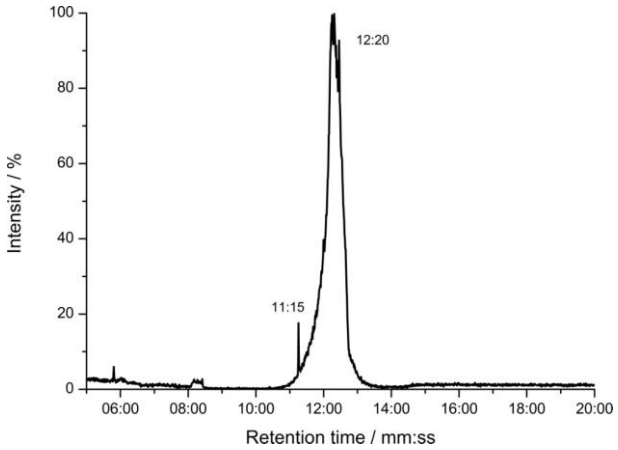

Figure 134. Gas chromatography spectrum of Irgalube 349 in $CDCl_3$

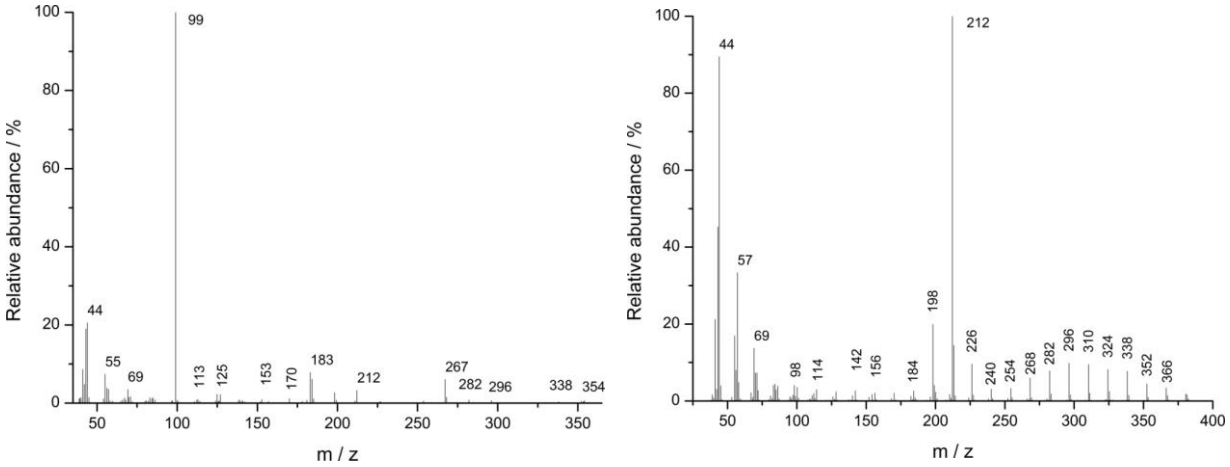

Figure 135. Mass spectra of Irgalube 349 at retention time of 11:15 (mm:ss) (left) and 12:14 (mm:ss) (right)

Diffuse reflectance infrared fourier transform spectroscopy (DRIFTS)

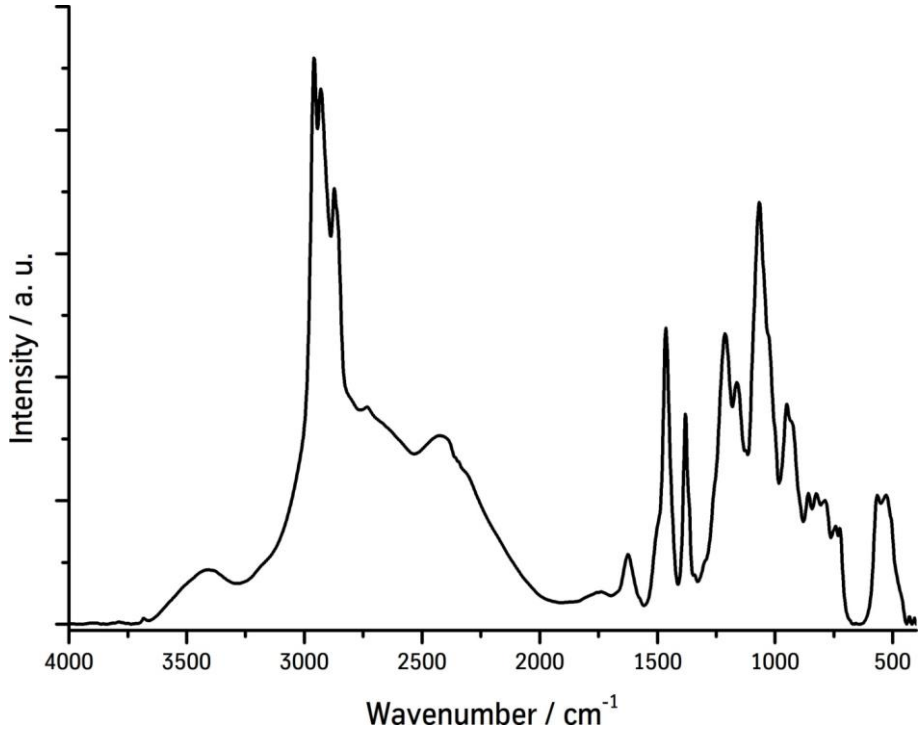

Figure 136. DRIFT spectrum pure Irgalube 349 with KBr

Raman spectroscopy

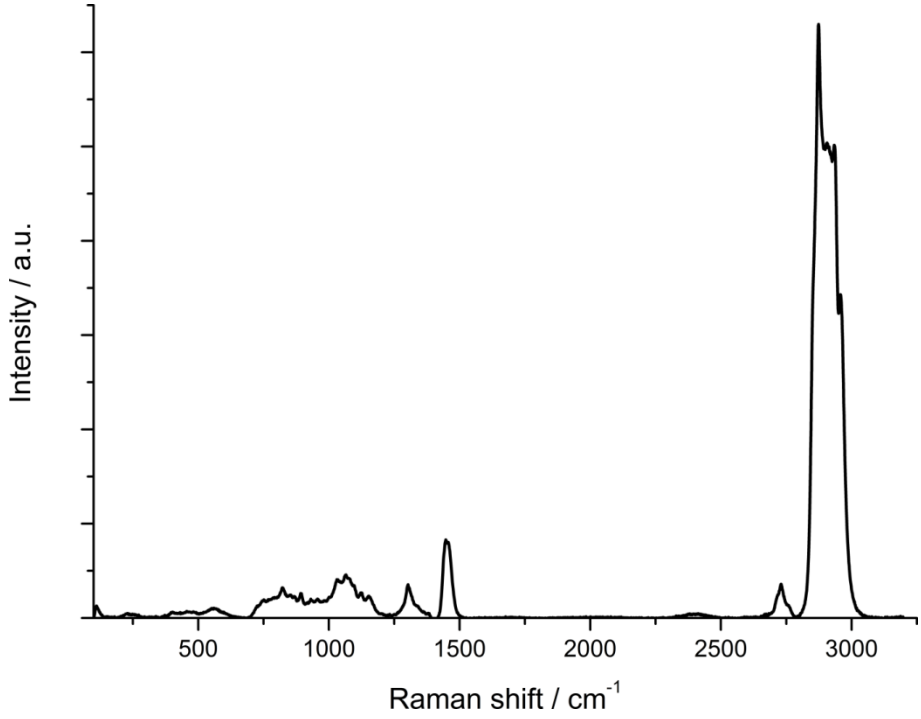

Figure 137. Raman spectrum of Irgalube 349

12.1.2 Adsorption on non-skin passed hot-dip galvanized steel (NSP-HDG)

Irgalube 349

X-ray photoelectron spectroscopy measurements (XPS)

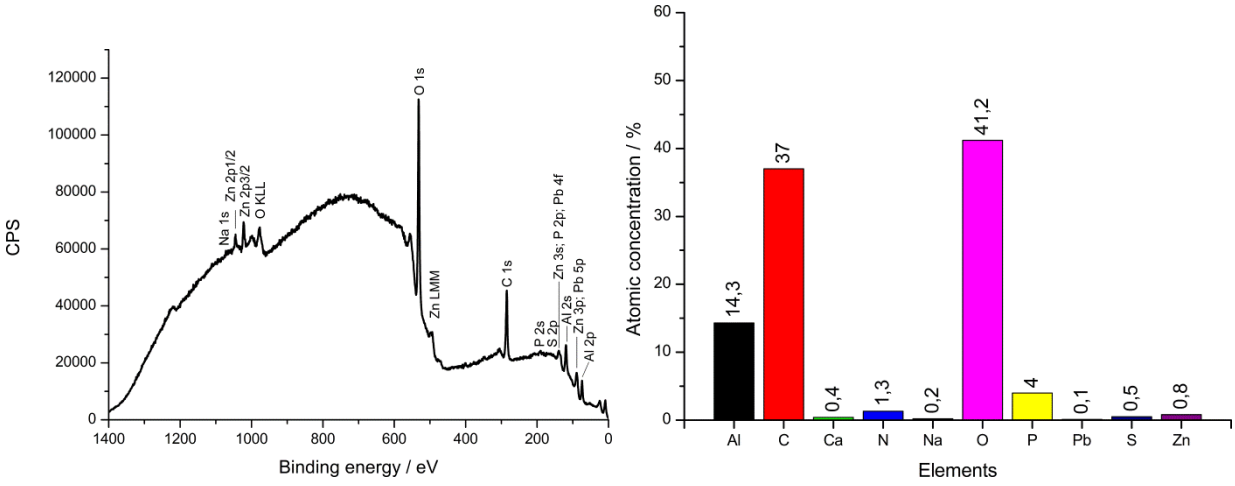

Figure 138. XPS survey (l.) and atomic concentrations (r.) of Irgalube 349 on NSP-HDG steel

The XPS survey in Figure 138 shows the expected elements of adsorbed Irgalube 349 on NSP-HDG like aluminum, carbon, oxygen, phosphorus and zinc along with small contaminations like calcium, nitrogen, sodium, lead and sulfur. The detailed atomic concentrations of all elements are also shown in Figure 138.

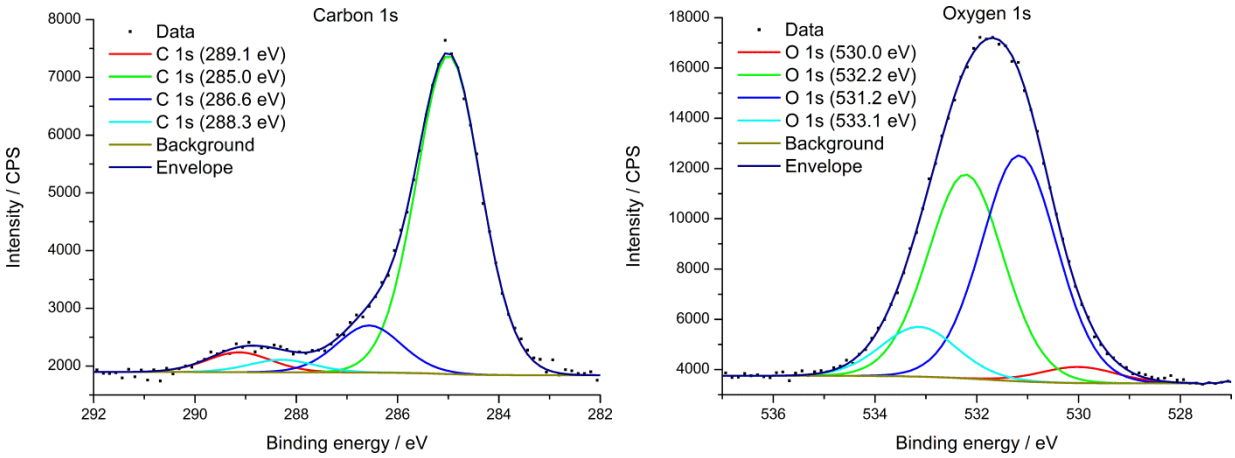

Figure 139. High-resolution XPS spectra of the *C 1s* (l.) and *O 1s* (r.) region of Irgalube 349 on NSP-HDG steel

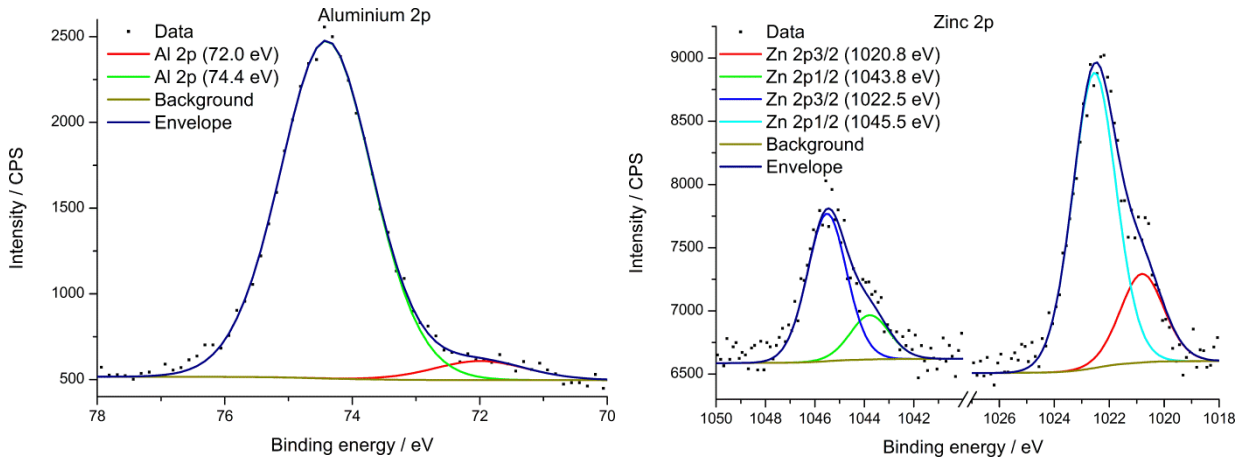

Figure 140. High-resolution XPS spectra of the *Al 2p* (l.) and *Zn 2p* (r.) region of Irgalube 349 on NSP-HDG steel

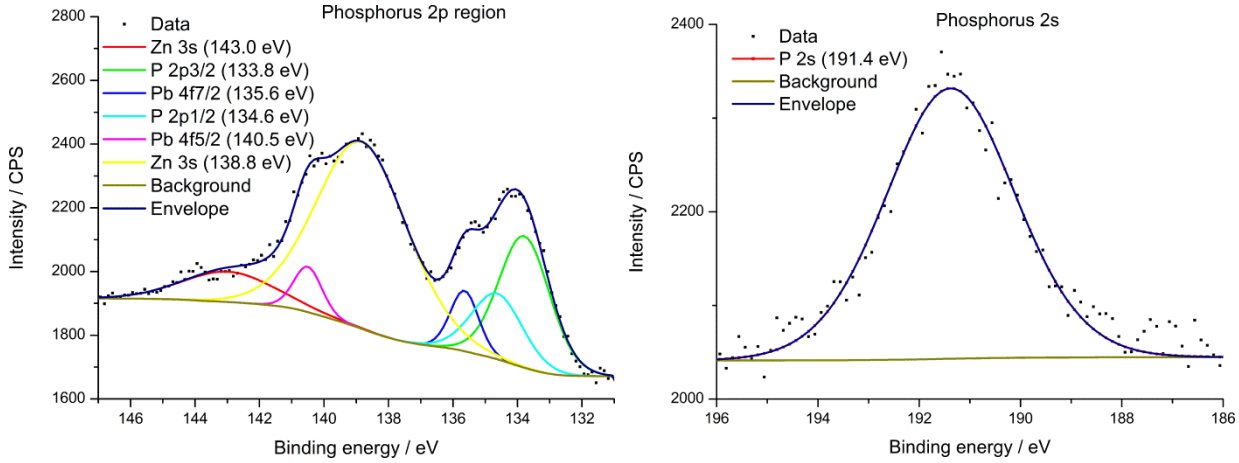

Figure 141. High-resolution XPS spectra of the *phosphorus 2p* (l.) and *P 2s* (r.) region of Irgalube 349 on NSP-HDG steel

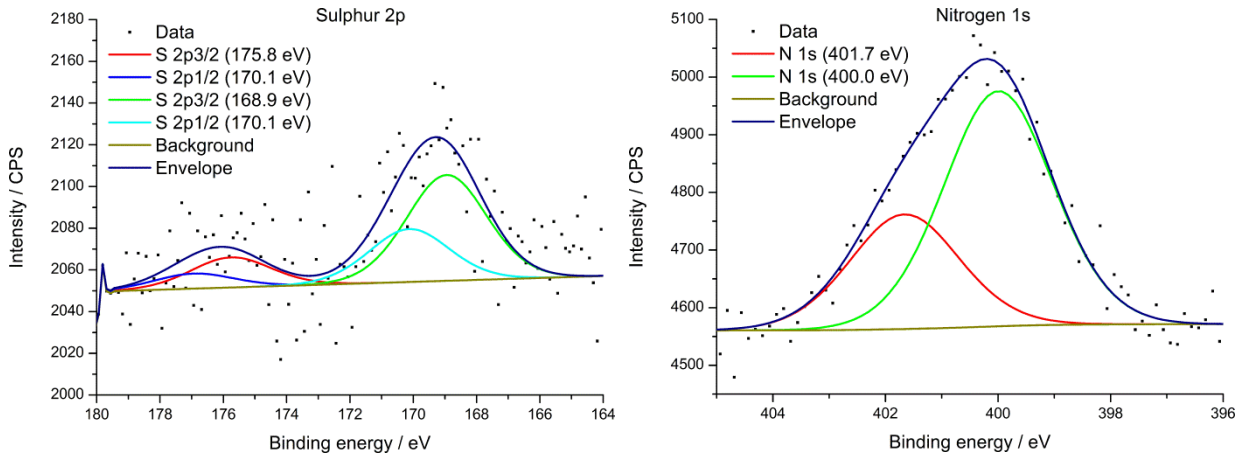

Figure 142. High-resolution XPS spectra of the *S 2p* (l.) and *N 1s* (r.) region of Irgalube 349 on NSP-HDG steel

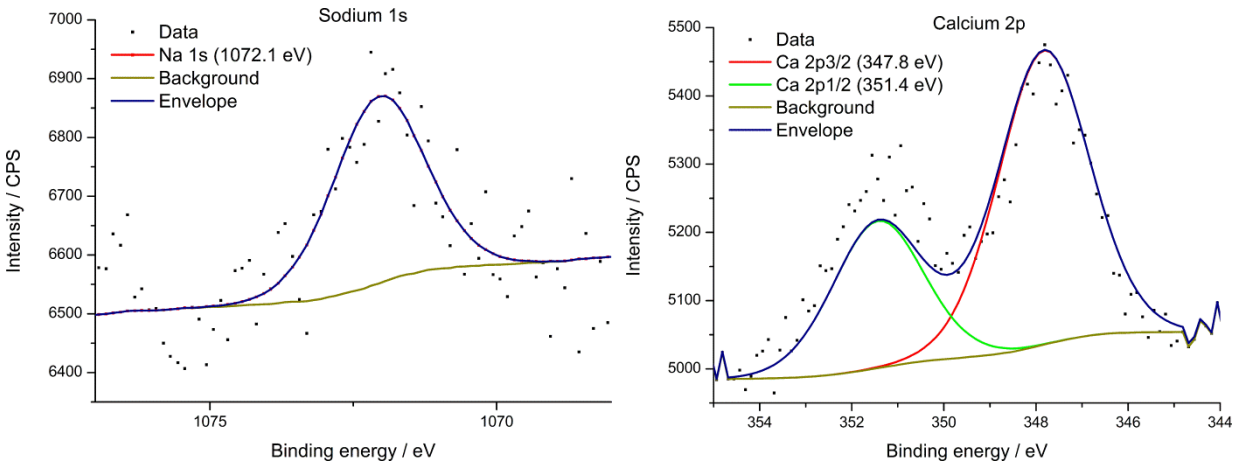

Figure 143. High-resolution XPS spectra of the *Na 1s* (l.) and *Ca 2p* (r.) region of Irgalube 349 on NSP-HDG steel

Time of flight secondary ion mass spectrometry (ToF-SIMS)

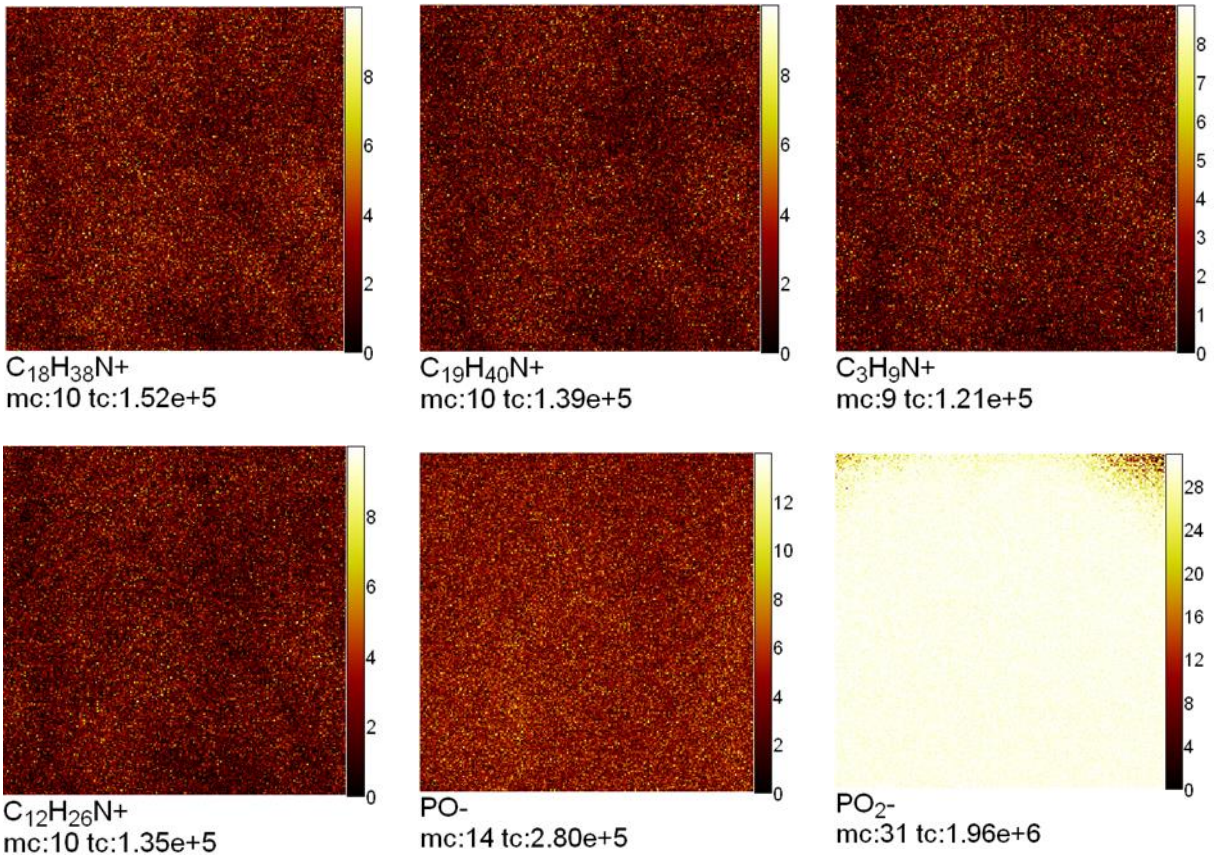

Figure 144. ToF-SIMS ion images of Irgalube 349 on NSP-HDG steel

12.1.3 Adsorption on pure zinc (Zn)

Irgalube 349

X-ray photoelectron spectroscopy measurements (XPS) (Osnabrück)

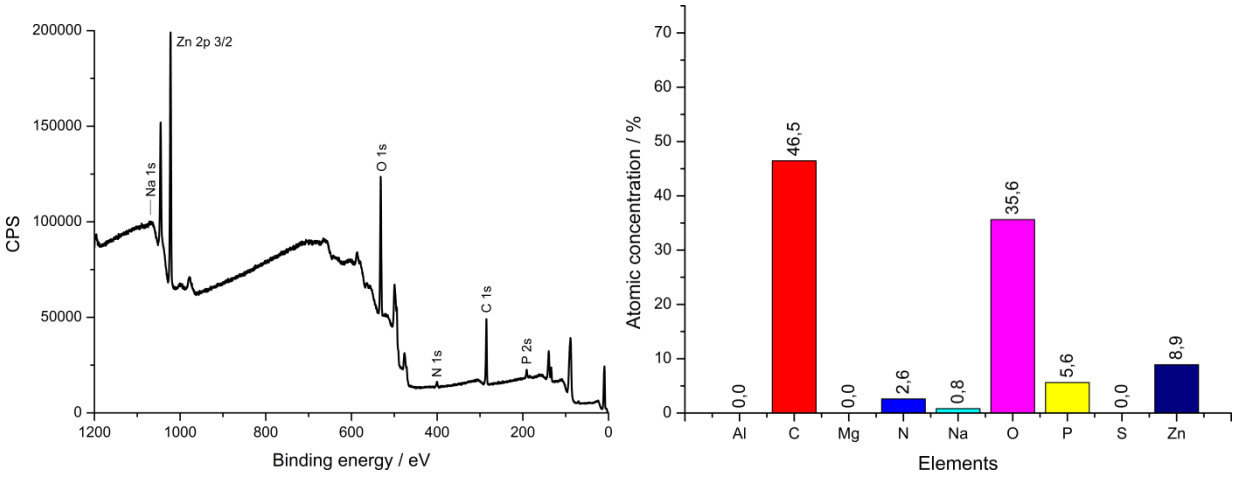

Figure 145. XPS survey (l.) and atomic concentrations (r.) of Irgalube 349 on Zn

The XPS survey (Figure 145; l.) of an Irgalube 349 treated zinc sample indicates a oxidized zinc surfaces with coverage of Irgalube 349. There is also a small contamination of sodium on the sample.

Figure 145 also shows the atomic concentrations evaluated out of this survey in full detail.

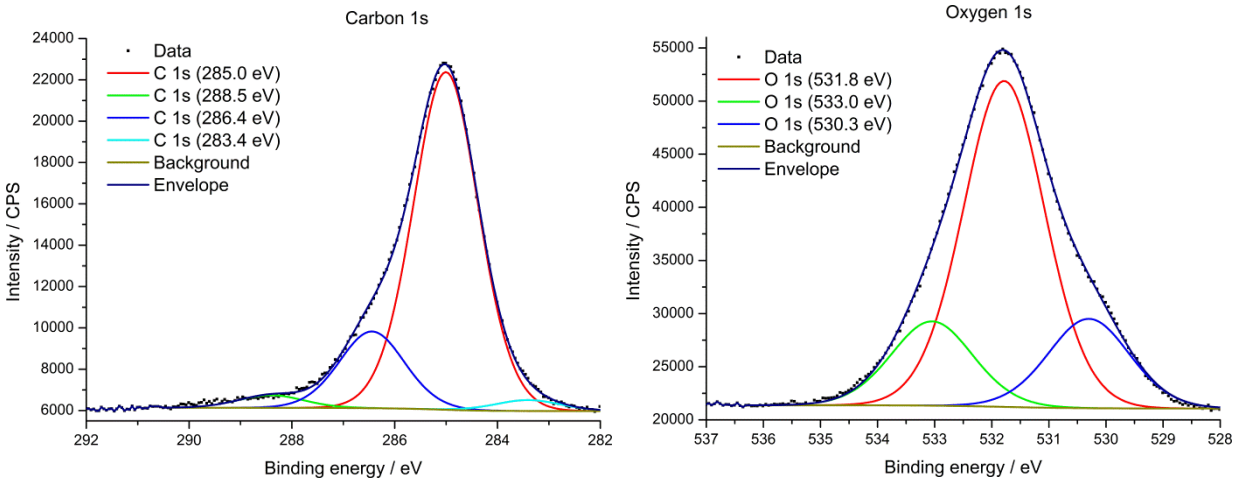

Figure 146. High-resolution XPS spectra of the *C 1s* (l.) and *O 1s* (r.) region of Irgalube 349 on Zn

High-resolution spectra for *C 1s* and *O 1s* measured on zinc-adsorbed Irgalube 349 are shown in Figure 146. Their curve fitting results after Shirley background subtraction are also shown in Figure 146.

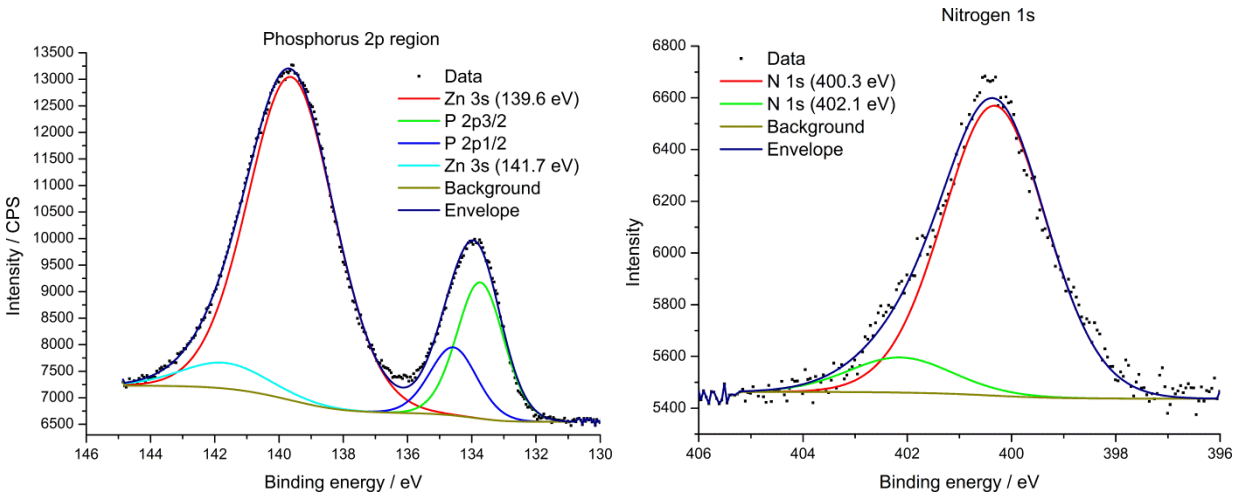

Figure 147. High-resolution XPS spectra of the *phosphorus 2p* (l.) and *N 1s* (r.) region of Irgalube 349 on Zn

The high-resolution XPS spectra of the *phosphorus 2p* region (Figure 147; l.) in the range between 146-130 eV shows a main peak of the *zinc 3s* orbital at 139.6 eV and a minor peak at 141.7 eV.

The signal of the *phosphorus 2p* orbital is separated in the two peaks *P 2p3/2* and *P 2p1/2* due to spin-orbit splitting. The peak of *P 2p3/2* (133.7 eV) is double that of the *P 2p1/2* (134.6 eV) peak. The two peaks are separated by 0.84 eV, which was used as constraint for fitting the phosphorus signal.

The *nitrogen 1s* signal (Figure 147; r.) consists of two peaks at 400.3 eV and 402.1 eV which couldn`t be further assigned.

12.1.4 Adsorption on zinc alloy (ZnAlMg)

Irgalube 349

X-ray photoelectron spectroscopy measurements (XPS) (Osnabrück)

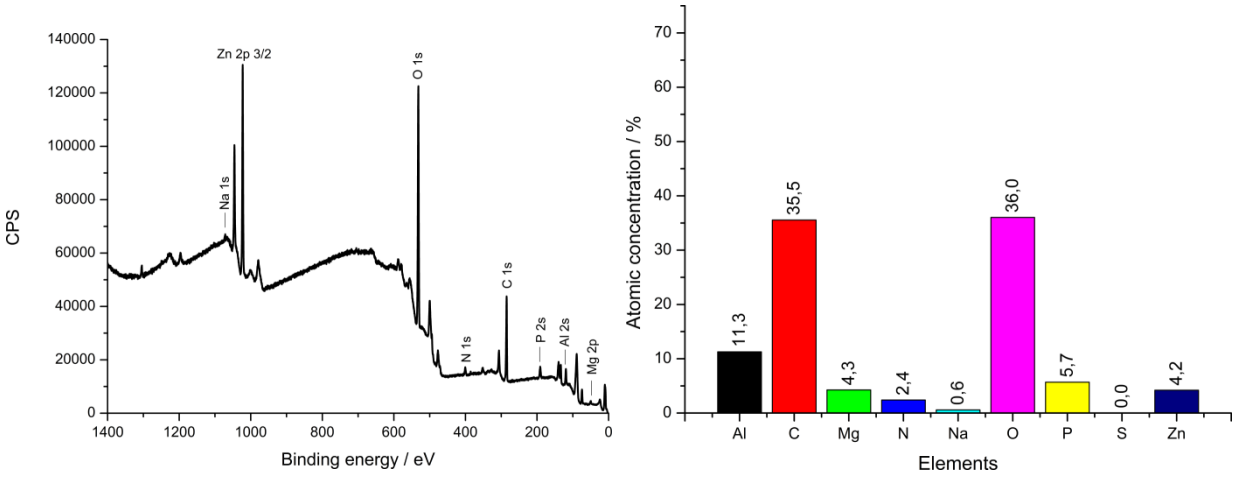

Figure 148. XPS survey (l.) and atomic concentrations (r.) of Irgalube 349 on ZnAlMg

The XPS survey of Irgalube 349 on ZnAlMg (Figure 148; l.) reveals the expected signals of Al, C, Mg, O, P and Zn. Additional signals of contaminations with nitrogen and sodium are observable. The evaluated atomic concentrations are also shown in Figure 148.

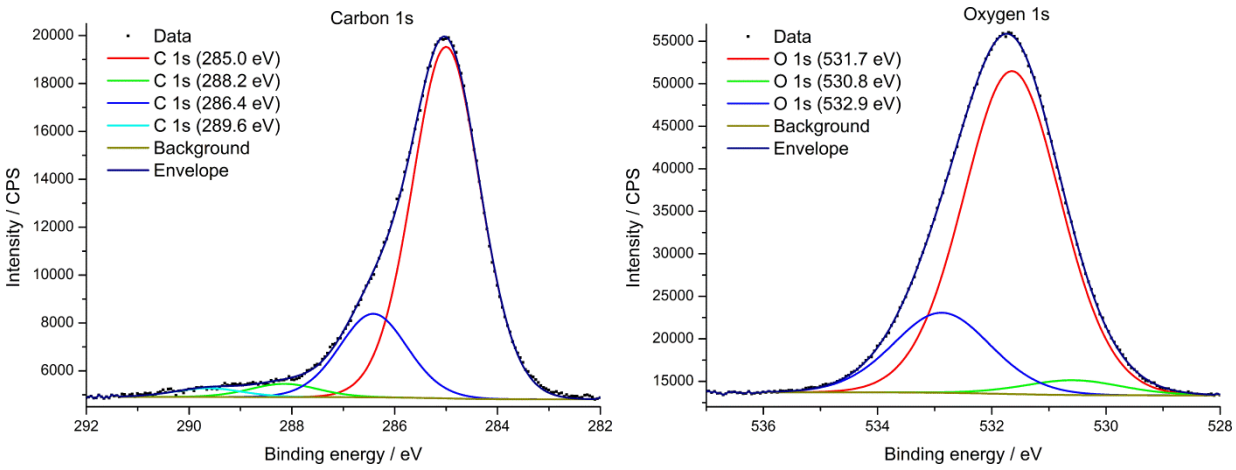

Figure 149. High-resolution XPS spectra of the *C 1s* (l.) and *O 1s* (r.) region of Irgalube 349 on zinc alloy

The *carbon 1s* high-resolution spectrum (Figure 149, l.) gives the best fit with four peaks, where the lowest peak at 285.0 eV is assigned to hydrocarbons. The peak at 286.4 eV is assigned to –C-OH or –COC-

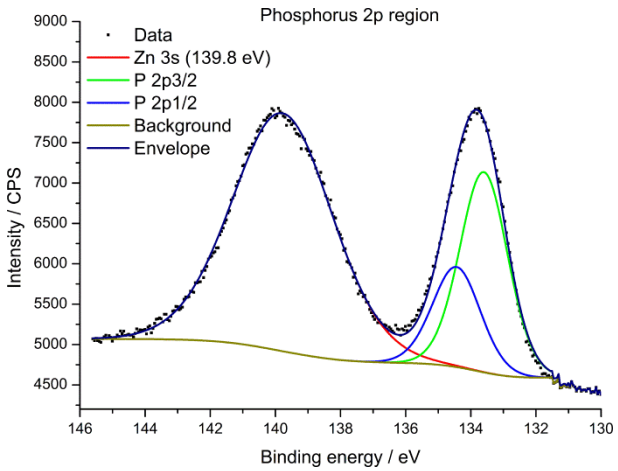

Figure 150. High-resolution XPS spectra of the *phosphorus 2p* region of Irgalube 349 on zinc alloy

12.2 Reactivity of forming additives during the friction process on ZnAl(0.5)

12.2.1 Dry strip-drawing

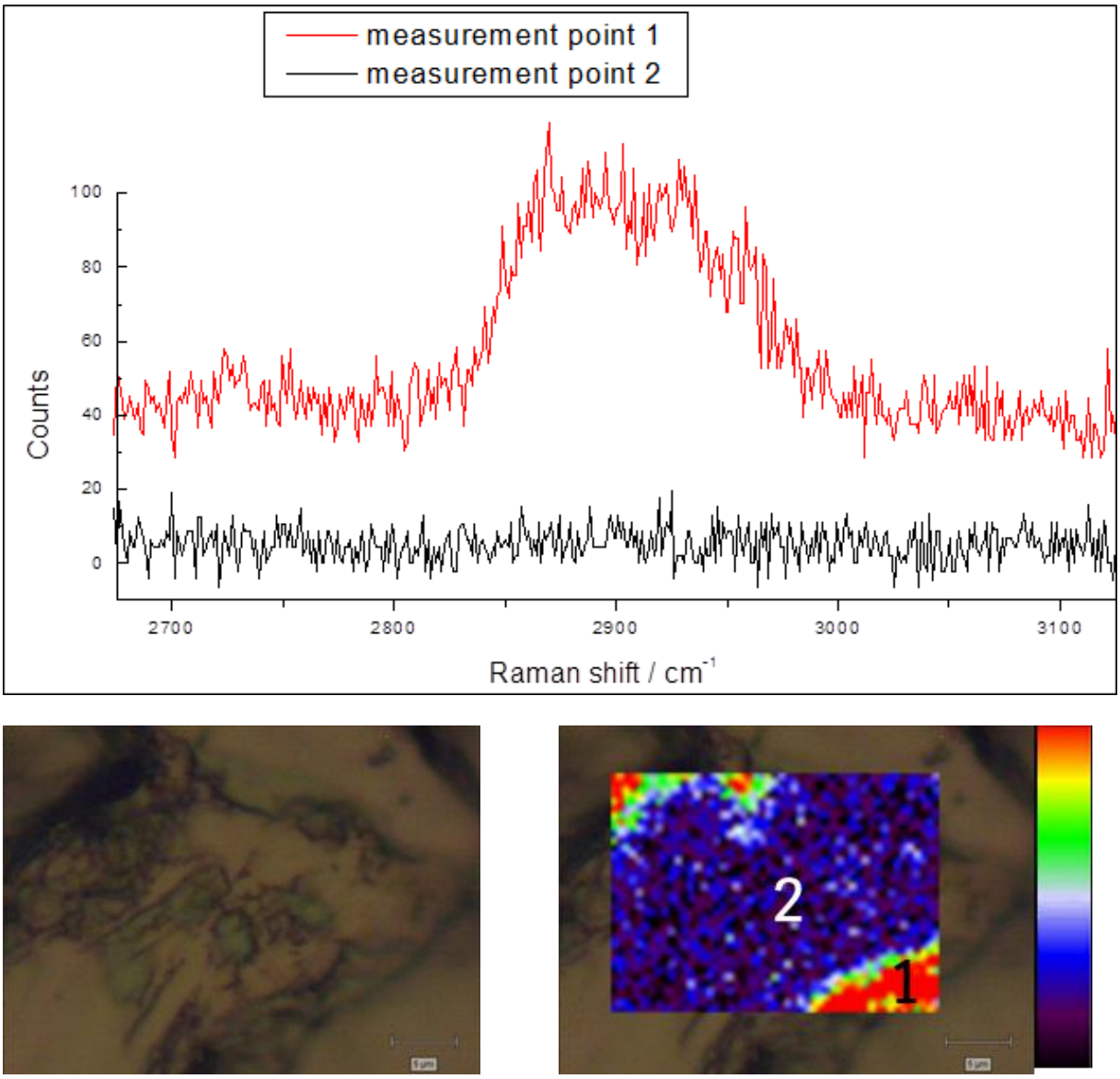

Figure 151. Streamline Raman-imaging of the C-H vibration region of Irgalube 349 on HDG

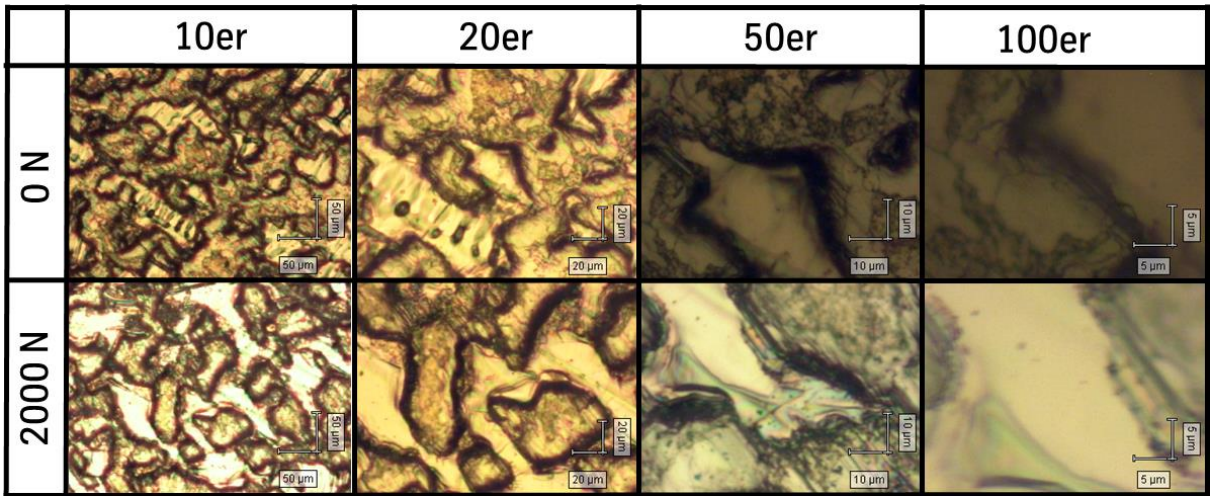

Figure 152. Microscope images of Irgalube 349 coated HDG stripes at various conditions

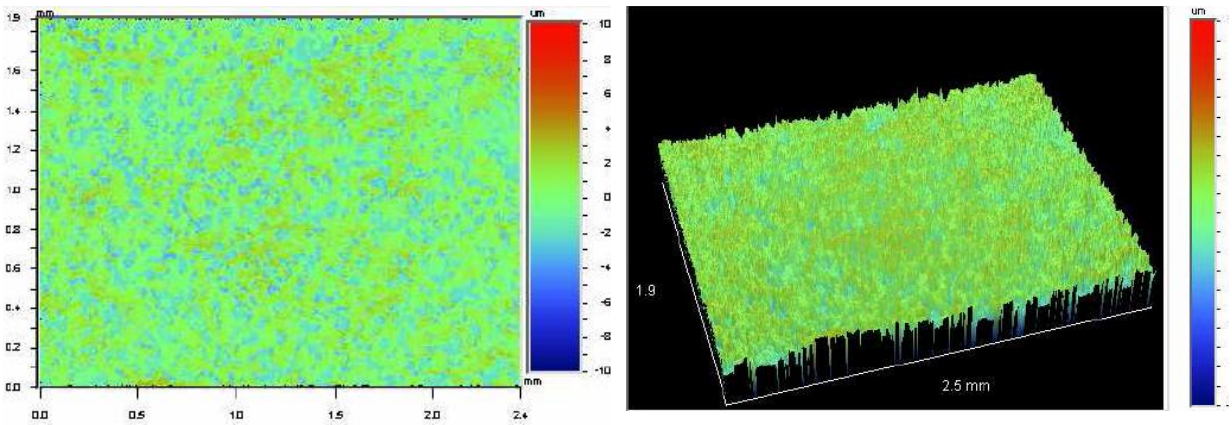

Irgalube 349

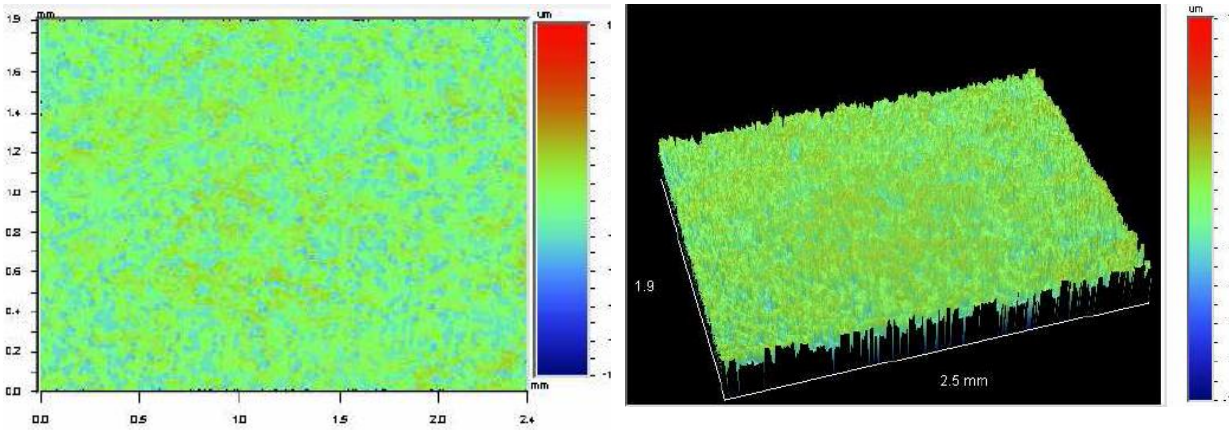

2000 N

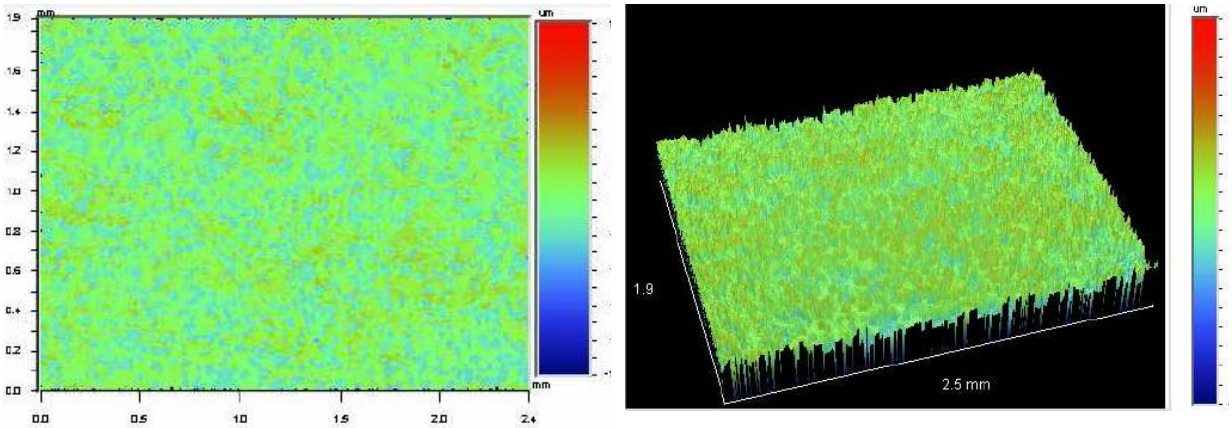

4000 N

Figure 153. 2D- and 3D- morphological maps of Irgalube 349 treated HDG samples before and after oil-free strip drawing

Table 18. Roughness parameters of Irgalube 349 samples after oil-free strip drawing

Roughness parameters:			
	0 N	**2000 N**	**4000 N**
R_z	8.40 µm	7.62 µm	7.44 µm
R_p	4.71 µm	5.29 µm	5.10 µm
R_t	10.81 µm	10.07 µm	9.04 µm
R_a	1.37 µm	1.25 µm	1.27 µm
R_q	1.58 µm	1.45 µm	1.46 µm
Surface Area	4.73 mm^2	4.71 mm^2	4.70 mm^2

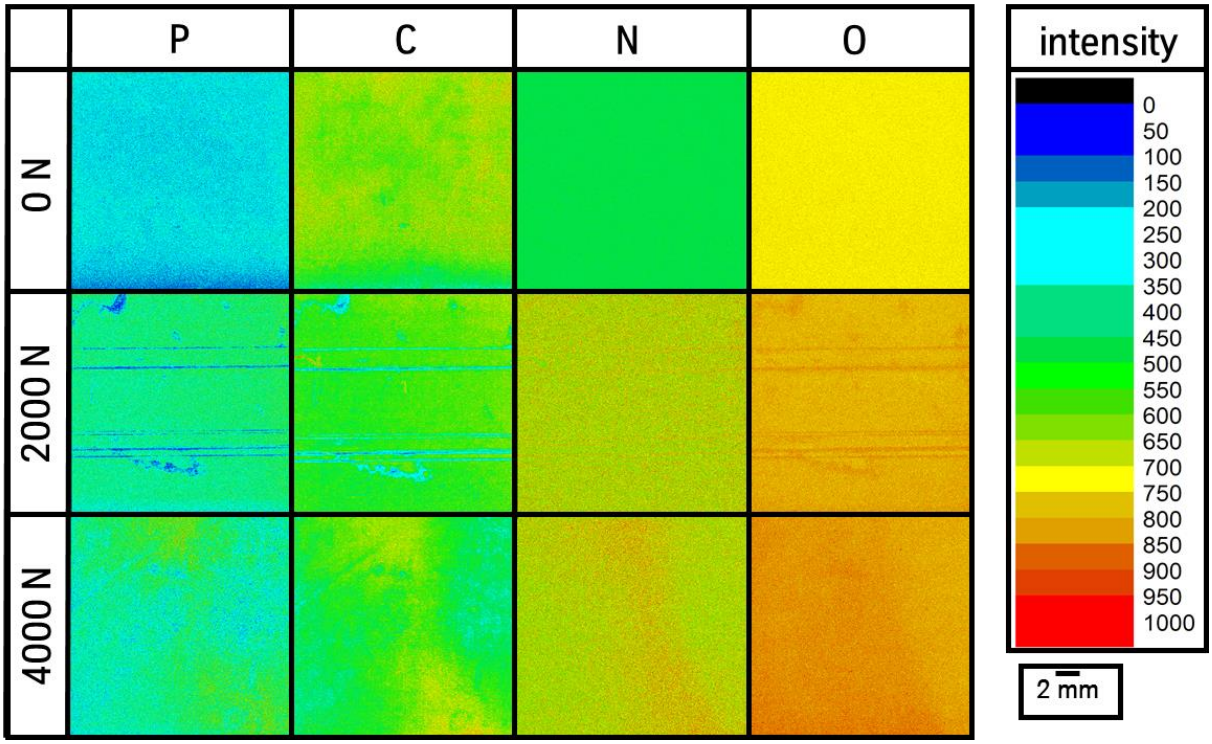

Figure 154. LIBS element distribution of Irgalube 349 coated HDG at various conditions

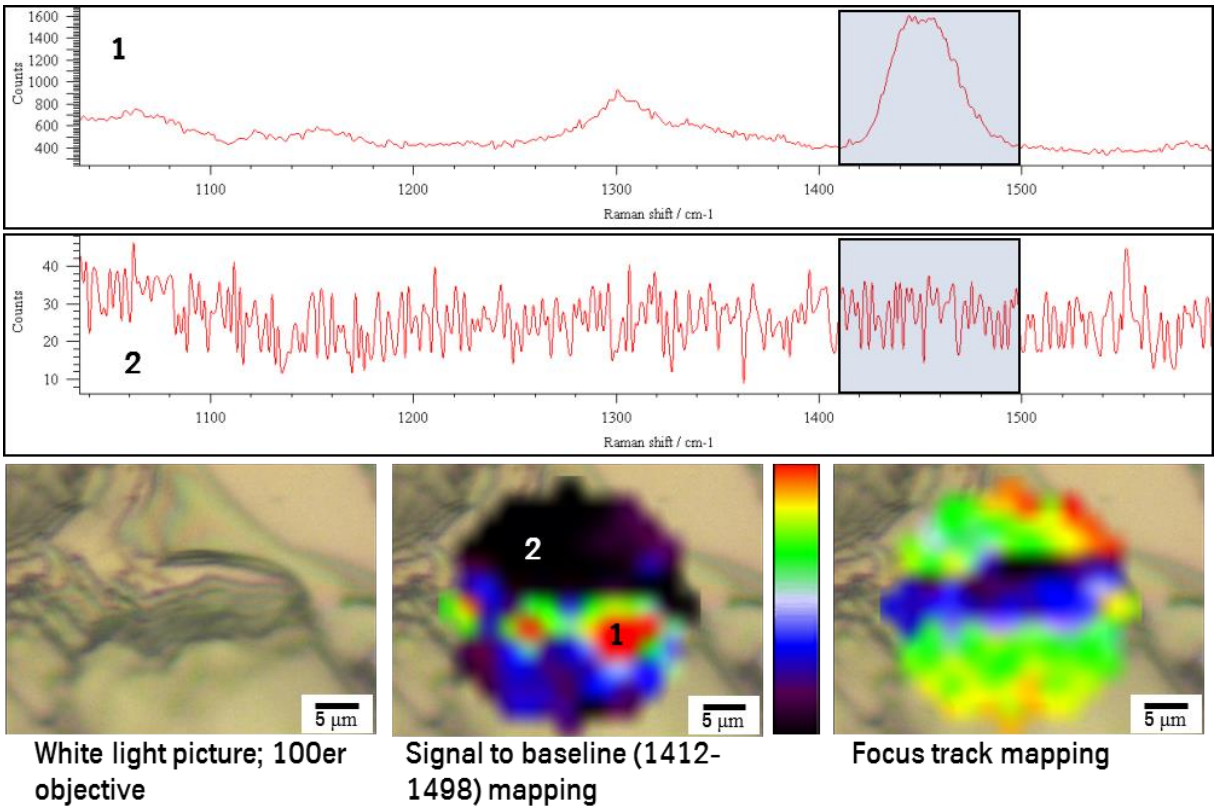

Figure 155. Static single point Raman mapping of Irgalube 349 on HDG after tribological treatment with 2000 N

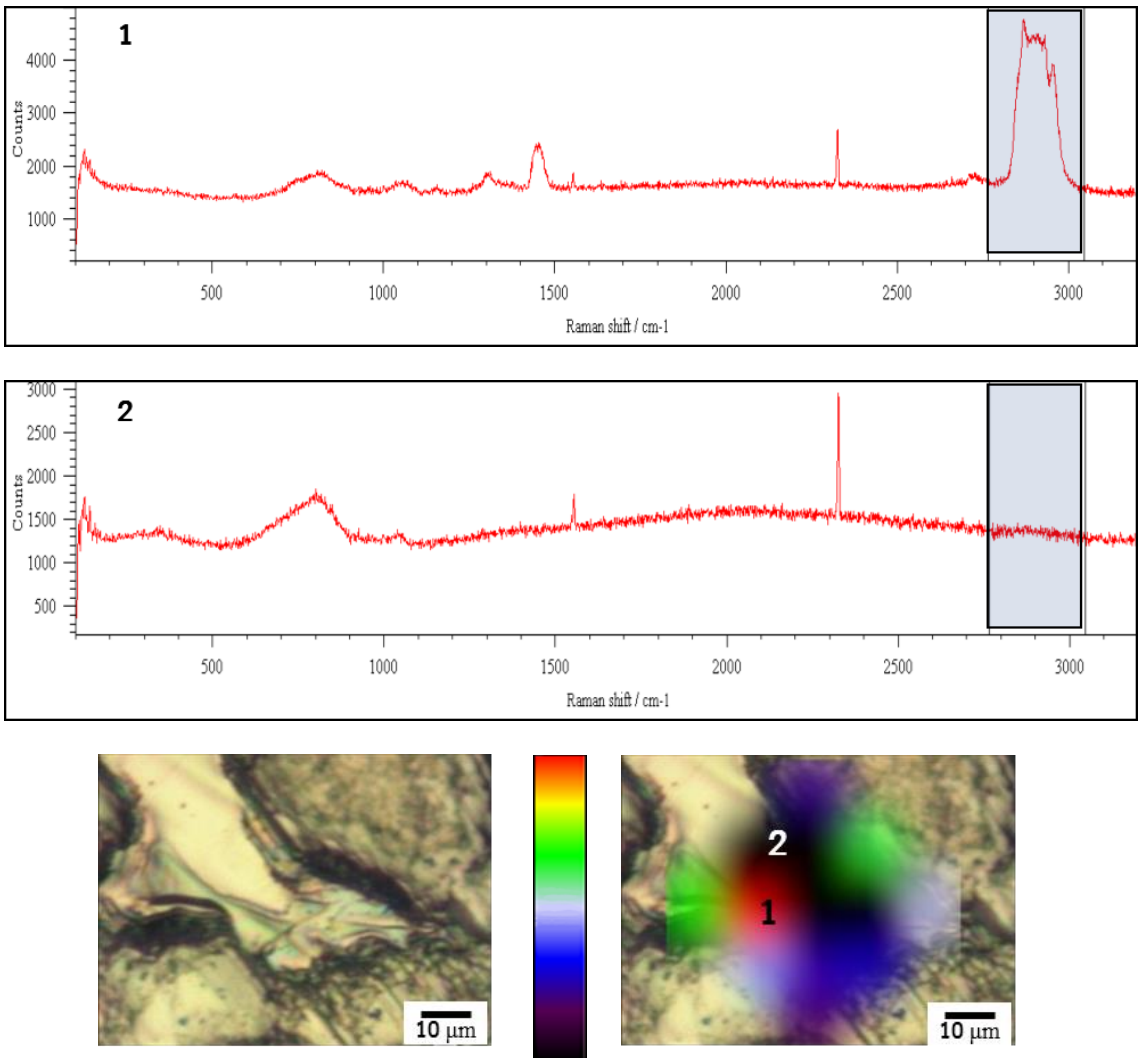

Figure 156. Static single point Raman mapping of Irgalube 349 on HDG after tribological treatment with 2000 N